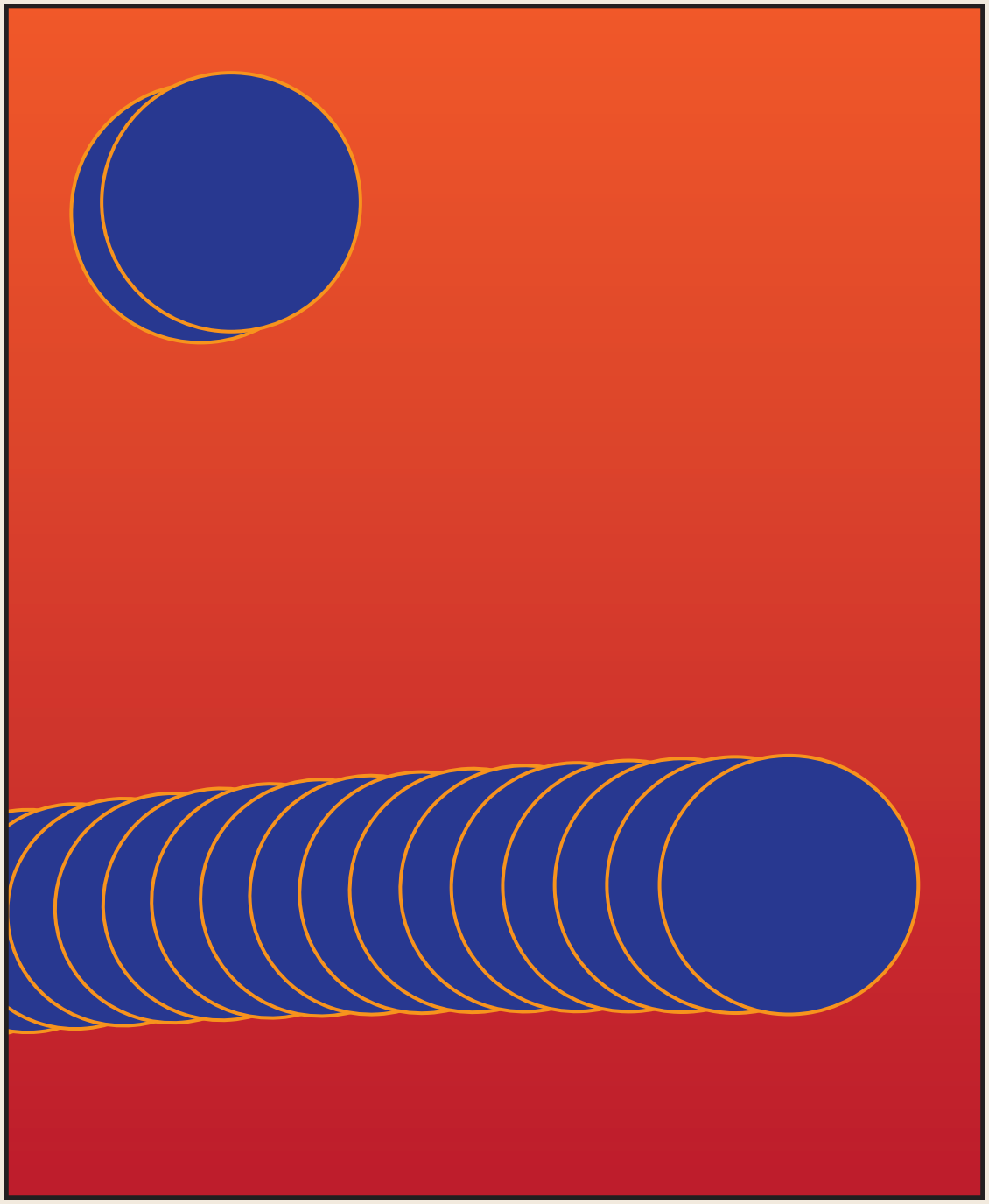
Hybrid spin-boson systems

quantum simulations, sensing and dynamics

Liam J. Bond



Hybrid spin-boson systems: quantum simulations, sensing and dynamics

ACADEMISCH PROEFSCHRIFT

ter verkrijging van de graad van doctor
aan de Universiteit van Amsterdam
op gezag van de Rector Magnificus
prof. dr. ir. P.P.C.C. Verbeek
ten overstaan van een door het College voor Promoties ingestelde commissie,
in het openbaar te verdedigen in de Agnietenkapel
op donderdag 11 juni 2026, te 13.00 uur

door

Liam Joseph Bond

geboren te Auchenflower

Promotiecommissie

Promotor:	dr. A. Safavi-Naini	Universiteit van Amsterdam
Copromotores:	dr. R. Gerritsma	Universiteit van Amsterdam
	dr. J. Minář	Universiteit van Amsterdam
Overige leden:	prof. dr. C.J.M. Schoutens	Universiteit van Amsterdam
	prof. dr. A.J. Daley	University of Oxford
	prof. dr. J.S. Caux	Universiteit van Amsterdam
	dr. V. Gritsev	Universiteit van Amsterdam
	dr. O. Katz	Cornell University

Faculteit der Natuurwetenschappen, Wiskunde en Informatica

The work described in this thesis was carried out at the Institute of Theoretical Physics (IOP) of the University of Amsterdam, Science Park 904, 1098 XH Amsterdam, The Netherlands, where a limited number of copies of this thesis are available. A digital version of this thesis can be obtained from https://dare.uva.nl.

The work described in this thesis has been supported by the Netherlands Organisation for Scientific Research (NWO), the Institute of Theoretical Physics (IOP) of the University of Amsterdam, and the Quantum Software Consortium (QSC).



To my family

List of publications

Publications forming the content of this thesis:

1. **L. Bond**, L. Lenstra, R. Gerritsma & A. Safavi-Naini. *Effect of micromotion and local stress in quantum simulations with trapped ions in optical tweezers*. Phys. Rev. A **106**, 042612 (2022).
2. **L. J. Bond**, C. H. Valahu, A. Shankar, T. R. Tan & A. Safavi-Naini. *Optimal Displacement Sensing with Spin-Dependent Squeezed States*. arXiv: 2510.25870 (2025).
3. **L. J. Bond**, M. J. Davis, J. Minář, R. Gerritsma, G. K. Brennen & A. Safavi-Naini. *Global variational quantum circuits for arbitrary symmetric state preparation*. Phys. Rev. Res. **7**, L022072 (2025).
4. **L. J. Bond**, A. Safavi-Naini & J. Minář. *Fast Quantum State Preparation and Bath Dynamics Using Non-Gaussian Variational Ansatz and Quantum Optimal Control*. Phys. Rev. Lett. **132**, 170401 (2024).
5. **L. J. Bond**, B. Gerritsen, J. Minář, J. T. Young, J. Schachenmayer & A. Safavi-Naini. *Open Quantum Dynamics with Variational Non-Gaussian States and the Truncated Wigner Approximation*. J. Chem. Phys. **161**, 184113 (2024).

Further publications:

6. I. Maran, **L. J. Bond**, J. T. Young, A. Safavi-Naini & R. Gerritsma. *Vibrationally coupled Rydberg atom-ion molecules*. Phys. Rev. Res. **7**, L022028 (2025).
7. C. Robalo Pereira, **L. J. Bond**, M. Mazzanti, R. Gerritsma & A. Safavi-Naini. *Fast Quantum Gates with Electric Field Pulses and Optical Tweezers in Trapped Ions*. Entropy **27**, 595 (2025).
8. M. J. Millican, V. G. Matsos, C. H. Valahu, T. Navickas, **L. J. Bond** & T. R. Tan. *Engineering Continuous-Variable Entanglement in Mechanical Oscillators with Optimal Control*. arXiv: 2505.20844 (2025).

My contribution to these publications:

1.–4. I performed the numerical simulations and led the theory development, manuscript writing and refereeing process.

5. I performed the numerical simulations and led the theory development for the non-Gaussian state content. I led the manuscript writing and refereeing process.

6.–7. I assisted with the development of the theory and numerical simulations, and provided feedback on the manuscript.

8. I developed the explanation for the success of the optimal control, and provided feedback on the manuscript.

Contents

Publications v

Contents vii

Introduction 1
I.1 Quantum simulations . . . 1
I.2 Quantum sensing . . . 3
I.3 Quantum state preparation . . . 4
I.4 Classical simulation of quantum dynamics . . . 5

Part I: Quantum simulations, sensing and state preparation 7

1 Theoretical background 9
1.1 Single trapped ion . . . 9
1.2 Trapped ion crystals . . . 11
1.2.1 Pseudopotential approximation . . . 12
1.2.2 Beyond the pseudopotential approximation . . . 14
1.2.3 Quantization . . . 16
1.3 Qubit states . . . 17
1.4 Ion-light interactions . . . 17
1.4.1 Resonant driving . . . 18
1.4.2 Near-resonant driving . . . 20
1.4.3 Off-resonant (dispersive) driving . . . 21
1.5 Optical tweezers . . . 22

2 Effect of micromotion and local stress 25
2.1 Engineering spin-spin interactions in optical tweezers . . . 26
2.1.1 Naive inclusion of micromotion . . . 26
2.1.2 Including micromotion during optimization . . . 27
2.1.3 First-order doppler modulation . . . 28
2.2 Local stress . . . 29
2.2.1 First-order approximation . . . 29

2.2.2 Optimization . . . 30
2.2.3 Intensity noise . . . 31
2.3 Conclusions . . . 32

3 Optimal many-body displacement sensing 33
3.1 Displacement sensing . . . 34
3.1.1 Spin-dependent squeezed states . . . 36
3.1.2 Phase-insensitive displacement sensing . . . 38
3.1.3 Multi-parameter displacement sensing . . . 40
3.2 Engineering spin-dependent squeezing . . . 43
3.2.1 Experimental protocol for fast and scalable spin-dependent squeezing . . . 43
3.2.2 Speed limit . . . 47
3.2.3 Numerical results . . . 47
3.3 Conclusion and outlook . . . 49
3.4 Supplemental Material . . . 50
3.4.1 Comparison to other reference states . . . 50
3.4.2 Review of quantum multi-parameter estimation . . . 53
3.4.3 Standard Quantum Limit and the Heisenberg Limit . . . 55
3.4.4 Metrological performance of spin-dependent squeezed-displaced states . . . 56
3.4.5 Measurement protocols and classical Fisher information . . . 62
3.4.6 Further details on the state preparation protocol . . . 67

4 Arbitrary symmetric spin state preparation 71
4.1 Dicke states . . . 72
4.2 State preparation protocol . . . 73
4.3 Dicke state preparation . . . 75
4.4 Quantum error correction codewords . . . 77
4.5 Realization in trapped ions . . . 78
4.6 Outlook . . . 79
4.7 Supplemental Material . . . 80
4.7.1 Errors due to laser intensity fluctuations . . . 80
4.7.2 Errors due to non-global Mølmer-Sørensen gate . . . 80
4.7.3 Hybrid quantum-classical algorithm . . . 81
4.7.4 Fidelity proxy . . . 83

Part II: Classical simulation of quantum dynamics 85

5 Theoretical background 87
5.1 Time-dependent variational principle . . . 87
5.2 Bosonic Gaussian states . . . 90
5.3 Superpositions of Gaussian states . . . 92
5.4 Open quantum systems . . . 95

5.4.1 Markovian master equation 96
5.4.2 Quantum trajectories 97

6 Fast quantum state preparation and bath dynamics 99
6.1 The model and variational ansatz 100
6.2 Results 101
6.3 Bath dynamics 101
6.4 Quantum optimal control 104
6.5 Outlook 106
6.6 Supplemental Material 107
6.6.1 Convergence of SCS ansatz 107
6.6.2 Non-adiabaticity of linear ramps 108
6.6.3 Scaling analysis of linear adiabatic ramp times 111
6.6.4 Adiabaticity of linear ramps in Fig. 6.3 114
6.6.5 Spin dynamics and phases with bath profiles 114
6.6.6 Realization of spin-boson model in trapped ions 115
6.6.7 Further details on simulations 117
6.6.8 Intuition for the SCS ansatz by Trotterization 118

7 Open quantum dynamics 119
7.1 Open dynamics: combining NGS with quantum trajectories 122
7.1.1 Equations of motion for non-Hermitian Hamiltonians 122
7.1.2 Quantum jumps 124
7.1.3 Time evolution 127
7.2 Truncated Wigner Approximation for spins and bosons 127
7.3 Results 130
7.3.1 Details of SCS and TWA simulations 131
7.3.2 Closed system dynamics 134
7.3.3 Open system dynamics 138
7.4 Conclusions and outlook 141
7.5 Supplemental Material 144
7.5.1 On the complex structure of the NGS ansatz 144
7.5.2 Benchmarking dynamics with single spin 145

Conclusions 147

8 Conclusions and Outlook 147

Appendices 151
A: Floquet modes and quantized ion motion with micromotion 151
B: Off-resonant ion-light interactions 155

Summary **159**

Samenvatting **161**

Bibliography **163**

Acknowledgments **187**

I

Introduction

> A beginning is the time for taking the most delicate care that the balances are correct.
>
> *Frank Herbert, Dune (1965)*

Why study quantum mechanical systems? A first answer is that, to the best of our knowledge, at a fundamental level everything obeys the laws of quantum physics. We should therefore study quantum systems to understand our Universe. A second, more applied answer is that there is an *advantage* to performing certain tasks using a quantum system instead of a classical one. This quantum advantage could be realized in essential fields such as simulation, sensing and computation.

Driven by both answers, over the past forty years there has been remarkable progress in our ability to precisely control quantum systems. In platforms such as trapped ions, neutral atoms and superconducting circuits, high-fidelity control of quantum information in tens or even hundreds of qubits is now a matter of course [6–8]. A common feature of many such platforms is that they are *hybrid spin-boson systems*, combining both spin and bosonic degrees of freedom. Spin-boson systems offer great potential both for studying fundamental physics and for realizing a quantum advantage.

The central question of this Thesis is, how can we understand and harness spin-boson systems? An overview of the structure and key results is shown in Fig. I.1. In Part One, we investigate how spin-boson systems can be used as *quantum simulators, sensors* and *computers* to realize a quantum advantage. Spin-boson systems are generally not amenable to exact analytic or classical numerical treatments, so in Part Two we develop efficient approximate classical methods for simulating their *quantum dynamics*.

I.1 Quantum simulations

The most natural task for realizing a quantum advantage is simulation [9, 10]. In *quantum simulation*, a well-controlled quantum system, called the quantum simulator, is programmed to emulate the behaviour of another system. An advantage is possible because classically simulating a quantum system can require a number of classical bits that grows exponentially with the quantum system's size [11, 12]. Quantum simulation therefore provides a powerful framework for exploring physical systems in regimes that are currently inaccessible to exact or classical methods.

I

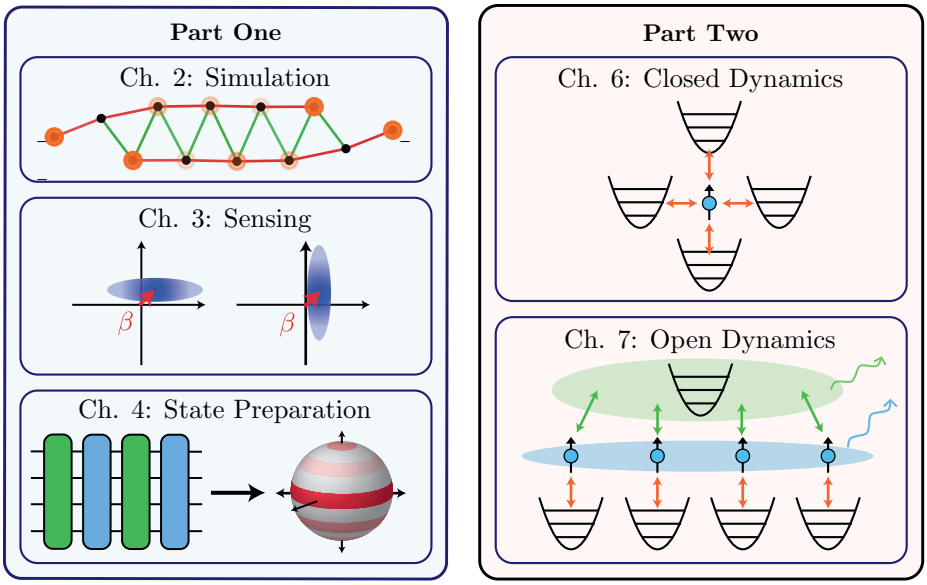


Figure I.1: **Schematic overview of this Thesis**. In Part One, we begin in Ch. 1 by introducing trapped-ion systems. We then study quantum simulations with trapped ions in optical tweezers in Ch. 2 based on Ref. [1], quantum-enhanced displacement sensing with many-body spin-boson systems in Ch. 3 based on Ref. [2], and global variational quantum circuits for symmetric spin state preparation in Ch. 4 based on Ref. [3]. In Part Two, we introduce the time-dependent variational principle, non-Gaussian states and open quantum systems in Ch. 5. Then, we use the non-Gaussian state formalism to study the closed dynamics of hybrid spin-boson systems in Ch. 6 based on Ref. [4], and open dynamics in Ch. 7 based on Ref. [5].

Quantum simulators are classified as either *digital* or *analogue*. Digital simulators operate by sequential application of discrete gate operations [12]. If the gate set is universal then any local, finite-dimensional Hamiltonian can be simulated efficiently, i.e. with polynomially-many resources [11, 13]. Digital quantum simulation has been experimentally demonstrated in platforms including trapped ions [14], superconducting circuits [15, 16] and neutral atoms [17].

By contrast, analogue quantum simulators operate by directly engineering the simulator's interactions to model those of the target system. Although this can be extremely efficient, the simulator's versatility crucially relies on the availability of many types of controllable interactions. Analogue quantum simulation has been experimentally demonstrated in platforms such as neutral atoms [18], trapped ions [19–23], polar molecules [24], trapped Rydberg atoms [25] and semiconductor quantum dots [26].

One of the leading analogue quantum simulation platforms is trapped-ion sys-

tems [27], in which N ions are spatially confined by electromagnetic fields. The qubit is encoded in two internal electronic energy levels. Trapped-ion qubits feature long coherence times and high-fidelity state initialization, manipulation and readout [28]. State-of-the-art coherence times exceeding one hour have been demonstrated in a single $^{171}Yb^{+}$ ion [29], while remarkable fidelities of $> 99.999\%$ for one-qubit gates and $> 99.99\%$ for two-qubit gates have been recently demonstrated in $^{40}Ca^{+}$ [30, 31]. To realize qubit-qubit interactions and perform quantum simulations of spin models, laser light is used to couple the internal states to the ions' collective motion. The resulting interactions are well-described by an *Ising model* [32–34],

$$\hat{H}_{\text{Ising}} = \sum_{i,j=1}^{N} J_{i,j} \hat{\sigma}_i^{\alpha} \hat{\sigma}_j^{\alpha}, \tag{I.1}$$

where $\hat{\sigma}_i^{\alpha}$ is the ith qubit's Pauli matrix with $\alpha = x, y, z$. The matrix $J_{i,j}$ describes the coupling strength between the ith and jth qubit, and approximately follows an inverse power law, $J_{i,j} \propto 1/d_{i,j}^{a}$, where $d_{i,j}$ is the inter-ion distance. The parameter a is somewhat tunable between $0 \lesssim a \lesssim 3$ [21], with special cases of all-to-all ($a = 0$) and dipole-dipole ($a = 3$) interactions.

To increase the programmability of $J_{i,j}$, we can add standing-wave optical potentials [35, 36] or optical tweezers [1, 37–39] to the system. In particular, Ref. [39] showed that optical tweezers can be used to engineer frustrated nearest-neighbor couplings in a 2D zig-zag trapped-ion crystal, although effects such as micromotion and optical tweezer misalignment were not taken into account. A natural question is therefore:

> **How do sources of experimental error such as micromotion or optical tweezer misalignment affect quantum simulations with trapped ions in optical tweezers?**

We answer this question in Ch. 2. We numerically demonstrate that the effects of micromotion can be compensated for when numerically optimizing the strength of the optical tweezers. We also show that the simulator is expected to be robust to tweezer misalignments, while the tweezer intensity should be stabilized to the sub-percent level.

I.2 Quantum sensing

Estimating physical quantities with ever-increasing precision has long underpinned the development of science and technology. Galileo's telescope provided transformative evidence for heliocentrism, while more recently, atomic clocks have redefined timekeeping and become essential for technologies such as the Global Positioning System. Quantum sensing, in which a quantum system is used to estimate the strength of a signal offers the potential for further gains in sensitivity [40]. In an ideal quantum system, the estimation uncertainty is limited by the variance of the

final measurement. To reduce this variance, we use initial states whose variance for one measurement operator is reduced (at the expense of increased variance for a second, non-commuting operator). This is due to Heisenberg's uncertainty principle, and for example applies to the position and momentum of a quantum particle [41]. If information about the signal is encoded in the reduced-variance operator, for an appropriately chosen measurement the estimation uncertainty will be correspondingly reduced. Realizing such *quantum-enhanced sensing* therefore critically depends on the choice of initial state and measurement observable.

One of the first proposals for quantum-enhanced sensing used squeezed states of light [42], which are now routinely used at the Laser Interferometer Gravitational-Wave Observatory (LIGO) for detecting with unprecedented sensitivity the gravitational waves emitted during black-hole mergers [43, 44]. Other paradigmatic examples of quantum-enhanced sensing include the use of squeezed or entangled spin states for spectroscopy, optical atomic clocks and phase sensing [45–49].

Quantum-enhanced sensing will also play a crucial role in searches for physics beyond the Standard Model [50–52]. Couplings between Standard Model fields and dark matter candidates such as millicharged dark matter, dark photons or axions are theorized to induce small bosonic displacements of a microwave field [52–56] or a mechanical resonator [51, 57, 58], which could be measured by a sufficiently sensitive *displacement sensor* [51–61]. Existing states that are suitable for quantum-enhanced displacement sensing [53, 62–72] do not take full advantage of the available degrees of freedom in *many-body* spin-boson platforms. Such many-body systems are ideal quantum sensors because they benefit from a *collective enhancement*, i.e. an effect that arises in a system of N constituents, but not in N independent systems of one constituent each. For example, in trapped-ion platforms with N ions, spin-boson cat states are prepared $\sqrt{N}$ times faster and displacement signals are amplified by $\sqrt{N}$, because the spin-motion coupling is $\sqrt{N}$ times stronger. Therefore, a natural question is:

What is the optimal initial state for displacement sensing in many-body spin-boson systems?

We answer this question in Ch. 3 using spin-dependent squeezed states – hybrid spin-boson states whose bosonic squeezed quadrature is conditioned on an auxiliary spin. We prove that such states are *optimal* for displacement sensing, and propose explicit experimentally-realized measurement protocols. We also provide a fast and scalable protocol for preparing spin-dependent squeezed states in trapped-ion systems.

I.3 Quantum state preparation

When operating a quantum system as a simulator, sensor or computer, it is essential to be able to initialize the system in a desired quantum state. In quantum simulation this enables the study of the state-dependence of phenomena such as quantum many-body scars [25], Floquet symmetry-protected topological phases [73]

and many-body dynamical phase transitions [23]. In quantum sensing, as discussed in Sec. I.2, a quantum sensor's performance critically depends on the initial state. And in quantum computing, a crucial prerequisite for quantum error correction is initialization in logical basis states [11]. Quantum state preparation itself is also a task that can realize a quantum advantage, for example in the context of quantum annealing [74] or quantum chemistry ground-state preparation [75].

One interesting class of states is *symmetric spin states* [76], which are defined as any state that is invariant under qubit permutation. A paradigmatic subset is the *Dicke states*, which describe collective excitations of a system of N spin-1/2 particles. Dicke states arise naturally in models such as the Dicke model [77], which describes light-matter interactions, and the Lipkin-Meshkov-Glick model [78], which describes N spins coupled collectively. Labeling the two states of each spin-1/2 as $|0\rangle$ and $|1\rangle$, and referring to $|1\rangle$ as an excitation, an example Dicke state is the $N = 3$ spin state with two excitations,

$$|\psi\rangle = \frac{1}{\sqrt{3}}(|011\rangle + |101\rangle + |110\rangle). \tag{I.2}$$

Recently, symmetric states have found utility in fields such as quantum error correction [79–81], quantum storage [82, 83], quantum networking [84] and quantum sensing [85]. Although there are many existing preparation protocols for Dicke states [86–95], preparation protocols for arbitrary symmetric states require either single-site addressing [96], which becomes experimentally demanding for hundreds of qubits, or a large detuning limit [97], which is typically slow. As such, we ask:

Can arbitrary symmetric spin states be efficiently prepared using only global control?

In Ch. 4 we answer this question in the affirmative. Using a variational quantum circuit built from global gates, specifically global rotations and global one-axis twisting, we show that arbitrary symmetric spin states can be prepared using at most $2N/3$ circuit layers.

I.4 Classical simulation of quantum dynamics

Quantum advantage is inherently comparative, so in Part Two of this Thesis we develop approximate classical methods for efficiently simulating the *quantum dynamics* of spin-boson systems. Advancing classical methods is important for narrowing the performance gap between quantum and classical methods, ensuring that any claims of quantum advantage are well-founded. Furthermore, classical methods can verify the output of quantum simulators, a particularly important task in the current era of noisy quantum hardware platforms [98].

Simulating quantum dynamics, either with a classical or a quantum simulator, is also important in its own right. For example, simulations of quantum dynamics can be used to optimize quantum gates [99], speed up quantum state preparation [4, 100], and to study physics, as discussed in Sec. I.1.

In the absence of scalable fault-tolerant quantum simulators, many approximate classical numerical methods have been developed for simulating quantum dynamics [101–103]. A particularly challenge is the simulation of spin-boson systems, because the bosonic Hilbert space is (even locally) unbounded. We therefore ask:

How can the dynamics of spin-boson systems be efficiently classically simulated?

For spin-boson systems, frequently-used classical numerical methods include tensor networks [104–106], the truncated Wigner approximation (TWA) [107] and the focus of this Thesis, the time-dependent variational principle (TDVP) with variational ansatz [108–116]. In Ch. 5 we review the TDVP and introduce our choice of variational ansatz, a non-Gaussian state (NGS) ansatz that is a superposition of Gaussian states. In Ch. 6 we use this framework to study ground state properties and real-time dynamics of the spin-boson model, which describes a single spin interacting with many bosonic modes [117]. We show that the NGS ansatz is efficient and controllable, even beyond the paradigm of Ohmic-type interactions. We also demonstrate fast quantum state preparation. In Ch. 7 we study the open dynamics of the Holstein-Tavis-Cummings model [104, 118], with the aim of laying the groundwork for applications such as efficient numerical studies of polaritonic chemistry or for robust quantum state preparation. We benchmark the NGS simulations against TWA, and show that there are regions where NGS outperforms TWA.

Finally, in Ch. 8 we conclude by summarizing the key scientific contributions of this Thesis, and discuss possible future research directions.

Part I

Quantum simulations, sensing and state preparation

Chapter 1

Theoretical background

"It's a trap!"

Admiral Ackbar, Return of the Jedi (1983)

In this chapter, we set the foundations for the rest of Part One. We introduce the Paul trap, and discuss the formation of stable Coulomb crystals of many ions, including a treatment of micromotion using Floquet theory. We then review ion-laser interactions in the resonant, near-resonant and off-resonant regimes, and show how these interactions enable trapped-ion platforms to operate as both universal quantum computers, and analogue quantum simulators of spin systems. Finally, we introduce optical tweezers, and review how they can be used to modify the phonon spectrum for increased trapped-ion quantum simulator programmability.

1.1 Single trapped ion

Consider a singly-charged ion at position $\boldsymbol{r} = (r_x, r_y, r_z)$. Supplying static (dc) fields and time-dependent (rf) components oscillating at frequency Ω_{rf}, the electric potential energy of the system is [119],

$$V_{\mathrm{trap}}(\boldsymbol{r}, t) = \frac{eU}{2} \sum_{\alpha=x,y,z} \sigma_\alpha r_\alpha^2 + \cos(\Omega_{\mathrm{rf}} t) \frac{e\tilde{U}}{2} \sum_{\alpha=x,y,z} \tilde{\sigma}_\alpha r_\alpha^2, \tag{1.1}$$

where e is the electric charge, U is the dc electrode peak-to-peak voltage, and $\tilde{U}$ is the rf electrode peak-to-peak voltage. The parameters σ_α and $\tilde{\sigma}_\alpha$ are geometrical factors that determine the field curvatures. A positively charged ion is spatially confined if the curvatures are positive. Satisfying the Laplace equation, $\nabla^2 V_{\mathrm{trap}} = 0$, implies $\sum_\alpha \sigma_\alpha = \sum_\alpha \tilde{\sigma}_\alpha = 0$. As such, the dc field curvature must be negative in at least one direction, which forbids a charged particle from being simultaneously confined in all three directions by local, static electric fields alone.

Classically, the ion's motion is described by the Lorentz force, $\boldsymbol{F}(\boldsymbol{r}, t) = m\ddot{\boldsymbol{r}} = e\boldsymbol{E}(\boldsymbol{r}, t)$. Here, $\ddot{\boldsymbol{r}} = d^2\boldsymbol{r}/dt^2$ is the acceleration, m is the ion's mass, and $\boldsymbol{E}(\boldsymbol{r}, t) =$

$-(1/e)\boldsymbol{\nabla} V_{\text{trap}}(\boldsymbol{r},t)$ is the electric field. In the Lorentz force we neglected the magnetic field term, which in Paul traps is weak [119]. The resulting equations of motion (eoms) for the ion positions are spatially decoupled, and can be written in the form of Mathieu equations [119],

$$\ddot{r}_\alpha(t) + [a_\alpha - 2q_\alpha \cos(\Omega_{\text{rf}} t)]\frac{\Omega_{\text{rf}}^2}{4} r_\alpha(t) = 0. \tag{1.2}$$

Here, we defined the (dimensionless) stability parameters,

$$a_\alpha = \frac{4eU\sigma_\alpha}{m\Omega_{\text{rf}}^2}, \qquad q_\alpha = -\frac{2e\tilde{U}\tilde{\sigma}_\alpha}{m\Omega_{\text{rf}}^2}, \tag{1.3}$$

which determine whether a particular electric field configuration stably traps an ion. Typically, $|a_\alpha| \ll 1$ and $|q_\alpha| \ll 1$, which is both a stable trapping regime and is experimentally accessible [119, 120].

In general, writing a closed-form solution to the Mathieu equation is challenging. Instead, in the regime of small stability parameters, $|a_\alpha| \ll 1$ and $|q_\alpha| \ll 1$, to first order a solution for the ion's motion is [119],

$$r_\alpha(t) \approx A_\alpha \cos(\Theta_\alpha t)\left[1 - \frac{q_\alpha}{2}\cos(\Omega_{\text{rf}} t)\right]. \tag{1.4}$$

Here, $\Theta_\alpha = \gamma_\alpha \Omega_{\text{rf}}/2$ are the *pseudopotential frequencies* with $\gamma_\alpha \approx \sqrt{a_\alpha + q_\alpha^2/2}$ the *characteristic exponents*. The amplitude A_α is determined by the initial conditions. Because Paul traps operate in the regime where $\Theta_\alpha \ll \Omega_{\text{rf}}$, Eq. (1.4) describes periodic motion at two distinct frequencies: the *secular motion* at frequencies Θ_α with amplitudes A_α, and the much faster *intrinsic micromotion* at frequencies $\Omega_{\text{rf}} \pm \Theta_\alpha$ with amplitudes $A_\alpha q_\alpha/2$. When $A_\alpha \neq 0$ and $q_\alpha \neq 0$, intrinsic micromotion is present along α. Additional, *excess micromotion* occurs when an extra external force displaces the ions from $A_\alpha = 0$. Potential sources of excess micromotion include stray electric fields, pickup of the rf signal by the electrodes supplying the static field, and phase differences between rf-electrodes [121].

Because the micromotion amplitude is a factor of $q_\alpha/2$ smaller than the amplitude of the secular motion, when $|q_\alpha| \ll 1$, in many cases it can be neglected. Then, $r_\alpha(t) \approx A_\alpha \cos(\Theta_\alpha t)$, which is identical to the solution of a time-independent harmonic oscillator at frequency Θ_α. We can therefore make the so-called *pseudopotential approximation*, and replace the driven harmonic trapping potential of Eq. (1.1) with a time-independent harmonic potential,

$$V_{\text{trap}}^{(\text{PP})}(\boldsymbol{r},t) = \frac{m}{2}\sum_\alpha \Theta_\alpha^2 r_\alpha(t)^2, \tag{1.5}$$

which is a significantly simpler description of the trapping fields.

1.2 Trapped ion crystals

Next, we generalize to N ions of the same mass. The total potential energy must now include the mutual Coulomb interactions between ions,

$$V_{\text{Coulomb}}(\boldsymbol{r},t) = \frac{e^2}{8\pi\epsilon_0}\sum_{i\neq j}\frac{1}{|\boldsymbol{r}_i(t)-\boldsymbol{r}_j(t)|}. \tag{1.6}$$

Here $\boldsymbol{r}_i = (r_{i,x}, r_{i,y}, r_{i,z})$ is the position of the ith ion, and ϵ_0 is the vacuum permittivity. It will be convenient to work with the vectorized notation,

$$\boldsymbol{r} = (r_{1,x}, r_{1,y}, r_{1,z}, r_{2,x}, \ldots, r_{N,z})^T. \tag{1.7}$$

Generalizing the single-ion trapping potential of Eq. (1.1) yields,

$$V_{\text{trap}}(\boldsymbol{r},t) = \frac{m\Omega_{\text{rf}}^2}{8}\sum_{i,\alpha}\left[a_\alpha - 2q_\alpha\cos(\Omega_{\text{rf}}t)\right] r_{i,\alpha}(t)^2. \tag{1.8}$$

Similarly to the $N = 1$ ion case of Sec. 1.1, in the regime of small stability parameters where micromotion may be neglected, $|a_\alpha| \ll 1$ and $|q_\alpha| \ll 1$, we can make the pseudopotential approximation and replace the driven trapping potential of Eq. (1.8) with a time-independent harmonic potential,

$$V_{\text{trap}}^{(\text{PP})}(\boldsymbol{r}) = \frac{m}{2}\sum_{i,\alpha}\Theta_\alpha^2 r_{i,\alpha}(t)^2, \tag{1.9}$$

where Θ_α are the pseudopotential frequencies, as defined in Eq. (1.4).

Regardless of whether we make the pseudopotential approximation or not, the interplay between the repulsive Coulomb interactions and the confining trapping potentials can result in the formation of stable *Coulomb crystals*. This occurs when the stability parameters a_α and q_α are chosen such that the characteristic exponents γ_α of the Mathieu equation, defined in Eq. (1.4), are real [119]. To describe the equilibrium positions and ion motion, we write the Lagrangian for N ions in a general potential $V(\boldsymbol{r},t)$,

$$L(\dot{\boldsymbol{r}},\boldsymbol{r}) = \frac{m}{2}\dot{\boldsymbol{r}}^T\dot{\boldsymbol{r}} - V(\boldsymbol{r},t), \tag{1.10}$$

The $3N$ classical equations of motion (eoms) for the ion positions are then obtained from the Euler-Lagrange equations. At this point, it is convenient to define a length scale l and introduce dimensionless coordinates, $\boldsymbol{r} = l\boldsymbol{u}$. We also introduce a dimensionless potential, $V(\boldsymbol{u}) = V(\boldsymbol{r})/(ml^2\tilde{\omega}^2)$, where $\tilde{\omega}$ is a characteristic frequency. The eoms are then,

$$\ddot{\boldsymbol{u}} + \tilde{\omega}^2\boldsymbol{\nabla}_u V(\boldsymbol{u},t) = 0. \tag{1.11}$$

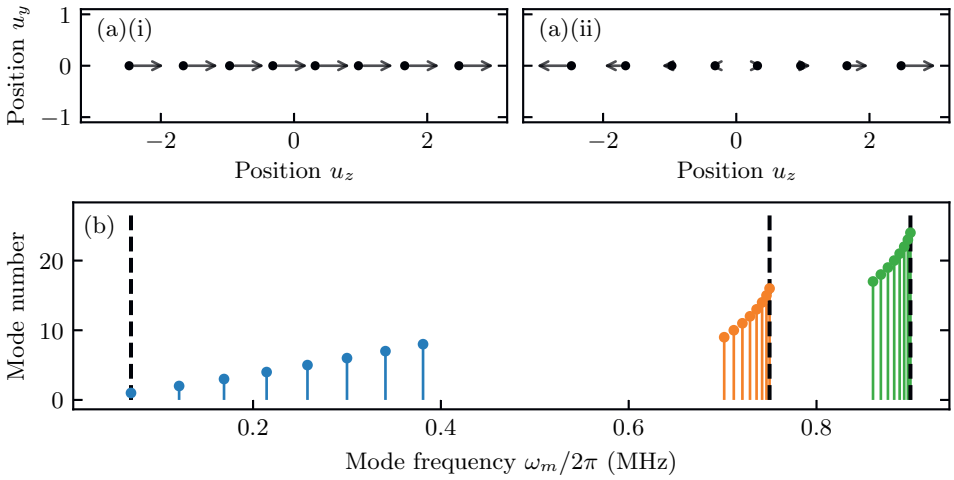


Figure 1.1: Trapped ion crystal in the pseudopotential approximation. **(a)** Dimensionless equilibrium positions (dots) of $N = 8$ ions trapped with pseudopotential frequencies $\boldsymbol{\Theta} = 2\pi \times (0.9, 0.75, 0.07)$ MHz. The weaker frequency in z leads to the formation of a 1D chain along z. The arrows show the normal modes, with panel (i) the $m = 1$ center of mass (com) mode and panel (ii) the $m = 2$ breathing mode. **(b)** Normal mode spectrum along x (green), y (orange) and z (blue). The com mode frequencies are marked by vertical dashed lines. The frequency separation between the axial frequencies (z) is significantly larger than the separation between transverse frequencies (x and y).

1.2.1 Pseudopotential approximation

After making the pseudopotential approximation, we search for time-independent *equilibrium positions* of the form $\boldsymbol{u}(t) = \boldsymbol{u}^{(0)}$. These are static positions where the ions will equilibrate to at zero temperature. Substituting into the eoms of Eq. (1.11) yields the condition,

$$\boldsymbol{\nabla} V(\boldsymbol{u}^{(0)}) = 0, \tag{1.12}$$

which defines the equilibrium positions as the points where the forces on the ions vanish. In general, Eq. (1.12) must be solved numerically. As shown in Fig. 1.1(a), choosing $\Theta_x, \Theta_y \gg \Theta_z$ results in a 1D chain of ions along z. On the other hand, $\Theta_x \gg \Theta_y, \Theta_z$ results in a 2D crystal in the $y - z$ plane, which we study in the next section, Sec. 1.2.2.

Next, we consider driving small ion motion, for example by applying an electric field. The positions of the ions can be described by adding a time-dependent displacement $\boldsymbol{q}(t)$ about their equilibrium positions,

$$\boldsymbol{u}(t) = \boldsymbol{u}^{(0)} + \boldsymbol{q}(t). \tag{1.13}$$

When $\boldsymbol{q}(t) \ll 1$, Taylor expanding the potential V to first-order and taking the gradient yields $\boldsymbol{\nabla} V(\boldsymbol{u}) \approx \boldsymbol{\nabla} V(\boldsymbol{u^{(0)}}) + \boldsymbol{H}\boldsymbol{q}(t)$. Here, $\boldsymbol{H} = \boldsymbol{\nabla}^2 V(\boldsymbol{u}^{(0)})$ is the $3N \times 3N$ real and symmetric Hessian matrix of V, evaluated at the equilibrium positions. The first term, $\boldsymbol{\nabla} V(\boldsymbol{u^{(0)}})$, vanishes due to Eq. (1.12). Substituting $\boldsymbol{u}(t)$ and the Taylor-expanded gradient into the eoms of Eq. (1.11) results in a system of coupled differential equations,

$$\ddot{\boldsymbol{q}}(t) + \tilde{\omega}^2 \boldsymbol{H}\boldsymbol{q}(t) = 0. \tag{1.14}$$

To decouple these eoms, we diagonalize $\boldsymbol{H} = \boldsymbol{B}\boldsymbol{\mu}\boldsymbol{B}^T$. The columns of $\boldsymbol{B}$ obey the eigenequation, $\boldsymbol{H}\boldsymbol{b}_m = \mu_m \boldsymbol{b}_m$, with $m = 1, \ldots, 3N$. Introducing the *normal modes*,

$$\boldsymbol{Q}(t) = \boldsymbol{B}^T \boldsymbol{q}(t), \tag{1.15}$$

we obtain decoupled eoms, $\ddot{\boldsymbol{Q}}(t) + \tilde{\omega}^2 \boldsymbol{\mu}\boldsymbol{Q}(t) = 0$. In terms of initial conditions $\boldsymbol{Q}(0)$ and $\dot{\boldsymbol{Q}}(0)$, the solution is,

$$\boldsymbol{Q}(t) = \boldsymbol{Q}(0)\cos(\sqrt{\boldsymbol{\mu}}\tilde{\omega}t) + \frac{\dot{\boldsymbol{Q}}(0)}{\sqrt{\boldsymbol{\mu}}\tilde{\omega}}\sin(\sqrt{\boldsymbol{\mu}}\tilde{\omega}t), \tag{1.16}$$

which describes the motion of $3N$ individual harmonic oscillators, each at the *eigenfrequency*, $\omega_m = \sqrt{\mu_m}\tilde{\omega}$. Inverting the normal mode definition of Eq. (1.16), the ith element of the $3N$-length vector of displacements evolves as,

$$q_i(t) = \sum_{m=1}^{3N} b_{m,i}\left[Q_m(0)\cos(\omega_m t) + \dot{Q}_m(0)\sin(\omega_m t)/\omega_m\right]. \tag{1.17}$$

We have therefore described the seemingly complicated motion of N trapped ions, all mutually interacting via Coulomb interactions, in terms of the simple motion of $3N$ independent harmonic oscillators.

In general, the eigenvectors $\boldsymbol{B}$ must be calculated numerically. However, some of the simple modes of a 1D chain can be described exactly. Without loss of generality we assume the chain lies along z, as in Fig. 1.1, and set the characteristic frequency $\tilde{\omega} = \Theta_z$. Along the axial ($z$) direction, the lowest frequency mode is the *center of mass* (com) mode, $\boldsymbol{b}_1 = (1, \ldots, 1)/\sqrt{N}$, at frequency $\omega_1 = \Theta_z$. This mode describes motion where the ions move in phase as if rigidly clamped together, as sketched in Fig. 1.1(a)(i). In each transverse direction, the com mode is the highest frequency mode for that direction, as observed in Fig. 1.1(b), where the orange (x) and green (y) clusters have their highest frequency mode located at the trapping frequency (marked by the dashed line). Returning to the axial direction, the second-lowest frequency mode is the *breathing mode*, which up to normalization is proportional to the equilibrium positions, $\boldsymbol{b}_2 \cong (u_1^{(0)}, \ldots, u_N^{(0)})$, at frequency $\omega_2 = \sqrt{3}\Theta_z$. The breathing mode describes motion where each ion's motion is proportional to its displacement from the trap center, as sketched in Fig. 1.1(a)(ii).

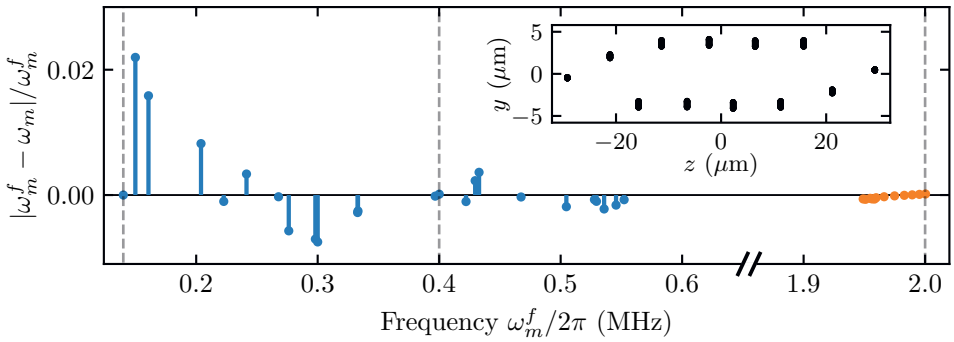


Figure 1.2: $N = 12$ ion 2D Coulomb Crystal. The stability parameters are $\boldsymbol{a} = (0.0187, -0.0189, 0.0001)$ and $\boldsymbol{q} = (0.2028, -0.2028, 0)$, with corresponding pseudopotential frequencies $\boldsymbol{\Theta} = 2\pi \times (2, 0.4, 0.14)$MHz. The rf frequency is $\Omega_{\text{rf}} = 2\pi \times 20$ MHz. **Inset**: Time-dependent equilibrium positions. There is no micromotion along z as $q_z = 0$. Along y, the micromotion amplitude is proportional to $u_{i,y}$. **Main:** Frequency differences between normal mode frequencies ω_m and Floquet quasienergies ω_m^f, normalized to ω_m^f. The out-of-plane modes along x, shown in orange, are decoupled from the in-plane modes and feature higher frequencies and a smaller bandwidth. Pseudopotential frequencies are denoted by vertical grey dashed lines. Because micromotion is a breathing mode oscillation, the center of mass mode frequencies are unchanged. All frequency differences are small (kHz) relative to the mode frequencies themselves (MHz).

1.2.2 Beyond the pseudopotential approximation

To treat the time-dependent potential, we follow Refs. [122, 123]. In general we will no longer be able to find time-independent equilibrium positions, and therefore we cannot obtain a simple condition like Eq. (1.12). Instead, we search for low-energy, periodic solutions $\boldsymbol{u}^{(0)}(t)$ with period $T = 2\pi/\Omega_{\text{rf}}$ [124, 125]. Such solutions can be found numerically by "cooling" the ions to zero temperature with a cooling force, e.g. a damping term $F_{\text{cool}} = -f(t)\dot{\boldsymbol{u}}$. The function $f(t)$ ramps from $f(0) = 1$ to $f(t_{\max}) = 0$, with a maximum ramp time $t_{\max}$ that must be sufficiently long to allow the ions to reach a low-energy, periodic orbit. After adding the cooling term and numerically solving the eoms until $t = t_{\max}$, $\boldsymbol{u}^{(0)}(t)$ is found by evolving the solution for a further rf period with $f(t) = 0$. Time-dependent equilibrium positions for an example $N = 12$ system are shown in the inset of Fig. 1.2. We observe micromotion along y that is proportional to u_y, as expected from Eq. (1.4). There is no micromotion along z because $q_z = 0$.

Next, displacements $\boldsymbol{q}(t)$ about the time-dependent equilibrium positions are described as,

$$\boldsymbol{u}(t) = \boldsymbol{u}^{(0)}(t) + \boldsymbol{q}(t). \tag{1.18}$$

Substituting Eq. (1.18) into the eoms of Eq. (1.11), after Taylor expanding the

gradient about $\boldsymbol{u}^{(0)}(t)$ and using the fact that $\boldsymbol{u}^{(0)}(t)$ is by construction a solution to the eoms, we obtain the same equations of motion as in Eq. (1.14), except where the Hessian is now time-dependent, $\boldsymbol{H}(t) = \boldsymbol{\nabla}^2 V(\boldsymbol{u}^{(0)}(t), t)$. The $3N$ second-order differential equations with periodic coefficients can be treated using *Floquet theory* by rewriting them as a system of $6N$ first-order differential equations,

$$\dot{\boldsymbol{\phi}}(t) = \begin{pmatrix} \mathbf{0} & \mathbf{1} \\ -\tilde{\omega}^2 \boldsymbol{H}(t) & \mathbf{0} \end{pmatrix} \boldsymbol{\phi}(t), \tag{1.19}$$

where we introduced $\boldsymbol{\phi} = (\boldsymbol{q}, \dot{\boldsymbol{q}})^T$. In experiments, the trap frequency Ω_{rf} is much faster than the timescale of the dynamics set by the pseudopotential frequency Θ_α. For example, for the simulations in Fig. 1.2, $\Omega_{\mathrm{rf}} = 2\pi \times 20$ MHz, while $\Theta_\alpha \approx 2\pi \times 1$ MHz. As such, we can focus on the solution to the eoms at integer multiples of the rf-period, $T = 2\pi/\Omega_{\mathrm{rf}}$. From Floquet theory, the solution $\boldsymbol{\phi}(nT)$ for any integer $n \in \mathbb{Z}$ is determined from the initial state $\boldsymbol{\phi}(0)$ via,

$$\boldsymbol{\phi}(nT) = \boldsymbol{M}^n \boldsymbol{\phi}(0). \tag{1.20}$$

Here, $\boldsymbol{M}$ is the *monodromy matrix*, which is constructed by solving Eq. (1.19) until $t = T$ using a matrix initial condition $\boldsymbol{\phi}(0) = \mathbb{1}$.

The solution of Eq. (1.20) is decoupled by diagonalizing the monodromy matrix, $\boldsymbol{M} = \boldsymbol{B}^{\mathrm{f}} \mathrm{diag}(e^{iT\boldsymbol{\omega}^{\mathrm{f}}}, e^{-iT\boldsymbol{\omega}^{\mathrm{f}}})(\boldsymbol{B}^{\mathrm{f}})^{-1}$, where $\boldsymbol{\omega}^{\mathrm{f}}$ are the $3N$ *quasienergies* that come in complex conjugate pairs if the solutions are stable. We introduce new canonical coordinates $\boldsymbol{Q}$ and $\boldsymbol{Q'}$,

$$\begin{pmatrix} \boldsymbol{Q} \\ \boldsymbol{Q'} \end{pmatrix} = \begin{pmatrix} -i\mathbb{1} & 0 \\ 0 & \mathbb{1} \end{pmatrix} (\boldsymbol{B}^{\mathrm{f}})^{-1} \boldsymbol{\phi}, \tag{1.21}$$

where the diagonal matrix ensures that the new coordinates satisfy the Poisson bracket, see Appendix 8 for details. Eq. (1.20) then reduces to,

$$\begin{pmatrix} \boldsymbol{Q}(nT) \\ \boldsymbol{Q'}(nT) \end{pmatrix} = \begin{pmatrix} e^{inT\boldsymbol{\omega}^{\mathrm{f}}} \boldsymbol{Q}(0) \\ e^{-inT\boldsymbol{\omega}^{\mathrm{f}}} \boldsymbol{Q'}(0) \end{pmatrix}, \tag{1.22}$$

which shows that in the decoupled basis, the new coordinates evolve by simply acquiring a phase that depends on the quasienergies. Inverting Eq. (1.21) yields the evolution of the original position and momentum coordinates in terms of the new canonical coordinates,

$$\begin{pmatrix} \boldsymbol{q}(nT) \\ \dot{\boldsymbol{q}}(nT) \end{pmatrix} = \begin{pmatrix} \boldsymbol{U} & 0 \\ 0 & -\boldsymbol{V} \end{pmatrix} \begin{pmatrix} ie^{inT\boldsymbol{\omega}^{\mathrm{f}}} \boldsymbol{Q}(0) + e^{-inT\boldsymbol{\omega}^{\mathrm{f}}} \boldsymbol{Q'}(0) \\ e^{inT\boldsymbol{\omega}^{\mathrm{f}}} \boldsymbol{Q}(0) + ie^{-inT\boldsymbol{\omega}^{\mathrm{f}}} \boldsymbol{Q'}(0) \end{pmatrix}, \tag{1.23}$$

where $\boldsymbol{B}^{\mathrm{f}} = \left(\begin{smallmatrix} \boldsymbol{U} & \boldsymbol{U}^* \\ \boldsymbol{V} & \boldsymbol{V}^* \end{smallmatrix}\right)$, and we used the fact that at $t = nT$, $\boldsymbol{U} \in \mathbb{R}$ and $\boldsymbol{V} \in i\mathbb{R}$ [126]. The coordinates $\boldsymbol{Q}$ are known as the *Floquet modes*.

1.2.3 Quantization

At ultra-cold temperatures, the ion motion must be treated quantum mechanically. Similarly to Ref. [119], we quantize the solutions of the equations of motion, which amounts to quantizing in the Heisenberg picture. This allows us to treat the pseudopotential and beyond-pseudopotential cases on an equal footing.

We begin with the pseudopotential case. We identify $lQ_m(0)$ as the initial position of the mth normal mode and $lm\dot{Q}_m(0)$ as the initial momentum. We quantize $lQ_m(0) \to \hat{x}_m(0)$ and $lm\dot{Q}_m(0) \to \hat{p}_m(0)$, and require $[\hat{x}_m(0), \hat{p}_n(0)] = i\delta_{mn}$. The normal mode evolution of Eq. (1.16) becomes,

$$\hat{x}_m(t) = \hat{x}_m \cos(\omega_m t) + \hat{p}_m \sin(\omega_m t)/(m\omega_m), \tag{1.24}$$

where $\hat{x}_m = \hat{x}_m(0)$ and $\hat{p}_m = \hat{p}_m(0)$. We can introduce canonical creation $\hat{a}_m^\dagger$ and annihilation $\hat{a}_m$ operators,

$$\hat{x}_m = \ell_m(\hat{a}_m^\dagger + \hat{a}_m), \qquad \hat{p}_m = im\omega_m\ell_m(\hat{a}_m^\dagger - \hat{a}_m), \tag{1.25}$$

which obey $[\hat{a}_m, \hat{a}_n^\dagger] = \delta_{m,n}$, and where $\ell_m = \sqrt{\hbar/(2m\omega_m)}$ is the *harmonic oscillator length scale* of the mth mode. From Eq. (1.17) the ith element of $3N$length vector of displacements therefore evolves in terms of the normal modes as,

$$\hat{x}_i(t) = \sum_{m=1}^{3N} b_{m,i}\ell_m(\hat{a}_m^\dagger e^{i\omega_m t} + \hat{a}_m e^{-i\omega_m t}), \tag{1.26}$$

The motion is therefore a linear combination of normal mode creation and annihilation operators, each evolving by simply acquiring a phase determined by their eigenfrequencies. The quantized normal modes are called *phonon modes*, with the eigenfrequencies known as the *phonon spectrum*.

Next, we consider the beyond-pseudopotential case. We promote the dimensionless canonical position and momentum coordinates to operators as $q_i \to \hat{x}_i$ and $\dot{q}_i \to \hat{p}_i$. In turn, the Q_m and Q'_m coordinates become operators that obey $[\hat{Q}_m(t), \hat{Q}_n(t')] = i\delta_{mn}$, see Appendix 8 for details. This commutator equals $i[\hat{a}, \hat{a}^\dagger]$, so we can choose the identification $\hat{Q}_m \to -i\hat{a}_m^\dagger$ and $\hat{Q}'_m \to \hat{a}_m$. From Eq. (1.23), the ion's physical position operator is then,

$$\hat{x}_i(nT) = \sum_{m=1}^{3N} b^{\mathrm{f}}_{m,i}\ell_m(\hat{a}_m^\dagger e^{inT\omega^{\mathrm{f}}_m} + \hat{a}_m e^{-inT\omega^{\mathrm{f}}_m}), \tag{1.27}$$

where the f superscripts on the Floquet modes $b^{\mathrm{f}}_{m,i}$ and quasienergies ω^{f}_m distinguish them from the pseudopotential normal modes and eigenenergies. Comparing Eq. (1.27) and Eq. (1.26), we observe that the Floquet modes play the same role as the normal modes, and the Floquet quasienergies play the same role as the eigenfrequencies. We have therefore described the quantum mechanical motion of a system of N trapped ions using normal modes in the pseudopotential case, and the Floquet modes in the time-dependent potential case.

1.3 Qubit states

Although the phonon modes can be used for quantum computations and simulations, for instance for bosonic quantum error correction with Gottesman-Kitaev-Preskill (GKP) states [127–130], trapped ions offer another useful degree of freedom, namely, the internal levels. Despite the fact that the electronic structure is complicated, if we can (i) reliably initialize the quantum state in a single electronic energy level, and (ii) drive isolated transitions between that level and a second energy level, we can effectively describe the system as a *two-level system*. The two levels are labeled as a ground state, $|g\rangle$, and an excited state, $|e\rangle$. The two-level Hamiltonian is,

$$\hat{H}_0 = \sum_{i=1}^{N} \frac{\omega_0}{2} \hat{\sigma}_i^z, \tag{1.28}$$

where $\hat{\sigma}_i^\alpha$ is the $\alpha = x, y, z$ Pauli matrix for the ith ion, and ω_0 is the energy splitting between the two levels. This system is also called a spin-1/2 system, and is said to encode a *qubit*, in which case the levels are equivalently labelled as $|\downarrow\rangle \equiv |g\rangle$ and $|\uparrow\rangle \equiv |e\rangle$, or $|0\rangle \equiv |g\rangle$ and $|1\rangle \equiv |e\rangle$.

The spin-1/2 system is categorized as either a *microwave qubit* with $\omega_0 \approx$ GHz, or an *optical qubit* with $\omega_0 \approx 10^2$ THz. Common ion species choices for microwave qubits include $^{171}\mathrm{Yb}^+$, $^{9}\mathrm{Be}^+$ or $^{25}\mathrm{Mg}^+$, while common choices for optical qubits include $^{40}\mathrm{Ca}^+$, $^{88}\mathrm{Sr}^+$ or $^{138}\mathrm{Ba}^+$ [131]. When relevant, in this thesis we focus on $^{171}\mathrm{Yb}^+$.

1.4 Ion-light interactions

Performing qubit-based quantum simulations and computations requires interactions between the qubits. In trapped-ion systems we can use laser light to couple each ion's internal states, i.e. each qubit, to the collective motion [131–133]. In the interaction picture with respect to $\hat{H}_0$ of Eq. (1.28), the coupling is,

$$\hat{H}_{\mathrm{int}}(t) = -\sum_{i=1}^{N} \frac{\Omega_i}{2} \left(\hat{\sigma}_i^- \exp[-i\omega_0 t + i\omega_L t - i\boldsymbol{k}\cdot\hat{\boldsymbol{x}}_i(t) + i\phi(t)] + \mathrm{h.c.} \right). \tag{1.29}$$

Here, Ω_i is the Rabi frequency of the ith ion, ω_L is the laser frequency, $\boldsymbol{k} = (k_x, k_y, k_z)$ is the effective wave-vector, and $\phi(t)$ is the phase of the laser. Note that Eq. (1.29) is obtained after the rotating wave approximation for $\omega_L, \omega_0 \gg \Omega_i$, which amounts to ignoring terms in the Hamiltonian rotating at frequency $\omega_0 + \omega_L$ [134]. The operators $\hat{\sigma}_i^\pm = (\hat{\sigma}_i^x \pm i\hat{\sigma}_i^y)/2$ are the Pauli raising (+) and lowering (−) operators.

In Eq. (1.29), we wrote the ith ion's position as $\hat{\boldsymbol{x}}_i(t) = (\hat{x}_{i,x}(t), \hat{x}_{i,y}(t), \hat{x}_{i,z}(t))^T$, and therefore the summation runs only from $i = 1, \ldots, N$. The position $\hat{x}_{i,\alpha}(t)$ of the ith ion along α is given by Eq. (1.26) or Eq. (1.27) in the pseudopotential

and beyond-pseudopotential cases, respectively. Using the same notation for both settings,

$$\boldsymbol{k}\cdot\hat{\boldsymbol{x}}_i(t)=\sum_{m=1}^{3N}\eta_{m,i}[e^{i\omega_m t}\hat{a}_m^\dagger+e^{-i\omega_m t}\hat{a}_m], \tag{1.30}$$

where we introduced the *Lamb-Dicke parameter* for the ith ion as,

$$\eta_{m,i}=\ell_m(k_x b_{m,3i-2}+k_y b_{m,3i-1}+k_z b_{m,3i}). \tag{1.31}$$

The $b_{m,i}$ elements refer to either the normal modes or the Floquet modes, and are ordered following the vectorized notation ordering of Eq. (1.7). For example, for the first ion, $i=1$, the elements $b_{m,1}$, $b_{m,2}$ and $b_{m,3}$ correspond to the x, y and z directions, respectively. The *Lamb-Dicke regime* is reached when $\sqrt{\langle\psi_m|\,\boldsymbol{k}\cdot\hat{\boldsymbol{x}}_i\,|\psi_m\rangle}\ll 1$, where $|\psi_m\rangle$ is the quantum state of the motion [131]. In this regime, Taylor expanding the exponential and ignoring terms beyond first-order yields,

$$\hat{H}_{\text{int}}(t)=-\frac{1}{2}\sum_{i=1}^{N}\Omega_i\left(e^{i\delta t+i\phi(t)}\hat{\sigma}_i^-[1-i\sum_{m=1}^{3N}\eta_{m,i}\hat{x}_m(t)]+\text{h.c.}\right), \tag{1.32}$$

where we defined the *detuning* of the laser frequency from the qubit frequency as $\delta=\omega_L-\omega_0$, and where $\hat{x}_m(t)=e^{i\omega_m t}\hat{a}_m^\dagger+e^{-i\omega_m t}\hat{a}_m$ is the position of the mth phonon mode. The first term inside the square brackets drives spin flips, while the second term couples each spin to the collective phonon modes. Note that the neglected higher-order terms can lead to errors, although they can be mostly compensated using strategies such as pulse shaping of the Rabi frequency [135].

1.4.1 Resonant driving

By appropriate choice of the detuning δ, specific terms in Eq. (1.32) are resonant. An energy diagram for the system is shown in Fig. 1.3(a), while Fig. 1.3(b) shows the three choices for δ that we consider:

1. Setting $\delta=0$ and keeping only resonant terms yields the *carrier transition*,

$$\hat{H}_{\text{c}}(t)=-\frac{1}{2}\sum_{i=1}^{N}\Omega_i\hat{\sigma}_i^\phi, \tag{1.33}$$

   we assumed that $\phi(t)=\phi$ is time-independent, and $\hat{\sigma}_i^\phi=\cos(\phi)\hat{\sigma}_i^x+\sin(\phi)\hat{\sigma}_i^y$. This Hamiltonian drives spin flips and leaves the motional state unchanged.

2. Setting the detuning to the negative of the center of mass mode frequency, $\delta=-\omega_{\text{com}}$, and keeping only resonant terms yields the *red sideband*[1],

$$\hat{H}_{\text{rsb}}(t)=\frac{i}{2}\sum_{i=1}^{N}\Omega_i\eta_{\text{com},i}\left(e^{i\phi(t)}\hat{\sigma}_i^-\hat{a}_{\text{com}}^\dagger-e^{-i\phi(t)}\hat{\sigma}_i^+\hat{a}_{\text{com}}\right), \tag{1.34}$$

[1]The terminology red sideband is used because the laser frequency is red, i.e. lower, detuned from the qubit frequency. To see this, note that for $\delta=-\omega_{\text{com}}$, $\omega_L=\omega_0-\omega_{\text{com}}$.

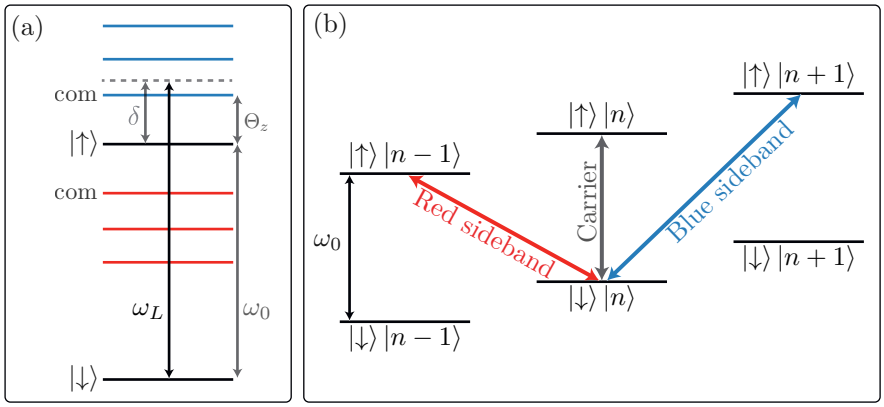


Figure 1.3: Ion-light interactions. **(a)** Energy diagram of the axial modes of a 1D chain along z including the blue and red sidebands. Laser light at frequency ω_L (black arrow) is detuned from the qubit slitting ω_0 by δ. Choosing $\delta = 0$ drives the carrier transition, while $\delta = -\omega_{\text{com}}$ and $\delta = \omega_{\text{com}}$ drive the red and blue sideband, respectively. For the 1D chain along z, $\omega_{\text{com}} = \Theta_z$. **(b)** The carrier transition ($\delta = 0$) drives spin flips between $|\downarrow\rangle$ and $|\uparrow\rangle$ without changing the motional state. The red sideband ($\delta = -\omega_{\text{com}}$) transfers excitations between spin and motion, taking $|\downarrow\rangle\,|n\rangle$ to $|\uparrow\rangle\,|n-1\rangle$. The blue sideband ($\delta = \omega_{\text{com}}$) simultaneously excites the spin and the motion, taking $|\downarrow\rangle\,|n\rangle$ to $|\uparrow\rangle\,|n+1\rangle$.

where we used "com" subscripts to distinguish com mode operators from the numerically indexed $\hat{x}_i$ operators that act on the ith ion. The red sideband, also known as the *Jaynes-Cummings Hamiltonian* [134, 136], describes the transfer of excitations between the com mode and the qubit.

3. Setting $\delta = \omega_{\text{com}}$ and keeping only resonant terms yields the *blue sideband*,

$$\hat{H}_{\text{bsb}}(t) = \frac{i}{2}\sum_{i=1}^{N}\Omega_i\eta_{\text{com},i}\left(e^{i\phi}\hat{\sigma}_i^{-}\hat{a}_{\text{com}} - e^{-i\phi}\hat{\sigma}_i^{+}\hat{a}_{\text{com}}^{\dagger}\right), \tag{1.35}$$

also known as the *anti-Jaynes-Cummings Hamiltonian*, which describes simultaneous excitation of the qubit and the phonon mode.

Finally, we include two tones in the laser frequency: the first at the red sideband $\delta = -\omega_{\text{com}}$ with phase $\phi_r(t)$, and the second at the blue sideband $\delta = \omega_{\text{com}}$ with phase $\phi_b(t)$. Again in the rotating wave approximation, keeping only resonant terms results in a *spin-dependent force*,

$$\hat{H}_{\text{sdf}}(t) = \hat{H}_{\text{rsb}}(t) + \hat{H}_{\text{bsb}}(t) = \frac{1}{2}\sum_{i}\Omega_i\eta_{\text{com},i}\left(\hat{a}_{\text{com}}e^{i\phi_d} + \hat{a}^{\dagger}e^{-i\phi_d}\right)\hat{\sigma}_i^{\phi_s}, \tag{1.36}$$

where we introduced the phase sum $\phi_s = (\phi_b + \phi_r)/2 + \pi/2$, and phase difference $\phi_d = (\phi_b - \phi_r)/2$. This Hamiltonian drives motional phase-space displacements

conditioned on the state of the qubit. The phase-space direction is controlled by ϕ_d. Spin-dependent forces can be used to prepare interesting non-classical states such as cat states [137] or grid states [138].

1

1.4.2 Near-resonant driving

Next, we drive the system with two tones symmetrically tuned near, but not resonant with, the red and blue sidebands [139, 140]. The detunings are $\delta = -\omega_{\text{com}} - \delta_{\text{com}}$, and $\delta = \omega_{\text{com}} + \delta_{\text{com}}$, where δ_{com} specifies the additional detuning from the com mode. If we set identical Rabi frequencies on all ions and choose $\phi_b = \phi_r = 0$, we obtain a global, near-resonant spin-dependent force,

$$\hat{H}_{\text{sdf}}(t, \delta_{\text{com}}) = \Omega\eta_{\text{com}} \left(\hat{a}_{\text{com}} e^{i\delta_{\text{com}}t} + \hat{a}^\dagger e^{-i\delta_{\text{com}}t}\right) \hat{J}_{\phi_s}, \tag{1.37}$$

where we assumed that $\omega_{\text{com}} \gg \delta$ to make the rotating wave approximation and ignore fast-rotating terms at $e^{\pm 2i(\omega_{\text{com}}+\delta)t}$. We also denoted $\eta_{\text{com},i} = \eta_{\text{com}}$ because the Lamb-Dicke parameter for the com mode is identical for all ions, and introduced the *collective spin operators*,

$$\hat{J}_\alpha = \frac{1}{2}\sum_{i=1}^{N} \hat{\sigma}_i^\alpha, \tag{1.38}$$

which satisfy the usual su(2) algebra, $[\hat{J}_x, \hat{J}_y] = i\hat{J}_z$, $[\hat{J}_z, \hat{J}_x] = i\hat{J}_y$ and $[\hat{J}_y, \hat{J}_z] = i\hat{J}_x$. The dynamics of a time-dependent Hamiltonian such as Eq. (1.37) can be written in terms of an infinite series using the *Magnus expansion* [141],

$$\hat{U}(t) = \exp\left(\sum_{k=1}^{\infty} \hat{\Theta}_k(t)\right), \tag{1.39}$$

with explicit expressions for $\hat{\Theta}_k(t)$ found in e.g. Ref. [142]. For the spin-dependent force $\hat{H}_{\text{sdf}}(t, \delta_{\text{com}})$, all terms beyond second order vanish identically. The dynamics are therefore described by the Magnus expansion truncated at second order,

$$\hat{U}(t) = \exp\left(-i\int_0^t \hat{H}(t_1)dt_1 - \frac{1}{2}\int_0^t \int_0^{t_1} [\hat{H}(t_1), \hat{H}(t_2)]dt_2 dt_1\right), \tag{1.40}$$

The first-order term is,

$$-i\int \hat{H}_{\text{sdf}}(t_1, \delta_{\text{com}}) = -i\frac{\Omega\eta_{\text{com}}}{\delta_{\text{com}}} \left([i - ie^{it\delta_{\text{com}}}]\hat{a} + \text{h.c.}\right) \hat{J}_{\phi_s}, \tag{1.41}$$

while the second-order term is,

$$-\frac{1}{2}\iint [\hat{H}_{\text{sdf}}(t_1, \delta_{\text{com}}), \hat{H}_{\text{sdf}}(t_2, \delta_{\text{com}})] = -i\frac{\Omega^2\eta_{\text{com}}^2}{\delta_{\text{com}}^2}[t\delta_{\text{com}} - \sin(t\delta_{\text{com}})]\hat{J}_{\phi_s}^2. \tag{1.42}$$

At generic times t, the first-order Magnus term generates spin-dependent displacements, and therefore entangles the spins and com mode. However, at specific times, the first-order term vanishes because the bosonic state performs a closed loop in phase space, at which point the motion decouples from the spins. The first non-trivial time when this occurs is $t = 2\pi/\delta_{\text{com}}$. Then, the second-order Magnus term completely describes the dynamics, resulting in the so-called *one-axis twisting unitary*,

$$\hat{U}_{\text{OAT}} = \exp\left(-i\frac{2\pi\eta_{\text{com}}^2\Omega^2}{\delta_{\text{com}}^2}\hat{J}_{\phi_s}^2\right). \tag{1.43}$$

This unitary generates *spin squeezing*, where the variance of the collective spin operator along one direction, $(\Delta\hat{J}_{\theta_1})^2$ is reduced at the expense of increased variance in a second direction, $(\Delta\hat{J}_{\theta_2})^2$ [46, 143]. One-axis twisting is a critical ingredient in our global variational quantum circuit of Ch. 4.

Finally, by illuminating only two ions at a time, the one-axis twisting Hamiltonian realizes a two-qubit entangling gate between the two selected ions. This digital entangling gate, when combined with single-qubit rotations of Eq. (1.33), is sufficient for universal quantum computation [32]. The two-qubit gate introduced here is said to operate in the *general-field regime*, and belongs to a class of gates known as the *Mølmer-Sørensen gates*, also sometimes called *phase gates* [139, 140].

1.4.3 Off-resonant (dispersive) driving

Next, we consider driving with two far-detuned tones [33, 34, 144, 145]. We choose symmetric detuning about the carrier, i.e. $-\delta$ with phase ϕ_r and δ with phase ϕ_b. Keeping all of the phonon modes, the interaction Hamiltonian is,

$$\hat{H}_{\text{2tone}}(t) = \sum_{i=1}^{N}\left[\frac{\Omega_i}{2}(e^{-i\delta t+i\phi_r} + e^{i\delta t+i\phi_b})\hat{\sigma}_i^-(1 - i\sum_{m=1}^{3N}\eta_{m,i}\hat{x}_m(t)) + \text{h.c.}\right]. \tag{1.44}$$

The dynamics are again solved by the second-order truncated Magnus expansion of Eq. (1.40), with details given in Appendix 8. If $\eta_{\text{com},i}\Omega_i \ll |\delta - \omega_m|$, known as the *dispersive* or *weak-field regime*, the first-order Magnus term describing spin-dependent displacements can be ignored. This can be understood in the rotating frame, where the large detuning means that the displacement's phase-space direction rotates rapidly, and therefore averages to zero. The dynamics are then completely described by the second-order Magnus term, which takes the form of dynamics generated by a time-independent Ising Hamiltonian,

$$\hat{H}_{\text{Ising}} = \sum_{i,j} J_{i,j}\hat{\sigma}_i^{\phi_s}\hat{\sigma}_j^{\phi_s}, \tag{1.45}$$

where the elements of the coupling matrix are defined as,

$$J_{i,j} = \Omega_i\Omega_j\sum_m \frac{\omega_m\eta_{m,i}\eta_{m,j}}{\delta^2 - \omega_m^2}. \tag{1.46}$$

The emergence of the Ising Hamiltonian can be understood as a many-mode, non-global generalization of the one-axis twisting Hamiltonian of Eq. (1.43). We observe that by operating in this regime where the dynamics is effectively described by a purely spin Hamiltonian, the trapped-ion system is operating as an analogue quantum simulator of an Ising Hamiltonian [145]. The simulator can be programmed by changing the detuning δ. In particular, for intermediate detunings the interaction strength decays as a power law, $J_{i,j} \propto d_{i,j}^{-a}$, where $d_{i,j}$ is the distance between the ith and jth ion and $0 \leq a \leq 3$ [21]. It can also be programmed by engineering the phonon modes, for example using optical tweezers [1, 37–39] or using standing-wave optical potentials [35, 36]. We review optical tweezers in the next section, Sec. 1.5.

Finally, note again that illuminating only two ions realizes a Mølmer-Sørensen gate. Here, the gate is said to operate in the *weak-field regime* [33], because it requires $\eta_{\mathrm{com},i}\Omega_i \ll |\delta - \omega_m|$ to ensure that the phonon modes are only virtually excited. The advantage of this regime is that the gate is effectively insensitive to the motional state, with the only requirement being the Lamb-Dicke regime [33].

1.5 Optical tweezers

Optical tweezers, which provide an additional confining potential, can augment the programmability of trapped-ion quantum simulators [1, 37–39]. Consider N tightly-focused laser beams along x, each centered on the equilibrium position $r_{i,\alpha}^{(0)}$ of a trapped ion. For a paraxial Gaussian beam with cylindrical symmetry supplying confinement in the $y-z$ plane only, the in-plane $(y-z)$ intensity is,

$$I_{\mathrm{tw}}(r_{i,\alpha}) = \frac{2P_0}{\pi w^2} e^{-2(r_{i,\alpha} - r_{i,\alpha}^{(0)})^2/w^2}, \tag{1.47}$$

where P_0 is the beam power and w the beam waist. The beam's electric field induces an atomic dipole moment described by the interaction potential $V(r) = -\operatorname{Re}(\alpha) I(r)/(2\epsilon_0 c)$, where c is the speed of light in vacuum and α is the complex polarizability [146]. The optical tweezer potential is therefore,

$$V_{\mathrm{tw}}(r_{i,\alpha}) = \frac{-\operatorname{Re}(\alpha) P_0}{c\epsilon_0 \pi w^2} \sum_{i=1}^{N} \sum_{\alpha=y,z} e^{-2(r_{i,\alpha} - r_{i,\alpha}^{(0)})^2/w^2}. \tag{1.48}$$

Provided that the ion remains close to the beam center, we can Taylor expand the Gaussian potential to first-order. Neglecting the constant offset term yields,

$$V_{\mathrm{tw}}(r_{i,\alpha}) \approx \frac{m}{2} \sum_{i=1}^{N} \sum_{\alpha=y,z} \nu_i^2 (r_{i,\alpha} - r_{i,\alpha}^{(0)})^2, \tag{1.49}$$

where we defined the *pinning frequency* as $\nu_i = \sqrt{4\alpha P_0/(\pi c \epsilon_0 m w^4)}$ by assuming that $\alpha > 0$. This additional, local confining potential does not change the equilibrium positions of Eq. (1.12) because the tweezers are focused at those points.

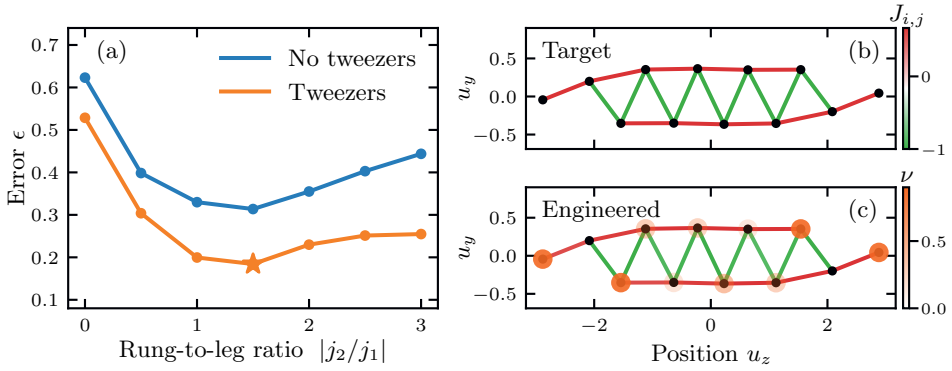


Figure 1.4: Quantum simulation of Ising Hamiltonian using 2D ion crystal and optical tweezers. **(a)** Normalized error ϵ between target J_T and engineered J_E coupling matrices without (blue) and with (orange) optical tweezers. For the point marked by the star, panel **(b)** shows the target interaction pattern and panel **(c)** shows the engineered pattern that was found when the detuning δ and pinning frequencies $\boldsymbol{\nu}$ were numerically optimized. The pinning frequency strength is denoted by the orange circles. The optimized detuning is $\delta = 2\pi \times 0.77$ MHz. We observe excellent visual agreement between target and engineered couplings. Adapted from Ref. [1, 147].

However, the Hessian $\boldsymbol{H}$ of Eq. (1.14) is shifted by a diagonal term,

$$\boldsymbol{H}_{\text{tw}} = \boldsymbol{H} + m\boldsymbol{\nu}^2, \tag{1.50}$$

where we defined the diagonal matrix $\boldsymbol{\nu} = \text{diag}(0, \nu_1, \nu_1, 0, \nu_2, \nu_2, \ldots, 0, \nu_N, \nu_N)$. The consequence of Eq. (1.50) is that the mode spectra and normal/Floquet modes depend on the pinning frequencies, which provides an additional control knob that can be used to engineer the $J_{i,j}$ Ising coupling matrix of Eq. (1.46).

Given the additional phonon-spectrum control provided by optical tweezers, how should we best choose the detuning δ and pinning frequencies $\boldsymbol{\nu}$ to realize Ising interactions of our choice? To do so, we define a target coupling matrix $\boldsymbol{J}_T$, and optimize δ and $\boldsymbol{\mu}$ such that the error ϵ between $\boldsymbol{J}_T$ and the engineered coupling, $\boldsymbol{J}_E$, is minimized. The error function is chosen as a matrix distance [39],

$$\epsilon = \frac{||\boldsymbol{J}_T - \boldsymbol{J}_E||}{||\boldsymbol{J}_T||}, \tag{1.51}$$

where $||.||$ is the Frobenius matrix norm.

To demonstrate the increased programmability, in Fig. 1.4 we use the in-plane modes of a 2D zig-zag crystal for quantum simulation of the Ising Hamiltonian. We consider a spin-ladder interaction graph, shown in panel (b). Here j_1 denotes the coupling strength along the legs (sides) of the ladder, and j_2 the coupling along the rungs. For various $j_2 < 0$ and fixed $j_1 = 1$, we numerically optimize

δ and $\boldsymbol{\nu}$ to minimize Eq. (1.51) using a maximum tweezer laser power of 30 W, beam waists of $w = 1\,\mu$m and detunings 0.3 MHz $\leq \delta/(2\pi) \leq$ 1.0 MHz. We also require that $|\delta - \omega_m| > 10$ kHz to ensure the phonon modes are only virtually excited. The numerical optimization is performed using simulated annealing in Optim.jl [148] and Julia [149]. Panel (a) shows the error ϵ as a function of the rung-to-leg ratio, $|j_2/j_1|$, without (blue) and with (orange) optical tweezers. Using optical tweezers results in consistently smaller error. For the point marked by the star, panel (b) shows the target interaction graph for $j_2 = -1.5$, while panel (c) shows the optimal engineered interaction graph when the detuning and pinning frequencies are optimized. The orange circles represent the pinning frequency strength. Visually, the agreement between the target and engineered coupling matrix is excellent. We study this system in more detail, including the effects of experimental errors such as micromotion, tweezer misalignment and tweezer intensity fluctuations in the next chapter, Ch. 2.

Chapter 2

Effect of micromotion and local stress

Based on
Physical Review A **106**, 042612, (2022) [1]

Reality is frequency inaccurate.

Douglas Adams, The Restaurant at the End of the Universe (1980)

The ability to program and control interactions provides the key to implementing large-scale quantum simulation and computation in trapped ion systems. As reviewed in the previous chapter, Ch. 1, trapped-ion quantum simulators allow for the simulation of spin-spin interactions which decay as $1/d^a$ where d is the distance between two ions and $0 \lesssim a \lesssim 3$. This is the direct result of the mechanism behind the interactions. The inter-ion interactions are phonon-mediated and as such depend on the spectrum and structure of the collective vibrational modes of the ion crystal [21, 150]. Recently it has been shown that the addition of optical tweezers to the typical trapped-ion platform produces a highly tunable quantum simulator in terms of connectivity, range, and sign of the interactions in both linear (or 1D) and triangular (2D) ion crystals in Paul traps [35, 37–39].

In this chapter, we study the robustness of the findings of Ref. [39] in the presence of experimental imperfections: micromotion, local stress, and intensity noise. We show that the effects of micromotion can be easily circumvented when designing and optimizing tweezer patterns. Furthermore, while local stress, whereby the tweezers apply small forces on individual ions, may appear to enable further tuning of the spin-spin interactions, any additional programmability is negligible.

2.1 Engineering spin-spin interactions in optical tweezers

We consider N ions in a Paul trap. As discussed in Ch. 1, the interplay between the external trapping potential and the Coulomb repulsion results in stable Coulomb crystals. The dimensionality of the crystal depends on the relative strength of the trapping potential along the different axes [151, 152]. In this chapter we focus on the case of a 2D zig-zag crystal in the $y-z$ plane. Tight confinement along x ensures the crystal forms in the $y-z$ plane, whilst a weaker potential along z compared to y (or vice-versa) leads to the formation of the zig-zag structure.

To characterize the effect of micromotion we study a $N = 12$ ion crystal using experimentally relevant trap parameters. As in Ch. 1 we use stability parameters $\boldsymbol{a} = (0.018704, -0.018900, 0.000196)$ and $\boldsymbol{q} = (0.202780, -0.202780, 0)$, and use an rf frequency of $\Omega_{\text{rf}} = 2\pi \times 20$ MHz. The corresponding pseudopotential frequencies are $\boldsymbol{\Theta} = 2\pi \times (2, 0.4, 0.14)$ MHz. The resulting equilibrium positions including micromotion, as well as the mode spectrum difference between the eigenfrequencies and the Floquet quasienergies are plotted in Fig. 1.2 of Ch. 1

On the experimental side, during the cooling of the ions the optical tweezers are turned off, and thus do not influence the ion crystal formation. After cooling, the tweezers must be turned on with a time-scale that is slow compared to the mode frequencies (~ 1 ms). The crystal remains stable as the ions only experience a local potential which further pins them in place. Also, parametric excitations are not possible as the tweezers correspond to local trap frequencies of a few hundred kHz, which is much smaller than the drive frequency (~ 20 MHz) [153].

2.1.1 Naive inclusion of micromotion

As discussed in Sec. 1.5 of Ch. 1, the addition of optical tweezers focused individually on each ion augments the programmability of the engineered Ising interaction matrix J_E. Here, we firstly make the pseudopotential approximation and numerically optimize the tweezer frequencies $\boldsymbol{\nu}$ and detuning δ to engineer a target coupling matrix J_T. The success of the optimization is quantified by the error function ϵ of Eq. (1.51), which is the relative error between the engineered J_E and the target J_T interaction matrices. During the optimization we assume that the equilibrium positions are unchanged by the tweezers. To justify this approximation we find that applying a large pinning frequency $\nu_i = 2\pi \times 10$ MHz on all ions causes an ion position change of ~ 10 nm, and that using the corrected ion positions with optimized tweezer frequencies causes a negligible change in ϵ on the order of 10^{-3}.

For the target coupling we choose a spin-ladder interaction, shown in Fig. 2.1(a), since it is challenging to realize in ion crystals using only the collective modes of the crystal in the absence of the tweezer potentials, as we showed in Fig. 1.4 of Ch. 1. It also offers variety via the coupling strength ratio j_2/j_1 enabling us to study the interplay of frustration and fluctuations, necessary ingredients for spontaneous continuous or discrete symmetry breaking in condensed matter systems. The ability

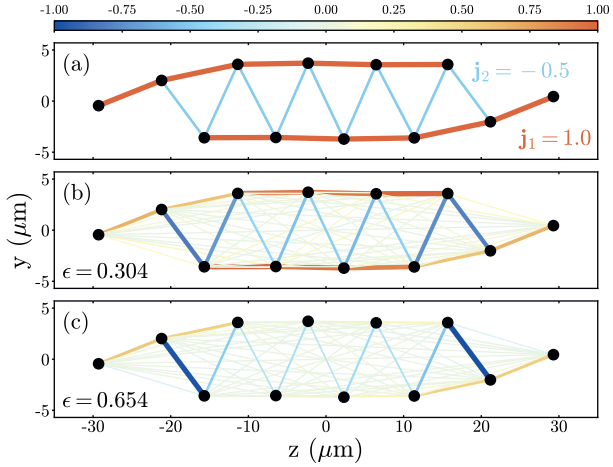


Figure 2.1: **(a)** Spin-spin couplings for the target zig-zag coupling J_T with $-j_2/j_1 = 0.5$. **(b)** Engineered couplings J_E in the pseudopotential approximation. With optical tweezers, the engineered target coupling has reasonably low error. **(c)** "Naive" inclusion of micromotion by using the tweezer parameters found in the pseudopotential case. The difference in mode structure results in a large increase in ϵ, making the tweezer solution found in the pseudopotential approximation unsuitable.

to tune the range of zig-zag couplings ($|j_2/j_1| \gg 1$) will allow us to study the phase diagram of this well-known frustrated magnetic system with no exact solution.

The numerical optimization procedure is performed with the same parameters as described in Sec. 1.5. Fig. 2.1(b) shows the optimal interaction graph and corresponding error $\epsilon_p = 0.304$ that can be realized in the pseudopotential approximation. Next, we "naively" account for micromotion by taking the optimal tweezer pattern found in the pseudopotential approximation and recalculating the error using the Floquet modes and quasienergies to compute the $J_{i,j}$ coupling matrix. As shown in Fig. 2.1(c), we find that $\epsilon_m = 0.654$. The difference $\epsilon_m - \epsilon_p = 0.350$ is significant, with the interaction graph showing little spin-ladder structure. As such, any optimization should include micromotion during the routine.

2.1.2 Including micromotion during optimization

Including micromotion during the optimization routine requires re-calculating the time-dependent Hessian with a given set of pinning frequencies $\boldsymbol{\nu}$ and solving the $6N$ Floquet equations to find the new mode structure. Although this procedure is computationally costly, for larger N the cost can be reduced by using the symmetry of the coupling matrix in the tweezer patterns. For example, the spin-ladder interaction is symmetric about $z = 0$ and thus the tweezer frequencies can be assumed

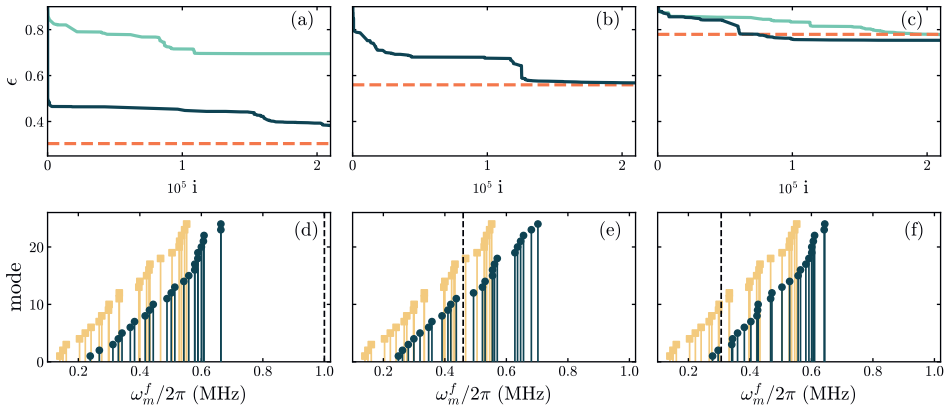


Figure 2.2: Panels **(a)**, **(b)** and **(c)** show the error ϵ as a function of optimization evaluations (i) for wave vectors $\boldsymbol{k} = [0, 1, 0]$, $\boldsymbol{k} = [0, 0, 1]$ and $\boldsymbol{k} = [0, 1, 1]$ respectively. The target coupling is the spin-spin ladder shown in Fig. 2.1. When including micromotion in the optimization (dark blue line) we obtain a similar ϵ as the pseudopotential case (dotted orange line). The k $= [0, 1, 0]$ case (panel a) shows the best performance due to the tighter confinement along y. Modulation (green line) has a detrimental effect in this scenario, as this is the direction where the micromotion amplitude is largest. Panels **(d)**, **(e)** and **(f)** show the native spectrum (yellow) and tweezer-modified spectrum (dark blue) corresponding to (a), (b) and (c) respectively. The black dashed line shows the optimized detuning δ. Note that $\left|\omega_m^f - \delta\right| < 10$kHz to maintain a dispersive spin-phonon coupling.

to obey the same symmetry. For the $N = 12$ ion Coulomb crystal we find that this is not a large enough system for this to necessary, and so optimize over all 12 tweezer frequencies. In Fig. 2.2 we plot the optimization of ϵ. When micromotion is included in the optimization (blue line), ϵ approaches the pseudopotential result (dashed orange). As such, micromotion itself is not a significant barrier to engineering interactions with optical tweezer.

2.1.3 First-order doppler modulation

The first order Doppler shift can have a significant impact on the spin-spin couplings. Following the procedure used in Ref. [121], to lowest order in a and q the laser field (up to a phase factor) in the reference frame of the moving ion is,

$$E_i(t) = \mathrm{Re}\left[\boldsymbol{E}_0 e^{i\boldsymbol{k}\cdot\hat{\boldsymbol{x}}_i} \sum_{n=-\infty}^{\infty} \mathcal{J}_n(\beta) e^{-i\omega t + in(\Omega_{\mathrm{rf}} t)}\right], \tag{2.1}$$

where ω is the frequency and $\boldsymbol{k}$ the wave vector, and $\mathcal{J}_n(\beta_i)$ the Bessel function. The (dimensionless) modulation index is $\beta_i = \frac{1}{2}\left|\sum_\alpha k_\alpha u_{i,\alpha}^{(0)} q_\alpha\right|$. The carrier transition

amplitude is modified by $\mathcal{J}_0(\beta_i)$, and thus the coupling matrix element is,

$$J_{i,j}^{\text{doppler}} = \mathcal{J}_0(\beta_i)\mathcal{J}_0(\beta_j)J_{i,j}, \tag{2.2}$$

where $J_{i,j}$ is the unmodulated coupling matrix element given in Eq. (1.46). Assuming a 411nm laser we include Doppler modulation in the optimization. The resulting ϵ is shown in Fig. 2.2. Although there is no Doppler modulation in z (because $q_z = 0$) nor x (because $u_{i,x}^{(0)} = 0$), there is significant modulation along y. The reduction in coupling strength depends on the distance of each ion from the $y = 0$ r.f. null, which makes it challenging to correct for using optical tweezers. While this ion-dependent source of error can be compensated by tuning the intensity on each ion of the laser beam implementing the spin-spin interactions, the extra infrastructure cost is prohibitive.

2.2 Local stress

In Section 2.1 we used tweezer beams centered on the average equilibrium positions of the ions to more accurately engineer spin-ladder interactions. However if the tweezer beams are offset from the equilibrium positions, the tweezers add not only a local trapping potential but also supply a force. In this section we investigate if this local stress enables further improvements to our engineered couplings. We show that tweezer offsets of up to 0.25 μm offer only small improvements to ϵ.

2.2.1 First-order approximation

For simplicity we assume that we have a geometry in which micromotion does not play a role. For tweezers with cylindrical symmetry supplying confinement in the $y - z$ plane only, the tweezer potential including an offset is,

$$V_{\text{tw}}(r_{i,\alpha}) = \frac{m}{2}\sum_{i=1}^{N}\sum_{\alpha=y,z}\nu_i^2(\tilde{r}_{i,\alpha} - \delta r_{i,\alpha})^2, \tag{2.3}$$

where $\tilde{r}_{i,\alpha} = r_{i,\alpha} - r_{i,\alpha}^{(0)}$ are the positions of the ions relative to their equilibrium positions and $\delta r_{i,\alpha}$ is the tweezer offset from $\tilde{r}_{i,\alpha}$.

Offsetting the tweezers changes the equilibrium positions of the ions. To find the new equilibrium positions $\mathbf{r}_i^{(0)} + \boldsymbol{\rho}_i$ we need to solve $\nabla_{\tilde{\mathbf{r}}} V_{\text{tot}} = 0$, where V_{tot} is the potential including the trapping, Coulomb and tweezer potentials. Solving this condition is computationally costly for large crystals, particularly when included in an optimization routine. Instead, as a first approximation we assume that the tweezers pull lightly on the ions, $\boldsymbol{\rho}_i/\boldsymbol{\delta r}_i \ll 1$. This is equivalent to treating the tweezers as a small perturbation compared to the Paul trap and Coulomb interactions. For simplicity we omit the x-direction, which is justified when the laser implementing the spin-spin interactions has no effective wave vector in the x-direction and the sound wave modes in the x-direction decouple, such as in a 2D ion crystal in the

$y-z$ plane. These prerequisites can be easily obtained by design. Denoting the Hessian matrix of $V_0 = V_{\text{trap}} + V_{\text{coulomb}}$ by D_0 and denoting the total potential including tweezers by V_{tot}, we expand $\nabla_{\tilde{\mathbf{r}}} V_{\text{tot}}(\rho)$ to first order,

$$\nabla_{\tilde{\mathbf{r}}} V_{\text{tot}}(\rho) \approx (\nabla_{\tilde{\mathbf{r}}} (\nabla_{\tilde{\mathbf{r}}} V_0(\tilde{\mathbf{r}})))_{\tilde{\mathbf{r}}=0} \ \boldsymbol{\rho} + \boldsymbol{\nu}^2(\boldsymbol{\rho} - \boldsymbol{\delta r}) = D_0(0)\boldsymbol{\rho} + \boldsymbol{\nu}^2(\boldsymbol{\rho} - \boldsymbol{\delta r}), \quad (2.4)$$

where $\boldsymbol{\nu}$ is a $2N \times 2N$ diagonal matrix with diagonal elements ν_i. Note the zeroth order term drops out since $(\nabla V_0)_{\tilde{\mathbf{r}}=0} = 0$ by definition. The lowest order shifts in the equilibrium positions are therefore,

$$\boldsymbol{\rho} \approx (D_{\text{tot}}(0))^{-1} \boldsymbol{\nu}^2 \delta \boldsymbol{r}, \quad (2.5)$$

where $D_{\text{tot}}(0) = D_0(0) + D_{\text{tw}}$ and $D_{\text{tw}} = \boldsymbol{\nu}^2$. To avoid calculating the Hessian $D_{\text{tot}}(\boldsymbol{\rho})$ directly from the new potential, we use an approximation to further reduce the computational cost,

$$D_{\text{tot}}(\boldsymbol{\rho}) \approx D_{\text{tot}}(0) + (\nabla_{\tilde{\mathbf{r}}}(D_0))_{\tilde{\mathbf{r}}=0} \ \boldsymbol{\rho} + \dots. \quad (2.6)$$

$D_{\text{tot}}(\boldsymbol{\rho})$ has new eigenfrequencies $\tilde{\omega}_m^{\text{str}}$ and eigenvectors $\tilde{\mathbf{b}}_m^{\text{str}}$ resulting in modified spin-spin interactions. Although only approximate, this equation gives insight into the effect of the local stress on the mode spectrum. Because both D_{tw} and D_{trap} are constant diagonal matrices, the derivatives of $D_{\text{tot}}(0)$ originate from the Coulomb interaction alone. Due to the long-range character of the Coulomb interactions we expect that the local stress should ease the simulation of long-range interactions. On the other hand, the local stress terms are higher order than the tweezer curvature terms, so we expect the capability of local stress to significantly change the mode spectrum to be limited. Although this suggests local stress will not offer improvements to our engineered couplings, the benefit is that errors due to misaligned tweezers are suppressed.

2.2.2 Optimization

We investigate numerically whether it is possible to improve on the results obtained in the previous section if the tweezers can supply local stress on the ions. For the $N = 12$ ion crystal we fix the tweezer pattern to the optimal solution found in Sec. 2.1 and optimize the tweezer offsets $0 \leq \boldsymbol{\delta r_i} \leq 0.25\,\mu\text{m}$. The offset bounds enable us to approximate the tweezers as harmonic. By fixing the tweezer parameters, we only need to optimize the $2N$ offset parameters, and therefore in the optimization routine can calculate the new equilibrium positions $\boldsymbol{r}_i^{(0)} = \boldsymbol{\rho}_i$ and Hessian directly. Optimizing the full parameter set (including the tweezer parameters) is possible, particularly with a two-step routine that firstly uses the approximate calculations of Eqs. 2.5 and 2.6 to determine if the parameters are promising, and then when the error falls below a set threshold uses the exact calculation to fine-tune the parameters and obtain the true error. We also optimize the full parameter set in this manner and find no difference to our fixed-tweezer optimization.

In Fig. 2.3 we vary the ratio $-j_2/j_1$ in the 12-ion spin-ladder and calculate the error as defined in Eq. (1.51). As expected, the inclusion of tweezers results in

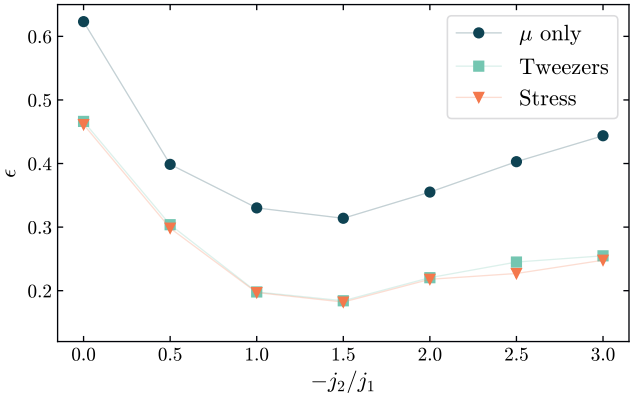


Figure 2.3: Error ϵ as a function of the spin-ladder coupling strength ratio $-j_2/j_1$. The error is smallest at $-j_2/j_1 = 1.5$ as this most closely resembles power-law interactions that can be well-engineered natively. The addition of tweezers offers significant improvement at all ratios, as we showed in Fig. 1.4 of Ch. 1. As predicted by our approximate expression Eq. (2.6), local stress of up to $0.25\,\mu$m only offers a small improvement. This suggests that the couplings are robust to tweezer misalignments.

significant improvements in engineering the target spin-spin interactions. However applying local stress to the ion crystal only results in minimal improvements. As such we conclude that in the perturbative regime local stress offers little benefit, but is reassuring since the interactions are therefore robust to tweezer misalignments.

2.2.3 Intensity noise

Finally, we study the effect of tweezer intensity fluctuations. We consider a worst-case shot-to-shot noise scenario, whereby an optimal set of tweezer frequencies ν are each subject to a fluctuation $\delta\nu$. Note that $\delta\nu \propto \sqrt{\delta P}$, where δP is the power fluctuation, since the square of the tweezer frequencies are proportional to the laser power. To simulate the noise we multiply an optimal tweezer pattern by a random fluctuation sampled from a normal distribution with standard deviation δP. We repeat the calculation $N_{\text{repeat}} = 10^4$ times and take the average. In Fig. 2.4 we plot ϵ versus the percentage noise in the tweezer power δP. We find that for typical experimental parameters intensity noise on the order of $\lesssim 1\%$ can have a noticeable impact on the engineered coupling. As such, intensity stabilization on the order of sub-percent is required to accurately engineer the target spin-ladder coupling.

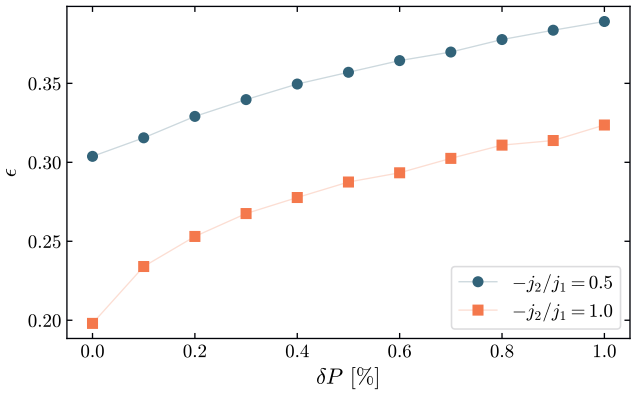


Figure 2.4: Error ϵ when tweezer intensity fluctuations δP are included for two different spin-ladder coupling strength ratios. The error is calculated assuming random Gaussian noise in the laser generating the optical tweezers at frequencies much slower than the coupling time.

2.3 Conclusions

Local optical potentials, supplied by optical tweezers, allow for analogue trapped-ion quantum simulators with an unprecedented level of programmability over the spin-spin interactions. We studied the robustness of this approach in a typical experimental setup, focusing on three sources of error: (i) micromotion, (ii) tweezer misalignment, and (iii) tweezer intensity noise. We used the ferromagnetic zig-zag model, with $j_1 > 0$ and $j_2 < 0$, to quantify the adverse effect of each source of error. Our choice of model is motivated by the fact that tweezers play a fundamental role in generating the target connectivity. Hence this model upper bounds the sensitivity of the scheme to the three sources of error listed above.

We showed that the effect of micromotion is two-fold. First, it shifts the motional mode spectrum, and second, it causes a first-order Doppler shift and in turn modulates the spin-spin couplings for each ion. We showed that although the motional mode shift is at the level of few percent, it must be included in the optimization of the tweezer frequencies to realize low-error coupling matrices. The first-order Doppler shift may be a major source of error along the weaker confinement direction when micromotion is the largest. In contrast, we find that in the limit where the tweezer potential is perturbative compared to the Paul trap and the Coulomb interactions, any additional stress and strain force on the ions due to the misalignment of the tweezers is negligible. Finally we find that the intensity noise should be controlled to the sub-percent level, as this shot-to-shot noise severely impacts the fidelity with which the target interactions can be realized.

Chapter 3

Optimal many-body displacement sensing

Based on
arXiv:2510.25870 (2025) [2]

Cassian: "Do you think anybody's listening?"
Jyn: "I do. Someone's out there"

Star Wars: Rogue One (2016)

Measuring the response of a system to estimate an unknown parameter underpins the development of science and technology. For example, the detection of gravitational waves at the Laser Interferometer Gravitational-Wave Observatory (LIGO) confirmed one of the most important predictions of the general theory of relativity [43, 154], while precision spectroscopy in atomic clocks has revolutionized timekeeping with fractional uncertainties now below 10^{-18} [49, 155]. At the same time, significant efforts have been devoted to using quantum systems for sensing theorized couplings between Standard Model fields and dark matter candidates such as dark photons, millicharged dark matter or axions [50, 51, 53]. Such couplings would induce ultra-small bosonic *displacements* of a microwave field [52–56] or a mechanical oscillator [51, 57–61], which could be measured by a sufficiently sensitive displacement sensor.

The sensitivity of the quantum sensor crucially depends on its initial reference state. Using a classical, uncorrelated reference state, the estimation uncertainty is lower bounded by the so-called standard quantum limit (SQL). For displacement sensing, the SQL is defined by bosonic coherent states and is constant, $\mathrm{SQL} \propto \mathcal{O}(1)$. As such, the sensitivity cannot be improved by simply increasing the amplitude of the coherent state. By instead using non-classical reference states and quantum measurement protocols, the estimation uncertainty is ultimately limited by Heisenberg scaling, $\mathrm{HS} \propto 1/\langle \hat{\mathrm{n}} \rangle$, where $\langle \hat{n} \rangle$ is the reference state's average bosonic occupation [40]. This is know as *quantum-enhanced sensing*.

Previous works have considered a range of different bosonic reference states for quantum-enhanced displacement sensing. Examples of states that can achieve sub-SQL sensitivities are Fock states [62, 63] and their (optimal) superpositions [64], phase-twirled squeezed states [65] and two- and four-component cat states [53, 66]. Simultaneous sub-SQL sensing of a displacement's real and imaginary phase-space component can also be achieved using, for example, single-mode grid states [67–69] and two-mode squeezed states [70–72].

However, the aforementioned reference states do not take full advantage of the available degrees of freedom in *many-body* experimental platforms, which feature exquisite control over both spin and bosonic degrees of freedom [127, 156–159]. Such many-body systems are ideal quantum sensors as they offer the possibility of *collective enhancement* for faster reference state preparation, or for amplification of the displacement signal. For example, spin-boson cat states are prepared $\sqrt{N}$ times faster in a trapped-ion system with N ions, while electric field sensing benefits from a $\sqrt{N}$ amplification of the displacement signal when using N ions [57]. While there are existing protocols for single-parameter displacement sensing in many-body systems [57, 160, 161], there is a lack of sensing protocols that utilize the advantages of many-body quantum systems for estimating a displacement's amplitude, or jointly estimating its real and imaginary components.

Here, we solve this problem by introducing many-body displacement sensing schemes using spin-dependent bosonic squeezed states – hybrid spin-boson states whose bosonic squeezed quadrature is conditioned on the state of an auxiliary spin. We prove that such states are *optimal* reference states for both amplitude and joint-parameter displacement sensing, with Quantum Cramér-Rao bounds that saturate the Heisenberg limit. We develop explicit measurement protocols that follow Heisenberg scaling and can be readily implemented on existing quantum hardware platforms. Finally, we propose a scalable protocol for preparing spin-dependent squeezed states in trapped ions that requires only global addressing, and numerically demonstrate that for $N = 20$ ions our protocol achieves 8.7 dB of spin-dependent squeezing 15 times faster than the usual approach of driving the second-order sidebands. Our state-preparation protocol also has immediate applications to quantum computing with both discrete [162–164] and continuous [165, 166] variable systems.

3.1 Displacement sensing

Consider a system of N spins and a single bosonic mode, prepared in a reference state, $|\psi_{\text{ref}}\rangle$. The reference state is subjected to a small, coherent displacement by an unknown amount $\beta \in \mathbb{C}$, described by the displacement operator, $\hat{D}(\beta) = \exp\big(\beta\hat{a}^\dagger - \beta^*\hat{a}\big)$. The resulting displaced state is,

$$|\psi(\boldsymbol{\theta})\rangle = \hat{D}(\beta)\,|\psi_{\text{ref}}\rangle\,, \tag{3.1}$$

which encodes a set of d real parameters, $\boldsymbol{\theta} = \{\theta_1, \theta_2, \ldots, \theta_d\}$. Here, $\boldsymbol{\theta}$ is related to β. We review quantum multi-parameter metrology in more detail in the Supple-

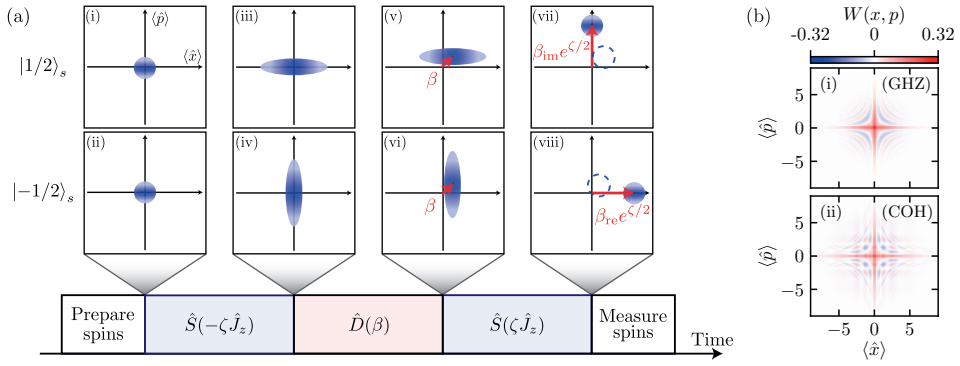


Figure 3.1: Phase-insensitive sensing of a displacement amplitude using spin-dependent squeezed states. **(a)** Pulse sequence of the sensing protocol. Top (bottom) row shows for $N = 1$ spin, schematic representations of the bosonic Wigner function associated with the spin $|1/2\rangle_s$ ($|-1/2\rangle_s$) state. After initialization to $|0\rangle_b |\psi_0\rangle_s \cong |0\rangle_b (|-1/2\rangle_s + |1/2\rangle_s)$, (panels (i) and (ii)), spin-dependent squeezing $\hat{S}(-\zeta\hat{J}_z)$ squeezes the bosonic mode conditioned on the spin state (panels (iii) and (iv)). The bosonic mode then undergoes an unknown displacement $\hat{D}(\beta)$ (panels (v) and (vi)). Finally, the spin-dependent squeezing is reversed (panels (vii) and (viii)). The signal's imaginary part, $\beta_{\rm im}$, is exponentially amplified in the $|1/2\rangle_s$ Hilbert space sector, while the real part, $\beta_{\rm re}$, is amplified in the $|-1/2\rangle_s$ sector. Unlike the phase-insensitive amplification protocol of Ref. [167], here the signal amplification is spin-dependent. Phase-insensitive information about the displacement is accessed via a spin measurement. Without spin-dependent squeezing, the final state is a purely bosonic displaced state (blue dashed circles). **(b)** Wigner function $W(x,p)$ of the bosonic states (i) $|\psi^{(\rm B)}_{\rm GHZ}\rangle \simeq |-N\zeta/2\rangle_b + |N\zeta/2\rangle_b$ and (ii) $|\psi^{(\rm B)}_{\rm COH}\rangle \simeq \sum_{m-J}^{J} \sqrt{\binom{N}{m+N/2}} |\zeta m\rangle_b$, with squeezing parameter $\zeta = 0.3$ and $N = 10$ spins. Both Wigner functions feature simultaneous squeezing along orthogonal quadratures, sub-Planck structure, and Z_4 symmetry. There is more phase space interference in (ii) due to the presence of additional states in the superposition.

mental Material of Sec. 3.4.

Our goal is to estimate $\boldsymbol{\theta}$ from a set of M independent measurement outcomes, $\boldsymbol{x} = \{x_1, \ldots, x_M\}$. The uncertainty of the estimation is quantified by the covariance matrix, $\boldsymbol{V}(\boldsymbol{\theta}) = \sum_{\boldsymbol{x}} p(\boldsymbol{x}|\boldsymbol{\theta})[\boldsymbol{\theta} - \tilde{\boldsymbol{\theta}}(\boldsymbol{x})][\boldsymbol{\theta} - \tilde{\boldsymbol{\theta}}(\boldsymbol{x})]^T$, where $p(\boldsymbol{x}|\boldsymbol{\theta})$ are the measurement probabilities and $\tilde{\boldsymbol{\theta}}(\boldsymbol{x})$ an unbiased estimator.

For a chosen reference state and measurement observable, minimizing over all possible unbiased estimators lower bounds $\boldsymbol{V}$ by the classical Fisher information matrix $\boldsymbol{F}$ according to the classical Cramér-Rao bound (CCRB),

$$\mathrm{Tr}(\boldsymbol{V}) \geq \mathrm{Tr}\big(\boldsymbol{F}^{-1}\big), \tag{3.2}$$

where $F_{ij} = \sum_k [\partial_i p(x_k|\boldsymbol{\theta})][\partial_j p(x_k|\boldsymbol{\theta})]/p(x_k|\boldsymbol{\theta})$, with $\partial_i = \partial/\partial\theta_i$, and set $M = 1$.

Also optimizing over all possible measurement observables, $\boldsymbol{V}$ is lower bounded by the quantum Fisher information matrix $\boldsymbol{Q}$ according to the quantum Cramér-Rao bound (QCRB) [168, 169],

$$\mathrm{Tr}(\boldsymbol{V}) \geq \mathrm{Tr}\big(\boldsymbol{Q}^{-1}\big), \tag{3.3}$$

where $Q_{ij} = \langle\psi(\boldsymbol{\theta})| \{\hat{L}_i, \hat{L}_j\} |\psi(\boldsymbol{\theta}\rangle /2$, with $\hat{L}_i$ the symmetric logarithmic derivative. In general, finding measurement observables whose classical Fisher information matrix saturates the quantum Fisher information matrix is non-trivial.

Typically, displacement sensing is performed in the paradigm of metrology by repetition, in which a single experimental shot – consisting of reference state preparation, linear interaction with the signal, and measurement – is repeated many times. It is therefore important to establish whether the relative phase between the reference state and the unknown displacement varies between experimental shots. This leads to two settings:

(i) *Phase-insensitive sensing of the displacement's magnitude*: If the phase varies between experimental shots, we can only estimate the displacement magnitude, so $\boldsymbol{\theta} = |\beta|$.

(ii) *Single- or multi-parameter sensing*: If the phase is fixed between shots, we can decompose $\beta = \beta_{\mathrm{re}} + i\beta_{\mathrm{im}}$. We can estimate a single parameter, so $\boldsymbol{\theta} = \{\beta_{\mathrm{re}}\}$ or $\boldsymbol{\theta} = \{\beta_{\mathrm{im}}\}$, or jointly estimate both parameters, so $\boldsymbol{\theta} = \{\beta_{\mathrm{re}}, \beta_{\mathrm{im}}\}$.

Minimizing the QCRB over all possible reference states yields the Heisenberg limit (HL). Here, we take the minimization to be over all possible single-mode bosonic reference states, see Sec. 3.4.3. In terms of the reference state's average mode occupation $\langle\hat{n}\rangle$, for single-parameter displacement sensing HL $= 1/(16\langle\hat{n}\rangle{+}4)$, for phase-insensitive amplitude sensing HL $= 1/(8\langle\hat{n}\rangle + 4)$ and for multi-parameter displacement sensing HL $= 1/(4\langle\hat{n}\rangle{+}2)$. If a metrology protocol's CCRB or QCRB equals the HL lower bound, we say that it "saturates the Heisenberg limit", and is therefore "optimal". If it falls inversely with $\langle\hat{n}\rangle$ but with a larger constant prefactor than that of the HL, we say that it "follows Heisenberg scaling".

3.1.1 Spin-dependent squeezed states

In this work, we consider reference states of the form,

$$|\psi_{\mathrm{ref}}\rangle = \hat{U} \,|0\rangle_b \,|\psi_0\rangle_s \,. \tag{3.4}$$

Here, $|0\rangle_b$ is the bosonic vacuum, and $|\psi_0\rangle_s = \sum_{m=-N/2}^{N/2} c_m \,|m\rangle_s$ is a collective spin state written with coefficients $c_m \in \mathbb{C}$ in the basis of Dicke states, $\hat{J}_z \,|m\rangle_s = m \,|m\rangle_s$, where the magnetization m is (half-)integer $-N/2 \leq m \leq N/2$, and where the collective spin operators are $\hat{J}_\alpha = \sum_{i=1}^{N} \hat{\sigma}_i^\alpha/2$ with $\alpha = x, y, z$. The unitary $\hat{U}$ entangles the spin and bosonic degrees of freedom; possible choices that have been previously studied include spin-dependent displacements [53, 57] or dispersive spin-boson interactions [160, 161].

We ask, for each of the metrology settings defined above, what is the optimal reference state? In Fig. 3.1(a) we sketch the Wigner function for one such state, which is generated by spin-dependent squeezing [162, 170],

$$\hat{S}(\zeta \hat{J}_z) = \exp\left(\frac{1}{2}(\zeta^* \hat{a}^2 - \zeta \hat{a}^{\dagger 2})\hat{J}_z\right), \tag{3.5}$$

where ζ is the squeezing parameter. The creation and annihilation operators, $\hat{a}^\dagger$ and $\hat{a}$, are related to position and momentum operators via $\hat{x} = \hat{a}^\dagger + \hat{a}$ and $\hat{p} = i(\hat{a}^\dagger - \hat{a})$, respectively. Spin-dependent squeezing is also known as conditional squeeze [165, 171, 172] or control-squeeze [173, 174]. In Sec. 3.2 we show how it can be implemented in a fast, scalable manner in trapped-ion systems. We write the reference state obtained from spin-dependent squeezing as,

$$|\psi_{\text{ref}}\rangle = \hat{S}(\zeta \hat{J}_z)\,|0\rangle_b\,|\psi_0\rangle_s = \sum_{m=-N/2}^{N/2} c_m\,|\zeta m\rangle_b\,|m\rangle_s\,, \tag{3.6}$$

where $|\zeta m\rangle_b = \hat{S}(\zeta m)\,|0\rangle_b = \exp\left(\zeta m(\hat{a}^2 - \hat{a}^{\dagger 2})/2\right)|0\rangle_b$ is a bosonic squeezed state. Without loss of generality we set $\zeta \in \mathbb{R}$, which is equivalent to setting the initial phase-space axis.

For $|\psi_0\rangle_s$, we focus on two particular choices: the Greenberger–Horne–Zeilinger (GHZ) state [175] and a coherent spin state (COH) pointing along x of the collective Bloch sphere,

$$|\psi_{\text{GHZ}}\rangle = \frac{1}{\sqrt{2}}\,|0\rangle_b\,(|-N/2\rangle_s + |N/2\rangle_s), \tag{3.7a}$$

$$|\psi_{\text{COH}}\rangle = e^{i\pi/2\hat{J}_y}\,|0\rangle_b\,|0\rangle_s = \sum_m c_m\,|0\rangle_b\,|m\rangle_s\,, \tag{3.7b}$$

where $c_m = 2^{-N/2}\sqrt{\binom{N}{m+N/2}}$ for the coherent spin state. It is instructive to visualize the reference states generated by spin-dependent squeezing from each of these initial collective spin states. For $N = 1$ spin, both spin states are the same. In Fig. 3.1(a) we separately plot the Wigner functions for the $m = 1/2$ (top row) and $m = -1/2$ (bottom row) Hilbert space sectors. The bosonic state is squeezed along orthogonal directions (panels (iii) and (iv)). In Fig. 3.1(b) we plot the Wigner functions of purely bosonic states that are analogous to the spin-boson states [1]. Panel (i) shows $|\psi^{(\text{B})}_{\text{GHZ}}\rangle \simeq |-N\zeta/2\rangle_b + |N\zeta/2\rangle_b$, panel (ii) shows $|\psi^{(\text{B})}_{\text{COH}}\rangle \simeq \sum_m c_m\,|\zeta m\rangle_b$, with both states written here up to normalization. We observe simultaneous squeezing along orthogonal quadratures, and Z_4 symmetric sub-Planck structure. As discussed in Refs. [173, 176, 177], these features indicate utility for the joint estimation of the real and imaginary components of a displacement signal, $\beta = \beta_{\text{re}} + i\beta_{\text{im}}$ [178].

[1] Note that the bosonic analogue states are not obtained by tracing out the spin degree of freedom, which would produce a mixed state.

3.1.2 Phase-insensitive displacement sensing

We begin in the setting where the phase between displacement and reference state varies between shots, which limits us to sensing the magnitude, $|\beta|$. The metrological utility is quantified by the QFI, cf. the QCRB of Eq. (3.3).

We consider any initial collective spin state with symmetric Dicke weights, i.e. $|c_m| = |c_{-m}|$. As we derive in the Supplemental Material of Sec. 3.4, the QFI is completely independent of β,

$$Q_{|\beta|} = 8 \sum_{m>0}^{N/2} |c_m|^2 \cosh(2\zeta m), \tag{3.8}$$

and grows exponentially with squeezing ζ, indicating metrological utility. The corresponding QCRB is,

$$V(|\beta|) = 1/Q_{|\beta|} \geq 1/(8\langle\hat{n}\rangle + 4), \tag{3.9}$$

where $\langle\hat{n}\rangle = \langle\psi_{\text{ref}}|\hat{n}|\psi_{\text{ref}}\rangle$. The Heisenberg limit for the estimation of $|\beta|$ is $1/(8\langle\hat{n}\rangle + 4)$, and therefore the QCRB saturates the Heisenberg limit. As such, as a function of the available resources (i.e. the mode occupation), the reference state is optimal for phase-insensitive estimation of the displacement's amplitude $|\beta|$.

Measurement protocol

Because the displaced reference state is spin-boson entangled, the metrological advantage is in a mixed spin-boson quadrature, which is often challenging to measure experimentally. This problem is solved by mapping the information to the spin degree of freedom using a time-reversal sequence, shown in Fig. 3.1(a). The sequence braids to a displacement that depends exponentially on the spin,

$$\hat{S}(\zeta\hat{J}_z)\hat{D}(\beta)\hat{S}(-\zeta\hat{J}_z) = \hat{D}(\hat{\beta}), \tag{3.10}$$

where $\hat{\beta} = \beta\cosh(\zeta\hat{J}_z) - \beta^*\sinh(\zeta\hat{J}_z)$.

We start by considering the sequence for a single spin initialized in $|0\rangle_b|\psi_0\rangle_s \simeq |0\rangle_b(|-1/2\rangle_s + |1/2\rangle_s)$. The final state is,

$$|\psi_f\rangle \simeq \hat{D}(\beta_-)|0\rangle_b|-1/2\rangle_s + \hat{D}(\beta_+)|0\rangle_b|1/2\rangle_s, \tag{3.11}$$

where $\beta_- = \beta_{\text{re}}\exp(\zeta/2) + i\beta_{\text{im}}\exp(-\zeta/2)$ and $\beta_+ = \beta_{\text{re}}\exp(-\zeta/2) + i\beta_{\text{im}}\exp(\zeta/2)$. The parameter β_{re} is exponentially amplified in the spin down Hilbert space sector, while β_{im} is exponentially amplified in the spin up sector (see panels (vii) and (viii) of Fig. 3.1(a)). For small displacements $|\beta| \ll 1$, after a $\pi/2$ spin rotation about $\hat{\sigma}_y$, the probability of measuring $|1/2\rangle_s$ is,

$$P_{1/2} = 1 - |\beta|^2\sinh(\zeta/2)^2 + \mathcal{O}(\beta^4), \tag{3.12}$$

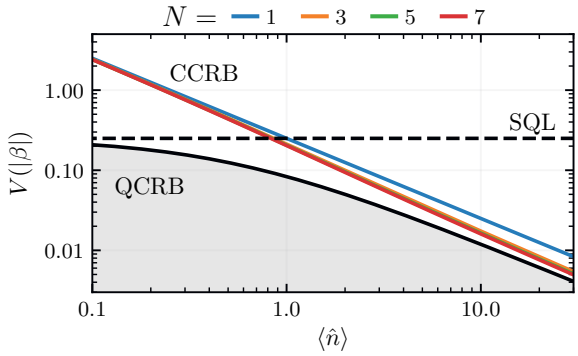


Figure 3.2: Metrological performance of spin-dependent squeezed coherent spin states, for phase-insensitive estimation of the displacement's magnitude, $|\beta|$. The classical Cramér-Rao bound (CCRB) for the time-reversal protocol and collective spin measurement (described in the main text) is plotted for increasing numbers of spins, N (solid colored lines). The CCRB is below the standard quantum limit (SQL, dashed black line) for all N at $\langle\hat{n}\rangle \gtrsim 1$. Moreover, the CCRB for $N = 1$ is 22 dB below the SQL at $\langle\hat{n}\rangle \approx 10$. The SQL is defined as the QCRB for bosonic coherent states, which for sensing of $|\beta|$ is SQL $= 1/4$. The CCRB is further compared to the quantum Cramér-Rao bound (QCRB, solid black line). At $\langle\hat{n}\rangle \gtrsim 1$, the CCRB for all N follows Heisenberg scaling, $\propto 1/\langle\hat{n}\rangle$. In this same regime, the CCRB for $N = 1$ spin is a factor of two larger than the QCRB. The prefactor decreases to one in the $N \to \infty$ limit.

which is phase-insensitive up to third order in β. In the limit $\beta \to 0$, the CFI is $F_{|\beta|} = 4\sinh(\zeta/2)^2 = 4\langle\hat{n}\rangle$, and therefore the CCRB is,

$$V(|\beta|) \geq 1/F_{|\beta|} = 1/(4\langle\hat{n}\rangle), \tag{3.13}$$

which follows Heisenberg scaling, $\propto 1/\langle\hat{n}\rangle$.

The metrological performance of our measurement protocol with a single spin is shown in Fig. 3.2, where we plot the CCRB (blue line) and compare it against the QCRB (black line) of Eq. (3.9). The CCRB diverges from the QCRB as $\langle\hat{n}\rangle \to 0$ because no information is mapped to the spin. For $\langle\hat{n}\rangle \gtrsim 1$, the CCRB follows QCRB scaling but remains a factor of two larger than the Heisenberg limit. When $\langle\hat{n}\rangle \gtrsim 1$ the CCRB falls below the standard quantum limit (SQL), which is defined by the use of bosonic coherent states as reference states, SQL $= 1/4$.

We next generalize the measurement protocol to N spins, which can potentially offer a beneficial collective enhancement. For spins initialized in a GHZ spin state, cf. Eq. (3.7a), after the time-reversal protocol we apply a rotated one-axis twisting unitary,

$$\hat{U}_{\mathrm{RT}} = \exp(-i\varphi\hat{J}_z)\exp(-i\pi\hat{J}_x^2/2)\exp(i\varphi\hat{J}_z), \tag{3.14}$$

and measure in the Dicke basis, where $\varphi = (-1)^{N/2}\pi/(2N)$. The only two states with non-zero measurement probabilities are $P_{N/2}$ and $P_{-N/2} = 1 - P_{N/2}$. For small displacements $\beta \ll 1$, they are,

$$P_{N/2} = 1 - |\beta|^2 \sinh(N\zeta/2)^2 + \mathcal{O}(\beta^4). \tag{3.15}$$

The corresponding CFI in the limit $\beta \to 0$ is $F_{|\beta|} = 4\sinh(N\zeta/2)^2 = 4\langle\hat{n}\rangle$. As a function of $\langle\hat{n}\rangle$, this many-spin CFI is identical to the single-spin result of Eq. (3.13). The advantage of using N spins lies in a potential collective enhancement. For example, in trapped ions there is a $\sqrt{N}$ amplification of the displacement signal, as well as a $\sqrt{N}$ reduction in state-preparation time, as we show later in Sec. 3.2.

Next, we consider N spins initialized in the coherent spin state of Eq. (3.7b). For small displacements $\beta \ll 1$, after a collective $\pi/2$ spin rotation about $\hat{J}_y$, the probability of measuring each Dicke state is phase-insensitive up to third order in β (Sec. 3.4 for derivation). The exact CFI is of the form,

$$F_{|\beta|} = \sinh(\zeta/2)^2 \sum_{i=0}^{N-1} a_i \cosh(i\zeta), \tag{3.16}$$

where the coefficients a_i are specified in the Supplemental Material of Sec. 3.4. The metrological performance is shown in Fig. 3.2, where we plot the CCRB, $1/F_{|\beta|}$, for increasing N, as well as the QCRB (black line) of Eq. (3.9) which is independent of N. For $\langle\hat{n}\rangle \approx 1$, the CCRB is a factor of approximately two larger than the QCRB. The CCRB is below the SQL (black dashed line) for $\langle\hat{n}\rangle \gtrsim 1$. Taking the limit $\langle\hat{n}\rangle \to \infty$, the ratio between the classical and quantum Fisher information is,

$$Q_{|\beta|}/F_{|\beta|} = 2^N/(2^N - 1), \tag{3.17}$$

which approaches one in the limit $N \to \infty$. Therefore, in this extreme regime, the CCRB for phase-insensitive sensing of the displacement's amplitude with spin-dependent squeezed coherent spin states saturates the Heisenberg limit, see Supplemental Material of Sec. 3.4

3.1.3 Multi-parameter displacement sensing

Next, we consider the setting where the phase is fixed between experimental shots, and perform joint estimation of β_{re} and β_{im}. For any symmetric Dicke weights $|c_{-m}| = |c_m|$, we prove in the Supplemental Material of Sec. 3.4 that the quantum Fisher information matrix is,

$$\mathbf{Q} = 8 \sum_{m>0}^{N/2} \left[|c_m|^2 \cosh(2\zeta m)\right] \mathbb{1} = (8\langle\hat{n}\rangle + 4)\mathbb{1}. \tag{3.18}$$

The corresponding multi-parameter QCRB is,

$$V(\beta_{\text{re}}) + V(\beta_{\text{im}}) \geq 1/(4\langle\hat{n}\rangle + 2), \tag{3.19}$$

which saturates the multi-parameter Heisenberg limit, and therefore symmetric Dicke weight spin-dependent squeezed states are optimal reference states. In the Supplemental Material of Sec. 3.4, we further study the multi-parameter QCRB as a function of the squeezing parameter ζ, and show that reference states obtained from GHZ spin states outperform those obtained from coherent spin states, because the mode occupation $\langle\hat{n}\rangle$ as a function of ζ is higher.

When jointly estimating two or more parameters, the optimal measurement for each parameter may be different, and the set of optimal measurements may be incompatible. If this is the case, the attainable estimation uncertainty, known as the Holevo-Cramér-Rao bound, is at most two times larger than the QCRB. The discrepancy is quantified by the asymptotic incompatibility R (see the Supplemental Material of Sec. 3.4 and Ref. [179]), which leads to the modified QCRB, $\mathrm{Tr}(\boldsymbol{V}) \geq (1+R)\,\mathrm{Tr}\big(\boldsymbol{Q}^{-1}\big)$ where $R \in [0,1]$. For symmetric Dicke weight spin-dependent squeezed state, we calculate the asymptotic incompatibility,

$$R = 1/(2\langle\hat{n}\rangle + 1), \tag{3.20}$$

and so the QCRB is asymptotically attainable in the infinite squeezing limit because $R \to 0$ when $\langle\hat{n}\rangle \to \infty$.

Measurement protocol

Similarly to the phase-insensitive setting, accessing the metrological advantage of the mixed spin-boson quadrature to perform multi-parameter displacement sensing is challenging. Here, we provide one possible measurement protocol that uses two ancilla qubits. As shown in Fig. 3.3(a), the sequence is built by wrapping the time-reversal sequence in spin-dependent displacements of strength g that are conditioned on the state of each ancilla. Each ancilla is then measured simultaneously and independently in the Dicke basis.

Our analysis focuses on the single spin case. When the spin-dependent squeezing is much larger than both the spin-dependent displacement, $\zeta \gg g$, and the displacement signal, $\zeta \gg \beta$, information about the displacement's real component is mapped only to the first ancilla, while information about the imaginary component is mapped only to the second ancilla. The probability of measuring the ith ancilla in the $|+\rangle$ state is then (see Supplemental Material of Sec. 3.4),

$$P_+^{(i)} = [1 + \cos^2(\phi_i)]/2, \tag{3.21}$$

where $\phi_1 = 2g\exp(\zeta)\beta_{\mathrm{re}}$, and $\phi_2 = -2g\exp(\zeta)\beta_{\mathrm{im}}$. In the limit $\beta \to 0$, the classical Fisher information matrix is $\mathbf{F} = 8g^2e^{2\zeta}\mathbb{1}$. The multi-parameter variance is therefore lower bounded by the CCRB according to,

$$V(\beta_{\mathrm{re}}) + V(\beta_{\mathrm{im}}) \geq 1/(4g^2e^{2\zeta}). \tag{3.22}$$

In Fig. 3.3(b), we show for various g the CCRB obtained from the approximate analytic expression of Eq. (3.22) (dotted lines) and from numerical simulations

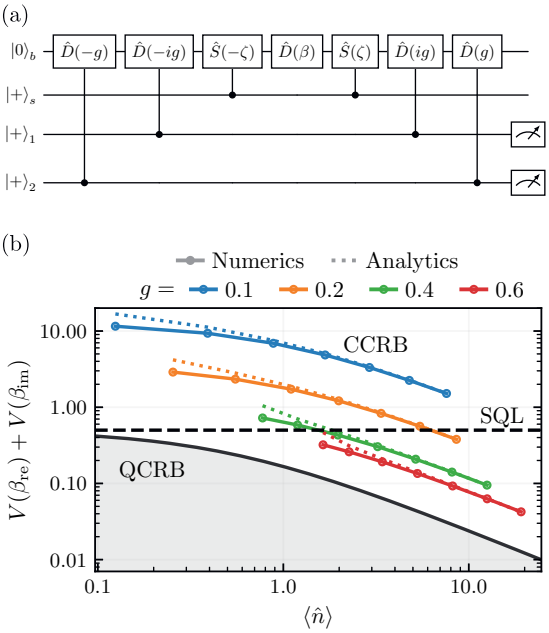


Figure 3.3: Joint estimation of the real and imaginary components of a displacement signal using spin-dependent squeezed states. **(a)** Example measurement protocol for joint parameter displacement estimation using spin-dependent squeezing, which uses two additional ancillary spins initialized in $|+\rangle_1$ and $|+\rangle_2$, respectively. Spin-dependent displacements conditioned on each ancilla map information about the real and imaginary components of the displacement signal to the ancillas, which are then individually measured. **(b)** Metrological performance of the measurement scheme for joint displacement parameter estimation. The classical Cramér-Rao bound (CCRB, colored lines) is shown for $N = 1$ spin at various spin-dependent displacement strengths g. For each value of g, we vary the squeezing parameter in the range $\zeta \in [0.2, 1.4]$ in steps of 0.2. Solid lines are obtained from numerics, dashed lines are analytics of Eq. (3.22). The CCRB is compared to the standard quantum limit (SQL, dashed black line), defined by the QCRB for bosonic coherent states, SQL $= 1/2$. For $g = 0.6$, the CCRB is below the SQL for mode occupations $\langle \hat{n} \rangle \gtrsim 1$. For fixed $\langle \hat{n} \rangle$, the CCRB approaches the quantum Cramér-Rao Bound (QCRB, solid black line) as g increases.

of the measurement sequence (solid colored dots). Due to the additional spin-dependent displacements in the time-reversal protocol, the reference state which is the state used to calculate $\langle \hat{n} \rangle$ includes the spin-dependent displacements. For all curves, when $\zeta \gg g$ we observe excellent agreement between theory and numerics. For increasing g, the curves are shifted to the right due to the larger $\langle \hat{n} \rangle$. For $\langle \hat{n} \rangle \gtrsim 1$, the CCRBs follow the Heisenberg scaling of the QCRB (black line), with a

prefactor that decreases with increasing g. At $g = 0.4$, the estimation uncertainty is below the SQL (black dashed line) when $\langle \hat{n} \rangle \gtrsim 1.5$.

3.2 Engineering spin-dependent squeezing

3.2.1 Experimental protocol for fast and scalable spin-dependent squeezing

In this section we introduce a protocol for the fast preparation of spin-dependent squeezed states in many-ion systems. Consider a system of N ions, each with an internal spin-1/2 degree of freedom with transition frequency ω_q, see Fig. 3.4(a). The combined action of the confining potentials and the Coulomb repulsion supports a set of motional normal modes, which are coupled to the spin degree of freedom via laser-induced interactions. Setting the laser frequency to $\omega_L = \omega_q + \omega_{\mathrm{COM}}$ or $\omega_L = \omega_q - \omega_{\mathrm{COM}}$ drives the first-order blue- or red-sideband, respectively, see Fig. 3.4(b). Here, ω_{COM} is the frequency of the center-of-mass (COM) mode, which describes uniform excitations of the ions. The strength of the first-order sidebands is linearly proportional to the Lamb-Dicke parameter $\eta = kx_0$, where k is the wave vector and $x_0 = \sqrt{1/(2m\omega)}$ is the harmonic oscillator length scale with m the ion mass, and where we set $\hbar = 1$. Setting $\omega_L = \omega_q + 2\omega_{\mathrm{com}}$ or $\omega_L = \omega_q - 2\omega_{\mathrm{com}}$ drives the second-order blue or red sideband, respectively, with strength quadratically proportional to the Lamb-Dicke parameter, $\propto \eta^2$.

Spin-dependent squeezing is commonly realized by simultaneously driving the second-order red and blue sidebands [131, 162, 163]. However, because trapped-ion experiments typically operate in the Lamb-Dicke regime where $\eta \ll 1$, the interaction strength is weak. Here, we realize spin-dependent squeezing with a stronger effective interaction strength by adapting the single-spin protocol of Ref. [170], with experimental demonstrations in Refs. [158, 180], to a many-spin system.

The spin-dependent squeezing protocol is realized by simultaneously driving the first-order sidebands at four different frequencies: one pair of red- and blue-sideband interactions with detuning $\Delta(t)$ and phase of zero, and another pair of red- and blue-sideband interactions with detuning $-\Delta(t)$ and phase $\phi(t)$, see Fig. 3.4(b). Performing a rotating wave approximation and moving to the interaction picture with respect to the spin and motion, the interaction Hamiltonian is,

$$\hat{H}(t) = g(t)\hat{a}\left[\hat{J}_x e^{-it\Delta(t)} + \hat{J}_y e^{it\Delta(t)} e^{-i\phi(t)}\right] + \text{h.c.}, \tag{3.23}$$

where $g(t) = \eta\Omega(t)/\sqrt{N}$ is the coupling strength between the collective spin and the bosonic mode, and $\Omega(t)$ is the Rabi frequency. To obtain $\hat{H}(t)$, we neglected off-resonant coupling of the sideband interactions to other motional modes, under the assumption that $\Delta(t)$ is small with respect to the frequency spacing between motional modes. Furthermore, we note that time-dependent control over $\Delta(t)$ and $\phi(t)$ has been previously demonstrated in trapped-ion experiments, see e.g. [181, 182]. In our companion work [183], we prove that $H(t)$ provides universal control

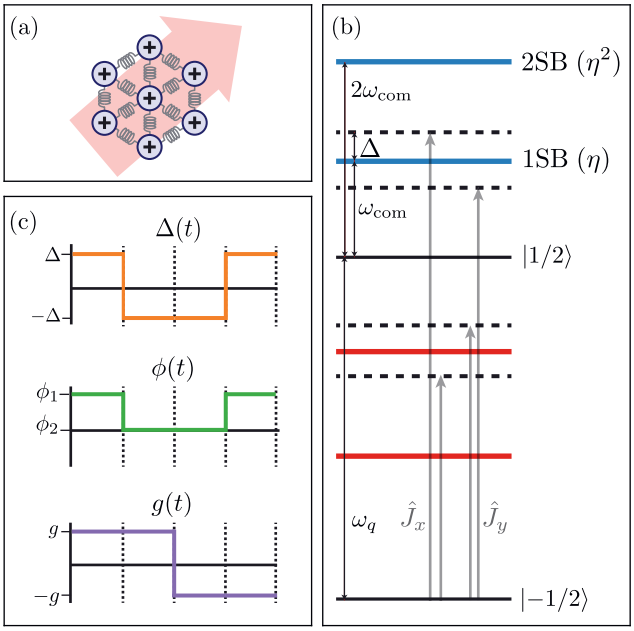


Figure 3.4: Experimental protocol for engineering fast and scalable spin-dependent squeezing in a trapped ion system. **(a)** We consider a system of N trapped ions coupled via laser interactions to their collective motional mode. **(b)** Energy diagram for $N = 1$ spin, without loss of generality. Multiple laser tones are tuned close to the first-order sidebands (1SB) that are $\pm\omega_{\text{COM}}$ from the carrier transition ω_q. A first bichromatic field driving interactions in the $\hat{J}_x$ basis is detuned by $\pm(\omega_{\text{COM}} + \Delta)$, while a second bichromatic field driving interactions in the $\hat{J}_y$ basis is detuned by $\pm(\omega_{\text{COM}} - \Delta)$ (grey lines). The resulting effective spin-dependent squeezing has an interaction strength $\propto \Omega^2\eta^2/\Delta^2$, offering a speed-up for appropriately chosen Δ over alternative approaches that use second-order sideband (2SB) interactions with a weaker coupling strength $\propto \Omega\eta^2$. **(c)** The laser detuning, phase and interaction strengths are dynamically modulated to obtain the desired spin-dependent squeezing interaction and to minimize unwanted errors from higher-order terms.

over the collective spin-boson Hilbert space, which was similarly shown for the single-spin case in Ref. [170].

The real-time dynamics generated by $\hat{H}(t)$ during evolution from t_0 to t are described by the Magnus expansion [141],

$$\hat{U}[t_0, t] = \exp\left(-i\hat{\Theta}_1[t_0, t] - \frac{1}{2}\hat{\Theta}_2[t_0, t] + \dots\right), \tag{3.24}$$

where the first- and second-order terms are, respectively,

$$\hat{\Theta}_1[t_0,t] = \int_{t_0}^{t} dt_1 \hat{H}(t_1), \tag{3.25a}$$

$$\hat{\Theta}_2[t_0,t] = \int_{t_0}^{t} dt_1 \int_{t_0}^{t_1} dt_2 [\hat{H}(t_1), \hat{H}(t_2)]. \tag{3.25b}$$

In our protocol, the laser parameters are dynamically modulated to obtain the desired interaction from the Magnus expansion and to minimize unwanted error terms, as discussed below. The parameters $\Delta(t)$, $\phi(t)$ and $g(t)$ are varied according to a stroboscopic sequence consisting of four segments, each of duration $\tau = 2\pi\ell/|\Delta|$ with $\ell \in \mathbb{Z}^+$ an adjustable parameter. The sequence is shown in Fig. 3.4(c).

During the first segment, the parameters are set to $\Delta(t) = \Delta$, $\phi(t) = \phi_1$ and $g(t) = g$. At the end of this segment, i.e. at $t = \tau$, the first-order Magnus term integrates to zero, $\hat{\Theta}_1[0,\tau] = 0$, because the integral is performed over a complete loop in phase space. The second-order Magnus term is non-zero,

$$\hat{\Theta}_2[0,\tau] = \frac{4\pi g^2 \ell}{\Delta^2}\left[(e^{-i\phi_1}\hat{a}^2 - \text{h.c.})\hat{J}_z - i(\hat{J}_x^2 - \hat{J}_y^2)\right], \tag{3.26}$$

where the first term is the desired spin-dependent bosonic squeezing. The second term is an unwanted error term that, for $N > 1$, describes rotated two-axis twisting [143, 184], and drives transitions between Dicke states. Its dynamics are undone during the second segment, in which $\Delta(t) = -\Delta$ and $\phi(t) = \phi_2$, while $g(t) = g$ is unchanged. At the end of the second segment, i.e. at $t = 2\tau$, the first-order Magnus term again integrates to zero, $\hat{\Theta}_1[\tau, 2\tau] = 0$, while the second-order term is,

$$\hat{\Theta}_2[\tau,2\tau] = -\frac{4\pi g^2 \ell}{\Delta^2}\left[(e^{-i\phi_2}\hat{a}^2 - \text{h.c.})\hat{J}_z - i(\hat{J}_x^2 - \hat{J}_y^2)\right], \tag{3.27}$$

which is identical to $\hat{\Theta}_2[0,\tau]$ up to a global sign change and after the replacement $\phi_1 \to \phi_2$. The total evolution after the first and second segments is described by the Baker–Campbell–Hausdorff (BCH) formula,

$$e^{\hat{\Theta}_2[\tau,2\tau]} e^{\hat{\Theta}_2[0,\tau]} = e^{\hat{\Theta}_2[0,\tau] + \hat{\Theta}_2[\tau,2\tau] + \cdots}, \tag{3.28}$$

from which we see that the phase-independent error-inducing two-axis twisting term always cancels, while the desired spin-dependent squeezing term survives if $\phi_1 \neq \phi_2$.

The third and fourth segments of the stroboscopic sequence are a repetition of the first two segments, but with $g(t) = -g$ [2]. Including these segments results in a many-body echo protocol which, to first order in BCH, cancels all odd-powered Magnus terms. This significantly increases the fidelity of the spin-dependent squeezing, as the leading-order Magnus error term, the third-order term, is canceled.

Both the Magnus expansion and the BCH formula introduce errors originating from higher-order error terms that are not entirely removed by the stroboscopic

[2] Note that $g(t) \to -g$ can be realized by phase control by sending $\phi_{1,2} \to \phi_{1,2} + \pi$

sequence. We first analyze the remaining leading error-terms from the Magnus expansion. For a fixed number of ions N, the strength of the nth-order Magnus term is $\mathcal{O}\left(g^n \ell/\Delta^n\right)$. Scaling $\ell \to \ell\Delta^2/g^2$ ensures that the second-order Magnus term is independent of g/Δ, while in the limit $g/\Delta \to 0$ the higher-order terms are small and can be neglected. Under this scaling of ℓ, the duration of the segment scales as $\tau \to \tau\Delta/g^2$, which indicates that reducing the strength of the higher-order Magnus terms requires longer segment durations. For non-fixed N, the magnitude of higher-order Magnus terms depends on the spin operators that arise from the nested commutators, because their matrix elements depend on N. In the Supplemental Material of Sec. 3.4, we study the magnitude of the third- and fourth-order Magnus terms with N, and show that they are all either bounded above, constant, or decreasing with N. Therefore, we expect our protocol to be scalable.

The leading-order BCH error term is, assuming a worst-case scaling of $J_z^2 \propto N^2$, $[\hat{\Theta}_2[0,\tau], \hat{\Theta}_2[\tau, 2\tau]] \sim g^4\ell^2N^2/\Delta^4 \sim \eta^4\Omega^4/\Delta^4$. This error is small when $g^2\ell/\Delta^2 \ll 1$, favoring shorter segment durations in the stroboscopic sequence. The amount of spin-dependent squeezing is increased by repeating the full stroboscopic sequence P times. The strength of the nth-order Magnus term is then $\mathcal{O}(g^n\ell P/\Delta^n)$, and therefore, to first order in the BCH formula, P plays an identical role to ℓ in ensuring that the desired second-order Magnus term is unchanged while $g/\Delta \to 0$ as required to make the higher-order Magnus terms vanish. That is, instead of scaling $\ell \to \ell\Delta^2/g^2$, we have $P \to P\Delta^2/g^2$.

The total duration of the spin-dependent squeezing protocol is calculated from the duration of a single segment, τ, and the number of times P that the four-step stroboscopic sequence is repeated,

$$t_f = 4P\tau = 8\pi\ell P/|\Delta|. \tag{3.29}$$

In the regime where higher-order Magnus and BCH terms can be neglected, i.e. when $g/\Delta \ll 1$ and $\ell g^2/\Delta^2 \ll 1$, the total evolution is effectively described by the unitary,

$$\hat{S}(\zeta \hat{J}_z) = \exp\left(\frac{1}{2}(\zeta^* \hat{a}^2 - \zeta \hat{a}^{\dagger 2})\hat{J}_z\right), \tag{3.30}$$

which exactly corresponds to the spin-dependent squeezing operation of Eq. (3.5) with,

$$\zeta = -\frac{8\pi g^2 \ell P(e^{i\phi_1} - e^{i\phi_2})}{\Delta^2}. \tag{3.31}$$

To maximize the magnitude of the squeezing parameter $|\zeta|$, we set $\phi_2 = \phi_1 - \pi$ which results in $e^{i\phi_1} - e^{i\phi_2} = 2e^{i\phi_1}$. The free parameter ϕ_1 provides control over the squeezing direction in phase space, while g, ℓ, P and Δ control both the squeezing amplitude and the relative strength of the higher-order Magnus and BCH terms. A large coupling strength g leads to faster spin-dependent squeezing, but can also require a large detuning Δ to ensure the higher-order error terms remain small. On the other hand, the number of phase space loops ℓ can be kept small, i.e. $\ell = 1$, while P is increased to achieve a larger squeezing magnitude $|\zeta|$.

3.2.2 Speed limit

We investigate the smallest achievable duration required to achieve a target squeezing magnitude in an ideal setting. To do so, we ignore higher-order error terms and consider evolution under the exact spin-dependent squeezing operator of Eq. (3.30). The duration t_f is minimized when only a single phase loop is performed with $\ell = 1$, and when the stroboscopic sequence is performed only once with $P = 1$, giving $t_f = 4\tau$. Starting from a spin-polarized state, $|-N/2\rangle_s$ or $|N/2\rangle_s$, the bosonic mode is squeezed by $z = |\zeta N/2|$. For a target z, using Eq. (3.29) and Eq. (3.31), the minimum protocol time t_f^* is,

$$t_f^* = \frac{\sqrt{\pi z}}{2g\sqrt{N/2}} = \frac{\sqrt{\pi z}}{\sqrt{2}\eta\Omega}, \tag{3.32}$$

which is independent of N. In comparison, the duration required to realize spin-dependent squeezing via the second-order sidebands is $t_f^* = 4z/(\eta^2\Omega)$ [162]. When neglecting higher-order terms, our protocol is therefore faster by a factor of $\sqrt{z}/\eta$. Trapped ion experiments commonly operate in the Lamb-Dicke regime where $\eta \ll 1$, in which our protocol is expected to be significantly faster than using the second-order sidebands. However, higher-order Magnus and BCH terms may prevent the protocol from saturating the speed bound. These terms are negligible only when $g/(\Delta\ell) \ll 1$ and $g^2/\Delta^2 \ll 1$, which requires $t_f \to t_f\Delta/g^2$. In the following section, we turn to numerics to further study the protocol's performance, including the impact of higher order terms.

3.2.3 Numerical results

Here, we numerically study the performance of the protocol in systems of up to $N = 40$ spins [3]. The performance is quantified using the fidelity $\mathcal{F} = |\langle\psi_t|\psi(t_f)\rangle|^2$, where $|\psi(t_f)\rangle$ is the final state after the stroboscopic protocol, and $|\psi_t\rangle$ is the ideal target state. The target state is a GHZ spin state that has been subjected to spin-dependent squeezing, $|\psi_t\rangle = \hat{S}(\zeta\hat{J}_z)\,|\psi_{\mathrm{GHZ}}\rangle$, cf. Eq. (3.7a). The performance of the protocol starting from spin-polarized states, $|0\rangle_b\,|-N/2\rangle_s$, is studied in the Supplemental Material of Sec. 3.4.

In Fig. 3.5(a), we plot the minimum protocol duration $t_{\min}$ (colored lines) required to prepare the target state $|\psi_t\rangle$ with fidelity $\mathcal{F} \geq 0.99$ versus the amount of bosonic squeezing in the target state, $z = |\zeta N/2|$. Because g, ϕ_1, ℓ and the target z are fixed, only P and Δ are left as free parameters in Eq. (3.31). To minimize $t_{\min}$ for a given target squeezing parameter, we iteratively increase P while obtaining Δ

[3] The simulations are performed by numerically solving the Schrödinger equation using QuantumOptics.jl [185] in Julia [149] with a Fock space truncation of $n_{\max} = 1660$. This permits us to simulate squeezing amplitudes of up to $|z| \leq 3$ with infidelities due to the truncation of the bosonic Fock space of less than $1 - \mathcal{F} \leq 10^{-4}$. We also simulate the dynamics with $n_{\max} = 1801$ and $n_{\max} = 2000$ to confirm that the finite truncation of bosonic Hilbert space does not impact our results.

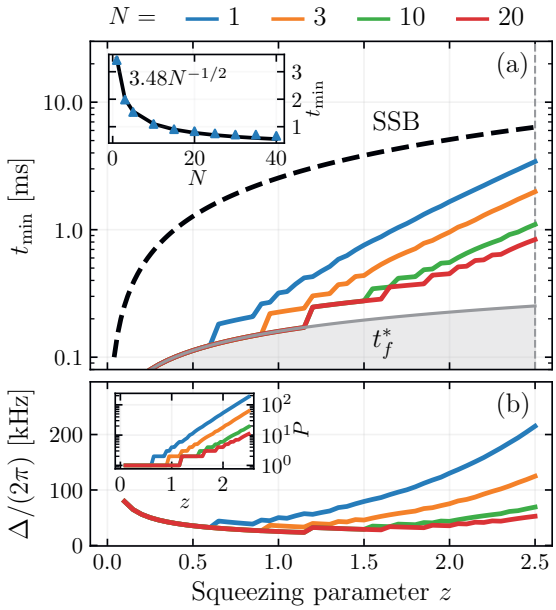


Figure 3.5: Performance of first-order sideband protocol to engineer spin-dependent squeezing in a crystal of N ions. **(a)** Minimum time $t_{\min}$ to prepare a spin-dependent squeezed state $|\psi_t\rangle = \hat{S}(\zeta \hat{J}_z)\,|\psi_{\mathrm{GHZ}}\rangle$ with fidelity $\mathcal{F} > 0.99$ versus squeezing parameter $z = \zeta N/2$. We use a typical coupling strength $g = 2\pi\times 5/\sqrt{N}$ kHz and set the phase space direction $\phi_1 = \pi$ and the number of phase loops per segment $\ell = 1$. The minimum time is numerically optimized for increasing numbers of ions, N, and is compared to the theoretical speed limit t_f^* (grey line). We further compare against the minimum time using second-order sidebands (2SB, black dashed line) using $\eta = 0.05$. In the inset, we fix the squeezing to $z = 2.5$ and plot the minimum time $t_{\min}$ for increasing N, up to $N = 40$ spins. Solid black line is a least-squares fit to $\propto 1/\sqrt{N}$. **(b)** Detuning Δ versus the target squeezing z for increasing number of spins, N. The inset plots the number of repetitions, P, of the stroboscopic modulation for varying squeezing z.

from Eq. (3.31), and report the smallest duration for which $\mathcal{F} > 0.99$. This process is repeated for increasing numbers of ions, N.

We first compare our protocol against the duration required to realize the same target state using the second-order sidebands (2SB, black dashed line). Overall, we find that the duration using our protocol is significantly smaller than 2SB for all target squeezings. At $z = 1$, the variance of the squeezed quadrature is 8.7 dB below that of a coherent state, calculated using $-10\log_{10}(e^{-2z})$. At this point, we observe an $\approx$ 8-fold reduction in protocol duration for $N = 1$, and a $\approx$ 15-fold reduction for $N = 10$ and $N = 20$.

We then compare the minimum duration of our protocol with the speed limit t_f^* (gray line) obtained in Eq. (3.32). For small amounts of squeezing, $z \lesssim 0.5$, we observe that $t_{\min}$ saturates t_f^* for all N. In this regime, higher-order Magnus terms are small, permitting $P = 1$ while achieving high fidelities. For moderate amounts of squeezing, $0.5 \lesssim z \lesssim 1.5$, $t_{\min}$ begins to deviate from t_f^*, because both P and Δ increase to ensure the higher-order Magnus terms remain small. The value of z at which $t_{\min}$ departs from t_f^* increases with N, since the most deleterious higher-order Magnus terms decrease in magnitude with N, as we show in the Supplemental Material of Sec. 3.4. The step-like behavior arises from the dependence of t_f on integer values of P, with steps becoming indistinguishably small at large z.

For large squeezing parameters $z \gtrsim 1.5$, we observe that the protocol duration $t_{\min}$ decreases with N. In the inset of Fig. 3.5(a), we plot $t_{\min}$ with increasing N (triangles) for a fixed squeezing of $z = 2.5$ (21.7 dB). We observe excellent agreement with a least-squares fit (black line) to $1/\sqrt{N}$. The $\sqrt{N}$ reduction in protocol duration is a unique feature of the stroboscopic protocol, and is a clear advantage over the 2SB approach. In the large squeezing regime, we observe an exponential growth of $t_{\min}$ with z. Specifically, for $z \gtrsim 2.5$, $t_{\min}$ approaches the 2SB duration, which is particularly prominent for $N = 1$. At extremely large squeezing amplitudes, we expect our protocol to be slower than the 2SB method. However, $z = 2.5$ ($\approx$ 22 dB of squeezing) is larger than existing experimental demonstrations of motional squeezing in a trapped ion, which typically achieve $\lesssim$ 20 dB of squeezing [99, 186, 187]. Therefore, we do not yet expect this to be a significant limitation of our protocol, and it can be well-mitigated by increasing the number of ions, N.

In Fig. 3.5(b), we plot the detuning Δ for each point in panel (a), and plot the corresponding number of stroboscopic repetitions P in the inset. For small squeezing parameters $z \lesssim 0.5$, Δ decreases with z because higher-order Magnus terms are negligible, allowing small values of P. We verify in the inset that $P = 1$ for all values of N in this range. In contrast, for $z \gtrsim 0.5$, the higher-order Magnus terms are no longer negligible. Their strength is reduced by increasing Δ to ensure that the desired second-order term remains significant, which is accompanied by an increase in P, again visible in the inset. Although larger Δ leads to higher theoretical fidelities, in experimental realizations this benefit should be traded off against the fact that larger Δ leads to both longer protocol times and larger off-resonant coupling to other motional modes. The Δ required to achieve a target theoretical fidelity at a given z can be lowered by increasing N, while off-resonant coupling can be reduced by employing strategies such as optimal control [182, 188].

3.3 Conclusion and outlook

We have shown that the quantum Cramér-Rao bound of spin-dependent squeezed states saturates the Heisenberg limit for phase-insensitive estimation of a displacement's magnitude, and for simultaneous estimation of a displacement's real and imaginary components. We proposed explicit measurement protocols that follow

Heisenberg scaling, and which can be readily implemented in current quantum hardware platforms. Moreover, we provided a protocol for preparing spin-dependent squeezed states in trapped-ion systems in a fast, scalable manner via dynamically modulated first-order sideband interactions.

A natural extension is to investigate the impact of noise on the preparation of spin-dependent squeezed states and on their metrological performance. Robustness to noise could potentially be engineered by using quantum control [99, 181, 182]. Beyond spin-dependent squeezed states, one could investigate the performance of alternative spin-boson entangling unitaries for preparing reference states. For example, dispersive interactions have been considered for single-parameter displacement estimation [160, 161], but to the best of our knowledge, their suitability for phase-insensitive displacement sensing has not yet been studied.

We note that there is a wide variety of reference states that have been previously studied for quantum-enhanced displacement sensing. In Sec. 3.4.1 of the Supplemental Material of Sec. 3.4, we provide a comparison of our spin-dependent squeezed states with other reference states. A detailed comparison of the metrological performance of various reference states in both ideal settings and in the presence of realistic experimental noise would be a valuable analysis that can guide experiments in choosing appropriate protocols tailored to their target hardware.

Looking forward, our phase-insensitive sensing protocol naturally extends to large ion crystals for detecting weak forces or electric fields that induce small displacements. Scaling to N ions both shortens the preparation time of spin-dependent squeezed states by $\sqrt{N}$ and amplifies the displacement signal by $\sqrt{N}$. The phase insensitivity is beneficial for dark-matter searches, where the displacement phase is typically unknown, eliminating the need for phase synchronization between the signal and the sensor [51, 57]. The same approach applies to quantum-logic enabled photon-recoil spectroscopy of molecular [189, 190] and highly charged ions [191, 192], which could benefit atomic clocks [193] and the search for new physics [194].

3.4 Supplemental Material

3.4.1 Comparison to other reference states

To contextualize our results, we provide in Table 3.1 a non-exhaustive comparison of our spin-dependent squeezed states with other reference states that are metrologically useful for displacement sensing. In the first row we report the standard quantum limit (SQL), which is defined by the QCRB of single-mode coherent states. In the second row we report the Heisenberg limit, which is the QCRB minimized over all possible single-mode bosonic states. For more details of both of these definitions, see Sec. 3.4.3. Below, for each reference state, column-by-column we report: (i) the definition of the state, where $\hat{D}(\alpha) = e^{\alpha\hat{a}^\dagger - \alpha^*\hat{a}}$ is the displacement operator, $\hat{S}(\zeta) = e^{(\zeta\hat{a}^{\dagger 2} - \zeta^*\hat{a}^2)/2}$ is the squeeze operator and $\hat{S}_2(\zeta) = e^{\zeta^*\hat{a}\hat{b} - \zeta\hat{a}^\dagger\hat{b}^\dagger}$ is the two-mode squeeze operator. (ii) The required physical resources, using the notation "b" for a bosonic mode and "s" for a spin (e.g. "1b, Ns" denotes 1 bosonic mode and

N spins). (iii) The QCRB for phase-aligned single-parameter estimation of β_{re} (or equivalently, β_{im}). (iv) The QCRB for phase-insensitive estimation of a displacement's magnitude, $|\beta|$. (v) The QCRB for joint-estimation of a displacement's real (β_{re}) and imaginary (β_{im}) components. (vi) Possible choices of measurement operators whose CCRB follow the corresponding QCRB. Green cell shading indicates that a reference state's QCRB follows Heisenberg scaling, $\propto 1/\langle\hat{n}\rangle$, while red indicates that it does not. (*) The variance $V(|\beta|)$ for squeezed states distinguishes that this result is for a phase-twirled squeezed state, see main text for details. (**) An exact definition for general single-mode grid states can be found in Ref. [130] with their application to displacement sensing in Refs. [67, 68]. (***) The measurements associated with the spin-dependent squeezed state are detailed in this work (see main text). For the measurement operators, $|n\rangle\langle n|$ is the projection onto the nth Fock state, $\hat{\Pi}$ is the bosonic parity operator, and $e^{il\hat{x}}$ and $e^{il\hat{p}}$ are modular operators where l is some modular length. The reported measurement operators are indicative only, and other choices may be possible. The list of reference states is non-exhaustive, and this table should serve as an exemplary comparison only.

For the phase-aligned sensing of either β_{re} or β_{im}, the Heisenberg limit (HL) is $1/(16\langle\hat{n}\rangle + 4)$, see Sec. 3.4.3. The QCRB for squeezed states and spin-dependent squeezed states saturate the HL, while the QCRB for single-mode Fock, single-mode grid, two-mode squeezed and spin-dependent squeezed states is a factor of two larger, and therefore follows but does not saturate the HL.

For phase-insensitive sensing of $|\beta|$, pure single-mode bosonic squeezed states cannot be used because their QCRB is phase-dependent, $Q_{|\beta|} = \langle\hat{n}\rangle/[\mathrm{c}(\varphi)^2 + 16\langle\hat{\mathrm{n}}\rangle^2\mathrm{s}(\varphi)^2]$. Instead, in Table 3.1 we report the QCRB for phase-twirled squeezed states [65]. Because the phase-twirled state is a mixed state, we use a double asterisk to distinguish it from all of the other (pure) reference states. The QCRB for spin-dependent displaced states is similarly phase-dependent. We leave the calculation of the performance of phase-twirled spin-dependent displaced states to future work. The HL for the estimation of $|\beta|$ is $1/(8\langle\hat{n}\rangle + 4)$, and therefore phase-twirled squeezed, single-mode Fock, single-mode grid, two-mode squeezed and spin-dependent squeezed states all saturate the HL.

For phase-aligned joint estimation of β_{re} and β_{im}, the SQL is 1/2. As such, the QCRB for squeezed states never falls below the SQL, while the QCRB for spin-dependent displaced states is never less than a factor of two smaller. The HL is $1/(4\langle\hat{n}\rangle + 2)$, and therefore single-mode Fock, single-mode grid, two-mode squeezed and spin-dependent squeezed states all saturate the HL.

We emphasize that single-mode Fock, single-mode grid, two-mode squeezed and spin-dependent squeezed states all exhibit identical metrological performance for displacement sensing. The differences between these states lie in the required experimental resources, their preparation protocols, and the observable that should be measured to access the metrological advantage. Spin-dependent squeezed states have the benefit that they (1) require a single bosonic mode and a minimum of one spin, with the capability to scale to N spins, (2) can be prepared in many-ion crystals in a fast and scalable manner, as we showed in Sec. 3.2 of the main text, and (3) have spin-measurement sequences that follow Heisenberg scaling, as we

Reference State	Definition	Res.	$V(\beta_{\mathrm{re}})$	$V(\lvert\beta\rvert)$	$V(\beta_{\mathrm{re}}) + V(\beta_{\mathrm{im}})$	Meas.
Standard quantum limit (SQL)	$\hat{D}(\alpha)\lvert 0\rangle_b$	1b	$\frac{1}{4}$	$\frac{1}{4}$	$\frac{1}{2}$	$\hat{x}$, $\hat{p}$
Heisenberg limit	-	1b	$\frac{1}{16\langle\hat{n}\rangle+4}$	$\frac{1}{8\langle\hat{n}\rangle+4}$	$\frac{1}{4\langle\hat{n}\rangle+2}$	-
Squeezed	$\hat{S}(\zeta)\lvert 0\rangle_b$	1b	$\frac{1}{16\langle\hat{n}\rangle+4}$	$\frac{1}{8\langle\hat{n}\rangle+4}$ *	$\langle\hat{n}\rangle+\frac{1}{2}$	$\lvert n\rangle\langle n\rvert$, $\hat{\Pi}$
Spin-dependent displaced [57]	$\hat{D}(\alpha\hat{J}_z)\lvert 0\rangle_b\lvert\psi\rangle_s$	1b, Ns	$\frac{1}{16\langle\hat{n}\rangle+4}$	-	$\frac{1}{16\langle\hat{n}\rangle+4}+\frac{1}{4}$	$\hat{J}_\alpha$
Single-mode Fock [62, 63]	$\hat{a}^{\dagger n}\lvert 0\rangle_b$	1b	$\frac{1}{8\langle\hat{n}\rangle+4}$	$\frac{1}{8\langle\hat{n}\rangle+4}$	$\frac{1}{4\langle\hat{n}\rangle+2}$	$\hat{\Pi}$
Single-mode grid [67, 68, 130]	**	1b	$\frac{1}{8\langle\hat{n}\rangle+4}$	$\frac{1}{8\langle\hat{n}\rangle+4}$	$\frac{1}{4\langle\hat{n}\rangle+2}$	$e^{il\hat{x}}$, $e^{il\hat{p}}$
Two-mode squeezed [71, 195]	$\hat{S}_2\lvert 0\rangle_b\lvert 0\rangle_b$	2b	$\frac{1}{8\langle\hat{n}\rangle+4}$	$\frac{1}{8\langle\hat{n}\rangle+4}$	$\frac{1}{4\langle\hat{n}\rangle+2}$	$\hat{x}_1$, $\hat{p}_2$
Spin-dependent squeezed (this work)	$\hat{S}(\zeta\hat{J}_z)\lvert 0\rangle_b\lvert\psi\rangle_s$	1b, Ns	$\frac{1}{8\langle\hat{n}\rangle+4}$	$\frac{1}{8\langle\hat{n}\rangle+4}$	$\frac{1}{4\langle\hat{n}\rangle+2}$	***

Table 3.1: **Comparison of reference states for displacement sensing.** For details, see main text.

proposed in Sec. 3.1 of the main text.

3.4.2 Review of quantum multi-parameter estimation

In this section, we review quantum multi-parameter estimation. For a more complete review, see e.g. Refs. [169, 196]. Consider a quantum state $\rho(\boldsymbol{\theta})$ that encodes a set of d real parameters, $\boldsymbol{\theta} = \{\theta_1, \dots, \theta_d\}$. The goal is to estimate $\boldsymbol{\theta}$ from a set of M independent measurement outcomes $\boldsymbol{x} = \{x_1, \dots, x_M\}$, using a locally unbiased estimator $\tilde{\boldsymbol{\theta}}(\boldsymbol{x})$, which returns an estimate for $\boldsymbol{\theta}$ given $\boldsymbol{x}$. The measurement outcomes $\boldsymbol{x}$ are described by a positive operator-valued measurement (POVM), $\boldsymbol{\Pi} = (\Pi_1, \Pi_2, \dots)$. The probability of a particular sequence of measurement outcomes is given by $p(\boldsymbol{x}|\boldsymbol{\theta}) = \prod_k p(x_k|\boldsymbol{\theta})$, where $p(x_k|\boldsymbol{\theta}) = \mathrm{Tr}(\Pi_k \rho(\boldsymbol{\theta}))$ is the probability of obtaining the measurement outcome x_k, with Π_k the associated measurement operator. Note that in the case of single-parameter estimation, all of the matrix expressions introduced below reduce to scalar quantities.

For a given quantum state $\rho(\boldsymbol{\theta})$, unbiased estimator $\tilde{\boldsymbol{\theta}}$ and POVM $\boldsymbol{\Pi}$, the uncertainty of the estimation is quantified by the covariance matrix,

$$\boldsymbol{V}(\boldsymbol{\theta}) = \sum_{\boldsymbol{x}} p(\boldsymbol{x}|\boldsymbol{\theta})[\boldsymbol{\theta} - \tilde{\boldsymbol{\theta}}(\boldsymbol{x})][\boldsymbol{\theta} - \tilde{\boldsymbol{\theta}}(\boldsymbol{x})]^T, \tag{3.33}$$

where the summation runs over all possible measurements. Minimizing over all possible unbiased estimators yields a lower bound for the variance, known as the classical multi-parameter Cramér-Rao bound,

$$\mathbf{V} \geq \frac{1}{M} \boldsymbol{F}^{-1}, \tag{3.34}$$

where $\boldsymbol{F}$ is the classical Fisher information matrix,

$$F_{ij} = \sum_k \frac{1}{p(x_k|\boldsymbol{\theta})} \partial_i p(x_k|\boldsymbol{\theta}) \partial_j p(x_k|\boldsymbol{\theta}), \tag{3.35}$$

where $\partial_i = \partial/\partial\theta_i$. Intuitively, the diagonal elements F_{ii} quantify the amount of information about θ_i that is contained in the measurement outcomes $\boldsymbol{x}$. The off-diagonal elements F_{ij} quantify the degree of correlation between θ_i and θ_j. The lower bound of Eq. (3.34) is minimized when the diagonal elements of $\boldsymbol{F}$ are maximized while the off-diagonal elements are minimized. It is often more convenient to work with a scalar quantity, so taking the trace of Eq. (3.34) lower bounds the sum of variances according to,

$$\mathrm{Tr}(\boldsymbol{V}) \geq \frac{1}{M} \mathrm{Tr}\big(\boldsymbol{F}^{-1}\big). \tag{3.36}$$

After setting $M = 1$, we refer to this as the classical Cramér-Rao bound (CCRB).

Additionally minimizing over all possible POVMs yields a lower bound on the variance known as the quantum multi-parameter Cramér-Rao bound,

$$\boldsymbol{V} \geq \frac{1}{M} \boldsymbol{Q}^{-1}, \tag{3.37}$$

where $\boldsymbol{Q}$ is the quantum Fisher information matrix (QFIM), whose elements are defined as,

$$Q_{ij} = \frac{1}{2}\mathrm{Tr}[\{\hat{L}_i, \hat{L}_j\}\rho(\boldsymbol{\theta})]. \tag{3.38}$$

The quantum multi-parameter Cramér-Rao bound depends only on the choice of reference state, $|\psi_{\mathrm{ref}}\rangle$. Here, $\hat{L}_i$ is the symmetric logarithmic derivative (SLD), defined implicitly via $\partial_i\rho(\boldsymbol{\theta}) = (\rho(\boldsymbol{\theta})\hat{L}_i + \hat{L}_i\rho(\boldsymbol{\theta}))/2$. Similarly to the multi-parameter classical Cramér bound, the quantum multi-parameter Cramér-Rao bound is minimized when the diagonal elements of $\boldsymbol{Q}$ are maximized while the off-diagonal elements are minimized. Taking the trace of Eq. (3.37) lower bounds the sum of variances according to,

$$\mathrm{Tr}(\boldsymbol{V}) \geq \frac{1}{M}\,\mathrm{Tr}\big(\boldsymbol{Q}^{-1}\big). \tag{3.39}$$

After setting $M = 1$, we refer to this as the quantum Cramér-Rao bound (QCRB). The QCRB is the main quantifier of a reference state's metrological utility.

For multi-parameter estimation, it is not always possible to attain the lower bound of Eq. (3.39). This is because the optimal POVM for the parameter θ_i may be different to the optimal POVM for the parameter θ_j, and there is no guarantee that the two different optimal POVMs are compatible. A necessary and sufficient condition for the attainability of Eq. (3.39) is that the Uhlmann curvature, $\mathbf{D}$, vanishes. That is, for all i, j,

$$D_{ij} = \mathrm{Tr}([\hat{L}_i, \hat{L}_j]\rho(\boldsymbol{\theta})) = 0. \tag{3.40}$$

The diagonal elements D_{ii} are zero by definition, while the off-diagonal elements D_{ij} reflect the degree of non-commutativity between a pair of SLDs, $\hat{L}_i$ and $\hat{L}_j$. Intuitively, Eq. (3.40) is required for the attainability of Eq. (3.39) because if $\mathbf{D}$ vanishes, then there exists a pair of SLDs that commute and whose simultaneous eigenstates can be used to construct a jointly optimal measurement. The deviation from Eq. (3.39) is quantified by the so-called asymptotic incompatibility [179],

$$R = ||i\boldsymbol{Q}^{-1}\boldsymbol{D}||_\infty, \tag{3.41}$$

where $||.||_\infty$ denotes the largest eigenvalue of the matrix. It is bounded as $0 \leq R \leq 1$. Provided that there are asymptotically many copies of the reference state, one obtains the following chain of inequalities,

$$\boldsymbol{V} \geq \frac{1+R}{M}\boldsymbol{Q}^{-1} \geq \frac{1}{M}\boldsymbol{Q}^{-1}. \tag{3.42}$$

The QCRB of Eq. (3.39) is therefore attainable within a factor of at most two. We briefly mention that a tighter bound is provided by the Holevo-Cramér-Rao bound [196], whose computation for spin-dependent squeezed states we leave to future work.

3.4.3 Standard Quantum Limit and the Heisenberg Limit

In this section we derive expressions for the standard quantum limit (SQL) and the Heisenberg limit (HL) for displacement sensing with a single bosonic mode. Consider a pure reference state $|\psi_{\text{ref}}\rangle$ that interacts linearly with a signal generated by $\hat{\mathcal{O}}$ according to $\hat{U}(\theta) = \exp(-i\theta\hat{O})$. For example, in the case of displacement sensing of an unknown displacement $\beta = \beta_{\text{re}} + i\beta_{\text{im}}$, the generator $\hat{\mathcal{O}}$ is a linear combination of the displacement $\hat{x} = \hat{a}^\dagger + \hat{a}$ and momentum $\hat{p} = i(\hat{a}^\dagger - \hat{a})$ operators.

Standard quantum limit

The standard quantum limit (SQL) for displacement sensing is defined as the QCRB obtained when using coherent states as reference states, i.e. $|\psi_{\text{ref}}\rangle = \hat{D}(\alpha)\,|0\rangle_b$, where $\alpha \in \mathbb{C}$ is the displacement amplitude. If the relative phase between the reference state and the displacement is fixed between, then with no loss of generality we may assume that either $\beta \in \mathbb{R}$, so the generator is $\hat{\mathcal{O}} = \hat{p}$, or $\beta \in i\mathbb{R}$, so the generator is $\hat{\mathcal{O}} = \hat{x}$. The variance for phase-aligned single-parameter estimation is then lower bounded according to,

$$V(\beta_{\text{re}}) \geq 1/4, \qquad V(\beta_{\text{im}}) \geq 1/4, \tag{3.43}$$

where we used the definition $Q = 4(\Delta\hat{O})^2_\psi$ for the single-parameter quantum Fisher information using pure reference states [169], and calculated the variances $(\Delta\hat{x})^2_{\psi_{\text{ref}}} = (\Delta\hat{p})^2_{\psi_{\text{ref}}} = 1$ for coherent states. For the joint estimation of β_{re} and β_{im}, the QFIM is $\mathbf{Q} = 4\mathbb{1}$, and therefore the sum of variances is lower bounded according to the QCRB as,

$$V(\beta_{\text{re}}) + V(\beta_{\text{im}}) \geq 1/2. \tag{3.44}$$

Finally, for phase-insensitive estimation of the displacement's magnitude $|\beta|$, calculating the single-parameter QCRB either by a change of basis of the QFIM or by phase-twirling coherent states, we obtain,

$$V(|\beta|) \geq 1/4. \tag{3.45}$$

We refer to all of these results as the standard quantum limit (SQL).

Heisenberg Limit

The Heisenberg limit is defined as the QCRB minimized over all possible single-mode bosonic reference states. If the relative phase between the reference state and the displacement is fixed, the QFI is upper bounded as,

$$Q \leq 4\left[2\langle\hat{n}\rangle + 1 + 2\sqrt{\langle\hat{n}\rangle(\langle\hat{n}\rangle - 1)}\right], \tag{3.46}$$

see e.g. Section 4.1.2 in Ref. [197]. The QCRBs of single-parameter displacement estimation, minimized over all possible reference states, are therefore lower bounded

by,

$$V(\beta_{\mathrm{re}}) \geq \frac{1}{8\langle\hat{n}\rangle + 4 + 8\sqrt{\langle\hat{n}\rangle(\langle\hat{n}\rangle - 1)}}, \qquad V(\beta_{\mathrm{im}}) \geq \frac{1}{8\langle\hat{n}\rangle + 4 + 8\sqrt{\langle\hat{n}\rangle(\langle\hat{n}\rangle - 1)}}. \tag{3.47}$$

For reference states with large mode occupations, $\langle\hat{n}\rangle \gg 1$, the minimized QCRBs simplify to,

$$V(\beta_{\mathrm{re}}) \geq \frac{1}{16\langle\hat{n}\rangle + 4}, \qquad V(\beta_{\mathrm{im}}) \geq \frac{1}{16\langle\hat{n}\rangle + 4}, \tag{3.48}$$

which we refer to as the Heisenberg limit for the single-parameter estimation of either β_{re} or β_{im}.

For the joint estimation of β_{re} and β_{im}, we note that the diagonal elements of the QFIM, $Q_{11} = 4(\Delta\hat{x})^2$ and $Q_{22} = 4(\Delta\hat{p})^2$, are maximized when the reference state is centered at the phase space origin, i.e. when $\langle\hat{x}\rangle = \langle\hat{p}\rangle = 0$. Then, the sum of variances is upper bounded using the fact that $\hat{x}^2 + \hat{p}^2 = 4\hat{n} + 2$, i.e. $\mathrm{tr}(V) \leq 4\langle\hat{n}\rangle + 2$. Using the fact that $\mathrm{tr}\left(V^{-1}\right)$ is minimized when V is proportional to the identify, we obtain the following minimized multi-parameter QCRB,

$$V(\beta_{\mathrm{re}}) + V(\beta_{\mathrm{im}}) \geq \frac{1}{4\langle\hat{n}\rangle + 2}. \tag{3.49}$$

which we refer to as the Heisenberg limit for the joint estimation of β_{re} and β_{im}.

Finally, for the estimation of the displacement magnitude $|\beta|$, a similar calculation using phase-averaged states, as performed in Ref. [65], yields,

$$V(|\beta|) \geq \frac{1}{8\langle\hat{n}\rangle + 4}, \tag{3.50}$$

which we refer to as the Heisenberg limit for phase-insensitive estimation of the displacement's magnitude, $|\beta|$.

3.4.4 Metrological performance of spin-dependent squeezed-displaced states

Here, we derive analytical expressions for the quantum Fisher information matrix (QFIM) for a reference state obtained by applying spin-dependent squeezing and a spin-dependent displacement to the bosonic vacuum and any collective spin state. Such a reference state can be written in the Dicke basis as,

$$|\psi(\alpha\hat{J}_z, \zeta\hat{J}_z)\rangle = \sum_m c_m \hat{D}(\alpha m)\hat{S}(\zeta m)\,|0\rangle_b\,|m\rangle_s\,, \tag{3.51}$$

with Dicke basis coefficients $c_m \in \mathbb{C}$. The spin-dependent displacement is controlled by $\alpha \in \mathbb{C}$, while without loss of generality we assume that the spin-dependent

squeezing parameter is $\zeta \in \mathbb{R}$. The reference state is then subjected to a spin-independent displacement $\hat{D}(\beta)$ with unknown $\beta \in \mathbb{C}$, producing,

$$|\psi(\boldsymbol{\theta})\rangle = \hat{D}(\beta)|\psi(\alpha\hat{J}_z, \zeta\hat{J}_z)\rangle, \tag{3.52}$$

where $\boldsymbol{\theta}$ is either $\boldsymbol{\theta} = |\beta|$ for phase-insensitive displacement amplitude sensing, or $\boldsymbol{\theta} = (\beta_{\mathrm{re}}, \beta_{\mathrm{im}})$ The reference state's metrological utility is quantified by the QFIM of Eq. (3.38), which is obtained by computing the symmetric log derivative (SLD). Because $|\psi(\boldsymbol{\theta})\rangle$ is a pure state, the SLD is defined as,

$$L_i = 2\partial_i\rho = 2(|\psi(\boldsymbol{\theta})\rangle\langle\partial_i\psi(\boldsymbol{\theta})| + |\partial_i\psi(\boldsymbol{\theta})\rangle\langle\psi(\boldsymbol{\theta})|). \tag{3.53}$$

Multi-parameter displacement sensing

For joint estimation where $\boldsymbol{\theta} = \{\beta_{\mathrm{re}}, \beta_{\mathrm{im}}\}$, computing the SLDs yields,

$$\partial_{\theta_1}|\psi\rangle = \sum_m c_m \left[-i\,\mathrm{Im}(2\alpha m + \beta)\,|e_{0,m}\rangle + e^{\zeta m}\,|e_{1,m}\rangle\right]|m\rangle\,, \tag{3.54a}$$

$$\partial_{\theta_2}|\psi\rangle = \sum_m c_m \left[i\,\mathrm{Re}(2\alpha m + \beta)\,|e_{0,m}\rangle + ie^{-\zeta m}\,|e_{1,m}\rangle\right]|m\rangle\,, \tag{3.54b}$$

where we defined the states $|e_{n,m}\rangle \equiv \hat{D}(\beta)\hat{D}(\alpha m)\hat{S}(\zeta m)\hat{a}^{\dagger n}\,|0\rangle_b/\sqrt{n!}$. After some calculations, see Ref. [2] for details, we arrive at,

$$\mathbf{Q} = 4\mathbf{DKD} + 4\begin{pmatrix}\sum_m |c_m|^2 e^{2\zeta m} & 0\\ 0 & \sum_m |c_m|^2 e^{-2\zeta m}\end{pmatrix}, \tag{3.55}$$

where we introduced the matrix $\mathbf{D} = \mathrm{diag}(1, -1)$ to make the off-diagonal elements negative. We also introduced $\gamma_m \equiv 2\alpha m + \beta$, and used the weighted covariance matrix $\mathbf{K}$ of $\mathbf{X} = (X_1, X_2, \ldots, X_n)^T$ with corresponding non-negative weights $\vec{w}$, whose elements are defined as,

$$\mathbf{K}_{X_j, X_k, \vec{w}} = \sum_i \omega_i (x_{ij} - \bar{x}_j)(x_{ik} - \bar{x}_k) \tag{3.56}$$

with $\bar{x}_j = \sum_i w_i x_{ij}$ the weighted mean. For our calculations, we substituted $\mathbf{X} = (\mathrm{Im}(\boldsymbol{\gamma}), \mathrm{Re}(\boldsymbol{\gamma}))$ and $w_i = |c_i|^2$, where $\boldsymbol{\gamma} = (\gamma_{-N/2}, \gamma_{-N/2+1}, \ldots, \gamma_{N/2})^T$. We can finally obtain a compact expression for the QFIM as a function of $\mathbf{K}$,

Limiting cases

Here, we consider three limiting cases of the general spin-dependent squeezed, spin-dependent displaced spin-boson reference state.

Spin-dependent squeezed states: When the reference state is spin-dependent squeezing only, i.e. when $\alpha = 0$, then $\gamma_m = \beta$ and therefore $\mathbf{K} = 0$. The QFIM is,

$$\mathbf{Q} = 4\begin{pmatrix}\sum_m |c_m|^2 e^{2\zeta m} & 0\\ 0 & \sum_m |c_m|^2 e^{-2\zeta m}\end{pmatrix}. \tag{3.57}$$

We observe that the off-diagonal elements vanish, and that the diagonal elements grow exponentially with ζ.

A special case is obtained when the initial spin state has symmetric Dicke basis weights, i.e. if $|c_{-m}| = |c_m|$. Spin states that satisfy this property include GHZ states and any coherent spin state in the $x-y$ plane of the collective Bloch sphere. Using the fact that $e^x + e^{-x} = 2\cosh(x)$, the QFIM for odd N (a similar expression holds for N even) simplifies to,

$$\mathbf{Q} = 8\sum_{m>0}\left[|c_m|^2\cosh(2\zeta m)\right]\mathbb{1} = (8\langle\hat{n}\rangle + 4)\mathbb{1}. \tag{3.58}$$

To obtain the last equality, we used the fact for spin-dependent squeezing acting on a spin state with symmetric Dicke weights, the average bosonic mode occupation is

$$\langle\psi(0,\zeta\hat{J}_z)|\hat{n}|\psi(0,\zeta\hat{J}_z)\rangle = \sum_m |c_m|^2\langle\zeta m|\hat{n}|\zeta m\rangle_b = 2\sum_{m>0}|c_m|^2\sinh^2(\zeta m), \tag{3.59}$$

where we used the identity $\sum_{m>0}|c_m|^2 = 1/2$ which arises from normalization, and the fact that the average bosonic occupation of a squeezed state with squeezing amplitude ζm is $\langle\hat{n}\rangle = \sinh^2(|\zeta m|)$. From the QFIM, the multi-parameter QCRB for the sum of the variances is,

$$V(\beta_{\rm re}) + V(\beta_{\rm im}) \geq 1/(4\langle\hat{n}\rangle + 2), \tag{3.60}$$

which we report in Eq. (3.19) of the main text. We emphasize that the QCRB saturates the multi-parameter Heisenberg limit of Eq. (3.49). Therefore, the reference state obtained by applying spin-dependent squeezing to any collective spin state with symmetric Dicke weights is optimal for the joint estimation of $\beta_{\rm re}$ and $\beta_{\rm im}$.

The attainability of the QCRB is determined by the Uhlmann curvature of Eq. (3.40). For the symmetric Dicke basis spin-dependent squeezed state,

$$\mathbf{D} = \begin{pmatrix} 0 & 4 \\ -4 & 0 \end{pmatrix}. \tag{3.61}$$

Because $\mathbf{D}$ does not vanish, the QCRB is, in general, not attainable. The deviation from the QCRB is quantified by the asymptotic attainability of Eq. (3.41),

$$R = 1/(2\langle\hat{n}\rangle + 1), \tag{3.62}$$

which is reported in Eq. (3.20) of the main text. In the limit $\langle\hat{n}\rangle \to \infty$, $R \to 0$. The QCRB is therefore asymptotically attainable within a prefactor of at most two, which decreases to one in the limit of infinite spin-dependent squeezing.

Spin-dependent squeezed, real spin-dependent displaced states: For purely real spin-dependent displaced and spin-dependent squeezed reference states, i.e. setting $\alpha, \zeta \in \mathbb{R}$ the QFIM is,

$$\mathbf{Q}(\alpha \in \mathbb{R}) = \begin{pmatrix} 4\sum_m |c_m|^2 e^{2\zeta m} & 0 \\ 0 & 4\mathbf{K}_{\mathrm{Re}(\gamma_m),\mathrm{Re}(\gamma_m),\vec{w}} + 4\sum_m |c_m|^2 e^{-2\zeta m} \end{pmatrix}. \tag{3.63}$$

The surviving diagonal element of the covariance matrix, $4\mathbf{K}_{\mathrm{Re}(\gamma_m),\mathrm{Re}(\gamma_m),\vec{w}}$, is the variance and is therefore strictly positive. Increasing α therefore increases $\mathbf{Q}_{22}$, which results in improved metrological utility for sensing β_{im}. When $\alpha \in i\mathbb{R}$ the metrological utility is improved for sensing β_{re}. Spin-dependent displacements can therefore be used to reduce the estimation uncertainty of either the real or imaginary component of a displacement signal.

Spin-dependent displaced states: For reference states without spin-dependent squeezing, i.e. $\zeta = 0$, the QFI is $\boldsymbol{Q} = 4\boldsymbol{DKD}$. For initial collective spin states with symmetric Dicke weights, $|c_m| = |c_{-m}|$,

$$\boldsymbol{Q} = 4\mathbb{1} + 16\sum_m |c_m|^2 \begin{pmatrix} \mathrm{Im}(\alpha m)^2 & \mathrm{Im}(\alpha m)\,\mathrm{Re}(\alpha m) \\ \mathrm{Im}(\alpha m)\,\mathrm{Re}(\alpha m) & \mathrm{Re}(\alpha m)^2 \end{pmatrix}. \tag{3.64}$$

For single-parameter sensing of either β_{re} or β_{im}, the QFI is maximized when the signal is orthogonal to the direction of the spin-dependent displacement that generated the reference state. The estimation of β_{re} therefore requires $\alpha \in i\mathbb{R}$, in which case,

$$Q_{\beta_{\mathrm{re}}} = 4 + 16\sum_m |c_m|^2\,\mathrm{Im}(\alpha m)^2 = 16\langle\hat{n}\rangle + 4, \tag{3.65}$$

where we used the fact that the average mode occupation of a spin-dependent displaced state is $\langle\hat{n}\rangle = \sum_m |c_m|^2|\alpha m|^2$. A similar result is obtained for single-parameter sensing of β_{im}. Spin-dependent displaced states that are appropriately phase-aligned therefore saturate the Heisenberg limit for single-parameter estimation of either β_{re} or β_{im}.

For multi-parameter sensing, in the limit $\beta \to 0$ and for initial symmetric Dicke weight collective spin states, the inverse of $\boldsymbol{Q}$ is,

$$\mathrm{Tr}\big(\boldsymbol{Q}^{-1}\big) = \frac{Q_{11}+Q_{22}}{-Q_{12}^2+Q_{11}Q_{22}} = \frac{1}{16\langle\hat{n}\rangle+4} + \frac{1}{4}. \tag{3.66}$$

In the limit $\langle\hat{n}\rangle \to \infty$, we obtain $\lim_{\langle\hat{n}\rangle\to\infty}(\mathrm{Tr}\big(\boldsymbol{Q}^{-1}\big)) = 1/4$. Therefore, the multi-parameter QCRB for spin-dependent displaced states is never small than a factor of two below the multi-parameter SQL of 1/2 that is obtained by using coherent states, cf. Sec. 3.4.3.

Phase-insensitive displacement magnitude sensing

Next, we consider phase-insensitive sensing of a displacement's magnitude by changing the basis of the QFIM from Cartesian coordinates to polar coordinates [169],

$$\boldsymbol{Q}[\rho(\boldsymbol{\theta})] = \boldsymbol{J}^T\boldsymbol{Q}[\rho(\boldsymbol{\theta'})]\boldsymbol{J}, \tag{3.67}$$

where $\boldsymbol{J}$ is the Jacobian matrix whose elements are defined as $J_{ij} = \partial\theta_i'/\partial\theta_j$. In polar coordinates, the parameters to be estimated are $\boldsymbol{\theta'} = \{|\beta|, \arg(\beta)\}$. The

Jacobian for Cartesian to polar coordinates is then,

$$\boldsymbol{J} = \frac{1}{|\beta|^2}\begin{pmatrix} |\beta|\beta_{\mathrm{re}} & |\beta|\beta_{\mathrm{im}} \\ -\beta_{\mathrm{im}} & \beta_{\mathrm{re}} \end{pmatrix}. \tag{3.68}$$

For reference states obtained by applying spin-dependent squeezing to symmetric-weight collective spin states, changing the basis of the QFIM of Eq. (3.58), the QFIM in polar coordinates $\boldsymbol{Q'}$ is,

$$\boldsymbol{Q'} = (8\langle\hat{n}\rangle + 4)\begin{pmatrix} 1 & 0 \\ 0 & |\beta|^2 \end{pmatrix}. \tag{3.69}$$

Note that Q_{22}, which corresponds to the estimation of the phase $\arg(\beta)$, depends on $|\beta|^2$. It vanishes in the limit of small displacements, $|\beta| \to 0$, because the phase in this regime is not well-defined. Focusing on displacement magnitude estimation, the QCRB is,

$$V(|\beta|) \geq 1/Q_{|\beta|} = 1/(8\langle\hat{n}\rangle + 4), \tag{3.70}$$

which is entirely independent of β, and saturates the Heisenberg limit, cf. Eq 3.50. Reference states obtained by applying spin-dependent squeezing to symmetric Dicke weight spin states are therefore optimal for the phase-insensitive estimation of the displacement's amplitude $|\beta|$.

Connection to many-mode bosonic squeezing

The usefulness of spin-dependent squeezed states for the joint estimation of β_{re} and β_{im} suggests a possible connection to other reference states. Here, we relate spin-dependent squeezing of N spins to bosonic squeezing of $N+1$ modes by introducing hybrid spin-boson operators,

$$\hat{a}_m = \hat{a}\,|m\rangle\langle m|_s\,, \tag{3.71}$$

which are distinguished from purely bosonic operator by the m subscript. The hybrid operators obey $[\hat{a}_m, \hat{a}_{m'}] = [\hat{a}_m^\dagger, \hat{a}_{m'}^\dagger] = 0,\ \forall\ m, m'$. However, the canonical commutation relations are modified due to a surviving spin projector, $[\hat{a}_m, \hat{a}_{m'}^\dagger] = \delta_{m,m'}\,|m\rangle\langle m|_s$, which arises because spin-dependent squeezing can be viewed as a direct sum of $N+1$ bosonic modes, rather than their tensor product.

Using the hybrid operators, spin-dependent squeezing can be written as an $(N+1)$-times product of single-mode squeezing operators,

$$\hat{S}(\zeta\hat{J}_z) = \prod_{m=-N/2}^{N/2} \exp\Big\{\frac{m}{2}(\zeta^*\hat{a}_m^2 + \zeta\hat{a}_m^{\dagger 2})\Big\}. \tag{3.72}$$

For $N = 1$, spin-dependent squeezed states correspond to two-mode squeezed states. Our metrological results can therefore be understood as a mapping from two-mode

squeeze states [71, 195]. Indeed, the Uhlmann curvature of Eq. (3.61) and the QFIM of Eq. (3.58) for spin-dependent squeezed states with symmetric Dicke weights are equivalent to the expressions obtained for two-mode squeezed vacuum states [195]. For $N > 1$, our results can be used to determine the metrological performance of bosonic squeezed states of $N + 1$ modes.

Finally, we note that we can introduce hybrid quadrature operators $\hat{x}_m = \hat{a}_m^\dagger + \hat{a}_m$ and $\hat{p}_m = i(\hat{a}_m^\dagger - \hat{a}_m)$, which obey $[\hat{x}_m, \hat{p}_{m'}] = 2i\delta_{m,m'} |m\rangle\langle m|_s$. Because $[\hat{x}_m, \hat{p}_{m'}] = 0$, $\forall\, m \neq m'$, the hybrid quadratures $\hat{x}_m$ and $\hat{p}_{m'}$ can be simultaneously measured, which is a useful property for multi-parameter displacement sensing.

Performance in terms of the squeezing parameter

In the main text, we analyzed the QCRB for spin-dependent squeezed reference states as a function of the mode occupation, $\langle \hat{n} \rangle$. Here, we analyze the QCRB as a function of the squeezing parameter, ζ. We focus on joint-parameter estimation of β_{re} and β_{im}; the performance is similar for the estimation of $|\beta|$.

In Fig. 3.6(a) we set $N = 1$ and plot the QCRB (black line) of spin-dependent squeezed states versus $\zeta/2$ (bottom axis). For comparison, the top axis shows $\langle \hat{n} \rangle$. The QCRB is always below the SQL (dashed line). We also show the QCRB of purely bosonic squeezed states (purple line), which scales as $\propto \langle \hat{n} \rangle$ and therefore never falls below the SQL.

In Fig. 3.6(b), we plot the change in mode occupation, $\langle \hat{n} \rangle$, as a function of the squeezing amplitude, $\zeta/2$, for states obtained by applying spin-dependent squeezing to two different collective spin states: GHZ (solid) and coherent (dashed). The average mode occupation increases faster for the GHZ state because the amount of squeezing is proportional to the magnetization m, and GHZ states maximally populate the largest $m = \pm N/2$ spin-polarized Dicke states. The same m dependence is responsible for the increasing mode occupations with higher N.

In Fig. 3.6(c) and (d), we plot the QCRB as a function of the squeezing parameter, $\zeta/2$, and the number of spins, N. We consider reference states obtained by applying spin-dependent squeezing to a GHZ spin state (panel (c)), and to a coherent spin state (panel (d)). At fixed N, the QCRB decreases when increasing ζ for both states. Similarly, at fixed ζ, the QCRB decreases when increasing N. We note that in trapped ion systems, spin-dependent squeezing generated via first- or second-order sidebands leads to a $\zeta \propto 1/N$ scaling (blue line) [162]. This results in a constant QCRB for GHZ states, but not for coherent spin states. In the latter case, ζ must scale approximately as $\zeta \propto 1/\sqrt{N}$ (green line) to ensure constant QCRB. Nevertheless, scaling to N ions when using coherent spin states remains advantageous due to the $\sqrt{N}$ amplification of the displacement signal [57]. Additionally, our protocol for realizing spin-dependent squeezing gives a $\sqrt{N}$ reduction in protocol time and therefore results in an effective scaling of $\zeta \propto 1/\sqrt{N}$.

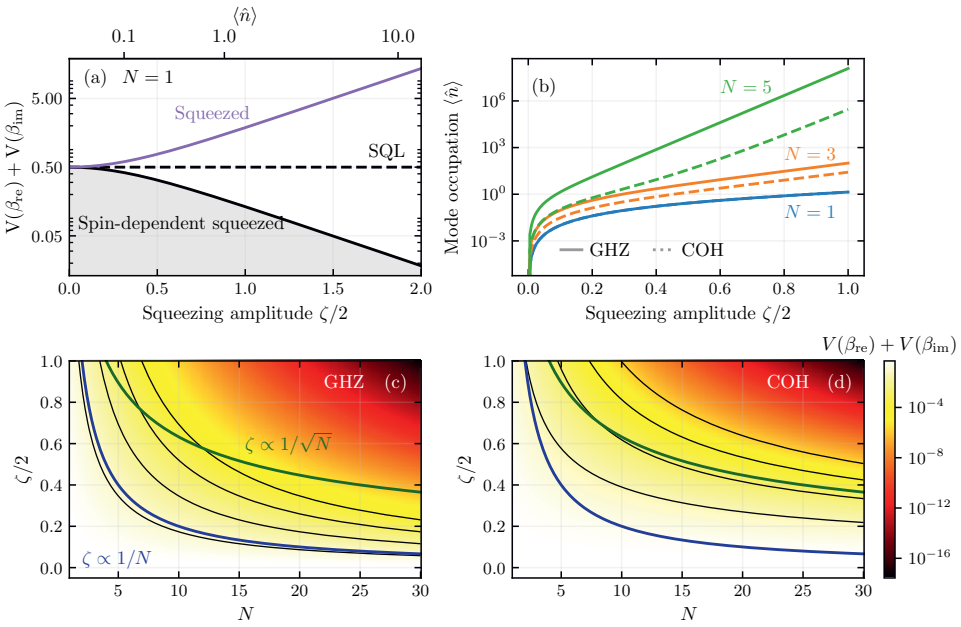


Figure 3.6: Metrological utility of spin-dependent squeezed states for the joint estimation of β_{re} and β_{im} versus the squeezing parameter, $\zeta/2$. **(a)** Case of $N = 1$ spin. The quantum Cramér-Rao bound (QCRB) for a spin-dependent squeezed state (black line) always falls below the SQL (dashed line). The SQL is defined by the QCRB for bosonic coherent states, SQL $= 1/2$. The QCRB for purely bosonic squeezed state (purple line) never falls below the SQL. **(b)** Bosonic mode occupation of states obtained by applying spin-dependent squeezing to either GHZ spin states (solid) or coherent spin states (dashed) for $N = 1$ (blue), $N = 3$ (orange) and $N = 5$ (green) spins. The occupation number grows with ζ and N. For fixed ζ and N, applying spin-dependent squeezing to GHZ states results in larger mode occupation than when applied to coherent spin states. **(c)** QCRB for reference states obtained by applying spin-dependent squeezing to GHZ spin states. Black lines are contour lines. The QCRB decreases with both N and ζ. The QCRB is constant when $\zeta \propto 1/N$ (blue line) **(d)** QCRB for reference states obtained by applying spin-dependent squeezing to coherent spin states. The QCRB is constant when $\zeta \propto 1/\sqrt{N}$ (green line).

3.4.5 Measurement protocols and classical Fisher information

Here, we analyze the time-reversal measurement schemes for estimating the displacement's magnitude, $|\beta|$, that were introduced in Sec. 3.1.2 of the main text.

The time-reversal sequence is composed of three steps,

$$\hat{S}(\zeta\hat{J}_z)\hat{D}(\beta)\hat{S}(-\zeta\hat{J}_z) = \hat{D}(\hat{\beta}), \tag{3.73}$$

where the equality is obtained by braiding the displacement and squeezing operators, and $\hat{\beta} = \beta\cosh(\zeta\hat{J}_z) - \beta^*\sinh(\zeta\hat{J}_z)$ is the spin-dependent displacement parameter.

Phase-insensitive amplitude estimation with a single spin

For $N = 1$ spin initialized in $|0\rangle_b|\psi_0\rangle_s = |0\rangle_b(|1/2\rangle_s + |-1/2\rangle_s)/\sqrt{2}$, the final state after the time-reversal sequence is,

$$|\psi_f\rangle = \frac{1}{\sqrt{2}}[\hat{D}(\beta_-)|0\rangle_b|-1/2\rangle_s + \hat{D}(\beta_+)|0\rangle_b|1/2\rangle_s], \tag{3.74}$$

where the spin-dependent displacement amplitudes are $\beta_- = \beta_{\rm re}e^{\zeta/2} + i\beta_{\rm im}e^{-\zeta/2}$ and $\beta_+ = \beta_{\rm re}e^{-\zeta/2} + i\beta_{\rm im}e^{\zeta/2}$. The probability of measuring $|1/2\rangle_s$ in the Dicke basis is, for $\beta \ll 1$,

$$P_{1/2} = 1 - |\beta|^2(\cosh(\zeta) - 1)/2 + \mathcal{O}(\beta^4), \tag{3.75}$$

which is phase-insensitive to third order in β. Using the fact that $P_{-1/2} = 1 - P_{1/2}$, the corresponding CFI is,

$$F_{|\beta|} = \left(\frac{1}{P_{1/2}} + \frac{1}{1-P_{1/2}}\right)\left(\frac{dP_{1/2}}{d|\beta|}\right)^2 = \frac{4 - 4\cosh(\zeta)}{|\beta|^2(\cosh(\zeta)-1) - 2} \underset{\beta\to 0}{=} 4\langle\hat{n}\rangle, \tag{3.76}$$

where the last equality holds in the regime $\beta \to 0$. We also used the relation $\langle\zeta/2|\,\hat{n}\,|\zeta/2\rangle = \sinh^2(\zeta/2) = (\cosh(\zeta) - 1)/2$, which correspond to the mode occupation of the (spin-dependent squeezed) reference state. The CFI diverges in the limit $\langle\hat{n}\rangle \to 0$, because the time-reversal protocol reduces to a bosonic displacement only, so no information is mapped to the spin. For $\langle\hat{n}\rangle \gtrsim 1$ the CFI is a factor of two larger than the QFI, cf. Eq 3.69, and therefore follows Heisenberg scaling.

Phase-insensitive amplitude estimation with GHZ spin states

For $N > 1$ spins initialized in a GHZ state, $|0\rangle_b|\psi_0\rangle_s = |0\rangle_b(|-N/2\rangle_s + |N/2\rangle_s)/\sqrt{2}$, the final state after the time-reversal sequence is,

$$|\psi_f\rangle = \frac{1}{\sqrt{2}}[\hat{D}(\beta_-)|0\rangle_b|-N/2\rangle_s + \hat{D}(\beta_+)|0\rangle_b|N/2\rangle_s], \tag{3.77}$$

where $\beta_- = \beta_{\rm re}e^{N\zeta/2} + i\beta_{\rm im}e^{-N\zeta/2}$ and $\beta_+ = \beta_{\rm re}e^{-N\zeta/2} + i\beta_{\rm im}e^{N\zeta/2}$. We apply a rotated one-axis twisting unitary to interfere the two spin states,

$$\hat{U}_{\rm RT} = \exp(-i\varphi\hat{J}_z)\exp(-i\pi\hat{J}_x^2/2)\exp(i\varphi\hat{J}_z), \tag{3.78}$$

where $\varphi = \frac{(-1)^{N/2}\pi}{2N}$. The rotations about $\hat{J}_z$ ensure phase coherence. Without them, the expectation value is $\sim \sin(2\beta_{\rm im}\beta_{\rm re}\sinh(2\xi))$, which is never phase-insensitive. Applying the rotated one-axis twisting unitary to the final state gives for even N, up to normalization,

$$\hat{U}_{\rm RT}\left|\psi_f\right\rangle \cong \hat{D}(\beta_-)\left|0\right\rangle_b\left[\left|J\right\rangle_s + \left|-J\right\rangle_s\right] + \hat{D}(\beta_+)\left|0\right\rangle_b\left[\left|J\right\rangle_s - \left|-J\right\rangle_s\right], \tag{3.79}$$

where $J = N/2$. The probability of measuring $\left|N/2\right\rangle_s$ in the Dicke basis is,

$$P_{N/2} = 1 - |\beta|^2\sinh(N\zeta/2)^2 + \mathcal{O}(\beta^4), \tag{3.80}$$

where the second equality is obtained when $\beta \ll 1$, and is phase-insensitive to third order in β. In the limit $\beta \to 0$, the CFI for the estimation of $|\beta|$ is,

$$F_{|\beta|} = \left(\frac{1}{P_{N/2}} + \frac{1}{1-P_{N/2}}\right)\left(\frac{dP_{N/2}}{d|\beta|}\right)^2 = 4\sinh(N\zeta/2)^2 = 4\langle\hat{n}\rangle, \tag{3.81}$$

which as a function of $\langle\hat{n}\rangle$ is the same sensitivity as for a single spin, cf. Eq. (3.76). For trapped ions, the advantage of using N spins comes from the $\sqrt{N}$ reduction in preparation time of the reference state, as shown in Sec. 3.2 of the main text, and the $\sqrt{N}$ amplification of the displacement signal [57].

Phase-insensitive amplitude estimation with coherent spin states

For $N > 1$ spins initialized in a coherent spin state pointing along the x-axis of the collective Bloch sphere, $\left|0\right\rangle_b\left|\psi_0\right\rangle_s = \left|0\right\rangle_b\sum_m c_m\left|m\right\rangle_s$ where $c_m = 2^{-N/2}\sqrt{\binom{N}{m+N/2}}$, the final state after the time-reversal sequence is,

$$\left|\psi_f\right\rangle = \sum_{m=-N/2}^{N/2} c_m\hat{D}(\beta_m)\left|0\right\rangle_b\left|m\right\rangle_s, \tag{3.82}$$

where $\beta_m = \beta_{\rm re}e^{\zeta m} + i\beta_{\rm im}e^{-\zeta m}$ are the spin-dependent displacement amplitudes. We apply a $\pi/2$ rotation about $\hat{J}_y$, which, in the Dicke basis, is written as,

$$e^{i\frac{\pi}{2}\hat{J}_y} = \sum_{m,m'=-N/2}^{N/2} d^{N/2}_{m',m}\left(\frac{\pi}{2}\right)\left|m'\right\rangle\!\left\langle m\right|_s. \tag{3.83}$$

The rotated state is therefore,

$$e^{i\hat{J}_y\pi/2}\left|\psi_f\right\rangle = \sum_{m,m'} c_m d_{m',m}\hat{D}(\beta_m)\left|0\right\rangle_b\left|m'\right\rangle_s, \tag{3.84}$$

where we dropped the Wigner d-function's $N/2$ superscript and $\pi/2$ dependence for notational simplicity. The probability of measuring $\left|m'\right\rangle_s$ in the Dicke basis is,

$$P_{m'} = \left[\sum_{m=-N/2}^{N/2} d_{m',m}c_m^*\left\langle 0,\beta_m\right|\right]\left[\sum_{m=-N/2}^{N/2} d_{m',m}c_m\left|\beta_m,0\right\rangle\right]. \tag{3.85}$$

We observe that for a coherent spin state pointing in the $x-y$ plane, the Dicke state coefficients obey the symmetry $c_m = c_{-m}$. Moreover, using the identity $d^{N/2}_{m',m}(\pi/2) = (-1)^{J+m'} d^{N/2}_{m',-m}(\pi/2)$, we can rewrite the sums in Eq. (3.85) as over positive m values only to obtain, for odd N (a similar expressions follows for N even),

$$\begin{aligned} P_{m'} = \sum_{m,n=1/2}^{N/2} d_{m',m} d_{m',n} c^*_m c_n [\langle \hat{D}^\dagger(\beta_m)\hat{D}(\beta_n)\rangle + \langle \hat{D}^\dagger(\beta_{-m})\hat{D}(\beta_{-n})\rangle \\ +(-1)^{N/2+m'}(\langle \hat{D}^\dagger(\beta_m)\hat{D}(\beta_{-n})\rangle + \langle \hat{D}^\dagger(\beta_{-m})\hat{D}(\beta_n)\rangle)], \end{aligned} \tag{3.86}$$

where the expectation values are computed with respect to the bosonic vacuum. When $\beta \ll 1$, the expectation values involving displacement operators appearing in the first and second line can be written as,

$$\langle \hat{D}^\dagger(\beta_m)\hat{D}(\beta_n)\rangle + \langle \hat{D}^\dagger(\beta_{-m})\hat{D}(\beta_{-n})\rangle = 2 - f(|\beta|^2) + \mathcal{O}(\beta^4), \tag{3.87a}$$

$$\langle \hat{D}^\dagger(\beta_m)\hat{D}(\beta_{-n})\rangle + \langle \hat{D}^\dagger(\beta_{-m})\hat{D}(\beta_n)\rangle = 2 - g(|\beta|^2) + \mathcal{O}(\beta^4), \tag{3.87b}$$

where exact expressions for the functions $f(|\beta|^2)$ and $g(|\beta|^2)$ are reported in Ref. [2]. Because these expressions are phase insensitive to third order in β, the probability $P_{m'}$ of Eq. (3.85) is also phase-insensitive to third order in β for all values of m'. Therefore, the measurement outcomes encode phase-insensitive information about the displacement's magnitude.

Computing the CFI for the estimation of $|\beta|$ requires summing over all m' and calculating derivatives, which is challenging to perform exactly for general N and ζ. Instead, we calculate exact expressions for the CFI for odd numbers of spins up to $N = 7$,

$$F^{(N=1)}_{|\beta|} = 2(\cosh(\zeta) - 1), \tag{3.88a}$$

$$F^{(N=3)}_{|\beta|} = \frac{1}{2}[9 + 8\cosh(\zeta) + 7\cosh(2\zeta)]\sinh(\zeta/2)^2, \tag{3.88b}$$

$$\begin{aligned} F^{(N=5)}_{|\beta|} = \frac{1}{32}[165 + 204\cosh(\zeta) + 188\cosh(2\zeta) + 52\cosh(3\zeta) + \\ 31\cosh(4\zeta)]\sinh(\zeta/2)^2, \end{aligned} \tag{3.88c}$$

$$\begin{aligned} F^{(N=7)}_{|\beta|} = \frac{1}{512}[2954 + 4192\cosh(\zeta) + 3953\cosh(2\zeta) + 1712\cosh(3\zeta) + \\ 1158\cosh(4\zeta) + 240\cosh(5\zeta) + 127\cosh(6\zeta)]\sinh(\zeta/2)^2. \end{aligned} \tag{3.88d}$$

From the above results, we conjecture that the CFI for odd N can be written in the general form,

$$F_{|\beta|} = \sinh(\zeta/2)^2 \sum_{i=0}^{N-1} a_i \cosh(i\zeta), \tag{3.89}$$

with coefficients $a_i \in \mathbb{R}$. We report this expression in Eq. (3.16) of the main text. To compare the CCRB to the QCRB, we compute the ratio between the QFI and the CFI for odd N up to $N = 9$. From these exact expressions, we conjecture that, in the limit $\zeta \to \infty$, the ratio follows the function,

$$Q_{|\beta|}/F_{|\beta|} = 2^N/(2^N - 1). \tag{3.90}$$

This expression is reported in Eq. (3.17). We observe that in the limit $N \to \infty$, the CFI converges to the QFI. In this extreme regime, the CCRB of the time-reversal sequence using reference states obtained by applying spin-dependent squeezing to coherent spin states therefore saturates the Heisenberg limit.

Multi-parameter estimation with a single spin

Next, we propose a measurement sequence for jointly estimating β_{re} and β_{im}. We consider $N = 1$ spin, and two ancilla qubits for readout. The measurement sequence, shown in Fig. 3.3 of the main text, requires wrapping the previous time-reversal sequence in bosonic displacements conditioned on the state of the ancillas, each with strength g. Note that for convenience, here we work with spin-dependent displacements that are $\hat{\sigma}_x$-conditioned, which are related by an ancilla basis rotation to the $\hat{\sigma}_z$-condition convention used in the main text, including in Fig. 3.3. The measurement sequence unitary is,

$$\begin{aligned} \hat{U}_p &= \hat{D}(g\hat{\sigma}_x^{(2)})\hat{D}(ig\hat{\sigma}_x^{(1)})\hat{D}(\hat{\beta})\hat{D}(-ig\hat{\sigma}_x^{(1)})\hat{D}(-g\hat{\sigma}_x^{(2)}) \\ &= \exp\Big\{2i\,\mathrm{Im}(ig\hat{\beta}^*\hat{\sigma}_x^{(1)})\Big\}\exp\Big\{2i\,\mathrm{Im}(g\hat{\beta}^*\hat{\sigma}_x^{(2)})\Big\}\hat{D}(\hat{\beta}), \end{aligned} \tag{3.91}$$

where $\hat{\sigma}_x^{(i)}$ acts on the ith ancilla. The spin-dependent displacement parameter is $\hat{\beta} = \beta\cosh(\zeta\hat{J}_z) - \beta^*\sinh(\zeta\hat{J}_z)$. Braiding is achieved using $\hat{D}(a)\hat{D}(b)\hat{D}(-a) = e^{2i\,\mathrm{Im}(ab^*)}\hat{D}(a)$. For a displacement signal $\beta = \beta_{\mathrm{re}} + i\beta_{\mathrm{im}}$, the ancilla rotations appearing in Eq. (3.91) are,

$$\mathrm{Im}(ig\hat{\sigma}_x^{(1)}\hat{\beta}^*) = g\hat{\sigma}_x^{(1)}\begin{pmatrix} e^{-\zeta}\beta_{\mathrm{re}} & 0 \\ 0 & e^{\zeta}\beta_{\mathrm{re}} \end{pmatrix}, \tag{3.92a}$$

$$\mathrm{Im}(g\hat{\sigma}_x^{(2)}\hat{\beta}^*) = -g\hat{\sigma}_x^{(2)}\begin{pmatrix} e^{\zeta}\beta_{\mathrm{im}} & 0 \\ 0 & e^{-\zeta}\beta_{\mathrm{im}} \end{pmatrix}. \tag{3.92b}$$

In the regime where the squeezing is much larger than the conditional displacements, $\zeta \gg g$, and the displacement signal, $\zeta \gg \beta$, terms proportional to $e^{-\zeta}$ are negligible, and we can rewrite $\hat{U}_p$ as,

$$\hat{U}_p \approx \exp\Big\{2ige^{\zeta}\beta_{\mathrm{re}}\,|{\downarrow}\rangle\langle{\downarrow}|_s\,\sigma_x^{(1)}\Big\}\exp\Big\{-2ige^{\zeta}\beta_{\mathrm{im}}\,|{\uparrow}\rangle\langle{\uparrow}|_s\,\sigma_x^{(2)}\Big\}\hat{D}(\hat{\beta}). \tag{3.93}$$

The system is initialized in $|\psi_0\rangle = |0\rangle_b\,|+\rangle_s\,|{\uparrow}\rangle_1\,|{\uparrow}\rangle_2$, where the ancillas are denoted by numerical indices. The probability of measuring the ith ancilla in the state $|{\uparrow}\rangle$ is,

$$P_{\uparrow}^{(i)} = [1 + \cos^2(\phi_i)]/2, \tag{3.94}$$

where we defined the rotation angles $\phi_1 = 2ge^{\zeta}\beta_{\rm re}$ and $\phi_2 = -2ge^{\zeta}\beta_{\rm im}$. The measurement of the first ancilla reveals information about $\beta_{\rm re}$ only, while measurement of the second ancilla reveals information about $\beta_{\rm im}$ only. For the two independent measurement distributions $P_{\uparrow}^{(1)}$ and $P_{\uparrow}^{(2)}$, the metrological utility is determined by the classical Fisher information matrix,

$$F_{j,k} = \sum_{i=1}^{2} \left(\frac{1}{P_{\uparrow}^{(i)}} + \frac{1}{1 - P_{\uparrow}^{(i)}} \right) \frac{\partial P_{\uparrow}^{(i)}}{\partial \theta_j} \frac{\partial P_{\uparrow}^{(i)}}{\partial \theta_k}. \tag{3.95}$$

In the limit $\beta \to 0$ the CFIM is $\mathbf{F} = 8g^2e^{2\zeta}\mathbb{1}$. For this measurement protocol, the multi-parameter variance is therefore lower bounded bounded according to the CCRB,

$$V(\beta_{\rm re}) + V(\beta_{\rm im}) \geq \mathrm{Tr}\big(\mathbf{F}^{-1}\big) = 1/(4g^2e^{2\zeta}) \tag{3.96}$$

which we report in Eq. (3.22) of the main text. The CCRB decreases as a function of the squeezing, ζ, and also as a function of the spin-dependent displacement strength, g. Although increasing g is a viable strategy to reduce the CCRB, maintaining the regime $\zeta \gg g$ which was used to derive Eq. (3.93) requires simultaneously increasing ζ. The metrological performance of the protocol is studied in Fig. 3.3.

3.4.6 Further details on the state preparation protocol

In this section, we provide additional derivations, error analysis and numerical simulations for our spin-dependent squeezed state preparation protocol of Sec. 3.2.

Derivation of Hamiltonian

The Hamiltonian in Eq. (3.23) of the main text is obtained by driving the first-order sidebands at four different frequencies: one pair of red- and blue- sideband interactions with detuning $\Delta(t)$, and another pair of red- and blue- sideband interactions with detuning $-\Delta(t)$. In the rotating frame with respect to the spin and the motion, ignoring all far-off-resonant motional modes, the four interaction Hamiltonians are,

$$\hat{H}_{\rm r1}(t) = \frac{g(t)}{2}(\hat{a}\hat{J}_+ e^{-i\phi_{\rm r1}(t) - it\Delta(t)} + \hat{a}^\dagger \hat{J}_- e^{i\phi_{\rm r1}(t) + it\Delta(t)}), \tag{3.97a}$$

$$\hat{H}_{\rm r2}(t) = \frac{g(t)}{2}(\hat{a}\hat{J}_+ e^{-i\phi_{\rm r2}(t) + it\Delta(t)} + \hat{a}^\dagger \hat{J}_- e^{i\phi_{\rm r2}(t) - it\Delta(t)}), \tag{3.97b}$$

$$\hat{H}_{\rm b1}(t) = \frac{g(t)}{2}(\hat{a}^\dagger \hat{J}_+ e^{-i\phi_{\rm b1}(t) + it\Delta(t)} + \hat{a}\hat{J}_- e^{i\phi_{\rm b1}(t) - it\Delta(t)}), \tag{3.97c}$$

$$\hat{H}_{\rm b2}(t) = \frac{g(t)}{2}(\hat{a}^\dagger \hat{J}_+ e^{-i\phi_{\rm b2}(t) - it\Delta(t)} + \hat{a}\hat{J}_- e^{i\phi_{\rm b2}(t) + it\Delta(t)}), \tag{3.97d}$$

where $\phi_{\rm r1}(t)$, $\phi_{\rm r2}(t)$, $\phi_{\rm b1}(t)$ and $\phi_{\rm b2}(t)$ are time-dependent phases. After setting $\phi_{\rm b1}(t) = -\phi_{\rm r1}(t)$, sending $\phi_{\rm r2}(t) \to \phi_{\rm r2}(t) + \pi/2$ and setting $\phi_{\rm b2}(t) \to -\phi_{\rm r2}(t) + \pi/2$,

the sum of all four Hamiltonians is,

$$\hat{H}(t) = g(t)\hat{a}\left[\hat{J}_x e^{-i\phi_{r1}(t)-it\Delta(t)} + \hat{J}_y e^{-i\phi_{r2}(t)+it\Delta(t)}\right] + \text{h.c.} \tag{3.98}$$

where we used the fact that $(\hat{J}_+ + \hat{J}_-)/2 = \hat{J}_x$ and $(-i\hat{J}_+ + i\hat{J}_-)/2 = \hat{J}_y$. Setting $\phi_{r1}(t) = 0$ and relabeling $\phi_{r2}(t) = \phi(t)$ yields the Hamiltonian reported in Eq. (3.23) of the main text.

Errors due to higher-order Magnus expansion terms

In Sec. 3.2 of the main text, we neglected higher-order Magnus terms. Here, we provide additional justification for this step.

We first note that third-order terms are of the form of $\hat{a}^3\hat{J}_x$ and $\hat{a}\hat{J}_x\hat{J}_z$, and fourth order terms are of the form $\hat{a}^4\hat{J}_z$, $\hat{a}^2\hat{J}_x^2$, $\hat{a}^2\hat{J}_z$, $\hat{a}^2\hat{J}_z\hat{J}_x$, $\hat{J}_x^2$ and $\hat{J}_z\hat{J}_x\hat{J}_y$. To investigate their effects, we plot, for each higher-order Magnus term as a function of N, the magnitude of the spin operator's matrix element that drives transitions out of the fully-polarized spin state (see Fig. 3.7). For example, for $\hat{J}_x$, the relevant matrix element is $\langle N/2-1|\hat{J}_-|N/2\rangle_s$, while higher-order spin operators will include powers of $\hat{J}_+$, $\hat{J}_-$ and the relevant element of $\hat{J}_z$. As another example, for $\hat{J}_x^2$, a relevant matrix element is $\langle N/2-2|\hat{J}_-^2|N/2\rangle_s$. In Fig. 3.7, we observe that all terms are either bounded above, constant or decreasing functions of N. In particular, the terms with cubic or quartic powers of creation and annihilation operators (green line in panel (a), purple line in panel (b)) are the most deleterious terms for the bosonic mode. These are also the terms whose spin operator's matrix element decreases as $1/N$. As such, we expect that our protocol can be scaled to many ions. Our numerical simulations presented in Fig. 3.5 supports this analysis, where we observe a $\sqrt{N}$ reduction in protocol time when scaling to N ions.

Numerical results: spin-polarized states and increased phase loops

Applying spin-dependent squeezing to a spin-polarized state such as $|N/2\rangle_s$ produces a simple product state, $|\zeta m/2\rangle_b|N/2\rangle_s$. Studying the performance of our protocol starting from this state is still instructive, because it reveals a strong dependence on the target squeezing angle, as seen in Fig. 3.8. In panel (a), we plot the minimum protocol time, $t_{\min}$, to prepare a target spin-dependent squeezed state, $|\psi_t\rangle = \hat{S}(\zeta\hat{J}_z)|0\rangle_b|N/2\rangle_s$, with fidelity $\mathcal{F} > 0.99$ for varying target angles $\theta = \arg(\zeta)$. We observe a strong dependence on θ, which can be understood from the first stroboscopic segment's third-order Magnus term,

$$\begin{aligned}\hat{\Theta}_3[0,\tau] = \frac{3g^3\tau^3}{4\pi^2}\Big[&-\hat{a}^3(e^{-2i\phi}\hat{J}_x + e^{-i\phi}\hat{J}_y) + \hat{a}^\dagger\hat{a}^2(\hat{J}_x + e^{-i\phi}\hat{J}_y)\\ &+\hat{a}(\hat{J}_x + e^{-i\phi}\hat{J}_y + 2i\hat{J}_z\hat{J}_y - 2ie^{-i\phi}\hat{J}_z\hat{J}_x)\Big] + \text{h.c.},\end{aligned} \tag{3.99}$$

where ϕ is the phase in the Hamiltonian during the segment. Several terms, including those that are cubic in bosonic creation and annihilation operators, are

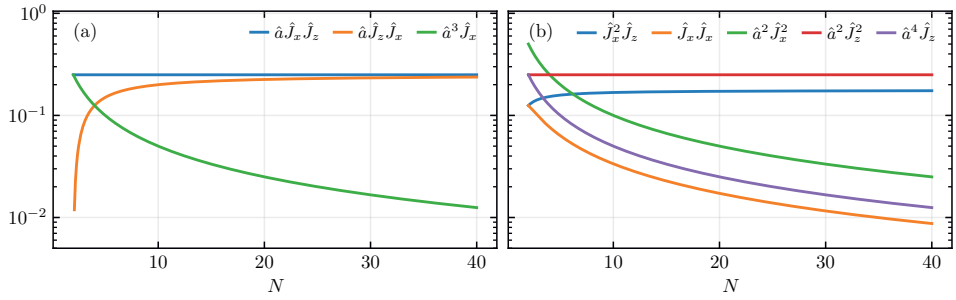


Figure 3.7: Magnitude of the spin operator matrix element that drives transitions out of the $|N/2\rangle_s$ Dicke state. **(a)** terms that appear at third order and **(b)** terms that appear at fourth order of the Magnus expansion. Although the higher-order Magnus terms include bosonic operators, which are included in the legend for clarity, the lines plotted are determined only by the collective spin operator's matrix elements. All terms are either bounded, constant, or decreasing functions of N. The most deleterious terms for the bosonic mode, i.e. those that are cubic and quartic in $\hat{a}$,$\hat{a}^\dagger$, decrease in strength as $1/N$.

independent of ϕ. As such, the target squeezing angle should be chosen so that terms independent of ϕ act in the anti-squeezed quadrature, and hence their effect is masked by the increased variance. This occurs when $\theta = \pi$, as seen in Fig. 3.8, where the protocol's duration is significantly reduced compared to when $\theta = 0$.

Next, we consider varying the number of phase-space loops, ℓ, of each stroboscopic segment. In Fig. 3.8(b), we set $N = 20$ and vary ℓ. The step-like behavior arises because a full phase-space loop must be completed, i.e. t_f must be an integer multiple of $2\pi/|\Delta|$ where Δ is the detuning. Increasing ℓ results in longer $t_{\min}$ because the higher-order Trotter terms are larger with ℓ. The benefit of increased ℓ is shown in panel (c), which plots the number of repetitions, P, of the four-step stroboscopic sequence. We observe that increasing ℓ results in smaller P, which means that fewer stroboscopic changes of the phase and detuning are required. This may be of benefit experimentally.

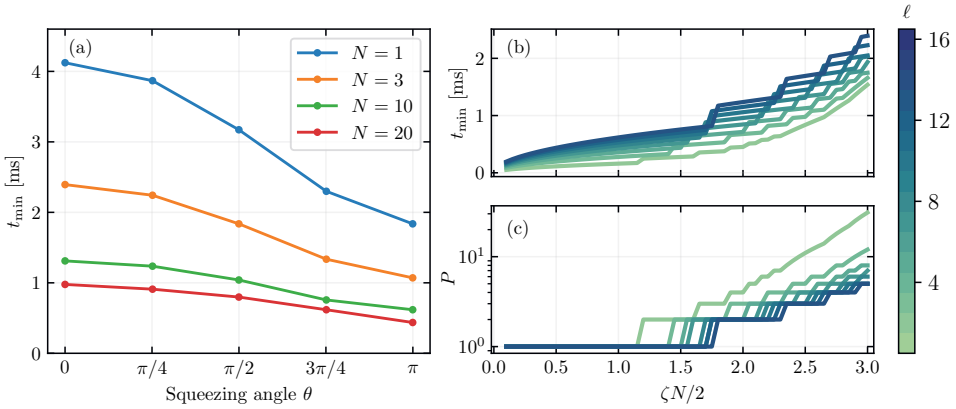


Figure 3.8: **(a)** Minimum protocol time, $t_{\min}$, to prepare the target spin-dependent squeezed state, $|\psi_t\rangle = \hat{S}(\zeta \hat{J}_z)\,|0\rangle_b\,|N/2\rangle_s$, with fidelity $\mathcal{F} > 0.99$ for various number of spins, N. The Hamiltonian parameters are the same as the main text, see Fig. 3.5. Here, we fix the target squeezing parameter's magnitude, $|\zeta| = 2.5$, and vary the squeezing angle, $\theta = \arg(\zeta)$. The protocol time decreases with N, and is minimized when $\theta = \pi$. **(b)** Minimum protocol time, $t_{\min}$, versus the amount of spin-dependent squeezing, $\zeta N/2$, for ℓ repetitions of a stroboscopic segment. Larger ℓ results in longer protocol times. **(c)** Number of times, P, that the four-step stroboscopic sequence is repeated. Increasing the number of times ℓ that each stroboscopic segment is repeated allows for decreased P.

Chapter 4

Arbitrary symmetric spin state preparation

Based on
Physical Review Research **7**, L022072, (2025) [3]

> "Poirot," I said. "I have been thinking."
> "An admirable exercise my friend. Continue it."
>
> Agatha Christie, Peril at End House (1932)

As discussed in Sec. I.3 of the Introduction, the operation of a quantum computer relies on our ability to prepare highly entangled quantum states, both as a step for quantum algorithms, and as codewords for quantum error correction (QEC). Despite recent remarkable experimental progress towards fault-tolerant quantum computing [6, 198, 199], the fragility of multi-partite entanglement to noise limits the fidelity of state preparation. Furthermore, the lack of single-site addressing in some experimental platforms has typically limited the variety of states that can be prepared to e.g. squeezed states. In light of these limitations, the choice of QEC scheme is important. Depending on its properties, certain QEC schemes may offer advantages both in terms of the types of errors that they can protect against [200], as well as their suitability of implementation to the particular hardware. One promising approach utilizes codewords which are symmetric states, i.e. superpositions of Dicke states [79–81]. The Dicke states are also relevant for quantum metrology [85], including error-corrected quantum sensing [201], quantum storage [82, 83] and quantum networking [84]. The need to overcome the intrinsic noise in NISQ devices has motivated the design of symmetric state preparation protocols that minimize the circuit depth. In particular, symmetric states have been prepared using one- and two-qubit gate circuits with depth $\mathcal{O}(N)$ [86, 87], and specific Dicke states with constant depth using measurements and classical computation [88].

In this chapter, we demonstrate that *arbitrary* superpositions of Dicke states can be engineered using linear-depth circuits with only global control. Specifically, we utilize a variational quantum circuit consisting of only global one-axis twisting and

global rotations, and thus do not demand local addressability nor ancilla qubits. We provide analytic and numerical evidence that the number of steps to synthesize an arbitrary N-qubit symmetric states scales as $2N/3$. Focusing on applications to QEC codewords, we show that only $P = 4$ and $P = 7$ steps are required to prepare QEC codewords of the $N = 9$ Ruskai [80] and $N = 13$ Gross [81] codes with infidelity $1 - \mathcal{F} < 10^{-4}$, respectively. We discuss the possible implementation in trapped ions, including a detailed analysis of expected sources of error. The limited resources required by our protocol make it immediately realizable on a broad range of experimental quantum simulation platforms.

4.1 Dicke states

4

We consider an ensemble of N qubits. The collective spin operators are defined as $\hat{J}_\alpha = (1/2)\sum_{j=1}^{N} \hat{\sigma}_j^\alpha$ where $\alpha \in \{x, y, z\}$ and $\hat{\sigma}_j^\alpha$ is the Pauli operator acting on the j-th qubit. Dicke states, denoted $|J, M\rangle$, are simultaneous eigenstates of the total spin operator $\hat{J}^2 = \hat{J}_x^2 + \hat{J}_y^2 + \hat{J}_z^2$ and $\hat{J}_z$. The quantum numbers J and M are defined by $\hat{J}^2 |J, M\rangle = J(J+1)|J, M\rangle$, $\hat{J}_z |J, M\rangle = M |J, M\rangle$ with $J \in \{0, \ldots, N/2\}$, and $M \in \{-J, \ldots, J\}$. We focus on the $N + 1$ symmetric $J \equiv N/2$ Dicke states, which in the single-particle $\hat{\sigma}_z$ basis are,

$$|J = N/2, M\rangle = \frac{1}{\sqrt{\lambda}} \sum_{\mathcal{P}} (|1\rangle^{J+M} \otimes |0\rangle^{J-M}), \tag{4.1}$$

where the normalization factor is $\lambda = \binom{2J}{J+M}$, and where the summation is over all permutations $\mathcal{P}$ of the ordering of the spins [1]. Dicke states feature entanglement that is persistent [202] and robust to particle loss [203–205] which makes them attractive for experimental realization, while also demonstrating useful sensing capabilities [206, 207]. Specifically, the N-qubit W-state $|N/2, -N/2 + 1\rangle$ is maximally pairwise entangled [208, 209], while the Dicke state with $N/2$ excitations $|N/2, 0\rangle$ saturates the quantum Cramér-Rao bound when sensing global rotations about the x-y axis [89]. There are many existing deterministic preparation protocols for Dicke states, including quantum circuit approaches that use one- and two-qubit gates [86–88], global pulse schemes [89–92], and others [93–95].

In addition to bare Dicke states, superpositions of Dicke states are of key interest. For example, the Greenberger–Horne–Zeilinger (GHZ) state $|\mathrm{GHZ}\rangle = |N/2, -N/2\rangle + |N/2, N/2\rangle$ is maximally entangled, represents a distinct class of multi-partite entanglement, exhibits phase sensing sensitivity below the standard quantum limit (SQL) [175, 210] and has been prepared in many experimental platforms [211–213]. More generally, superpositions over more of the Dicke states form the logical basis states of various QEC codes including Pauli exchange error correcting codes [80] and large spin codes [81]. The weighting of individual Dicke states

[1] For example, the four $N = 3$ symmetric Dicke states are $|3/2, -3/2\rangle = |000\rangle$, $|3/2, -1/2\rangle = 1/\sqrt{3}(|001\rangle + |010\rangle + |100\rangle)$, $|3/2, 1/2\rangle = 1/\sqrt{3}(|011\rangle + |101\rangle + |110\rangle)$ and $|3/2, 3/2\rangle = |111\rangle$

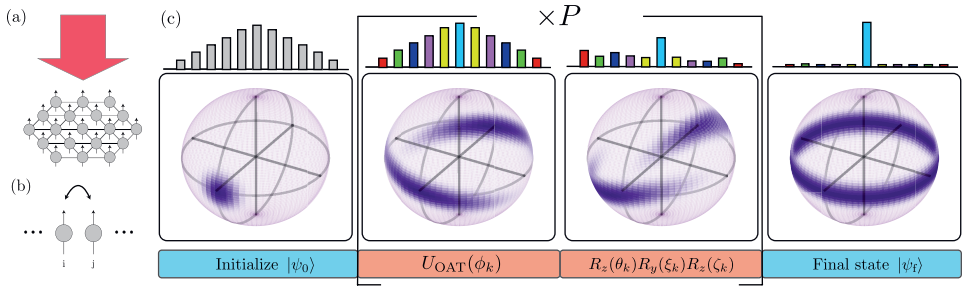


Figure 4.1: **(a)** The protocol Eq. (4.2) utilizes operations that act globally on a collection of N qubits. **(b)** The Dicke states are symmetric, i.e. any two qubits i and j can be interchanged without changing the quantum state. **(c)** Schematic representation of the protocol. The system is initialized in a coherent spin state (CSS) $|\psi_0\rangle = |\bar{\theta}, \bar{\phi}\rangle$. Next, one-axis twisting $\hat{U}_{\mathrm{OAT}}$ generates spin squeezing. For relatively small ϕ_k the CSS is spin squeezed; for larger ϕ_k the probability distribution separates across the Bloch sphere, as is the case sketched here. Next, the state is rotated about an arbitrary axis. These two operations are repeated P times, with parameters numerically optimized to minimize the infidelity $1-\mathcal{F}$. Above the Bloch spheres, to highlight the connection to amplitude amplification, we sketch the $N+1$ basis state amplitudes with coloring representing complex phase. In this perspective, $\hat{U}_{\mathrm{OAT}}$ applies a phase that depends non-linearly on the excitation number M, with the rotation then amplifying or attenuating the amplitude conditioned on the phase that was applied. Repeated application of $\hat{U}_{\mathrm{OAT}}$ and $\hat{R}$ with optimized parameters can therefore maximize the amplitude of a target state.

in each of these logical basis states are chosen to satisfy the Knill-Laflamme QEC conditions [214]. Existing protocols to prepare such specific, highly entangled superpositions of Dicke states typically require single-site addressability [96] or a large detuning limit [97]. Below, we alleviate these constraints and propose to prepare Dicke state superpositions using a global variational quantum circuit.

4.2 State preparation protocol

Global variational quantum circuits have been previously proposed [215–218] and demonstrated experimentally [219] for the preparation of squeezed quantum states for quantum metrology. Here, instead of optimizing the variational parameters to maximize a property of the target state (such as the squeezing amplitude or phase sensitivity), we employ such circuits to prepare target symmetric quantum states by minimizing the infidelity $1-\mathcal{F} = 1 - |\langle\psi_t|\psi_f\rangle|^2$, where $|\psi_t\rangle$ is a chosen target state, $|\psi_f\rangle = U_{\mathrm{tot}}|\psi_0\rangle$ the final state and $|\psi_0\rangle$ the initial state. As sketched in

Fig. 4.1, the circuit of P layers is,

$$\hat{U}_{\text{tot}} = \prod_{k=1}^{P} [\hat{R}(\theta_k, \xi_k)\hat{U}_{\text{OAT}}(\phi_k)], \tag{4.2}$$

and consists of: (i) global rotations $\hat{R}(\theta_k, \xi_k) = \hat{R}_z(\theta_k)\hat{R}_y(\xi_k)$, and (ii) global one-axis twisting $\hat{U}_{\text{OAT}}(\phi) = e^{i\phi\hat{J}_z^2}$, where $\phi = gt$ with g the coupling strength and t the evolution time [46]. Because $\hat{R}_z$ commutes with $\hat{U}_{\text{OAT}}$, for $P \geq 2$ the global rotation $\hat{R}$ is about an arbitrary axis. Although the fidelity can be efficiently computed classically because the symmetric space dimension is $N + 1$, in the Supplemental Material of Sec. 4.7 we discuss how an upper bound on the infidelity can be efficiently computed on quantum devices for a hybrid classical-quantum algorithm approach, which may be a preferred option to mitigate certain hardware errors.

The capability of the protocol to prepare superpositions of Dicke states can be understood using amplitude amplification, as sketched in Fig. 4.1. To emphasize the versatility of the variational circuit, we note that $\hat{U}_{\text{OAT}}$ and $\hat{R}$ provide universal control over the symmetric subspace [218, 220]. Although a general explicit expression for the optimal parameters for arbitrary symmetric state synthesis is a complicated task, a simple consistency argument for the minimum number of gates P^* to prepare a general symmetric state can be made as follows: accounting for the coefficients and normalization of the $N + 1$ basis states, a general state in the symmetric $J = N/2$ subspace is described by $2N$ real parameters. As each protocol step is characterized by three free parameters θ, ξ, ϕ, the preparation of an arbitrary symmetric state requires $P^* = 2N/3$ steps.

We numerically verify the scaling relation for P^* by generating $N_{\text{Haar}} = 200$ Haar random states as target states and optimizing the protocol's variational parameters to minimize $1 - \mathcal{F}$. Obtaining (and verifying) a global minima is challenging, as in general the optimization landscape can contain many local minima. However, if the system is controllable [2], then every local minima is a global minima [221]. As such, performing only local optimization of the parameters we expect a sharp transition in target state infidelity at some $P \geq P^*$ as the system becomes controllable.

In Fig. 4.2 we plot the infidelity $1-\mathcal{F}$ as a function of P for various N up to $N = 50$. We perform local gradient-based optimization using BFGS [222] in Julia [149] with Optim.jl and LineSearches.jl [148], and terminate the optimization once the infidelity passes below a threshold $\epsilon = 10^{-12}$. As expected, as P increases the infidelity decreases, with a relatively sharp transition as the system becomes controllable. In the inset of Fig. 4.2 we plot the location of the transition as a function of N, showing excellent agreement with the scaling obtained from counting, $P^* = 2N/3$. As shown in the inset we further verify this prediction by optimizing the parameters for $N_{\text{Haar}} = 200$ Haar random states using $P = \lceil 2N/3 \rceil + c$ gates

[2] If there exists a control field $C(t)$ such that $\delta\mathcal{P}_{i\to f}/\delta C(t) = 0\ \forall 0 \leq t \leq T$, where $\mathcal{P}_{i\to f} = |\langle\psi_f| U_{\text{tot}} |\psi_0\rangle|^2$ is the transition element for a transition from an initial (final) state $|\psi_0\rangle$ ($|\psi_f\rangle$) for some finite protocol time T, then the system is controllable.

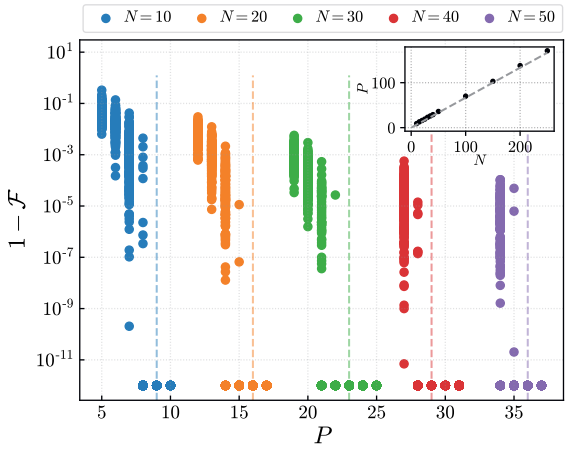


Figure 4.2: Infidelity $1-\mathcal{F} = 1-|\langle\psi_t|\psi_f\rangle|^2$ vs. circuit depth P for various N. Each data point is a Haar random target state; we draw $N_{\text{Haar}} = 200$ targets for each N. The variational parameters are classically optimized using a local optimization algorithm. As the system becomes controllable, all local minima become global minima, which corresponds for each N to the sharp decrease in infidelity as P increases (marked with vertical dashed lines). Inset: location of the transition as a function of N (black points) for up to $N = 250$, demonstrating excellent agreement with the scaling prediction $P^* = 2N/3$ (grey dashed).

with a small constant offset c [3] for $N = 100$, $N = 150$, $N = 200$ and $N = 250$, verifying that all states can be prepared with infidelities below the optimization termination threshold $\epsilon = 10^{-12}$. Therefore the protocol Eq. (4.2) is an efficient preparation protocol for synthesizing arbitrary symmetric states. To the best of our knowledge this improves upon previous global control protocols, which required N steps only in a large detuning limit [97] or using excited Rydberg states [223], and $\mathcal{O}(N^4)$ steps for arbitrary unitary synthesis [218].

4.3 Dicke state preparation

Next, we demonstrate the preparation of specific states, beginning with bare Dicke states. Because the gate sequence Eq. (4.2) starts with the application of $\hat{U}_{\text{OAT}}$, for the initial state we choose a global rotation acting on $|N/2, -N/2\rangle$, which is a coherent spin state (CSS) $|\psi_0\rangle = |\bar{\theta}, \bar{\phi}\rangle$, i.e. an eigenstate of the spin component

[3] An offset c in the number of gates $P = \lceil 2N/3 \rceil + c$ is needed to reach fidelities below the numerical termination threshold $\epsilon = 10^{-12}$. For $N = 10$ to $N = 150$ the offset is either $c = 2$ or $c = 3$, depending on the ceil function. For $N = 200$ and $N = 250$ the offset is $c = 4$, to give the numerical optimization more overhead to reach the termination threshold. Specifically, for $N = [100, 150, 200, 250$ we use $P = [70, 103, 138, 171]$ gates.

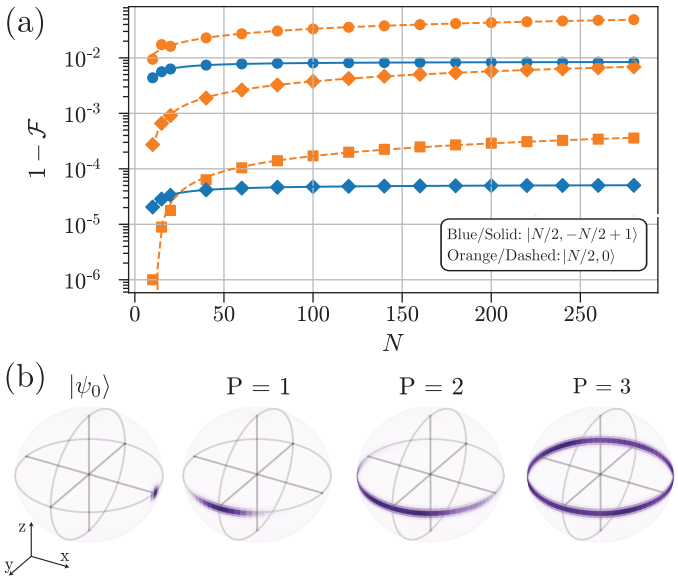


Figure 4.3: **(a)** Theoretical infidelity $1-\mathcal{F}=1-|\langle\psi_{\rm t}|\psi_{\rm f}\rangle|^2$ to prepare: the the W state $|N/2,-N/2+1\rangle$ (solid blue) and $N/2$ excitation state $|N/2,0\rangle$ (dashed orange) using the protocol $\hat{U}U_{\rm tot}$ Eq. (4.2) for $P=2$ (dots), $P=3$ (diamonds) and $P=4$ (squares). The lines show a power law fit, with excellent agreement. Both target states can be prepared with small theoretical infidelities $1-\mathcal{F}<10^{-3}$ in $P=3$ and $P=4$ gate steps respectively in systems as large as $N=300$ qubits. **(b)** The su(2) Husimi Q-representation for the $P=3$ solution that prepares $|N/2,0\rangle$ with $N=300$. The optimized initial coherent spin state starts along x, with the subsequent interleaving of one-axis twisting and global rotations leading to the preparation of $|\psi_t\rangle$ with $1-\mathcal{F}\sim 10^{-2}$.

in the $(\bar{\theta},\bar{\phi})$ direction. The parameters $(\bar{\theta},\bar{\phi})$ are also numerically optimized, and thus the total number of free parameters is $3P+2$. Both here and in the next section, the numerical optimization uses a multi-start Monte Carlo search, with local optimization using L-BFGS [224].

Firstly, we prepare the Dicke state with $N/2$ excitations, $|\psi_{\rm t}\rangle=|N/2,0\rangle$. This state is metrologically useful: when the state used for sensing is $|N/2,0\rangle$, the uncertainty in the measured angle ϵ of a rotation $e^{-i\epsilon\hat{J}_y}$ saturates the Cramér-Rao bound, $(\Delta\epsilon)^2=2/[N(N+2)]$ and features entanglement that is robust to particle loss [203–205, 225, 226]. In Fig. 4.3(a) we plot (dashed orange) $1-\mathcal{F}$ as a function of N for $P=2$ (circles), $P=3$ (diamonds) and $P=4$ (squares). The infidelity is remarkably robust to increasing qubit number, with $P=4$ gates sufficient to prepare the target state in up to $N=300$ qubits with $1-\mathcal{F}\lesssim 10^{-2}$. The dashed lines show a power law fit with excellent agreement, emphasizing the slow increase of infidelity with N for $N\gtrsim 50$. In Fig. 4.3(b) we plot the evolution of

the $N = 300$ state under the $P = 3$ gate sequence solution using the su(2) Husimi Q-Representation $Q(\theta, \phi) = \langle \theta, \phi | \rho | \theta, \phi \rangle$ of a state ρ where $|\theta, \phi\rangle$ is a CSS. Clearly visible is the effect of spin squeezing, whose repeated application combined with global rotations results in the preparation of $|N/2, 0\rangle$.

Secondly, we prepare the N-qubit W state, $|N/2, -N/2+1\rangle$. In Fig. 4.3(a), we plot (solid blue) the infidelity to prepare the W-state with $P = 2$ (circles) and $P = 3$ (diamonds) [4]. We find that the W state can be prepared in systems of up to $N = 300$ qubits with small infidelities $1 - \mathcal{F} < 10^{-4}$ in only $P = 3$. Thus, our protocol can be used to prepare these two Dicke states in up to $N = 300$ qubits in $\mathcal{O}(1)$ gate steps.

4.4 Quantum error correction codewords

Next, we prepare specific superpositions of Dicke states for QEC. Pauli exchange errors are two-qubit errors that arise due to interactions between qubits, for example due to dipole-dipole interactions. Physically, exchange errors are similar to bit flip errors, with the additional constraint that a qubit will flip if and only if its neighbor is different. Codes such as the 9-qubit Shor code [227] cannot distinguish between exchange errors and phase errors. The Ruskai code [80] exploits the permutation invariance of Dicke states to correct all one qubit errors and Pauli exchange errors. The explicit codewords for $N = 9$ are,

$$|R_0\rangle = |9/2, -9/2\rangle /2 + \sqrt{3/4}\,|9/2, 3/2\rangle\,, \tag{4.3a}$$

$$|R_1\rangle = |9/2, 9/2\rangle /2 + \sqrt{3/4}\,|9/2, -3/2\rangle\,. \tag{4.3b}$$

As a second example, we consider the Gross codes [81]. Designed such that the logical single-qubit Clifford operations are global rotations, the Gross code is immune, to first order, to errors that correspond to global rotations. As such, the code utilizes interactions that are native to many experimental platforms, and protects against the typically most deleterious sources of noise, including both T_1-type relaxation and T_2-type dephasing errors. The smallest collective spin for which this code can be constructed is $N = 13$. It utilizes the two following states $|\tilde{G}_{0,1}\rangle = c_1\,|13/2, 13/2\rangle + c_2\,|13/2, 5/2\rangle + c_3\,|13/2, -3/2\rangle + c_4\,|13/2, -11/2\rangle$, where the coefficients for $|\tilde{G}_0\rangle$ are $c_1 = \sqrt{910}/56$, $c_2 = -3\sqrt{154}/56$, $c_3 = -\sqrt{770}/56$ and $c_4 = \sqrt{70}/56$; and for $|\tilde{G}_1\rangle$ are $c_1 = \sqrt{231}/84$, $c_2 = \sqrt{1365}/84$, $c_3 = -\sqrt{273}/28$ and $c_4 = -\sqrt{3003}/84$. The explicit codewords are then,

$$|G_0\rangle = \frac{\sqrt{105}}{14}|\tilde{G}_0\rangle + \frac{\sqrt{91}}{14}|\tilde{G}_1\rangle, \tag{4.4}$$

where $|G_1\rangle$ follows from $|G_0\rangle$ by a global spin flip.

[4] The superposition of all states with only one qubit not excited $|N/2, N/2-1\rangle$ can be prepared using the same sequence by applying a global spin flip at the end of the sequence, and that optimizing for $|N/2, N/2-1\rangle$ rather than $|N/2, -N/2+1\rangle$ does not offer any potential for improvement as the initial state is an optimized CSS.

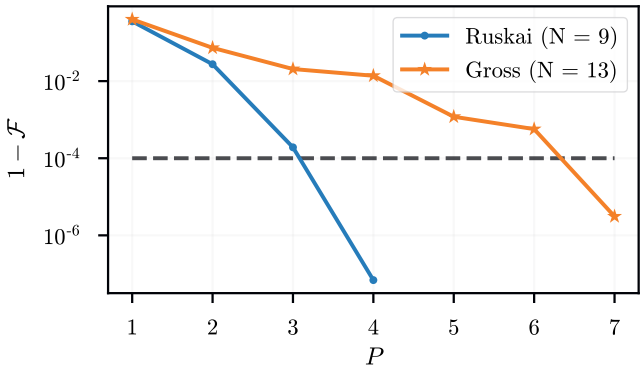


Figure 4.4: Infidelity to prepare the $N = 9$ Ruskai $|R_1\rangle$ and $N = 13$ Gross $|G_0\rangle$ codewords using the optimized gate sequence as a function of P. Despite being highly specific superpositions of Dicke states, we numerically find solutions that can prepare both target states with infidelities $1 - \mathcal{F} < 10^{-4}$ in $P = 4$ and $P = 7$ gate steps for $|R_1\rangle$ and $|G_0\rangle$, respectively.

In Fig. (4.4) we plot the infidelity of the state $|\psi_f\rangle$ prepared using the optimized gate protocol Eq. (4.2) with target states $|\psi_t\rangle = |R_1\rangle$ (blue with dots) and $|\psi_t\rangle = |G_0\rangle$ (orange with stars). We find solutions that prepare the codewords with infidelities $1 - \mathcal{F} < 10^{-4}$ in only $P = 4$ and $P = 7$ gate steps, respectively. Therefore, our protocol provides a pathway towards the implementation of large N-qubit QEC codes utilizing only global addressability of the qubits constituting the codeword.

4.5 Realization in trapped ions

As discussed in Sec. 1.4 of Ch. 1, the one-axis twisting unitary $\hat{U}_{\mathrm{OAT}}$ can be realized in trapped ions by off-resonantly driving the center of mass (COM) mode [21, 23, 144, 211, 228]. As discussed in Sec. 1.4 of Ch. 1, considering N ions in a linear Paul trap, two global beams detuned from the red and blue sidebands by δ leads to the following Hamiltonian in the interaction picture,

$$\hat{H}_I = \Omega\eta(\hat{a}_{\mathrm{com}}e^{i\delta t} + \hat{a}^\dagger e^{-i\delta t})\hat{J}_z, \tag{4.5}$$

see also Eq. (1.43). Here we assumed the Lamb-Dicke regime, and where $\hat{a}$ ($\hat{a}^\dagger$) are the annihilation (creation) operators of the COM mode, η the Lamb-Dicke parameter and Ω the Rabi frequency. Note that although we require the Lamb-Dicke regime, our protocol is otherwise insensitive to temperature and therefore does not require ground state cooling [144, 229]. Evolving for time $t_f = 2\pi/\delta$ results in a closed loop in phase space such that the motion decouples from the

spin degree of freedom. The effective evolution is described by one-axis twisting, $\hat{U}_{\mathrm{OAT}} = \exp\left(-i\phi\hat{J}_z^2\right)$ with $\phi = 2\pi\eta^2\Omega^2/\delta^2$ the area enclosed [139]. Our optimized solutions are typically $\phi \sim 1$. Setting $\eta\Omega = 2\pi \times 20$ kHz and $\delta = 2\pi \times 20$ kHz results in $t_{\mathrm{f}} = 50$ μs and $\phi = 2\pi$. The total protocol duration T is therefore $T = Pt_{\mathrm{f}}$, and thus for all the gate sequences we present $T \lesssim 350$ μs.

Here we study the effects of off-resonant driving and dephasing, with laser intensity fluctuations and non-global beams further analyzed in the Supplemental Material, see Sec. 4.7. Off-resonant driving of the other modes leads to non-uniform spin-dependent phases. Assuming a typical trap frequency $\omega = 2\pi \times 2$ MHz, the stretch mode, which is the leading order correction, is detuned by $(\sqrt{3}-1)\omega + \delta$. The area enclosed by the stretch mode is $\sim 10^{-2}$ times smaller than the area enclosed by the COM mode, and thus for realistic parameters unwanted off-resonant driving of the collective modes is negligible compared to the effects of dephasing, which we consider below.

We use a realistic dephasing rate $\gamma = 2\pi \times 5$ Hz. The off-diagonal coherences of the GHZ state decay as $\sim e^{-\gamma N t}$, such that the fidelity can be roughly estimated as $F \sim 1/2(1 + e^{-\gamma N t})$. We assume that the rotations are noise-free, as they can be performed fast relative to the spin squeezing. For the $N = 9$ Ruskai and $N = 13$ Gross protocols, using the $P = 4$ and $P = 7$ gate sequences respectively, assuming the ideal protocol prepares the state with perfect fidelity, we estimate noisy fidelities $\mathcal{F} \sim 97\%$ and $\mathcal{F} \sim 93\%$ respectively. Reducing the dephasing rate to $\gamma = 2\pi \times 1$Hz increases the Ruskai and Gross codeword fidelities to $\mathcal{F} \sim 99\%$ and $\mathcal{F} \sim 98\%$ respectively. Furthermore, parametric amplification can increase the squeezing amplitude achieved in a given t_{f} [230], whilst multiple Raman beatnotes can reduce off-resonant driving enabling a larger δ [231, 232]. Such techniques, when combined with achievable reductions in dephasing noise, could bring state preparation infidelities of the Gross and Ruskai codewords below QEC thresholds in the near-term.

4.6 Outlook

We showed that global variational circuits of linear depth can prepare arbitrary superpositions of Dicke states. The circuit can be easily realized across a variety of experimental platforms. Its implementation could lead to the preparation of interesting and useful entangled states, with applications in quantum metrology and quantum error correction.

Finally, we note that the set of realizable interactions depends on the experimental platform, e.g. in cavity QED experiments dispersive interactions can be used to engineer the generator $\sin(\hat{J}_z + \varphi)$ [89], whilst addressing the second red and blue sidebands in trapped ions can produce $\cosh(r\hat{J}_z) + \cos(\varphi)\sinh(r\hat{J}_z)$. These Hamiltonians can replace $\hat{U}_{\mathrm{OAT}}$; or the inclusion of more than one flavor of phase gate in the protocol could provide additional geometric control, potentially reducing the total number of gate steps required.

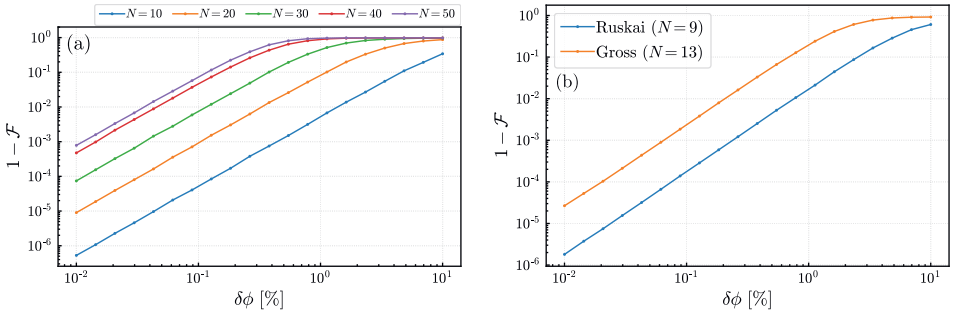


Figure 4.5: Averaged infidelity including shot-to-shot laser intensity fluctuations during the preparation of **(a)** one Haar random state and **(b)** Ruskai and Gross codewords. The scaling factor $\delta\phi$ enters the standard deviation $\delta\phi \times \phi_k$ of the Gaussian from which the noisy one-axis twisting parameter ϕ_k is sampled. The infidelity is proportional to $\delta\phi$ and N.

4

4.7 Supplemental Material

4.7.1 Errors due to laser intensity fluctuations

In this section we study the effect of laser intensity fluctuations on the protocol given in Eq. (4.2) of the main text. We focus on an implementation in trapped ions, and consider worst-case shot-to-shot noise. We assume that the noise is proportional to the one-axis twisting duration, and simulate the noise by multiplying each one-axis twisting parameter ϕ_k by a fluctuation randomly sampled from a Gaussian distribution with standard deviation $\delta\phi \times \phi_k$, where $\delta\phi$ is a scaling factor [1]. We obtain an average infidelity by averaging the noisy protocol infidelity over 200 realizations of the random Gaussian sampling. In Fig. 4.5 we plot the resulting averaged infidelity as a function of $\delta\phi$ for (a) one Haar random state for various values of N, and (b) the $N = 9$ Ruskai and $N = 13$ Gross codewords. For the sake of demonstration, the Haar random state is chosen from the $N_{\text{Haar}} = 200$ random states that were generated for Fig. 4.2 of the main text by choosing the state whose protocol parameters had the smallest total one-axis twisting amplitude, i.e. the smallest $\Phi = \sum_i |\phi_i|$. As expected, as both N and $\delta\phi$ increase the infidelity increases until saturation $1 - \mathcal{F} = 1$ at large $\delta\phi$. We note that the infidelity of both codewords remains low, $1 - \mathcal{F} \lesssim 2 \times 10^{-4}$ and $1 - \mathcal{F} \lesssim 2 \times 10^{-3}$ for Ruskai and Gross respectively, even up to fluctuations as large as $\delta\phi = 0.1\%$.

4.7.2 Errors due to non-global Mølmer-Sørensen gate

In this section we consider the effect of non-global one-axis twisting. As discussed in Eq. (4.5) of the main text, in trapped ions one-axis twisting is realized with a Mølmer-Sørensen interaction. If the laser intensity of the Raman beam is nonuni-

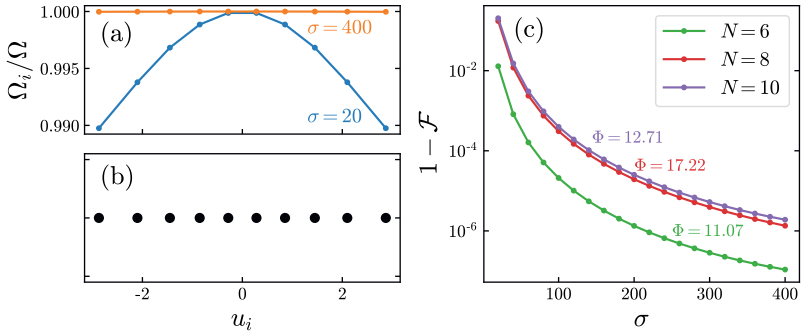


Figure 4.6: **(a)** Gaussian distribution of standard deviation σ for Ω_i, with the dots showing the value for Ω_i sampled at the dimensionless positions of the ions u_i for $N = 10$. **(b)** Equilibrium positions for a $N = 10$ ion chain. **(c)** Infidelity vs Gaussian standard deviation σ. The infidelity increases with increasing N and increasing total one-axis twisting amplitude Φ.

form, the Rabi frequency Ω becomes site-dependent, so that the interaction Hamiltonian Eq. (4.5) becomes,

$$\hat{H}'_I(\Omega_i) = \eta(\hat{a}e^{-i\delta t} + \hat{a}^\dagger e^{i\delta t}) \sum_i \frac{\Omega_i \hat{\sigma}_i^z}{2}, \tag{4.6}$$

see also Sec. 1.4 of Ch. 1. We simulate the effect of a non-uniform Raman beam by drawing Ω_i from a Gaussian function of standard deviation σ at x-values corresponding to the dimensionless positions of the ions $u_i = x_i/\ell$ as discussed in Sec. 1.2 of Ch. 1 and shown here in Fig. 4.6(a)-(b). We fix $\eta = 1$, $\Omega = 2\pi \times 20$ kHZ and vary the detuning δ so as to realize the desired one-axis twisting angle ϕ according to $\phi = 2\pi\eta^2\Omega^2/\delta^2$. In panel (c) we plot the resulting infidelity as a function of σ for the preparation of the middle Dicke state $|J = N/2, 0\rangle$ for $N = 6$, $N = 8$ and $N = 10$. As expected the infidelity increases with increasing N, as seen in the order of magnitude increase in infidelity when going from $N = 6$ to $N = 10$ for a given standard deviation value σ. The infidelity also increases with the total one-axis twisting duration $\Phi = \sum_i \phi_i$, as seen in the similarities between the $N = 8$ and $N = 10$ curve, which have $\Phi = 17.22$ and $\Phi = 12.71$, respectively. Thus, finding optimal parameters that minimize the total one-axis twisting duration is crucial for minimizing the effect of non-global one-axis twisting.

4.7.3 Hybrid quantum-classical algorithm

In this section we provide details on how the variational circuit of Eq. (4.2) of the main text can be implemented as a hybrid quantum-classical algorithm [216, 217, 219, 233, 234]. Specifically we consider how the cost function (infidelity) can be efficiently measured on a quantum device and then fed to the classical optimizer.

The advantage of this approach is that the optimization is noise-aware, potentially enabling the mitigation of certain types of noise. For example, a naive strategy to minimize the effect of dephasing on the fidelity is to minimize the total one-axis twisting duration. The hybrid quantum-classical approach natively incorporates the effect of dephasing into the cost function by evaluating the infidelity on-device, such that the classical optimization algorithm can balance finding the (noiseless) ideal parameters with minimizing the total one-axis twisting gate time.

For the following, we assume that although the experimenter only has global control over the qubits, they have individual qubit readout, as is often the case in platforms such as trapped ions. Then, permutationally invariant (PI) tomography can be used to compute the fidelity of the prepared state with respect to the target state using $\mathcal{O}(N^2)$ global measurement settings, where a global measurement setting is defined as a choice of single-qubit observable $\hat{A}_j = a_{j,x}\hat{\sigma}_x + a_{j,y}\hat{\sigma}_y + a_{j,z}\hat{\sigma}_z$ measured simultaneously (globally) on all N qubits, i.e. $\hat{A}_j^{\otimes N}$. Below we briefly review PI quantum tomography following Ref. [235].

Firstly, the PI density matrix is defined as,

$$\rho_{\mathrm{PI}} = \frac{1}{N!}\sum_k \hat{\Pi}_k \rho \hat{\Pi}_k, \tag{4.7}$$

where $\hat{\Pi}_k$ is the qubit permutation operator and ρ the density matrix. A symmetric state ρ is invariant under the action of $\hat{\Pi}_k$ and thus $\rho = \rho_{\mathrm{PI}}$. To obtain ρ_{PI} from experimentally accessible measurements, note that ρ_{PI} can be written as a linear combination of $\mathcal{D}_N = \binom{N+2}{N} = \frac{1}{2}(N^2+3N+2)$ operators of the form $(\hat{\sigma}_x^{\otimes k}\hat{\sigma}_y^{\otimes l}\hat{\sigma}_z^{\otimes m}\mathbb{1}^{\otimes n})_{\mathrm{PI}}$, where $k+l+m+n = N$ and where the $(\cdot)_{\mathrm{PI}}$ notation indicates an operator of the form of Eq. (4.7). To avoid measuring $(\hat{\sigma}_x^{\otimes k}\hat{\sigma}_y^{\otimes l}\hat{\sigma}_z^{\otimes m}\mathbb{1}^{\otimes n})_{\mathrm{PI}}$ directly which would require single-qubit control, note the decomposition [235],

$$\langle(\hat{\sigma}_x^{\otimes k}\hat{\sigma}_y^{\otimes l}\hat{\sigma}_z^{\otimes m}\mathbb{1}^{\otimes n})_{\mathrm{PI}}\rangle = \sum_j^{\mathcal{D}_N} c_j^{(k,l,m)} \langle(\hat{A}_j^{\otimes(N-n)} \otimes \mathbb{1}^{\otimes n})_{\mathrm{PI}}\rangle, \tag{4.8}$$

where $c_j^{(k,l,m)}$ are real coefficients and $\hat{A}_j^{\otimes(N-n)}$ the j-th measurement setting acting on $(N-n)$ qubits. The choice of coefficients $c_j^{(k,l,m)}$ and measurement settings $\hat{A}_j$ is not arbitrary. The optimal choices can be found using numerical optimization techniques as detailed in Ref. [235].

Next, observe that the choice of measurement setting $\hat{A}_j$ appearing in the RHS of Eq. (4.8) is independent of k, l and m. For a given j, all of the expectation values $\langle(\hat{A}_j^{\otimes(N-n)} \otimes \mathbb{1}^{\otimes n})_{\mathrm{PI}}\rangle$ for $0 \leq n \leq N$ can be reconstructed in post-processing from the coincidence counts of the global measurement setting $\hat{A}_j^{\otimes N}$. The quantities to be measured appearing on the right-hand side are therefore entirely independent of the coefficients k, l, m and n appearing on the left-hand side.

As such, for all values of k, l, m and n, $\langle(\hat{\sigma}_x^{\otimes k}\hat{\sigma}_y^{\otimes l}\hat{\sigma}_z^{\otimes m}\mathbb{1}^{\otimes n})_{\mathrm{PI}}\rangle$ can be reconstructed from the coincidence counts of an optimized set of $\mathcal{D}_N$ global measure-

ment settings $\{\hat{A}_j^{\otimes N}\}_{j=1}^{\mathcal{D}_N}$ with optimized coefficients $c_j^{(k,l,m)}$. Therefore, ρ_{PI} can be obtained using $\mathcal{D}_N$ global measurement settings.

Finally, we note that in the case of leakage from the PI density matrix, i.e. due to any non-global operations or decoherence sources, the fidelity between the target PI state ρ_{PI} and the experimentally prepared state ρ can be efficiently lower bounded [235].

4.7.4 Fidelity proxy

Although the number of measurement settings required to perform PI tomography scales efficiently (quadratically) with N, here we discuss how under certain assumptions, a proxy for the fidelity cost function can be obtained using only a single measurement setting. Firstly, we assume that the target state $|\psi_t\rangle$ can be written in the $J = N/2$ Dicke state basis with real coefficients,

$$|\psi_t\rangle = \sum_{i=-J}^{J} b_i \,|J,i\rangle\,, \qquad b_i \in \mathbb{R}. \tag{4.9}$$

Many states of interest are of the form of Eq. (4.9), including any single Dicke state and both Gross and Ruskai codewords [80, 81]. For a given Dicke state $|J,m\rangle$ we denote its corresponding density matrix $\rho_{J,m} = |J,m\rangle\langle J,m|$, which has a one at position $(m+N/2+1, m+N/2+1)$ and zeros elsewhere.

Next, for an experimentally prepared state ρ_{exp} and a target state $\rho_t = |\psi_t\rangle\langle\psi_t|$, we define,

$$\mathbb{F}(\rho_{\mathrm{exp}}, \rho_t) = \sum_{i=-J}^{J} \mathrm{Tr}\{\rho_{\mathrm{exp}}\rho_{J,i}\}\,\mathrm{Tr}\{\rho_t\rho_{J,i}\}, \tag{4.10}$$

as a proxy for the fidelity. In words, $\mathbb{F}$ measures the inner product between objects $(\mathrm{Tr}\{\rho_{\mathrm{exp}}\rho_{J,i=-J}\},\ldots,\mathrm{Tr}\{\rho_{\mathrm{exp}}\rho_{J,i=J}\})$ and $(\mathrm{Tr}\{\rho_t\rho_{J,i=-J}\},\ldots,\mathrm{Tr}\{\rho_t\rho_{J,i=J}\})$, which correspond to the decomposition of ρ_{exp} and ρ_t on the Dicke state basis. Although $\mathbb{F}$ does not provide any information about the overall coherence of the quantum state, it does give information about our ability to coherently prepare a specific Dicke state $|J,i\rangle$ (which in the computational basis can be highly entangled) with target population $|b_i|^2$. Using the fact that $\rho_{J,m}$ can be written as a sum over powers of $\hat{J}_z$ as $\rho_{J,m} = \sum_{i=0}^{N} c_{i,m}\hat{J}_z^i$ for coefficients $c_{i,m} \in \mathbb{R}$ (for proof see below), the fidelities of ρ_{exp} with respect to each $\rho_{J,m}$ can be written as,

$$\mathrm{Tr}\{\rho_{\mathrm{exp}}\rho_{J,m}\} = \sum_{i=0}^{N} c_{i,m}\,\mathrm{Tr}\Big\{\hat{J}_z^i\rho_{\mathrm{exp}}\Big\}. \tag{4.11}$$

The expectation values $\mathrm{Tr}\Big\{\hat{J}_z^i\rho_{\mathrm{exp}}\Big\}$ can in turn be decomposed using [236],

$$\hat{J}_\alpha^n = \sum_{i=0}^{n} d_{i,\alpha} \sum_k \Big[\hat{\Pi}_k\hat{\sigma}_\alpha^{\otimes i} \otimes \mathbb{1}^{\otimes(N-i)}\hat{\Pi}_k\Big]\,, \qquad \alpha \in \{x,y,z\}, \tag{4.12}$$

where the summation over k is over all permutations of the qubit ordering, and where the coefficients $d_{i,\alpha}$ are defined by the expansion. For example, for $\alpha = x, n = 3$ we have $d_{0,1,2,3,\alpha} = 0, 7/8, 0, 6/8$ because $\hat{J}_x^3 = \frac{1}{8}(\hat{\sigma}_x^{(1)} + \hat{\sigma}_x^{(2)} + \hat{\sigma}_x^{(3)})^3 = \frac{6}{8}\hat{\sigma}_x^{(1)}\hat{\sigma}_x^{(2)}\hat{\sigma}_x^{(3)} + \frac{7}{8}(\hat{\sigma}_x^{(1)} + \hat{\sigma}_x^{(2)} + \hat{\sigma}_x^{(3)})$ where $\hat{\sigma}_x^{(i)}$ acts on the ith qubit.

The RHS of Eq. (4.12) can always be reconstructed from the coincidence counts of a single measurement setting $\hat{\sigma}_z^{\otimes N}$. Thus the populations $\mathrm{Tr}\{\rho_{\mathrm{exp}}\rho_{J,m}\}$ for all $m \in \{-J, \ldots, J\}$, and therefore fidelity proxy $\mathbb{F}$ of Eq. (4.10) can be obtained from a single measurement setting $\hat{\sigma}_z^{\otimes N}$.

A limitation of $\mathbb{F}$ is that, although it provides information about our ability to coherently prepare the state $|J, i\rangle$ with weight $|b_i|^2$, it does not give any information about the coherence of the overall superposition. For example, perhaps instead of preparing the coherent superposition $|\psi\rangle = 1/\sqrt{|b_k|^2 + |b_l|^2}(b_k\,|J, k\rangle + b_l\,|J, l\rangle)$, we prepared the mixed state $\rho = |b_k|^2\,|J, k\rangle\langle J, k| + |b_l|^2\,|J, l\rangle\langle J, l|$. One straightforward strategy to mitigate this is to use $\mathbb{F}$ during an initial optimization step before switching to full PI tomography, or to use full PI tomography as a verification of the parameters optimized using $\mathbb{F}$.

Proof that $\rho_{J,m} = \sum_{i=0}^{N} c_{i,m}\hat{J}_z^i$. First, note that in the basis of the Dicke states $\{|J = N/2, i = -J \ldots J\rangle\}$, $\rho_{J,m}$ is always a diagonal matrix with a one at position $(m + N/2 + 1, m + N/2 + 1)$. Because $\hat{J}_z$ is diagonal, $\mathrm{diag}(\hat{J}_z) = [-N/2, -N/2 + 1, \ldots, N/2 - 1, N/2]$ and its powers are simply $\mathrm{diag}(\hat{J}_z^i) = [(-N/2)^i, (-N/2 + 1)^i, \ldots, (N/2 - 1)^i, (N/2)^i]$, with every $\hat{J}_z^i$ for $0 \leq i \leq N$ linearly independent. The equation $\rho_{J,m} = \sum_{i=0}^{N} c_{i,m}\hat{J}_z^i$ can be vectorized into a set of $N + 1$ linear equations with $N + 1$ variables by defining $x = \{c_{i,m}\}_{i=0}^{N}$, $b = \mathrm{diag}(\rho_{J,m})$ and the $(N + 1) \times (N + 1)$ coefficient matrix $A = \{\mathrm{diag}(\hat{J}_z^i)\}_{i=0}^{N}$, such that the equation reduces to standard form $Ax = b$. Because the columns of A are each from a given $\hat{J}_z^i$ for $0 \leq i \leq N$, all columns are linearly independent. Thus A is invertible, yielding the unique solution $x = A^{-1}b$.

Part II

Classical simulation of quantum dynamics

Chapter 5

Theoretical background

> Truth is much too complicated to
> allow anything but approximations.
>
> John von Neumann (1947)

In this chapter we set the stage for Part Two of this Thesis. We begin by reviewing the time-dependent variational principle and the formalism of bosonic Gaussian states. We then introduce the non-Gaussian state ansatz that forms the basis of Ch. 6 and Ch. 7. Finally, we discuss the study of open quantum systems, including the quantum trajectories unraveling method.

5.1 Time-dependent variational principle

Consider a closed quantum system evolving under a Hamiltonian $\hat{H}(t)$. The state of the system at time t, $|\Psi(t)\rangle$, is determined from the initial state, $|\Psi(0)\rangle$, by the Schrödinger equation,

$$\frac{d\,|\Psi(t)\rangle}{dt} = -i\hat{H}(t)\,|\Psi(t)\rangle\,. \tag{5.1}$$

As discussed in the Introduction, finding *exact* analytical or classical numerical solutions to the Schrödinger equation for many-body quantum systems is typically challenging. However, there are regimes where further analytic or efficient classical numerical treatments are possible. For example, weak interactions which allow for perturbative treatments [41], bounded entanglement which allows for density matrix renormalization group and tensor network methods [237, 238], or wavefunction structure which allows for variational methods [108, 109, 239, 240].

In this thesis, we focus on variational methods. In particular, variational methods that allow for efficient classical numerical simulation of a quantum system's dynamics. We briefly note one other prominent class of variational methods, namely *variational quantum algorithms* (VQA) [241], in which classical numerics are used to optimize the variational parameters of a parametrized quantum circuit. Examples of such algorithms include the variational quantum eigensolver (VQE) [234]

and the quantum approximate optimization algorithm (QAOA) [242]. We used a VQA in Ch. 4, in which we classically optimized the parameters of a variational quantum circuit for efficient preparation of arbitrary symmetric spin states.

The crucial starting point of any variational method is the choice of *variational ansatz*. For efficient classical simulation of real-time dynamics, one chooses a variational quantum state, $|\psi[\boldsymbol{z}(t)]\rangle$, to stand in for the true quantum state, $|\Psi(t)\rangle$. Here, $\boldsymbol{z}(t) \in \mathbb{R}^M$ is a vector of M time-dependent real numbers that parameterizes the ansatz. We drop the t dependence of $\boldsymbol{z}(t)$ for notational simplicity. Choosing a variational ansatz typically requires balancing the *expressiveness* of the ansatz, so that the physical features of interest can be captured up to a desired accuracy, with the *simplicity* of the ansatz, so that the description is efficient.

Substituting the variational state into the Schrödinger equation yields a dynamical equation for the variational parameters,

$$\sum_{\mu} \dot{z}_\mu \, |v_\mu(\boldsymbol{z})\rangle = -i\hat{H}(t) \, |\psi(\boldsymbol{z})\rangle \,, \tag{5.2}$$

where we introduced the *tangent vectors*,

$$|v_\mu(\boldsymbol{z})\rangle = \frac{\partial \, |\psi(\boldsymbol{z})\rangle}{\partial z_\mu}. \tag{5.3}$$

The set of all tangent vectors defines the *tangent space* $\mathcal{T}_\psi$, which is a Hilbert subspace that specifies the allowed directions along which the variational state may evolve. Although the left-hand side of Eq. (5.2) necessarily lies in the tangent space, there is no guarantee that the right-hand side does. This is rectified by employing the *Lagrangian*, *Dirac-Frenkel* or *McLachlan* variational principle [109, 239]. We choose the Dirac-Frenkel variational principle, which directly projects Eq. (5.2) back to the tangent space using the projection operator,

$$\hat{P}_v = \sum_{\mu} |v_\mu(\boldsymbol{z})\rangle \, \langle v_\mu(\boldsymbol{z})| \,, \tag{5.4}$$

as sketched in Fig. 5.1. Applying $\hat{P}_v$ to Eq. (5.2), we obtain a system of coupled first-order differential equations for the variational parameters [239],

$$\dot{z}_\nu = -(\omega_{\mu\nu})^{-1} \frac{\partial E(\boldsymbol{z}, t)}{\partial z_\mu}, \tag{5.5}$$

where $E(\boldsymbol{z}, t) = \langle \psi(\boldsymbol{z})| \, \hat{H}(t) \, |\psi(\boldsymbol{z})\rangle$ is the energy and $\omega_{\mu\nu} = 2 \operatorname{Im} \langle v_\mu | v_\nu \rangle$ is the *symplectic form*. Solving Eq. (5.5) is equivalent to *locally* minimizing at each time step the Hilbert space distance between the variational ansatz and the true quantum state [240].

In addition to real-time dynamics, we can describe *imaginary-time dynamics* by making the replacement $it \to \tau$. This is useful for studying ground-state physics because in the infinite-time limit $\tau \to \infty$, provided that all eigenvalues are positive,

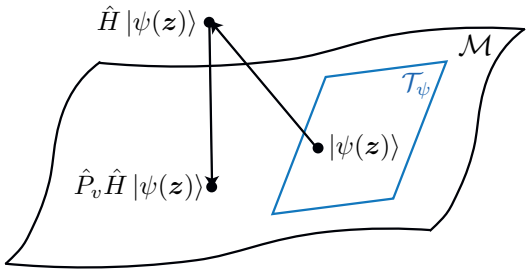


Figure 5.1: Time-dependent variational principle. The variational ansatz $|\psi(\boldsymbol{z})\rangle$ lives in a variational manifold $\mathcal{M}$. The tangent space $\mathcal{T}_\psi$ is spanned by the set of tangent vectors $|v_\mu\rangle$. The right-hand side of the Schödinger equation, $\hat{H}(t)\,|\psi(\boldsymbol{z})\rangle$, may lie outside of the tangent space. The Dirac-Frenkel variational principle projects the state back to the tangent space using the projection operator $\hat{P}_v$ of Eq. (5.4).

exact imaginary-time evolution will converge to the ground state. In this case the variational parameters evolve according to [239],

$$\dot{z}_\nu = -(g_{\mu\nu})^{-1}\frac{\partial E(\boldsymbol{z},t)}{\partial z_\mu}, \tag{5.6}$$

where $g_{\mu\nu} = 2\,\mathrm{Re}\,\langle v_\mu|v_\nu\rangle$ is the *metric* of the tangent space. Note that although non-exact imaginary-time evolution may become trapped in local minima and therefore fail to converge to the ground state, if the ansatz is sufficiently descriptive this is typically less likely to occur for imaginary-time evolution than for other methods, such as gradient descent methods [243].

Finally, we note that for real variational parameters $\boldsymbol{z} \in \mathbb{R}^M$, the tangent space $\mathcal{T}_\psi$ is a real vector space embedded in a complex Hilbert space. As such, for each $|v_\mu\rangle$ there is no guarantee that $i\,|v_\mu\rangle$ also lies in $\mathcal{T}_\psi$. We can project $i\,|v\rangle_\mu$ back to $\mathcal{T}_\psi$ using [109],

$$\hat{P}_\psi i\,|v_\nu\rangle = 2\,|v_\mu\rangle\,G^{\mu\sigma}\mathrm{Re}\,\langle v_\sigma|\,i\,|v_\nu\rangle = J^\mu{}_\nu\,|v_\mu\rangle\,, \tag{5.7}$$

where $J^\mu{}_\nu = -G^{\mu\sigma}\omega_{\sigma\nu}$ is the *complex structure*. If $\boldsymbol{J}^2 \neq -\mathbb{1}$ the projection is non-trivial, and $i\,|v_\mu\rangle$ does not lie in the tangent space. On the other hand, if $\boldsymbol{J}^2 = -1$ on every tangent space, the tangent space is called a *Kähler space*, and $i\,|v_\nu\rangle = J^\mu{}_\nu\,|v_\mu\rangle$. For Kähler spaces the three variational principles (Lagrangian, McLachlan and Dirac-Frenkel) coincide, and incorrect couplings in the equations of motion are avoided [109]. The ansatzes considered in this thesis satisfy this property, as we prove later in Ch. 7.

5.2 Bosonic Gaussian states

The paradigmatic choice of variational ansatz is the *Gaussian state*. Our review of Gaussian states mainly follows Ref. [244]. Consider a system of N_b bosonic modes. The canonical position and momentum operators are, in vectorized notation,

$$\hat{\boldsymbol{r}} = (\hat{x}_1, \ldots, \hat{x}_{N_b}, \hat{p}_1, \ldots, \hat{p}_{N_b})^T. \tag{5.8}$$

For this choice of ordering, the canonical commutation relations are,

$$[\hat{r}_i, \hat{r}_j] = i\Omega_{ij}, \tag{5.9}$$

where Ω_{ij} is a symplectic block-diagonal matrix,

$$\boldsymbol{\Omega} = \begin{pmatrix} 0 & \mathbb{1}_{N_b} \\ -\mathbb{1}_{N_b} & 0 \end{pmatrix}. \tag{5.10}$$

For a pure bosonic quantum state $|\Psi\rangle$, the *s-ordered characteristic function* is defined as $\chi^s(\boldsymbol{\kappa}) = \langle\Psi|\, \hat{D}_W(\boldsymbol{\kappa})\, |\Psi\rangle\, e^{s||\kappa||^2/2}$. Here, $\boldsymbol{\kappa} \in \mathbb{R}^{2N_b}$ defines a point in phase space, and the many-mode *Weyl operator* is $\hat{D}_W(\boldsymbol{\kappa}) = \exp\big(i\hat{\boldsymbol{r}}^T\boldsymbol{\Omega}\boldsymbol{\kappa}\big)$, which generates phase-space displacements. The characteristic functions completely define phase-space *quasi-probability distributions* according to,

$$W^s(\boldsymbol{\xi}) = \frac{1}{\pi^2}\int_{\mathbb{R}^{2N}} \chi^s(\boldsymbol{\kappa}) e^{i\boldsymbol{\kappa}^T\boldsymbol{\Omega}\boldsymbol{\xi}} d^{2N}\boldsymbol{\kappa}, \tag{5.11}$$

where $\boldsymbol{\xi} \in \mathbb{R}^{2N_b}$. Quasi-probability distributions can be roughly understood as specifying the (quasi-)probability of measuring the quantum state at a given point in phase space. They can take on negative values, which are indicators of non-classicality [245]. The choices of $s = -1$, $s = 0$ and $s = 1$, are known as the *Husimi Q-Function*, the *Wigner function*, and the *P-representation*, respectively. We focus on the Wigner function, which we denote simply by $W(\boldsymbol{\xi})$.

We can now define *bosonic Gaussian states* as any quantum state whose Wigner function is Gaussian. That is, the Wigner function of a Gaussian state can always be written as,

$$W(\boldsymbol{\xi}) = \frac{1}{\pi^{N_b}} \frac{1}{\sqrt{\det(\boldsymbol{\Gamma})}} e^{-(\boldsymbol{\xi}-\boldsymbol{\Delta})^T\boldsymbol{\Gamma}^{-1}(\boldsymbol{\xi}-\boldsymbol{\Delta})}, \tag{5.12}$$

where the first-order moments $\boldsymbol{\Delta}$ are,

$$\Delta_i = \langle \hat{r}_i \rangle \tag{5.13}$$

and the second-order moments $\boldsymbol{\Gamma}$, also known as the *covariance matrix*, are,

$$\Gamma_{ij} = \langle \hat{r}_i\hat{r}_j + \hat{r}_j\hat{r}_i \rangle - 2\Delta_i\Delta_j. \tag{5.14}$$

Because a Gaussian state's Wigner function can always be written in the form of Eq. (5.12), Gaussian states are completely defined by their first- and second-order

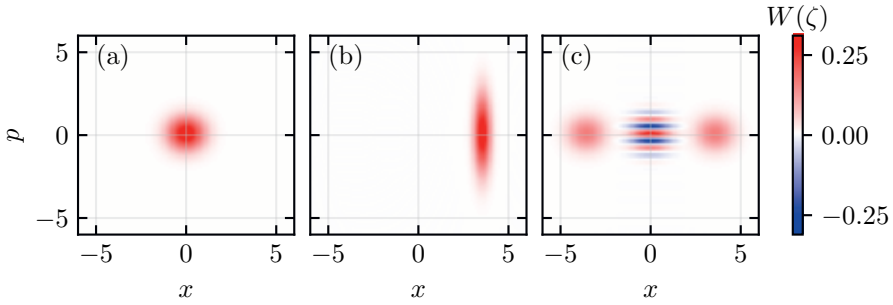


Figure 5.2: Single-mode Wigner functions. **(a)** The bosonic vacuum, $\mathbf{\Delta} = \mathbf{\Gamma} = 0$. **(b)** Squeezed-displaced state with $\mathbf{\Delta} = (\sqrt{2}\alpha, 0)^T$ and $\mathbf{\Gamma} = \mathrm{diag}(e^{-2r}, e^{2r})$ with $\alpha = 2.5$ and $r = 0.8$. **(c)** Superposition of coherent states (bosonic cat state), $|\psi_{\mathrm{cat}}\rangle \cong |\alpha\rangle + |-\alpha\rangle$ with $\alpha = 2.5$. Panels (a) and (b) are Gaussian. Although the quantum state in panel (c) is non-Gaussian, it is exactly described by a superposition of two coherent states.

5

moments [244]. In Fig. 5.2 we plot the Wigner function of two single-mode bosonic Gaussian states: the bosonic vacuum in panel (a), and a squeezed-displaced state in panel (b). Both Wigner functions resemble two-dimensional Gaussian functions in x and p, as expected. In contrast, in Fig. 5.2(c) we plot the Wigner function of a superposition of two coherent states. The is known as a *bosonic cat state*, and is clearly non-Gaussian. An important feature is the areas of Wigner negativity (blue regions), which cannot be captured by a Gaussian state ansatz because they are unique features of non-Gaussian states [245].

Gaussian states have two important properties. Firstly, they can be non-classical and many-mode entangled, as exemplified by the single-mode squeezed state and the two-mode squeezed state, respectively. Secondly, expectation values can be calculated analytically. This is because we can write the expectation value of an operator $\hat{\mathcal{O}} = f(\hat{a}_k, \hat{a}_k^\dagger)$ as,

$$\langle \hat{\mathcal{O}} \rangle = \int_{\mathbb{R}^{2N_b}} W(\boldsymbol{\kappa}) \tilde{f}(\boldsymbol{\kappa}) d^{2N_b}\boldsymbol{\kappa}, \tag{5.15}$$

where $\tilde{f}(\kappa) = f(\kappa_k + i\kappa_{k+N_b}, \kappa_k - i\kappa_{k+N_b})$ follows from the replacement $\hat{a}_k \to \kappa_k + i\kappa_{k+N_b}$ and $\hat{a}_k^\dagger \to \kappa_k - i\kappa_{k+N_b}$. Provided that $\tilde{f}$ grows at most polynomially so that the integral converges, for Wigner functions $W(\boldsymbol{\kappa})$ that are Gaussian, Eq. (5.15) can be evaluated exactly [246].

Finally, note that we introduced Gaussianity in the context of quantum states of closed bosonic systems. More broadly, there is an extensive literature studying Gaussianity, including Gaussian states of spin [46, 247], fermionic [108] and open quantum systems [248], as well Gaussian operations and processes more generally [249, 250].

5.3 Superpositions of Gaussian states

Gaussian state ansatzes are useful because they often capture essential ground state and dynamical features, while remaining amenable to exact analytical and classical numerical treatments. However, their descriptiveness is fundamentally limited. A natural question is therefore, is there a variational ansatz that is more descriptive, while still being analytically or classically numerically tractable?

One such ansatz is a *superposition of Gaussian states*, which we generically call a *non-Gaussian states* (NGS). Here, we introduce the ansatz closely following our work in Ref. [5]. For a system of N_s spins-1/2 and N_b bosonic, the ansatz is,

$$|\psi(\boldsymbol{z})\rangle = \sum_{\sigma=1}^{2^{N_s}} \sum_{p=1}^{N_p} \hat{U}_p^\sigma \, |\sigma, 0\rangle \, . \tag{5.16}$$

The sum over σ is over the 2^{N_s} spin basis states[1], while the sum over p produces for each spin degree of freedom a superposition of N_p bosonic Gaussian states, generated by the unitary $\hat{U}_p^\sigma$. This ansatz has been successfully used in the study of systems ranging from the Kondo impurity problem [252], central spin model [110], spin-Holstein models [111], Bose and Fermi polarons [112, 113, 253], and (sub/super) Ohmic spin-boson models [4]. The closely-related Davydov state ansatz has been used in the study of molecular crystals and polaritonic physics [114, 115, 118, 254–257]. Other possible choices of ansatz include superpositions of photon-added coherent states [258] or multi-configuration time-dependent Hartree ansatzes [116], as well as closely-related ansatzes based on Bogoliubov coupled-cluster theory [259].

For the unitary that generates the Gaussian state, in this thesis we choose,

$$\hat{U}_p^\sigma = e^{\kappa_p^\sigma + i\theta_p^\sigma} \hat{D}(\boldsymbol{\alpha}_p^\sigma) \hat{S}(\boldsymbol{\zeta}_p^\sigma). \tag{5.17}$$

The parameters κ and θ control the weight and relative phase of each Gaussian state. The many-mode displacement $\hat{D}(\boldsymbol{\alpha})$ and squeezing $\hat{S}(\boldsymbol{\zeta})$ operators are,

$$\hat{D}(\boldsymbol{\alpha}) = \prod_{k=1}^{N_b} \hat{D}(\alpha_k) = \prod_{k=1}^{N_b} \exp\left[\alpha_k \hat{a}_k^\dagger - \alpha_k^* \hat{a}_k\right], \tag{5.18a}$$

$$\hat{S}(\boldsymbol{\zeta}) = \prod_{k=1}^{N_b} \hat{S}(\zeta_k) = \prod_{k=1}^{N_b} \exp\left[\frac{1}{2}\left(\zeta_k^* \hat{a}_k^2 - \zeta_k \hat{a}_k^{\dagger 2}\right)\right], \tag{5.18b}$$

where we dropped the σ and p indices for simplicity, and used the convention that many-mode operators appear with bold parameters. The complex numbers α_k and

[1] The number of spin configurations in this ansatz scales exponentially with the number of spins, which prevents our ansatz from efficiently describing many-spin systems. Addressing this issue by, for example combining the non-Gaussian ansatz for the bosons with tensor-network techniques for the spins or with non-Gaussian fermionic ansatz and spin-fermion mappings such as Jordan-Wigner or Majoranization [108, 111, 251], is a matter of future work. We discuss an alternative approach, namely using the Holstein-Primakoff representation of the spins, in Ch. 7.

ζ_k, which describe the displacement and squeezing of the kth mode respectively, can be decomposed into real variational parameters as $\alpha_k = x_k + iy_k$ and $\zeta_k = r_k e^{i\phi_k}$. The total number of real variational parameters is $M = 2^{N_s} N_p(2 + 4N_b)$.

Here, we chose the Gaussian unitary to be a product of single-mode displacement and squeezing operators. This is not the most general choice for a Gaussian unitary, because it does not include a many-mode squeezing operator $e^{-i\hat{\boldsymbol{r}}^T \mathbb{M} \hat{\boldsymbol{r}}}$, where $\mathbb{M}$ is a symmetric matrix [108, 109]. We find that the inclusion of many-mode squeezing complicates all subsequent analytical manipulations, and therefore we leave its inclusion to future work.

For $N_p > 1$, the NGS ansatz can describe non-Gaussian states that Gaussian ansatz cannot. In fact, because the set of coherent states form an over-complete basis for the bosonic Hilbert space, in the limit $N_p \to \infty$, even without squeezing ($\boldsymbol{\zeta} = 0$), the ansatz approaches the true wavefunction, $|\psi(\boldsymbol{z})\rangle \to |\Psi\rangle$. Although the inclusion of squeezing is intended to enhance the descriptive power of the ansatz at finite N_p, for the matter-light type Hamiltonians that we study (e.g. Rabi [260], spin-boson [117] and Holstein-Tavis-Cummings [261] models), at fixed N_p we typically do not observe a substantial accuracy improvement when squeezing is included. This is shown in Ch. 7. A simple counter-example of a Hamiltonian for which squeezing would greatly reduce the required N_p is a squeezing Hamiltonian [134]. We refer to the displacement-only ansatz as the ***superposition of coherent state* (SCS) ansatz**.

Expectation values for the NGS ansatz can be computed exactly. Any spin-boson operator $\hat{A}$ can be written as $\hat{A} = \sum(\hat{A}_\mathrm{s} \otimes \hat{A}_\mathrm{b})$. Here, $\hat{A}_\mathrm{s}$ acts on the spin degrees of freedom, while $\hat{A}_\mathrm{b}$ acts on the bosonic degrees of freedom and can be decomposed into monomials of bosonic operators as $\hat{A}_\mathrm{b} = \bigotimes_{k=1}^{N_b} \hat{A}_\mathrm{b}^{(k)}$. For $N_s = 1$ spin (the many-spin case follows similarly), the expectation value of $\hat{A}_\mathrm{s} = \hat{\sigma}_x$ is,

$$\langle\psi|\, \hat{\sigma}_x \hat{A}_\mathrm{b} \,|\psi\rangle = \sum_{p,p'}^{N_p} \langle 0|\, \hat{U}_{p'}^{\uparrow\dagger} \hat{A}_\mathrm{b} \hat{U}_p^{\downarrow} \,|0\rangle + \mathrm{h.c.}, \tag{5.19}$$

and similarly for the other Pauli matrices. Because $\hat{U}_p^\sigma$ is a product of single-mode operators, the many-mode overlap reduces to a product of single-mode overlaps,

$$\langle 0|\, \hat{U}_{p'}^{\sigma'\dagger} \hat{A}_\mathrm{b} \hat{U}_p^\sigma \,|0\rangle = \prod_{k=1}^{N} \langle 0|\, \hat{S}^\dagger(\zeta_{k,p'}^{\sigma'}) \hat{D}^\dagger(\alpha_{k,p'}^{\sigma'}) \hat{A}_\mathrm{b}^{(k)} \hat{D}(\alpha_{k,p}^\sigma) \hat{S}(\zeta_{k,p}^\sigma) \,|0\rangle\,, \tag{5.20}$$

Provided that $\hat{A}_b^{(k)}$ can be written as a sum of polynomials of creation and annihilation operators, the single mode overlaps are evaluated using the fact that for any pure bosonic states $|\Theta\rangle$ and $|\Phi\rangle$[2],

$$\langle\Theta|\, (\hat{a}^\dagger)^m \hat{a}^n \,|\Phi\rangle_s = \left(\frac{\partial}{\partial\beta}\right)^m \left(-\frac{\partial}{\partial\beta^*}\right)^n \chi_g^s(\beta)\Big|_{\beta=0}, \tag{5.21}$$

[2] note a similar identity holds for open quantum states, obtained by using ρ and the trace.

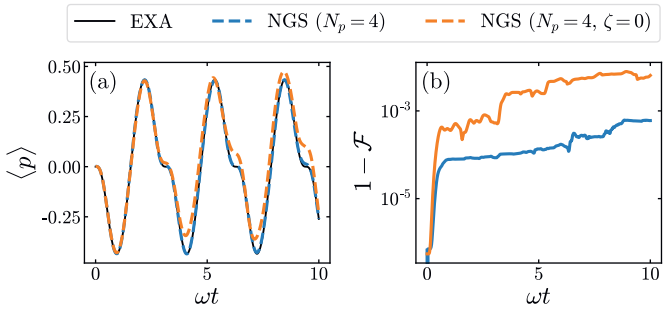


Figure 5.3: **(a)** Anharmonic oscillator dynamics calculated with the NGS ansatz of Eq. (5.16) (blue dashed) and the squeezing-free SCS ansatz (orange dashed), both with $N_p = 4$. The initial state is $|\psi(0)\rangle = \hat{D}(1)\,|0\rangle$. The full NGS ansatz is in closer agreement with exact numerics (solid black) compared to the squeezing-free SCS ansatz. **(b)** Fidelity $\mathcal{F}(t) = |\langle\Psi(t)|\psi(t)\rangle|$ with $|\Psi(t)\rangle$ the quantum state obtained from exact numerics. Both the NGS and squeezing-free SCS ansatz capture the dynamics with small infidelities $1 - \mathcal{F} < \mathcal{O}(10^{-2})$. Figure is from Ref. [5].

where $\chi_g^s(\beta) = \langle\Theta|\,\hat{D}_W(\beta)\,|\Phi\rangle\, e^{s|\beta|^2/2}$ is a generalization of the s-ordered characteristic function with $s = 1$ ($s = -1$) denoting (anti-)normal ordering of the creation and annihilation operators. Computing $\chi_g^s(\beta)$ for the single-mode overlaps of Eq. (5.20) simply requires expressions for the overlap between two single-mode Gaussian states, which are known analytically, see e.g. Ref. [262]. Therefore, expectation values for the NGS ansatz of Eq. (5.16) can be computed analytically.

In addition to expectation values, solving the equations of motion of Eq. (5.5) and Eq. (5.6) requires computing the overlap between tangent vectors, which were defined in Eq. (5.3). For the NGS ansatz the tangent vectors can be written as,

$$|v_\mu\rangle = \prod_{k'\neq k}^{N_b}\left[\hat{D}(\alpha_{k'})\hat{S}(\zeta_{k'})\right]\frac{\partial}{\partial z_{\sigma,p,k,\ell}}\left[e^{\kappa+i\theta}\hat{D}(\alpha_k)\hat{S}(\zeta_k)\right]|\sigma,0\rangle\,, \tag{5.22}$$

which only requires calculating the tangent vector of a single-mode Gaussian state, i.e. $\frac{\partial}{\partial z_{\sigma,p,k,\ell}} e^{\kappa+i\theta}\hat{D}(\alpha_k)\hat{S}(\zeta_k)\,|0\rangle$. The single-mode calculation proceeds as: (i) using the disentangled forms of the displacement and squeezing operators, we normal order $\hat{D}(\alpha_k)\hat{S}(\zeta_k)\,|0\rangle$ so that only $\hat{a}^\dagger$ operators remain. We then (ii) compute the derivative, which (iv) enables us to obtain concise analytic expressions for the tangent vectors and (v) use Eq. (5.21) to evaluate the resulting overlaps. For a full explanation of the procedure, including explicit expressions for the tangent vectors after disentangling and normal-ordering of the operators, see our work in Ref. [5].

Example: Quantum anharmonic oscillator As an example of the NGS and TDVP machinery and to illustrate the role of squeezing in the ansatz, in Fig. 5.3 we consider the dynamics of a simple anharmonic oscillator, $\hat{H} = \omega\hat{a}^\dagger\hat{a} + \mu(\hat{a}^\dagger\hat{a})^2$

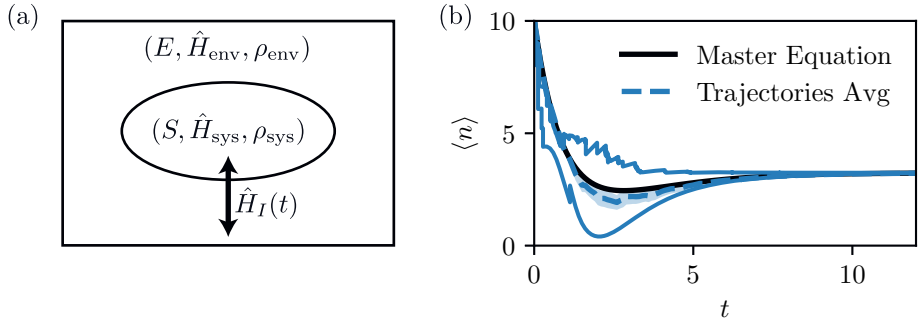


Figure 5.4: Open quantum systems. **(a)** Schematic of an open quantum system, adapted from Ref. [267]. A system S in a mixed quantum state ρ_{sys} evolves under the Hamiltonian $\hat{H}_{\text{sys}}$. It interacts with an environment E in ρ_{env} and evolving under $\hat{H}_{\text{env}}$. Interactions between S and E are described by $\hat{H}_{\text{int}}(t)$. **(b)** Numerical simulation of a pumped cavity, $\hat{H} = \eta(\hat{a} + \hat{a}^\dagger)$ with jump operator $\hat{c} = \sqrt{\kappa}\hat{a}$. Adapted from Ref. [185]. We set $\eta = 0.9$ and $\kappa = 1$. Simulations are performed with the Markovian master equation (black line), and an average over $n_{\text{traj}} = 20$ quantum trajectories (dashed blue line), with standard error shown by the shaded region. In the two example individual quantum trajectories (solid blue lines) we observe segments of smooth, continuous non-Hermitian evolution interrupted by discrete quantum jump events.

in the strong coupling regime, $\omega = \mu = 1$ [263–266]. The NGS ansatz uses $N_p = 4$ coherent states. We observe that the ansatz containing squeezing (dashed blue line) is in better agreement with the true state $|\Psi\rangle$ (solid black line, obtained from exact numerical solution of the Schrödinger equation) than the squeezing-free ansatz (dashed orange line). However, both the NGS and SCS ansatz (orange dashed line) capture the dynamics with small infidelities, $1 - \mathcal{F} < \mathcal{O}(10^{-2})$.

5.4 Open quantum systems

Next, to set the stage for Ch. 7 where we study open dynamics with the NGS ansatz, here we review the study of open quantum systems. Our review closely follow Ref. [267]. Consider a quantum system S and an *environment* E, as shown in Fig. 5.4(a). We assume that the Hamiltonian of the total system can be written as,

$$\hat{H}_{\text{tot}}(t) = \hat{H}_{\text{sys}} \otimes \mathbb{1}_{\text{env}} + \mathbb{1}_{\text{sys}} \otimes \hat{H}_{\text{env}} + \hat{H}_I(t), \tag{5.23}$$

where $\hat{H}_{\text{sys}}$ is the Hamiltonian for S, $\hat{H}_{\text{env}}$ the Hamiltonian for E, and $\hat{H}_I(t)$ the Hamiltonian that describes interactions between S and E. The system is distinguished from the environment by the fact that all observables of interest act on S, i.e. all operators are of the form $\hat{O}_{\text{sys}} \otimes \mathbb{1}_{\text{env}}$. Assume that the initial state of the

total system at time t_0 is in a mixed state,

$$\rho(t_0) = \sum_\alpha w_\alpha \left|\psi_\alpha(t_0)\right\rangle\!\left\langle\psi_\alpha(t_0)\right|, \tag{5.24}$$

with positive weights w_α and normalized pure quantum states $|\psi_\alpha(t_0)\rangle$. In the interaction picture with respect to $\hat{H}_{\text{sys}}$ and $\hat{H}_{\text{env}}$, the density matrix evolves according to the von Neumann equation,

$$\dot{\rho}(t) = -i[\hat{H}_I(t), \rho(t)]. \tag{5.25}$$

We are interested in the system, which is described by the reduced density matrix, $\rho_{\text{sys}} = \text{Tr}_{\text{env}}(\rho)$. Here, Tr_{env} denotes the partial trace over the environment's degrees of freedom. The evolution of the system is therefore described by,

$$\dot{\rho}_{\text{sys}}(t) = -i\,\text{Tr}_{\text{env}}[\hat{H}_I(t), \rho(t)]. \tag{5.26}$$

5

5.4.1 Markovian master equation

Solving the above exact dynamical equations is often challenging. For example, typically the environment is not controllable, nor is a precise microscopic description possible. Furthermore, if the environment is modeled as a continuum with an infinite number of degrees of freedom, as in for example a single spin coupled to a continuum of modes [117], then obtaining exact dynamics requires solving an infinite hierarchy of equations of motion. Instead, we can make three key assumptions:

1. *Born approximation*: the coupling between the system and the environment is weak, so system-environment correlations are negligible. As such, at all times the state of total system is well-approximated by $\rho(t) \approx \rho_{\text{sys}}(t) \otimes \rho_{\text{env}}$.

2. *Markov approximation*: the environment has no long-term memory of interactions with the system. Specifically, in the interaction picture writing $\hat{H}_I(t) = \sum_\alpha \hat{A}_\alpha(t) \otimes \hat{B}_\alpha(t)$ where $\hat{A}_\alpha$ ($\hat{B}_\alpha$) acts on the system (environment), the approximation is that the two-time environment correlation functions are homogeneous in time, $\text{tr}(\hat{B}_\alpha(t)\hat{B}_\beta(t')\rho) = C(t,t') = C(t-t')$ and decay on a timescale τ_E that is much shorter than the system's relaxation time, τ_S. That is, $\tau_E \ll \tau_S$. This makes the Master equation time-local.

3. *Rotating-wave (secular) approximation*: fast-rotating terms average out and may be neglected. For a system with a discrete, non-degenerate spectrum that can be diagonalized as $\hat{H}_{\text{sys}}\left|\epsilon\right\rangle = \epsilon\left|\epsilon\right\rangle$, each system operator can be written as $\hat{A}_\alpha = \sum_\omega \hat{A}_\alpha(\omega)$. Here $\hat{A}_\alpha(\omega) = \sum_{\epsilon'-\epsilon=\omega} \hat{\Pi}(\epsilon)\hat{A}_\alpha\hat{\Pi}(\epsilon')$, with $\hat{\Pi}(\epsilon) = \left|\epsilon\right\rangle\!\left\langle\epsilon\right|$ and the summation over all eigenenergy differences $\epsilon' - \epsilon$ equaling ω. The approximation is that in the interaction picture, $e^{i(\omega-\omega')t}$ terms oscillate rapidly when $\omega' \neq \omega$ compared to when $\omega' = \omega$, and therefore average to zero and may be neglected.

After making these assumptions and returning to the Schrödinger picture, Eq. (5.25) reduces to a Markovian *master equation* in *Lindblad form* [267–269],

$$\dot{\rho}_{\text{sys}} = -i[\hat{H}_{\text{sys}} + \hat{H}_{\text{LS}}, \rho_{\text{sys}}] + \sum_m \hat{c}_m \rho_{\text{sys}} \hat{c}_m^\dagger - \frac{1}{2}\left\{\hat{c}_m^\dagger \hat{c}_m, \rho_{\text{sys}}\right\}, \tag{5.27}$$

where $\hat{H}_{\text{LS}}$ is known as the *Lamb shift* Hamiltonian that leads to renormalization of the system's eigenenergies due to the system-environment interactions, and which is often neglected. The operators $\hat{c}_m$ are *Lindblad operators*, also known as *jump operators*, which act on the system to describe dissipative dynamics.

5.4.2 Quantum trajectories

Although the Markovian master equation of Eq. (5.27) is often more tractable than the exact von Neumann equation of Eq. (5.25), it still requires evolving a density matrix. For a system of N_s spins-1/2 and N_b bosonic modes each with a Fock space cutoff of $n_{\max}$, this requires evolving square matrices of width $2^{N_s}(n_{\max})^{N_b}$. An alternative approach is to use the *quantum trajectories* method [270–274], in which a pure quantum state $|\psi\rangle$ evolves *stochastically*. This only requires propagating a vector of $2^{N_s}(n_{\max})^{N_b}$ elements. The method consists of two types of evolution:

1. Continuous evolution with the Schrödinger equation under an effective *non-Hermitian* Hamiltonian,

$$\hat{H}_{\text{eff}} = \hat{H} - \frac{i}{2}\sum_m \hat{c}_m^\dagger \hat{c}_m = \hat{H} - i\hat{K}. \tag{5.28}$$

2. Interruptions to the continuous evolution by discrete, instantaneous evolution events, where the jump operator $\hat{c}_m$ acts on the time-evolved wavefunction as $|\psi(t)\rangle \to \hat{c}_m |\psi(t)\rangle$.

The continuous evolution is interrupted once the square of the wavefunction norm decays below a uniform random number $0 \leq \epsilon \leq 1$, i.e. once $|\psi(t)|^2 < \epsilon$. For multiple jump operators, the mth operator $\hat{c}_m$ is chosen with probability proportional to $\langle\psi(t)|\,\hat{c}_m^\dagger \hat{c}_m\,|\psi(t)\rangle$. After a jump event, the quantum state is renormalized, a new random number is drawn, and the procedure continues until the final time is reached. The evolution of a quantum state during a single (stochastic) evolution from the initial to final time is called a *quantum trajectory*. To recover the same observables that one would obtain from the master equation, observables are computed for each trajectory and averaged over n_{traj} trajectories.

When observables of interest can be obtained with sufficient accuracy using fewer trajectories than the size of the Hilbert space, quantum trajectories can be more efficient than solving the master equation [271, 273, 275]. In the context of the non-Gaussian ansatz of Eq. (5.16), quantum trajectories has the additional benefit of allowing the direct use of the non-Gaussian state ansatz, along with all of the previously-developed machinery for real- and imaginary-time dynamics,

to study open quantum dynamics. We use this framework in Ch. 7. Finally, we briefly note that quantum trajectories can also be combined with other approximate numerical methods such as the time-dependent Gutzwiller ansatz [276, 277], tensor networks [278, 279] and the truncated Wigner approximation [280].

Chapter 6

Fast quantum state preparation and bath dynamics

Based on
Phys. Rev. Lett. **132**, 170401, (2024) [4]

> Great things are done by a series
> of small things brought together.
>
> Vincent Van Gogh

In this chapter we demonstrate that the non-Gaussian ansatz constitutes a natural framework to study physics in non-perturbative regimes, and propose a novel approach to quantum many-body state preparation by combining the non-Gaussian ansatz with optimal control [281–284]. Specifically, we implement a superposition of coherent state (SCS) ansatz [114, 115, 254–257, 285] and extend previous studies of the paradigmatic (sub/super) Ohmic spin-boson model [117, 268, 286–293] to in principle arbitrary couplings. The choice of the spin-boson model is motivated by the fact that it plays a major role in the description of impurity problems, whilst also encompassing many platforms that are currently used for quantum simulation and computing, ranging from superconducting circuits to trapped ions [187, 294–306]. In particular, recent realizations of the quantum Rabi-Hubbard [307] and Rabi models [308, 309] represent an ideal test-bed to experimentally probe the here-presented theoretical results.

We study (i) the convergence of the SCS ansatz, highlighting the limitations of the leakage as a control parameter and instead proposing a quantifiable measure of convergence based on the number of coherent states, (ii) the onset of chaos of the bosonic bath quantified by out-of-time-order correlators (OTOCs), demonstrating its robustness with respect to the spin-bath couplings and (iii) fast non-adiabatic quantum many-body state preparation, including the preparation of near-critical

ground states. For one mode, we achieve a reduction in infidelity of up to ≈ 60 (≈ 10) times compared to linear (optimized local adiabatic) ramps; for many modes we achieve a reduction in infidelity of up to ≈ 5 times compared to non-adiabatic linear ramps.

6.1 The model and variational ansatz

We consider the spin-boson model, where the interaction of a two-level system with a bath of N harmonic oscillators is described by the Hamiltonian,

$$\hat{H} = \frac{\Delta}{2}\hat{\sigma}_x + \sum_{k=1}^{N} \epsilon_k \hat{b}_k^\dagger \hat{b}_k - \frac{1}{2}\hat{\sigma}_z \sum_{k=1}^{N} g_k(\hat{b}_k^\dagger + \hat{b}_k). \tag{6.1}$$

Here Δ describes the tunneling strength, ϵ_k the mode frequency and g_k the interaction between the spin and k-th mode. The Hamiltonian of Eq. (6.1) conserves the parity $\hat{P}_{\text{ex}} = e^{i\pi \hat{N}_{\text{ex}}}$, where $\hat{N}_{\text{ex}} = 1/2(\hat{\sigma}_x + 1) + \sum_k \hat{b}_k^\dagger \hat{b}_k$ counts the total number of excitations.

Typically the spin-boson model is studied with an Ohmic ($s = 1$), sub-Ohmic ($s < 1$) or super-Ohmic ($s > 1$) bath, with the couplings described by $\sum_k g_k^2 \delta(\omega - \epsilon_k) = 2\alpha\omega_c^{1-s}\omega^s\Theta(\omega_c - \omega)$. Here $\omega > 0$, ω_c is a high-frequency cut-off and α is a dimensionless measure of the spin-bath interaction strength. We choose a mode discretization $\epsilon_k = \omega_c k/N$, $k = 1, 2, \ldots, N$. Note that we do not enforce any restrictions on any of the relevant energy scales, i.e. Δ, ϵ_k, g_k or ω_c. In particular, we do not require that ω_c is the largest energy scale. Such tunability is motivated by the possibility of realizing the spin-boson model with tunable parameters in trapped ions, see Sec. 6.6.6 of the Supplemental Material.

To simulate real- and imaginary-time dynamics we use a superposition of coherent state (SCS) variational ansatz, introduced in Eq. (5.16), with the time-dependent variational principle (TDVP). We comment on the intuition behind the suitability of the SCS ansatz for the spin-boson model and the role of squeezing in Sec. 6.6.8 of the Supplemental Material. Typically, the quality of an ansatz's TDVP evolution is quantified by a leakage,

$$\Lambda(t) = ||(\partial_t + i\hat{H}(t))\,|\psi(\boldsymbol{z})\rangle\,||, \tag{6.2}$$

which measures the rate at which the state ansatz leaves the variational manifold under the action of the Hamiltonian $\hat{H}(t)$. From the leakage, the fidelity of the ansatz with respect to the true state $|\Psi(t)\rangle$ at time t can be bounded by [310],

$$\mathcal{F}(t) = |\,\langle\Psi(t)|\psi(\boldsymbol{z})\rangle\,|^2 \geq \left(1 - \int_0^t d\tau \Lambda(\tau)]^2/2\right)^2. \tag{6.3}$$

6.2 Results

Firstly, we benchmark the performance of the SCS ansatz of Eq. (5.16) by considering the spin-boson Hamiltonian of Eq. (6.1) with a single mode, also known as the quantum Rabi model (QRM). In this case the Ohmic coupling reduces to $g = \sqrt{2\alpha}\epsilon$ (with $\omega_c = \epsilon$), so we use g and α interchangeably. The QRM features a crossover from a bi- to quad-polaron state at the critical coupling strength $g_c = 2\sqrt{\epsilon^2 + \sqrt{\epsilon^4 + (g_{c0}/2)^4}}$. In the so-called thermodynamic limit $\Delta/\epsilon \to \infty$ the crossover corresponds to a quantum phase transition from a normal to a superradiant phase at $g_{c0} = \sqrt{\epsilon\Delta}$ [311, 312].

In Fig. 6.1, in panels (a) and (b) we show the order parameter $\langle\hat{\sigma}_x\rangle$ of the ground state in the vicinity of the crossover, and the real-time dynamics for a quench from an initial state $|\psi(t=0)\rangle = |0\rangle|+\rangle$. We see fast convergence to the exact diagonalization (ED) results for a moderate N_p. The respective fidelities are shown in panels (c) and (d). The dotted lines in Fig. 6.1(d) show the fidelity bound from the right-hand side of Eq. (6.3). The bound appears to be relatively loose, in that it overestimates the actual decay of the fidelity. Although the leakage provides at least some control over the accuracy, the SCS ansatz of Eq. (5.16) has the advantage that it offers the number of coherent states as a control parameter. In particular $|\psi(t)\rangle \to |\Psi(t)\rangle$ in the limit $N_p \to \infty$. As such, considering the real-time dynamics of an observable $\hat{\mathcal{O}}$, we introduce a *convergence* criterion,

$$(\Delta\hat{\mathcal{O}}/\bar{\mathcal{O}})^{(N_p)}(T) = \frac{\int_0^T \mathrm{d}t|\hat{\mathcal{O}}^{(\max[N_p])}(t) - \hat{\mathcal{O}}^{(N_p)}(t)|}{|\int_0^T \mathrm{d}t\hat{\mathcal{O}}^{(N_p)}(t)|}, \tag{6.4}$$

which quantifies the relative (time-integrated) change in the evolution of the observable with respect to the maximum considered N_p. Here $\hat{\mathcal{O}}^{(N_p)}(t) = \langle\psi(t)|\hat{\mathcal{O}}|\psi(t)\rangle$ is the expectation value obtained with N_p coherent states in the SCS ansatz. We note that similar convergence criteria have been discussed in Refs. [254, 285].

With these definitions at hand, we return to the Ohmic spin-boson Hamiltonian of Eq. (6.1) and show ground state properties and real-time dynamics for $N = 10$ modes in panels (e) and (f), respectively, of Fig. 6.1. The inset of panel (e) plots the variance $\mathrm{var}(\hat{H}) = \langle\hat{H}^2\rangle - \langle\hat{H}\rangle^2$, which we use as a control quantity because $\mathrm{var}(\hat{H}) = 0$ for the ground state. We see rapid improvement for $N_p > 1$, with relatively worse performance near the critical point $\alpha_c \approx 5$. This is expected because our ansatz does not include squeezing, which is a property of the ground state near the critical point [312]. In the inset of panel (f) we plot $(\Delta\hat{\mathcal{O}}/\bar{\mathcal{O}})^{(N_p)}(T)$ for $\hat{\mathcal{O}} = \hat{\sigma}_x$. We find $N_p \gtrsim 5$ sufficient to accurately capture real-time dynamics, with $N_p \gtrsim 10$ highly accurate.

6.3 Bath dynamics

The ansatz of Eq. (5.16) can be used to further quantify the bath dynamics. To this end we evaluate the fidelity OTOC, $F = \langle\hat{W}^\dagger(t)\hat{V}^\dagger\hat{W}(t)\hat{V}\rangle$ with $\hat{V} = |\psi(0)\rangle\langle\psi(0)|$

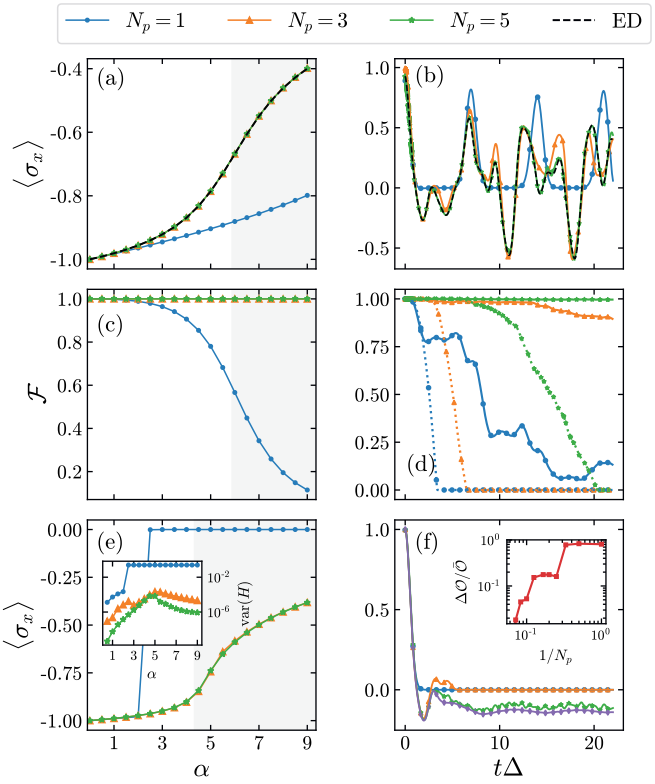


Figure 6.1: **Single mode**: (a) Order parameter $\langle \hat{\sigma}_x \rangle$ of the $P_{\text{ex}} = 1$ ground state and (c) fidelity $\mathcal{F} = |\langle \Psi_{\text{gs}} | \psi_{\text{gs}} \rangle|^2$ for $\epsilon/\Delta = 0.15/1.0$. The white/grey regions indicate the phase boundary between the normal/superradiant phase in the thermodynamic limit with the critical point $g_c = \sqrt{\epsilon\Delta}$. (b) Time evolution of $\langle \hat{\sigma}_x \rangle$ from initial state $|0\rangle|+\rangle$ for $\epsilon/\Delta = 1.0/1.1$, $g/\Delta = 2.0/1.1$. (d) The fidelity $\mathcal{F} = |\langle \Psi(t) | \psi(t) \rangle|^2$ (solid) with the lower bound obtained from the leakage (dotted), cf. Eq. (6.3). **Many modes**: (e) Order parameter $\langle \hat{\sigma}_x \rangle$ for $N = 10$ modes. For illustration, we also include the perturbative result with critical point $\alpha_c \approx 1 + \Delta/2\omega_c$ separating the delocalized (white) and localized (grey) phases [117, 287]. The inset plots var($\hat{H}$), which is largest near α_c due to the absence of squeezing in the ansatz. Panel (f) shows real-time dynamics from initial state $|0\rangle|+\rangle$, with the purple line $N_p = 16$. Parameters are $\omega_c/\Delta = 1.0/1.1$ and $\alpha = 4.0$.

the projector on the initial state and $\hat{W} = \exp(i\delta\phi\hat{G})$ [313–315]. For a small perturbation $\delta\phi \ll 1$, $1 - F \propto \text{var}(\hat{G})$. We choose $\hat{G} = \hat{x}_k = \hat{b}_k^\dagger + \hat{b}_k$, the position quadrature of the k-th mode. Such fidelity OTOCs have been considered in the analysis of chaos in the QRM in Ref. [316], where it was found that the scrambling time t^* corresponding to the maximum of var($\hat{x}$) in the superradiant phase and for

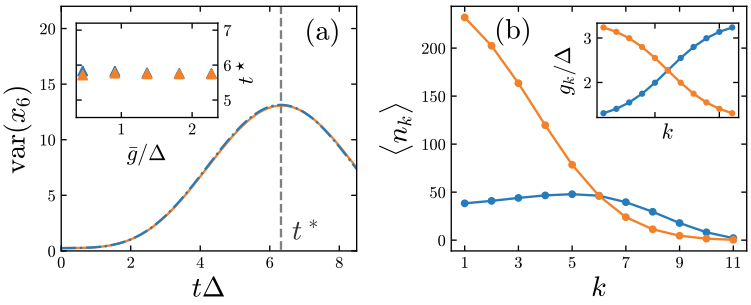


Figure 6.2: **(a)** Bath mode position quadrature of the mid-k ($k = 6$) mode for a quench from a state $|\psi(t = 0)\rangle = |0\rangle\,|+\rangle$ for the coupling profiles g_k^+ (blue, dashed) and g_k^- (orange, solid), see Eq. (6.5) and the inset in panel (b). The vertical dashed line indicates the scrambling time t^* corresponding to the first maximum of $\mathrm{var}(\hat{x}_6)$. The inset shows t^* vs. coupling amplitude $\bar{g}$ for the two profiles. **(b)** The occupation of the bath modes at the scrambling time. Parameters are $\omega_c/\Delta = 1/1.1$, $\bar{g}/\Delta = 1/1.1$ and $N = 11$, $N_p = 10$.

6

a quench from a vacuum depends only weakly on the exact value of the coupling g in the thermodynamic limit $\Delta/\varepsilon \to \infty$.

We demonstrate the versatility of the ansatz by moving beyond the paradigm of Ohmic-type baths. We consider a set of equally spaced k-modes with coupling profiles,

$$g_k^{\pm} = \frac{\bar{g}}{2}\tanh[\pm 0.25(k - \lceil N/2 \rceil)] + \bar{g}, \tag{6.5}$$

as shown in the inset of Fig. 6.2(b). In the Supplemental Material of Sec. 6.6 we investigate the convergence of the ansatz with coherent state number N_p for a variety of bath profiles including sub- and super-Ohmic ones. Here, we study quench dynamics for both $g_k^{\pm}$ from $|\psi(t = 0)\rangle = |0\rangle\,|+\rangle$ for $N = 11$ modes far from the thermodynamic limit with $\Delta/\omega_c = 1.1$. In Fig. 6.2(a) we show the variance $\mathrm{var}(\hat{x}_6)$ of the mid-coupling (sixth) mode with the scrambling time t^* indicated. The inset shows the dependence of t^* as a function of the coupling strength amplitude $\bar{g}$ (here all the couplings correspond to the (pseudo-) coherent dynamics in the phase diagram, see Supplemental Material of Sec. 6.6) and the corresponding bosonic excitation number distribution at t^* is shown in Fig. 6.2(b). We find that the weak dependence of t^* from the QRM in the superradiant phase and thermodynamic limit seems to be a robust feature that persists in the many mode case with very different coupling profiles and far from perturbative limits, see the Supplemental Material of Sec. 6.6. We leave this interesting opening for future systematic investigations and turn to the application of the ansatz to fast quantum state preparation.

6.4 Quantum optimal control

Adiabatic state preparation, where a Hamiltonian's parameters are changed such that the state during time evolution corresponds to the instantaneous ground state, is an often-employed paradigm with many applications. A prototypical example where this scheme fails is the preparation of critical states, as the adiabatic criterion cannot be satisfied due to the closure of the gap [1]. Going beyond adiabatic schemes requires the design of ramp protocols that generate a dynamical trajectory that takes the initial state to the target final state. Both determining the critical ground state and designing non-adiabatic ramp protocols can be challenging for systems with many bosonic modes. The TDVP framework offers an ideal setup to implement such ramp protocols with quantum optimal control methods.

We consider the chopped-random basis (CRAB) protocol [212, 282], an optimization technique that optimizes the ramp of a control parameter by applying corrections in the form of a truncated Fourier decomposition. A CRAB-optimized ramp protocol can be non-adiabatic, and thus its speed is not limited by the gap. Let us first consider the quantum Rabi model. In analogy to the preparation of ground states by tuning the coupling g [309, 318], we consider $g(t) = (g_f t/t_f)\, f(t)$, where g_f is the target coupling determining the corresponding ground state and where $f(t)$ is a Fourier decomposition into M harmonics,

$$f(t) \cong 1 + \sum_{j=1}^{M} A_j \sin(\nu_j t) + B_j \cos(\nu_j t), \tag{6.6}$$

where the normalization factor is $1/(1 + \sum_j B_j)$ to ensure that $g(t_f) = g_f$. Also, $\nu_j = 2\pi j(1 + r_j)/t_f$, $r_j \in \{0, 1\}$ are random integers, and the coefficients A_j, B_j are the optimization parameters. Using random numbers and repeating the optimization several times avoids the need to include r_j as optimization parameters, whilst still enabling a large parameter search area and fast convergence [319].

To assess the protocol's performance we prepare a target ground state in the vicinity of the crossover (phase transition), which is located at coupling g_c. Specifically, we evaluate the preparation time t_f needed to prepare the target state with fidelity $\mathcal{F} > 0.99$. We compare against a linear ramp protocol $g(t) = g_f t/t_f$, and a local adiabatic (LA) ramp obtained by solving the differential equation $\gamma = |\Delta^2(g)/\dot{g}(t)|$, where $\Delta(g)$ is the instantaneous energy gap between the ground and first coupled excited state, and $\gamma \gg 1$ an adiabaticity parameter [320, 321]. In Fig. 6.3(a), we plot infidelity versus preparation time for the CRAB, linear and LA ramp protocols. The corresponding coupling ramp profiles $g(t)$ are plotted in panel (b). For a set t_f the CRAB protocol offers a significant reduction in infidelity of ≈ 60 times and ≈ 10 times compared to linear and optimized adiabatic ramps, respectively. To verify that the CRAB ramp generates non-adiabatic evolution, in Fig. 6.3(c) we show the overlap $|\langle \Psi_{\mathrm{gs}}(t)|\psi(t)\rangle|^2$ of the variational state with the instantaneous ground state $|\Psi_{\mathrm{gs}}(t)\rangle$ (we also verify that the variational state corresponds to the exact evolution $|\langle \Psi(t)|\psi(t)\rangle|^2 \approx 1$).

[1] This has motivated the design of alternative protocols such as in [317].

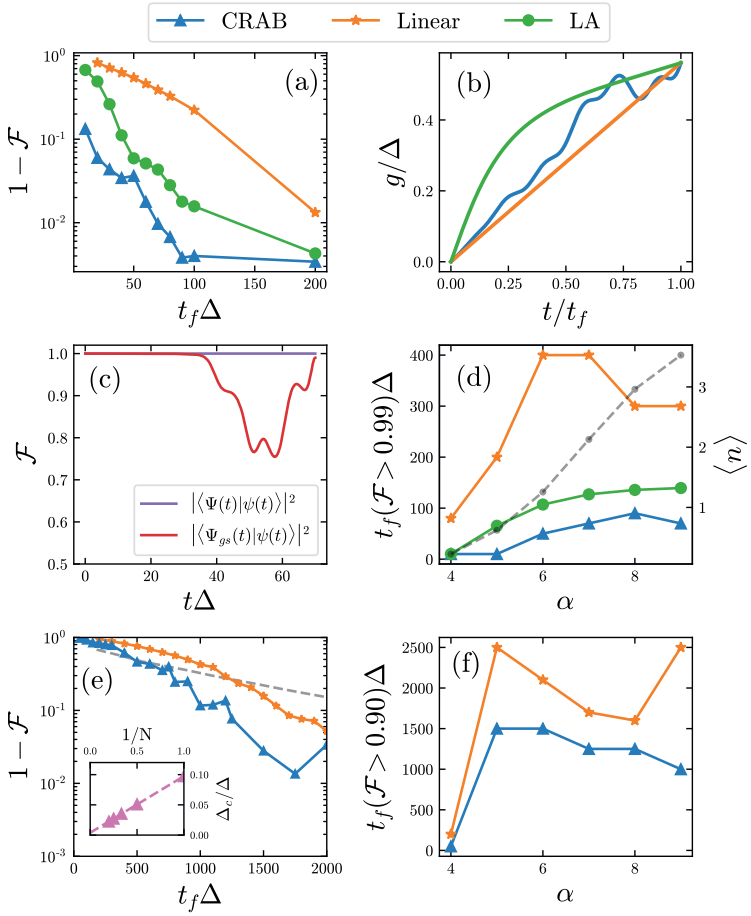


Figure 6.3: **Single mode**: (a) The infidelity $1-\mathcal{F}$, $\mathcal{F} = |\langle\psi_{\rm gs}|\psi(t_f)\rangle|^2$, where $|\psi_{\rm gs}\rangle$ is the target ground state with $\alpha = 7$, and $|\psi(t_f)\rangle$ the state prepared with CRAB, Linear and LA ramps. An example of the three ramps for $t_f = 70$ is shown in (b). In panel (c) we verify the accuracy of the CRAB simulation (purple) and its non-adiabaticity (red) by computing the overlap with the instantaneous ground state $|\Psi_{\rm gs}(t)\rangle$. Panel (d) shows the minimum ramp times required to prepare a target ground state at α with fidelity $\mathcal{F} > 0.99$. The right-axis shows the ground state boson number (grey dashed line). **Many modes**: (e) Infidelity for CRAB and Linear ramp protocols vs. ramp time for $N = 10$ modes with finite size scaling of the minimum gap (inset). For comparison we show the grey dashed line obtained by extrapolating the Linear ramp data from panel (a), see Supplemental Material of Sec. 6.6. (f) Ramp times required to prepare the target state with fidelity $\mathcal{F} > 0.90$ vs. α, see text for details. Parameters used: $N_p = 5$, $\omega_c/\Delta = 0.15$.

In Fig. 6.3(d) we show the preparation times for the three protocols versus the coupling α, as well as the ground state boson number (grey dashed). The CRAB optimization clearly outperforms both linear and LA ramp protocols: up to ≈ 10 times and ≈ 2 times faster than linear and optimized adiabatic ramps respectively.

For many modes with $N = 10$ and Ohmic couplings, we determine the target ground state for each α using the imaginary-time eoms of Eq. (5.6). The infidelity for a given ramp time t_f for the linear and CRAB protocols is shown in Fig. 6.3(e). The inset shows the finite-size scaling of the gap [2]. The grey dashed line, obtained by extrapolating the data for $\mathcal{F} = 0.9$ from Fig. 6.3(a) and using the scaled gap is shown for comparison, see Sec. 6.6 for details.

Next, we consider the target fidelity $\mathcal{F} > 0.9$, as very high target fidelities are more stringent on the quality of the approximation (requiring sufficiently large N_p), cf. Fig. 6.1(f). Fig. 6.3(f) shows the preparation times t_f vs. α. Here, the adiabaticity parameter $\gamma = O(1)$, cf. the Supplemental Material of Sec. 6.6, which indicates that the linear ramp times result in non-adiabatic evolution, which here is sufficient to reach the target $\mathcal{F} = 0.9$ with only a mild improvement factor ≈ 2 in the preparation times using the CRAB protocol, cf. the Supplemental Material of Sec. 6.6. This should be contrasted with $\gamma \approx 10 - 20$ in Fig. 6.3(d) resulting in higher improvement factor of ≈ 10 using the CRAB protocol.

6.5 Outlook

We have demonstrated the application of a superposition of coherent state variational ansatz to study bath dynamics beyond (sub/super) Ohmic couplings and combined it with quantum optimal control for fast quantum state preparation. As next steps, it would be interesting to investigate the bath dynamics in such non-perturbative setting including entanglement growth between the bath modes mediated by the spin or the possible absence of bound on OTOCs in such a star-graph like configuration [322], targeting experimental verification with trapped ions [308, 309]. Another straightforward extension of our analysis is the computation of the gap through linear response [108, 109] and considering carrier ramp profiles beyond the linear one, such as the LA profile in Fig. 6.3(b). This is likely to further reduce the state preparation times. Remarkably, already the simpler Gaussian version of the ansatz [323] allows for efficient description of systems in higher dimensions [324] or to extract scaling exponents at the phase transition [325].

Finally, we note that there are intense efforts underway to use the bosonic degrees of freedom in NISQ devices, particularly trapped ions, for quantum computing, quantum chemistry and quantum error correction [129, 326–329]. Such approaches require robust bosonic state preparation. In this context, it would be interesting to extend the combination of non-Gaussian states with quantum optimal control to a larger class of systems, including open dynamics [5, 103, 258,

[2] Here the gap refers to the distance to the first excited state in the same parity sector as the ground state.

330–332], and to potentially embed it within hybrid classical-quantum variational approaches [241, 327, 328]

6.6 Supplemental Material

6.6.1 Convergence of SCS ansatz

In this section we study the convergence of the SCS ansatz $|\psi(\boldsymbol{z})\rangle$ to the true state $|\Psi(t)\rangle$ as a function of coherent state number N_p using a variety of different spin-bath coupling profiles.

Although the performance of the SCS ansatz of Eq. (5.16) for various couplings has been previously studied, see for example [114, 256, 285, 292], for completeness we begin by studying sub-Ohmic ($s < 1$), Ohmic ($s = 1$) and super-Ohmic ($s > 1$) bath profiles. In what follows we use $s = -1$, $s = 1$ and $s = 2$ for sub-Ohmic, Ohmic and super-Ohmic, respectively.

In Fig. 6.4 we benchmark the performance of the SCS ansatz against ED when computing both ground state (panel (a)) and real-time dynamics (panel (b)). For a single mode the coupling profile reduces to $g = \sqrt{2\alpha}\epsilon$ with $\omega_c = \epsilon$, so there is no distinction between (sub/super) Ohmic. As expected, we find that increasing N_p leads to increased accuracy. To obtain high accuracy real-time dynamics at late times $t\Delta \sim 50$ we use $N_p = 10$ coherent states, at which point the evolution of $\langle\hat{\sigma}_x\rangle$ is indistinguishable from ED. In the inset of panel (b) we also benchmark our convergence measure of Eq. (6.4) using $\hat{\mathcal{O}} = \hat{\sigma}_x$ as the operator of interest and $N_p = 15$ as the reference N_p for the comparison, with the SCS converging with increasing N_p.

In Fig. 6.5 we turn to the many mode case with $N = 10$ and plot ground state energies obtained using imaginary-time evolution with sub-Ohmic (panel (a), $s = -1$), Ohmic (panel (b), $s = 1$) and super-Ohmic (panel (c), $s = 2$) coupling profiles. For the sub- and super-Ohmic profiles, $N_p = 1$ is already sufficient to capture the ground state energy with reasonable accuracy. Higher accuracy is obtained with higher N_p as expected, as confirmed in panel (d) where we plot the convergence of the ground state energy variance.

In Fig. 6.6 we plot real-time dynamics for $N = 10$ with the same three Ohmic-type coupling profiles ($s = -1, 1$ and 2 respectively). The main panels show the dynamics of $\langle\hat{\sigma}_x\rangle$, with increasingly dark color denoting increasing numbers of coherent states according to $N_p = 1, 2, 3, 4, 5, 10$, with the black dotted line showing $N_p = 15$. This $N_p = 15$ is what we use as the comparison N_p in our convergence criteria of Eq. (6.4), which we plot in the insets as a function of $1/N_p$. We see that the difference between $N_p = 10$ and $N_p = 15$ is small, as confirmed when viewing the actual dynamics seen in the main panels, particularly at early times $t\Delta \lesssim 5$. These results generalize the result presented in Fig. 6.1 beyond Ohmic couplings to sub-Ohmic and super-Ohmic, and show that the SCS ansatz is able to accurately capture ground state properties and real-time dynamics for a variety of bath profiles.

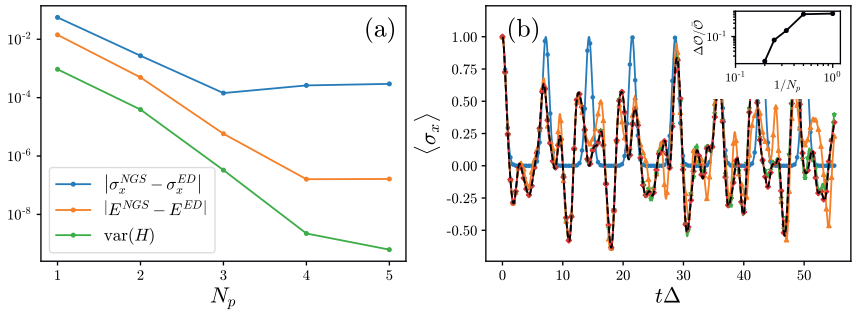


Figure 6.4: **Single mode:** (a) difference between ED- and SCS-obtained ground state properties $\langle \hat{\sigma}_x \rangle$ (blue) and $\langle \hat{H} \rangle$ (orange). In the figure, NGS refers to the non-Gaussian SCS ansatz. As N_p increases, the SCS becomes more accurate. The variance of the ground state energy $\mathrm{var}(\hat{H})$ is shown in green to confirm convergence with increasing N_p. The increase in $|\hat{\sigma}_x^{\mathrm{NGS}} - \hat{\sigma}_x^{\mathrm{ED}}|$ for $N_p = 4, 5$ is likely due to the numerical tolerances of the differential equation solver. Parameters used are $\epsilon/\Delta = 0.15$, $\alpha/\Delta = 4$. (b) Real-time dynamics with $N_p = 1$ (blue), $N_p = 3$ (orange), $N_p = 5$ (green) $N_p = 10$ (red). The coherent state ansatz ($N_p = 1$) does capture the initial fast decay $\langle \hat{\sigma}_x \rangle \to 0$, but it is not accurate beyond $t\Delta \gtrsim 2$ due to its constraint $\langle \hat{\sigma}_x \rangle \geq 0$. By $N_p = 5$ coherent states the dynamics are highly accurate, capturing the essential features including spin coherence revivals, and by $N_p = 10$ the SCS dynamics are indistinguishable from the ED result (black dashed) even at late times $t\Delta \sim 50$. In the inset we plot our convergence quantity of Eq. (6.4) for $\hat{\mathcal{O}} = \hat{\sigma}_x$ with the reference $N_p = 15$. Parameters for the real-time dynamics are $\epsilon/\Delta = 1.0/1.1$, $\alpha/\Delta = 2/1.1$.

Next, we further highlight the versatility of the SCS ansatz by turning to more general bath profiles. For consistency we use g_- as defined in Eq. (6.5), with $N = 11$ modes. In Fig. 6.7 we plot the ground state energy in panel (a) and its variance in panel (b). We also consider real-time dynamics, plotting the evolution of $\langle \hat{\sigma}_x \rangle$ in panel (c), and the x-quadrature of the middle bath mode $\mathrm{var}(\hat{x}_6)$ in panel (d). Darker colors represent higher numbers of coherent states from $N_p = 1, 2, 3, 4, 5, 10, 15$, with the black dotted line denoting $N_p = 20$. More coherent states are required to accurately simulate the real-time dynamics than the ground state. We check convergence in the inset, with the red dot highlighting $N_p = 10$ that we use in Fig. 6.2. The $N_p = 10$ result is accurate, particularly for $\mathrm{var}(\hat{x}_6)$, justifying our use of $N_p = 10$.

6.6.2 Non-adiabaticity of linear ramps

In this section we study the linear ramps of Fig. 6.3 in more detail. We begin with a single mode ($N = 1$). In Fig. 6.3(d), the minimum ramp time t_f required to prepare the target ground state $|\psi_{\mathrm{gs}}(\alpha)\rangle$ with $1 - \mathcal{F} < 0.01$ increases with α, before

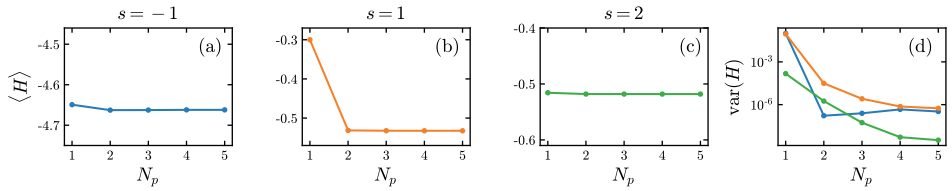


Figure 6.5: **Many modes:** Ground state energy $\langle \hat{H} \rangle$ obtained using imaginary-time evolution with sub-Ohmic (panel (a), $s = -1$), Ohmic (panel (b), $s = 1$) and super-Ohmic (panel (c), $s = 2$) coupling profiles. The energy variance $\mathrm{var}(\hat{H})$ for each profile is shown in panel (d). Parameters used are $\omega_c/\Delta = 0.15$ and $\alpha/\Delta = 4$.

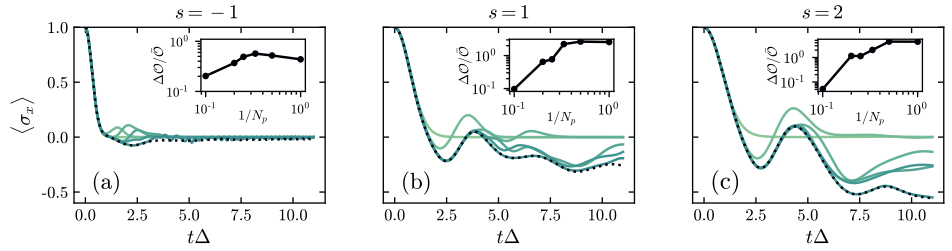


Figure 6.6: **Many modes:** Real-time dynamics obtained using SCS for $N = 10$ modes with sub-Ohmic (panel (a), $s = -1$), Ohmic (panel (b), $s = 1$) and super-Ohmic (panel (c), $s = 2$) coupling profiles. Increasing color denotes increasing numbers of coherent states, $N_p = 1, 2, 3, 4, 5, 10$, whilst the black dotted line shows $N_p = 15$. With the coherent state ansatz $N_p = 1$, $\langle \hat{\sigma}_x \rangle \geq 0$ by constraint as in Fig. 6.5, requiring $N_p > 1$ to capture the dynamics, see also Sec. 6.6.8 . The inset plots the convergence quantity of Eq. (6.4), $\hat{\mathcal{O}} = \hat{\sigma}_x$, as a function of $1/N_p$, with the maximum $N_p = 15$. Parameters used are $\omega_c/\Delta = 1.0/1.1$ and $\alpha/\Delta = 2/1.1$.

decreasing again at $\alpha \gtrsim 7$. This is counter-intuitive, because the ramp speed is set by the critical gap, which is smallest at the critical point α_c [3]. Provided $\alpha > \alpha_c$, preparing ground states of increasing α should therefore always require a larger t_f.

In Fig. 6.8(a,b) we plot the infidelity $1 - \mathcal{F} = 1 - |\langle \psi_{\mathrm{gs}}(\alpha) | \psi(t_f) \rangle|^2$, with $\alpha = 4, 5, \ldots, 9$ and $\alpha = 10, 11, \ldots, 15$ respectively, lines colored light to dark. The SCS state calculation (solid lines) agrees well with exact diagonalization (ED) (dashed lines). For $\alpha \geq 7$, we see a surprisingly rapid and oscillatory decay in infidelity, with the number of local minima increasing for increasing α.

To further investigate this behaviour, we verify our intuition that longer ramps should monotonously correspond to more adiabatic evolution. In Fig. 6.8(c) we plot

[3] Here and in the following and with a slight abuse of nomenclature we refer to critical gap and critical coupling strength to the minimal value of the gap and the corresponding coupling strength even in the crossover regime, i.e. away from the critical point in the thermodynamic sense. Such situation occurs for instance in the quantum Rabi model for finite Δ/ϵ. See also Sec. 6.6.3.

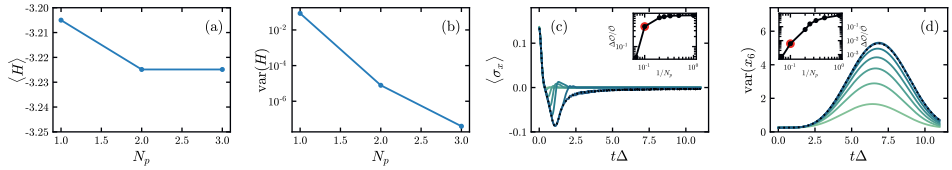


Figure 6.7: **Many modes:** Ground state energy (a) and its variance (b) as a function of N_p for the spin-boson model of Eq. (6.1) with the bath coupling profile g_-, cf. Eq. (6.5) and $N = 11$. We see rapid convergence with only a small $N_p \sim 3$ required to accurately obtain the ground state energy. Parameters are $\omega_c/\Delta = 1$. Panels (c) and (d) show real-time dynamics of $\langle \hat{\sigma}_x \rangle$ and var(x_6), respectively. Darker colors denote larger N_p, with $N_p = 1, 2, 3, 4, 5, 10, 15$ and the black dotted line $N_p = 20$. In the insets we plot the convergence quantity for each panel's observable, with $N_p = 20$ the reference number of coherent states. The red dot highlights $N_p = 10$, which we use in Fig. 6.2. We observe convergence for larger N_p, as expected. From the main panel (d), we see that $N_p > 10$ is sufficient to quantitatively predict the location and height of the peak, as required for the analysis in Fig. 6.2. Parameters are $\omega_c/\Delta = 1/1.1$.

6

the maximum infidelity of the instantaneous state with the instantaneous ground state, $\max[1 - \mathcal{F}(t)] = \max_{0 \le t \le t_f}[1 - |\langle \psi_{\rm gs}(t)|\psi(t)\rangle|^2]$. As expected the infidelity always decreases as t_f increases, while increasing as α increases.

Finally, in Fig. 6.8(d) we compare $t_f\Delta = 250$ (pink) and $t_f\Delta = 400$ (olive) ramp profiles. The left axis (solid lines) shows $1 - \mathcal{F}(t) = 1 - |\langle \psi_{\rm gs}(t)|\psi(t)\rangle|^2$, while the right axis (dashed lines) shows the ramp profile $g(t)/\Delta$. The dashed horizontal line shows the critical point $g_c = 2\sqrt{\epsilon^2 + \sqrt{\epsilon^4 + (g_{c0}/2)^4}}$ where $g_{c0} = \sqrt{\epsilon\Delta}$. Note that $g = \sqrt{2\alpha}\epsilon$ and $\epsilon = \omega_c$ for $N = 1$. We see the non-adiabaticity is located near the critical point, as expected. Despite the fact that the $t_f\Delta = 250$ ramp is less adiabatic than the $t_f\Delta = 400$ ramp, the dynamics are such that $|\Psi(t)\rangle$ returns to the ground state with higher fidelity. The minimum linear ramp time required to achieve $F \ge 0.99$ is therefore not actually realized by a fully adiabatic ramp.

Next, we consider ground state preparation in the many-mode case ($N = 10$). Fig. 6.9 plots the final infidelity $1 - \mathcal{F} = 1 - |\langle \psi_{\rm gs}(\alpha)|\psi(t_f)\rangle|^2$. The target ground state is obtained using the imaginary-time eoms of Eq. (5.6), while real-time dynamics are computed using the real-time eoms of Eq. (5.5), both with $N_p = 5$. We note that this data remains consistent with the limiting case $(1 - \mathcal{F}) \to 0$ as $t_f \to \infty$. We observe non-monotonous decay of the infidelity as t_f increases, which is reminiscent of the single-mode behaviour. Thus, the many-mode linear ramp is also non-adiabatic.

We have shown that both the single and many-mode linear ramp protocols are in fact non-adiabatic. As a consequence, the comparison presented in Fig. 6.3 between CRAB and linear ramp protocols is not a comparison between CRAB and adiabatic ramp protocols. If we were to restrict the linear ramp to being adiabatic,

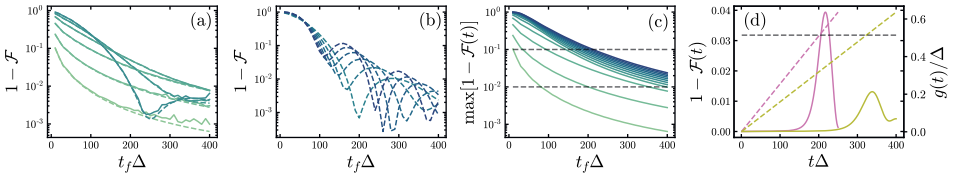


Figure 6.8: **Single mode:** The final infidelity $1-\mathcal{F} = 1 - |\langle\psi_{\rm gs}(\alpha)|\psi(t_f)\rangle|^2$ with $\alpha = 4, 5, \ldots, 9$ (a) and $\alpha = 10, 11, \ldots, 15$ (b), lines colored light to dark. The dynamics are computed with ED (dashed) and SCS (solid) with $N_p = 5$. We verify that longer ramps are always more adiabatic by plotting (c) the maximum infidelity between the instantaneous state and the instantaneous ground state. Finally, we show (d) two example ramp profiles $t_f\Delta = 250$ and $t_f\Delta = 400$. Surprisingly, despite being less adiabatic, the final state of the $t_f\Delta = 250$ ramp has a higher fidelity with the target state than the $t_f\Delta = 400$ ramp. Parameters used are $\omega_c/\Delta = 0.15$

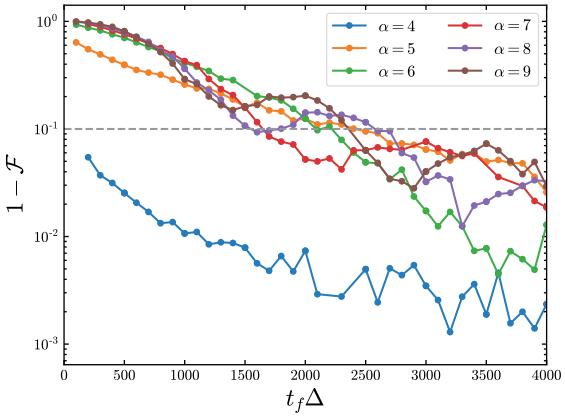


Figure 6.9: **Many modes:** Infidelity $1-\mathcal{F} = 1 - |\langle\psi_{\rm gs}(\alpha)|\psi(t_f)\rangle|^2$ for $N = 10$ modes, calculated from real-time equations of motion with the SCS ansatz and $N_p = 5$. Note the non-monotonous decay in infidelity, similar to the single-mode result. The minimum t_f required to prepare the target state with infidelity $1-\mathcal{F} < 0.1$ corresponds to the first time each α line crosses the dashed horizontal line. Parameters used are $\omega_c/\Delta = 0.15$.

the factor by which the CRAB protocol outperforms the linear ramp would increase, particularly at large α.

6.6.3 Scaling analysis of linear adiabatic ramp times

In this section we use the adiabatic theorem to estimate the scaling of the adiabatic linear ramp times with α and the number of modes. We firstly review the

adiabatic theorem, obtaining a lower bound on adiabatic ramp times. Secondly, we numerically verify this bound for a single mode by changing α. We then extend our analysis to the many-mode case to make predictions about the ramp time in regimes where ED is not tractable.

We begin with the adiabatic theorem. Following Ref. [320], we denote the eigenstates of a time-dependent Hamiltonian $\hat{H}(t)$ as $|E_k(t), t\rangle$, with corresponding eigenvalues $E_k(t)$, and where $k = 0$ labels the ground state. The *critical gap* is defined as the minimum gap between the two smallest magnitude connected eigenvalues E_0 and E_j,

$$\Delta_c = \min_{0\leq t\leq t_f}[E_j(t) - E_0(t)]. \tag{6.7}$$

From the adiabatic theorem, if we prepare the system at $t = 0$ in the ground state $|E_0, 0\rangle$ and let it evolve under $\hat{H}(t)$ until $t = t_f$, then the overlap between $|E_0, 0\rangle$ and the final state $|\psi(t_f)\rangle$ is lower bounded by $|\langle E_0, t_f|\psi(t_f)\rangle|^2 \geq 1 - \epsilon^2$ if $\left|\left\langle d\hat{H}/dt\right\rangle_{j,0}\right| \Delta_c^{-2} \leq \epsilon, \forall\ t$, where ϵ is a small number and $\langle d\hat{H}/dt\rangle_{j,0} = \langle E_j, t|\, d\hat{H}/dt\, |E_0, t\rangle$ is the matrix element describing the coupling strength between the two eigenstates. We consider the spin-boson Hamiltonian of Eq. (6.1). The ground state parity is $P_{\text{ex}} = 1$, while the first (second) excited state parity is $P_{\text{ex}} = -1$ $(+1)$. The relevant gap is therefore between E_0 and E_2.

For a single mode ($N = 1$), the time-dependent parameter is the coupling strength $g(t)$ which follows a linear ramp profile $g(t) = g_f t/t_f$. The matrix element is $|d\hat{H}/dt| = g_f/(2t_f)\hat{\sigma}_z(\hat{b}^\dagger + \hat{b})$, and thus the linear ramp is adiabatic if,

$$t_f \gg g_f|\langle\hat{\sigma}_z(\hat{b}^\dagger + \hat{b})\rangle_{2,0}|/(2\Delta_c^2). \tag{6.8}$$

For many-modes, the linear ramp profile is $g_k(t) = g_{k,f}t/t_f$ and thus the matrix element is $|d\hat{H}/dt| = 1/(2t_f)\sum_k g_{k,f}\hat{\sigma}_z(\hat{b}_k^\dagger + \hat{b}_k)$. The linear ramp is therefore adiabatic if,

$$t_f \gg |\langle\sum_k g_{k,f}\hat{\sigma}_z(\hat{b}_k^\dagger + \hat{b}_k)\rangle_{2,0}|/(2\Delta_c^2). \tag{6.9}$$

We now turn to results, beginning with $N = 1$. Fig. 6.10(a) plots the energy spectrum as a function of α. Note that in the normal phase $\alpha \leq \alpha_c$, Δ_c as defined in Eq. (6.7) is always defined at t_f as the gap narrows with increasing α. Fig. 6.10(b) shows the minimum t_f required to adiabatically prepare the target state $|\psi_{\text{gs}}(\alpha)\rangle$. We calculate t_f using two methods. Firstly, by numerically calculating the gap and matrix element to determine the right-hand side of Eq. (6.8). Because the right-hand side of Eq. (6.8) is related to t_f by an inequality, we normalize to the $\alpha = 15$ result, yielding a scaling of $t_f(\alpha)/t_f(\alpha = 15)$ (purple triangles). The second method is a real-time numerical simulation of the linear ramp, which enables us to find the minimum ramp time t_f such that $1 - \langle\Psi_{\text{gs}}(t)|\Psi(t)\rangle \leq 0.10\ \forall\ 0 \leq t \leq t_f$ (green circles). Here, the specific choice of the infidelity value at each time step is arbitrary and should be chosen $\ll 1$ to ensure the adiabaticity. Note that this corresponds

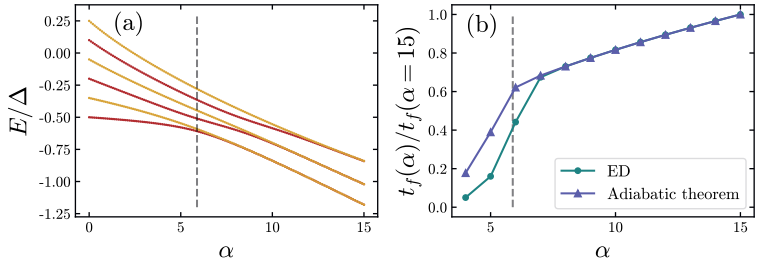


Figure 6.10: **Single mode:** (a) Energy spectrum with parities $P_{\text{ex}} = 1$ (red) and $P_{\text{ex}} = -1$ (gold). The dotted vertical line denotes the critical point α_c. In panel (b) we extract t_f from ED (green circles), as described in the text. In the same panel, we compare to the estimate obtained from the adiabatic theorem (purple triangles). We find the adiabatic theorem estimate to be accurate in the superradiant phase, but not the normal phase. Parameters used are $\omega_c/\Delta = 0.15$.

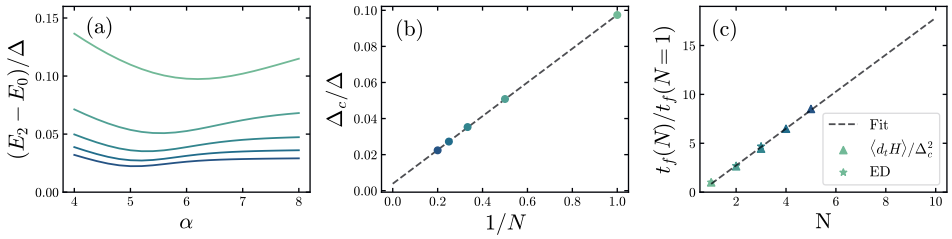


Figure 6.11: **Many modes**: The gap (a) between the ground and first parity-connected eigenstates for $N = 1, 2, \ldots, 5$ (light to dark). In panel (b) we plot Δ_c as a function of $1/N$, with the black dashed line a linear fit. In panel (c) we plot Eq. (6.9) for $N = 1, \ldots, 5$ (triangles), where the gap and matrix element are calculated using ED. We perform a linear fit (black dashed line) to extrapolate t_f to larger t. For small N we simulate the real-time ramp dynamics and determine the minimum t_f such that $1 - \mathcal{F}(t) = 1 - |\langle\psi_{\text{gs}}(t)|\psi(t)\rangle|^2 \leq 0.1 \; \forall \; t$ (stars). Parameters used are $\omega_c/\Delta = 0.15$.

to the first time each α line crosses the dashed horizontal line at $1 - \mathcal{F}(t) = 0.1$ in Fig. 6.8(c). Comparing the adiabatic to ED, we find that both agree well in the super-radiant phase. However, in the normal phase the adiabatic theorem overestimates t_f.

Next, we predict the scaling of t_f with mode number. Fig. 6.11(a) plots the gap as a function of α for $N = 1, \ldots, 5$ obtained with ED. Panel (b) plots the critical gap Δ_c as a function of $1/N$, as well as a linear fit (dashed black line) allowing for extrapolation for N beyond the reach of ED. In principle the many-mode spectra can also be obtained using SCS [109], which we leave for future work.

In Fig. 6.11(c) we numerically calculate the right-hand side of Eq. (6.9) for

$N = 1, \ldots, 5$ with $\alpha = 7$ (triangles). To extrapolate beyond $N = 5$, we perform a linear fit (black dashed line). We are able to verify the t_f scaling for small mode numbers ($N = 1, 2, 3$) using a real-time ED simulation to determine the minimum ramp time such that $1 - \langle \Psi_{\text{gs}}(t) | \Psi(t) \rangle \leq 0.10 \; \forall \; 0 \leq t \leq t_f$ when preparing $|\Psi_{\text{gs}}(\alpha = 7)\rangle$ (stars). We see excellent agreement between the ED result and the adiabatic criterion Eq. (6.9).

Considering a specific example of $N = 10$, from Fig. 6.11(c) we have $t_f(N = 10)/t_f(N = 1) \approx 18$. From Fig. 6.8, preparing $|\psi_{\text{gs}}(\alpha = 7)\rangle$ with infidelity $1 - \mathcal{F} < 0.1$ requires $t_f(N = 1) \approx 170$. Therefore, $t_f(N = 10) \approx 3 \times 10^3$ for $N = 10$. In contrast, in Fig. 6.3 we find that the CRAB protocol prepares the same state with the same infidelity in $t_f = 1.25 \times 10^3$, which is over twice as fast.

We note that although we have only performed this analysis for $|\psi_{\text{gs}}(\alpha = 7)\rangle$, we expect the findings to be robust in the localized phase (i.e. $\alpha > \alpha_c$). Further work is needed to investigate the scaling in the delocalized phase due to the inaccurate prediction in the normal phase of the QRM, see Fig. 6.10.

6.6.4 Adiabaticity of linear ramps in Fig. 6.3

In this section we evaluate the adiabaticity of the linear ramps used in Fig. 6.3. We consider the adiabaticity parameter $\gamma = \left| \Delta_c^2 / \langle d\hat{H}/dt \rangle_{2,0} \right|$, which measures the extent to which a change in the Hamiltonian $\hat{H}(t)$ is adiabatic; i.e. a ramp is adiabatic if $\gamma \gg 1$. In Fig. 6.12 we plot the adiabaticity parameter γ (left axis, solid lines) for both single (a) and many modes (b) using a given t_f (right axis, dashed line). The t_f is from Fig. 6.3(d,f), noting that the target infidelity $1 - |\langle \psi_{\text{gs}} | \psi(t_f) \rangle|^2$ used to obtain the t_f is $1 - \mathcal{F} \leq 0.01$ for $N = 1$ and $1 - \mathcal{F} \leq 0.1$ for $N = 10$.

Here, the single-mode adiabaticity parameter $\gamma \approx 20$ indicates that the ramp is relatively adiabatic, although less so at large α. The CRAB protocol, which is not constrained to be adiabatic, is able to prepare the same state about ≈ 10 times faster. In contrast, for $N = 10$, $\gamma \approx O(1)$, indicating that, although sufficient to satisfy $1 - \mathcal{F} < 0.1$, the linear ramps of Fig. 6.3(f) are non-adiabatic. This small γ contributes to the fact that the CRAB protocol produces the same state only ≈ 2 times faster, a mild improvement.

6.6.5 Spin dynamics and phases with bath profiles

Here we briefly comment on the spin dynamics and the possible underlying phases in spin-boson models with the bath couplings Eq. (6.5). First we note that the phase diagram of the spin-boson model has been extensively studied for the case of sub-Ohmic, Ohmic and super-Ohmic baths characterized by the spectral density $J(\omega) \propto \alpha \omega^s$ with $0 < s < 1$, $s = 1$ and $s > 1$ respectively [117]. There, one finds delocalized and localized equilibrium phases in the $s - \alpha$ plane as has been demonstrated in a number of works [117, 285–287, 289] with the ground state expectation value of the magnetization, $\langle \hat{\sigma}_z \rangle_{\text{gs}}$, as the order parameter. Alternatively, a standard approach is to characterize the system through its non-equilibrium behaviour as

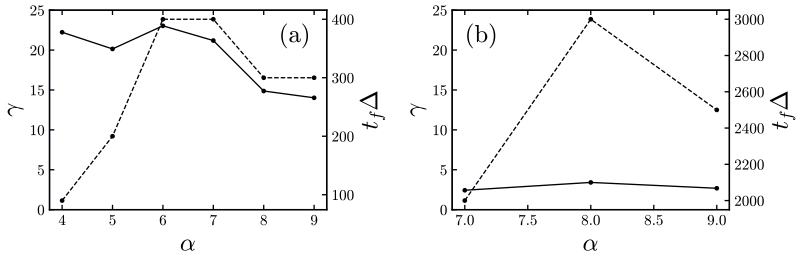


Figure 6.12: Adiabaticity parameter γ (solid line, left axis) and ramp time $t_f\Delta$ (dotted line, right axis). For $N = 1$ (a), note the decrease in γ at large α. The t_f is obtained from Fig. 6.3(d), i.e. by determining the minimum t_f such that $1 - \mathcal{F} = 1 - |\langle\psi_{\rm gs}|\psi(t_f)\rangle|^2 \leq 0.01$. For $N = 10$ (b), $\gamma \sim \mathcal{O}(1)$. The ramp is less adiabatic than the single-mode case because we determine t_f with a higher infidelity threshold as in Fig. 6.3(f), namely by finding the minimum t_f such that $1 - \mathcal{F} = |\langle\psi_{\rm gs}|\psi(t_f)\rangle|^2 \leq 0.1$.

quantified by the dynamics of the magnetization $\langle\hat{\sigma}_z(t)\rangle$ when quenched from a fully polarized $\langle\hat{\sigma}_z(t=0)\rangle = \pm 1$ state. The typical cases are a coherent (underdamped) or incoherent (overdamped) oscillations with $\langle\hat{\sigma}_z(t)\rangle$ reaching the equilibrium value in the $t \to \infty$ limit. Additionally, a situation with a single oscillation before reaching the equilibrium is sometimes referred to as pseudo-coherent [293]. Note that the coherent (incoherent) evolution does not in general correspond to the underlying delocalized (localized) equilibrium phases [285, 289].

Fig. 6.13 plots time evolution of $\langle\hat{\sigma}_z\rangle$ for varying strength of the coupling $\bar{g}$ for the two profiles g_k^+ in panel (a) and g_k^- in panel (b), see Eq. (6.5). Similarly to the (sub/super) Ohmic cases [285, 293], one can see a transition from a coherent to pseudo-coherent dynamics as $\bar{g}$ is increased from $\bar{g} = 0.5$ to $\bar{g} = 2.5$, the values used in the analysis of the scrambling time t^* in Fig. 6.2(a). There, t^* is only weakly dependent on the actual value of $\bar{g}$. We could verify that this holds also in the case of the Rabi model in both the normal and superradiant phases, see also [316], with the reservation that t^* also depends on the initial state from which the quench is being performed. We leave a detailed investigation of these issues, including the dynamics and the phase diagram for non-standard couplings such as in Eq. (6.5), to future studies.

6.6.6 Realization of spin-boson model in trapped ions

In trapped ion systems, the bosonic modes are collective phonon modes that arise due to the mutual Coulomb repulsion between the ions which are confined by a trapping potential. Spin-boson coupling is typically achieved using a spin-dependent force, which is realized either via a spatially dependent AC Stark shift [21, 333], or via the simultaneous driving of a two-photon Raman transition near the red and blue sidebands [119]. In particular, following recent theoretical proposals [318,

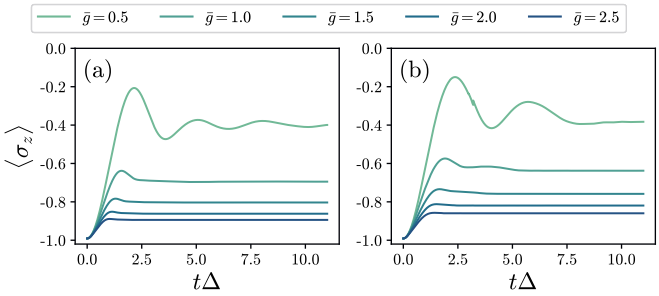


Figure 6.13: Magnetization dynamics $\langle\hat{\sigma}_z(t)\rangle$ for a quench from an initial state with $\langle\hat{\sigma}_z(t=0)\rangle = -1$ for the couplings of the form (a) g_k^+ and (b) g_k^-, see Eq. (6.5). For increasing couplings $\bar{g}$ one can see a transition from coherent (oscillations with multiple maxima) to pseudo-coherent (oscillation with a single maximum) behaviour for both g_k^+ and g_k^-. This qualitatively agrees with the behaviour observed in spin-boson models with (sub/super) Ohmic couplings [285, 293].

6

334], the single-mode variant of the spin-boson model, the quantum Rabi model, was realized in trapped ion platforms, enabling the study of real-time dynamics, ground state preparation and phase transitions [308, 309].

In this section we propose an experimentally feasible realization of the many-mode spin-boson model that enables broad tunability over the parameter space. Similar to Ref. [318], our proposed implementation utilizes a pair of Raman beams inhomogeneously detuned from the red and blue sidebands. However, we employ multiple spectral components, which enables the simultaneous driving of the red and blue sidebands of multiple modes. This has been demonstrated in experiment, see for example Refs. [335, 336]. The broad tunability of our realization unlocks the study of the spin-boson model both beyond the paradigm of (sub/super)-Ohmic couplings, as well as in the intermediate mode number regime ($N \approx 10$ modes).

The Hamiltonian is,

$$\hat{H}_0 = \hat{H}_{\text{qubit}} + \hat{H}_{\text{phonon}} = \frac{\omega_0}{2}\sum_i \hat{\sigma}_i^z + \sum_k \omega_k \hat{b}_k^\dagger \hat{b}_k. \tag{6.10}$$

Here $\hat{\sigma}_i^\alpha$ with $\alpha = x, y, z$ are Pauli operators acting on the ith qubit, and $\hat{b}_k^\dagger$ ($\hat{b}_k$) is the creation (annihilation) operator for phonon mode k with frequency ω_k. The spin and phonon degrees of freedom are coupled by a pair of Raman beams, each with multiple spectral components. In a frame rotating with $\hat{H}_{\text{qubit}}$, the Hamiltonian describing the interaction is,

$$\hat{H}_{\text{int}} = \sum_{q=1,2}\sum_j \frac{\Omega_q}{2}\left(\hat{\sigma}_j^+ e^{i\sum_k \eta_{k,j,q}(\hat{b}_k^\dagger + \hat{b}_k) + (\omega_0 - \omega_{q,k})t} + \text{h.c.}\right), \tag{6.11}$$

where q indexes the pair of Raman beams, Ω_q is the Rabi frequency and $\eta_{k,j,q} =$

$k_q b_{jk}\sqrt{\hbar/(2m\omega_k)}$ the Lamb-Dicke parameter. Here k_q is the wavevector of Raman beam k, and $\omega_{q,k}$ the frequencies.

We choose $\omega_{1,k}$ ($\omega_{2,k}$) to off-resonantly drive the blue (red) sideband with detunings δ_k^{b} (δ_k^{r}). That is, $\omega_{1,k} = \omega_0+\omega_k+\delta_k^{\mathrm{b}}$, $\omega_{2,k} = \omega_0-\omega_k+\delta_k^{\mathrm{r}}$. Moving to the rotating frame with respect to $\hat{H}_{\mathrm{phonon}}$, assuming the Lamb-Dicke regime $\eta_{k,j,q}\sqrt{\langle \hat{b}_k^\dagger \hat{b}_k\rangle} \ll 1$ to expand the exponentials to the lowest order in η with $\eta_{k,j,1} \approx \eta_{k,j,2} \equiv \eta_{k,j}$, and making a rotating wave approximation, we obtain,

$$\hat{H}_{\mathrm{int}} = \sum_j \sum_k \frac{\eta_{j,k}\Omega_{j,k}}{2}\left[\hat{b}_k^\dagger e^{i\delta_k^{\mathrm{r}} t} + \hat{b}_k e^{i\delta_k^{\mathrm{b}} t}\right]\hat{\sigma}_j^- + \mathrm{h.c.}. \tag{6.12}$$

Next, we require that the motional modes couple only to a single qubit, which can be achieved by using the Raman beams to address only a single ion. Making a unitary transformation with respect to $\hat{H}_1 = 1/4\sum_n(\delta_n^{\mathrm{b}}+\delta_n^{\mathrm{r}})\hat{\sigma}^z + \frac{1}{2}\sum_n(\delta_n^{\mathrm{b}}-\delta_n^{\mathrm{r}})\hat{b}_n^\dagger\hat{b}_n$ yields,

$$\hat{H}_{\mathrm{int}} = \sum_k \frac{\eta_{i,k}\Omega_{i,k}}{2}[(\hat{b}_k^\dagger + \hat{b}_k)e^{-it\delta(N-1)/2}]\hat{\sigma}^- + \mathrm{h.c.} + \hat{H}_1, \tag{6.13}$$

where we set $\delta_n^{\mathrm{b}} + \delta_n^{\mathrm{r}} = \delta\,\forall\, n$. Making a unitary transformation with respect to $\hat{H}_2 = (1/4)\delta(N-1)\hat{\sigma}^z$ clears the time-dependence, yielding,

$$\hat{H}_{\mathrm{SB}} = -\frac{\delta}{4}\hat{\sigma}^z + \frac{1}{2}\sum_k(\delta_k^b - \delta_k^r)\hat{b}_k^\dagger\hat{b}_k + \frac{1}{2}\sum_k \eta_k\Omega_k(\hat{b}_k^\dagger + \hat{b}_k)\hat{\sigma}^x \tag{6.14}$$

After a global $-\pi/2$ spin rotation about $\hat{\sigma}_y$ which maps $\hat{\sigma}^x \to \hat{\sigma}^z$, $\hat{\sigma}^z \to -\hat{\sigma}^x$, we identify $\hat{H}_{\mathrm{SB}}$ as Eq. (6.1) with,

$$\Delta = \delta/4, \qquad \epsilon_k = (\delta_k^b - \delta_k^r)/2, \qquad g_k = -\eta_k\Omega_k. \tag{6.15}$$

The flexibility to tune δ_k^{b}, δ_k^{r} and Ω_k for each mode translates in the desired (in principle arbitrary) tunability of the parameters of the resulting spin-boson Hamiltonian of Eq. (6.14).

6.6.7 Further details on simulations

All simulations are performed using Julia v1.8. The equations of motion are solved using DifferentialEquations.jl [337], and the optimal control performed with Optim.jl using a Nelder-Mead algorithm [148]. Exact diagonalization was performed using a combination of our own implementation and QuantumOptics.jl [185].

Computing the equations of motion requires computing the tangent vectors $|v_\mu\rangle$ and the overlaps $\langle v_\mu|v_\nu\rangle$ to construct the symplectic form $\omega_{\mu\nu}$ and metric $g_{\mu\nu}$. We obtain the tangent vectors and overlaps analytically, enabling us to construct both ω and g analytically. We obtain their pseudo-inverse, used in the equations of motion of Eq. (5.5), numerically.

Note that the equations of motion are degenerate if the initial state of at least two coherent states is the same. This means that at least one coherent state is

unnecessary, and our equations of motion are over-parametrized. In this scenario, this leads to the two coherent states with the same initial state evolving identically, which reduces our ansatz of N_p coherent states to an effective $N_p - 1$ coherent states. To avoid this degeneracy, we always initialize the system such that each coherent state has a slightly different initial state. For the initial vacuum state $|\psi\rangle = |+\rangle\,|0\rangle$, we randomly initialize each parameter as $z_\mu \in [0, 0.01]$. Fidelities between different initial states are then typically $\mathcal{F} > 0.99$. For quantitative studies, such as the comparison between linear ramps and CRAB when $N = 10$, we use the same initial state for both the linear and CRAB ramp.

Finally, we comment on numerical instability. We observe points where the precision required to evaluate the pseudo-inverse and eoms exceeds the target precision of our differential equation solver. Trajectories that pass through these points can therefore be calculated, but at increased computational cost. To avoid this, we exploit the randomness of the initial state (already required to distinguish the coherent states) to generate a nearly identical initial state with nearly identical evolution, but which may not pass through the exact same point of numerical instability. We find this is sufficient to deal with the majority of cases.

6.6.8 Intuition for the SCS ansatz by Trotterization

In this section we motivate the use of the SCS ansatz to describe the spin-boson model by sketching the dynamics generated by $\hat{H}$ using a Trotter expansion. Consider the spin-boson Hamiltonian Eq. (6.1). For simplicity, we set $\omega = 0$,

$$\hat{H} = g(\hat{b} + \hat{b}^\dagger)\hat{\sigma}_z + \Delta\hat{\sigma}_x/2. \tag{6.16}$$

Real-time evolution under $\hat{H}$ for a small time step δt is described by the generator $\hat{U} = e^{-i\hat{H}\delta t}$, which, using a first order Trotterization, is approximated as,

$$\hat{U} = e^{-i\hat{H}\delta t} \approx \hat{U}_1\hat{U}_2 = e^{-i\epsilon_1(\hat{b}+\hat{b}^\dagger)\hat{\sigma}_z}e^{-i\epsilon_2\hat{\sigma}_x}, \tag{6.17}$$

where $\epsilon_1 = -g\delta t/2$, $\epsilon_2 = \Delta\delta t/4$, where we require that $\epsilon_1, \epsilon_2 \ll 1$. Starting with an initial state $|\psi(t=0)\rangle = |\downarrow\rangle$, applying $\hat{U}_2$ and then $\hat{U}_1$ yields a state of the form,

$$\hat{U}_1\hat{U}_2\,|\downarrow\rangle = c_1\,|\alpha + \epsilon_1\rangle\,|\uparrow\rangle + c_2\,|\alpha - \epsilon_1\rangle\,|\downarrow\rangle\,, \tag{6.18a}$$

with coefficients $c_i \in \mathbb{C}$. We see that $\hat{U}_1$ generates a spin-dependent displacement, whilst $\hat{\sigma}_x$ rotates the spins. Note that the bosonic state in the $|\uparrow\rangle$ subspace is simply a coherent state, and similarly for $|\downarrow\rangle$. Again applying $\hat{U}_1\hat{U}_2$ yields,

$$\hat{U}_1\hat{U}_2\hat{U}_1\hat{U}_2\,|\downarrow\rangle = (\tilde{c}_1\,|\alpha + 2\epsilon_1\rangle + \tilde{c}_2\,|\alpha\rangle)\,|\uparrow\rangle + (\tilde{c}_3\,|\alpha\rangle + \tilde{c}_4\,|\alpha - 2\epsilon_1\rangle)\,|\downarrow\rangle\,, \tag{6.19a}$$

with new coefficients $\tilde{c}_i$. Now, the bosonic state in the $|\uparrow\rangle$ ($|\downarrow\rangle$) subspace is a linear combination of two coherent states. The repeated application of $\hat{U}_1$ and $\hat{U}_2$ generates increasingly long linear combinations of coherent states, which motivates the SCS ansatz as an effective choice of ansatz for the spin-boson model.

Chapter 7

Open quantum dynamics

Based on
J. Chem. Phys. **161**, 184113, (2024) [5]

Bilbo: "It's a dangerous business, Frodo, going out your door."

J.R.R. Tolkien, The Lord of the Rings (1968)

Advances in the control of quantum systems over the past decade have led to the development of a range of platforms for investigating almost-coherent quantum dynamics. However, in the absence of robust fault-tolerant operations, studies of these platforms must contend with various sources of noise induced by couplings to an environment. These noisy intermediate-scale quantum (NISQ [98]) devices can often be arbitrarily controlled, opening possibilities of creating states far out of equilibrium. In light of this, understanding the out-of-equilibrium dynamics of open quantum many-body systems has become of great interest, e.g. for understanding and realizing a quantum advantage in the NISQ era, as discussed in the Introduction.

A particularly challenging class of problems arises for systems containing both spin and bosonic degrees of freedom with an (even locally) unbounded Hilbert space, applicable to quantum simulation and computation platforms ranging from superconducting circuits to trapped ions [187, 294–306], to paradigmatic problems in impurity physics [338, 339], quantum chemistry [326], or polaritonic chemistry [340]. The ubiquity and complexity of spin-boson Hamiltonians has led to the development of various techniques for their study and characterization. These include methods for the bosonic space, namely path integral techniques [289–291, 293], effective Hamiltonian formulation [341–344] or lightcone conformal truncation used predominantly in high-energy physics [345–347], as well as methods such as non-equilibrium Monte Carlo or tensor networks [104, 105, 348], which have allowed for the simulation of (open) out-of-equilibrium dynamics of quantum many-body systems [273, 275, 349–360], also in large-system scenarios. However, these methods are often constrained to one-dimensional setups, closed systems, or to a mesoscopic

number of particles, or a combination thereof.

The number and breadth of the aforementioned approaches illustrates that no single method can tackle the range of systems described by spin-boson type Hamiltonians or even the full parameter space of a specific model. As such, it is important to pinpoint the strengths and shortcomings of each method. In this Chapter, we undertake a comparative study between two methods: (i) the time-dependent variational ansatz using *non-Gaussian* states (NGS) [108, 109], specifically a superposition of coherent state (SCS) ansatz, and (ii) the truncated Wigner approximation (TWA) combined with its generalization to discrete spaces, discrete truncated Wigner approximation (DTWA). Fig. 7.1(a),(b) shows a schematic of each method. These methods may allow us to circumvent some of the aforementioned limitations [102, 107–109, 361] and have recently been generalized to open quantum systems [258, 280, 362–367]. Analyzing fundamental quantum effects in macroscopic limits can thus be enabled with NGS and TWA approaches.

In NGS, as discussed in Ch. 5 one exploits the continuous variable structure of bosonic states to build a time-dependent variational wavefunction ansatz of non-Gaussian states. Here, we specifically use a superposition of bosonic coherent states (SCS). This method has been successfully applied to studies of systems ranging from the Kondo impurity problem [252], central spin [110], spin-Holstein models [111], Bose and Fermi polarons [112, 113, 253], and (sub/super) Ohmic spin-boson models [4]. We also note that the closely related Davydov state ansatz has been applied in studies of molecular crystals and polaritonic physics [114, 115, 118, 254–257].

TWA is a semi-classical approach that factorizes the phase space functions (Weyl symbols) that describe a quantum observable in the phase space representation. As such, TWA is reminiscent of a product-state mean-field ansatz on Hilbert space. Like the latter, TWA allows one to treat systems with very large sizes ($\mathcal{O}(10^4)$ particles), while still capturing some essential quantum features such as spin-squeezing or entanglement [102, 368–372]. TWA can be easily adapted to systems with both bosonic and discrete degrees of freedom, combining sampling strategies from continuous [373] and discrete Wigner functions [102, 107, 361].

Here, we consider the open and closed dynamics of a spin-boson Hamiltonian featuring multiple spins coupled to a discrete set of bosonic modes via Holstein and Tavis-Cummings couplings, thus ensuring broad applicability of our results. We begin in Sec. 7.1 by extending the variational NGS to open quantum systems using the quantum trajectories method. We discuss TWA with its discrete variant DTWA for closed and open systems in Sec. 7.2. In Sec. 7.3 we introduce the Holstein-Tavis-Cummings spin-boson Hamiltonian, which we use to compare both methods over a range of parameters. Finally in Sec. 7.4 we summarize our findings and discuss how each method can be improved to increase its accuracy and/or applicability both in terms of systems to which they can be applied, and also in terms of the observables that can be accessed.

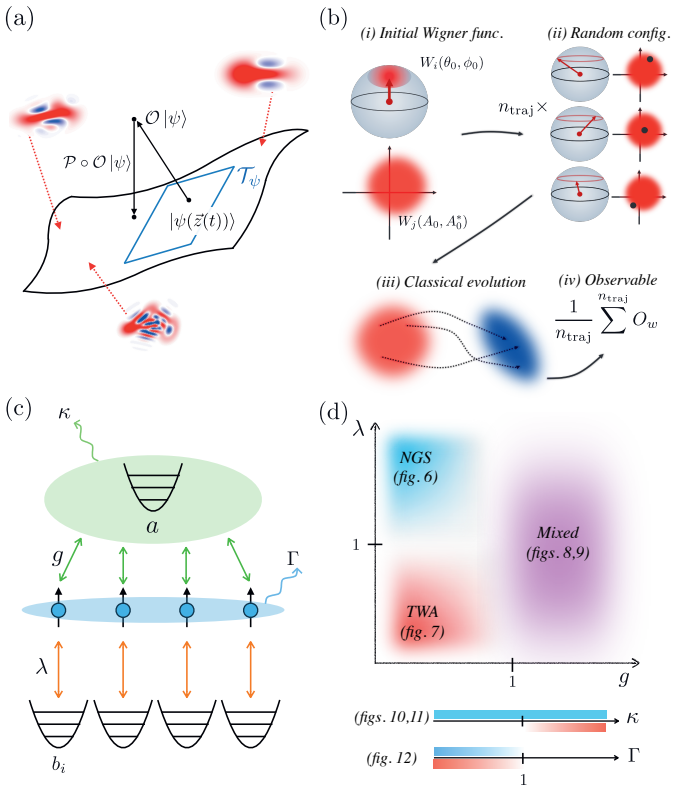


Figure 7.1: **(a)** Schematic overview of NGS. The ansatz $|\psi(\boldsymbol{z}(t))\rangle$ is a point in a manifold embedded in Hilbert space. For different variational parameters, we can describe different quantum states (some example Wigner functions are shown). The action of an operator $\hat{\mathcal{O}}$, which can be a Hamiltonian $\hat{H}$, non-Hermitian Hamiltonian $\hat{H}_{\rm eff}$, or quantum jump $\hat{c}$, can cause the state to leave the variational manifold, so the state is projected back using the projector $\hat{\mathcal{P}}$. **(b)** Schematic depiction of TWA. (*i*) The initial quantum state of the spin and bosonic degrees of freedom can be represented by the spin $W_i(\theta_0,\phi_0)$ and bosonic $W_j(A_0,A_0^*)$ Wigner functions, respectively. (*ii*) Classical phase-space points are individually sampled from the initial Wigner functions for each degree of freedom and (*iii*) evolve according to classical (stochastic) equations of motion. (*iv*) Expectation values are evaluated in phase space by computing the average of the associated Weyl symbols over $n_{\rm traj}$ phase-space trajectories. **(c)** NGS and TWA apply to generic spin-boson systems. Here we sketch the system studied in this Chapter: N_s spins-1/2 interacting with a common mode a with strength g and particle loss at rate κ. Each spin also interacts with a mode b at strength λ. The spins undergo collective loss at rate Γ. **(d)** Schematic summary of our results illustrating the regimes where each method tends to perform well together with the reference to figures studying the dynamics in the respective parameter regimes, see Fig. 7.4 and Sec. 7.3 for more details.

7.1 Open dynamics: combining NGS with quantum trajectories

There are several options for extending the NGS machinery to open dynamics. For instance, in Ref. [258], which in turn builds on the developments in Ref. [362], an ansatz for the density matrix was developed. This was then used to formulate the master equation and corresponding equations of motion governed by the Lindbladian. Here, we discuss how a variational state ansatz, such as the NGS ansatz introduced in Eq. (5.16), can be used within the quantum trajectories framework, which we reviewed in Sec. 5.4.2.

7.1.1 Equations of motion for non-Hermitian Hamiltonians

As discussed in Sec. 5.4.2, quantum trajectories consists of two types of evolution: continuous evolution under an effective non-Hermitian Hamiltonian $\hat{H}_{\text{eff}}$, and discrete quantum jump events. We begin by deriving equations of motion for evolution under $\hat{H}_{\text{eff}}$ following the procedure in Ref. [239]. The variational ansatz $|\psi\rangle$ evolves according to the Schrödinger equation,

$$\partial_t |\psi\rangle = -i\hat{H}_{\text{eff}} |\psi\rangle , \tag{7.1}$$

where the effective Hamiltonian is defined in Eq. (5.28) as $\hat{H}_{\text{eff}} = \hat{H} - \frac{i}{2}\sum_m \hat{c}_m^\dagger \hat{c}_m = \hat{H} - i\hat{K}$. McLachlan's variational principle requires the variation of the norm resulting from the Schrödinger equation to vanish, $\delta||(d/dt + i\hat{H}_{\text{eff}})|\psi\rangle|| = 0$. It is more convenient to work with the square norm,

$$||(\frac{d}{dt} + i\hat{H}_{\text{eff}})|\psi\rangle||^2 = \sum_{\mu,\nu} A_{\mu\nu}\dot{z}_\mu\dot{z}_\nu + \Big[i\langle v_\mu|\hat{H}_{\text{eff}}\rangle\dot{z}_\mu + \text{h.c.}\Big] + \langle \hat{H}_{\text{eff}}^\dagger \hat{H}_{\text{eff}}\rangle, \tag{7.2}$$

where empty kets refer to $|\psi\rangle$, and $A_{\mu\nu} = \langle v_\mu|v_\nu\rangle$ is the overlap between the μth and νth tangent vector. After making the substitutions,

$$C_\mu = \langle\psi|\hat{H}|v_\mu\rangle , \tag{7.3a}$$

$$D_\mu = \langle\psi|\hat{K}|v_\mu\rangle , \tag{7.3b}$$

and taking the variation, we obtain the equations of motion,

$$\sum_\nu \text{Re}[A_{\mu\nu}]\dot{z}_\nu = \text{Re}[D_\mu] + \text{Im}[C_\mu]. \tag{7.4}$$

The matrix $2\,\text{Re}[A_{\mu\nu}]$ is precisely the metric $g_{\mu\nu}$ of the tangent space introduced in Eq. (5.6). The vector $\text{Re}[D_\mu]$ can be related to gradients of the expectation value of the non-Hermitian part of $\hat{H}_{\text{eff}}$, $\partial_\mu\langle\hat{K}\rangle$, using,

$$2\,\text{Re}[\langle v_\mu|\hat{K}|\psi\rangle] = \langle v_\mu|\hat{K}|\psi\rangle + \text{h.c.} = \partial_\mu\langle\hat{K}\rangle, \tag{7.5}$$

where we used $\hat{K} = \hat{K}^\dagger$. For the SCS ansatz, expectation value gradients such as $\partial_\mu \langle \hat{K} \rangle$ can be computed analytically following the procedure in Sec. 5.3.

Although $\mathrm{Im}[C_\mu]$ can be computed from the overlap definition of Eq. (7.3a), if the tangent space is a Kähler manifold (i.e. if $J^2 = -1$, cf. Sec. 5.1), then from the relation $J^\mu{}_\nu \, |v_\mu\rangle = i \, |v_\nu\rangle$, within our existing real- and imaginary-time evolution framework it is more convenient to relate $\mathrm{Im}[C_\mu]$ to the complex structure $J^\mu{}_\nu$ and the gradient $\partial_\mu \langle \hat{H} \rangle$ using,

$$2 \, \mathrm{Im}[C_\nu] = i \, \langle v_\nu | \, \hat{H} \, | \psi \rangle - i \, \langle \psi | \, \hat{H} \, | v_\nu \rangle = - \sum_\mu J^\mu{}_\nu \, \partial_\mu \langle \hat{H} \rangle . \tag{7.6}$$

Because $J^\mu{}_\nu = -G^{\mu\sigma} \omega_{\sigma\nu}$, the non-Hermitian eoms of Eq. (7.4) can therefore be computed from $g_{\mu\nu}$, $\omega_{\mu\nu}$, $\partial_\mu \langle \hat{H} \rangle$, and $\partial_\mu \langle \hat{K} \rangle$. For an ansatz with M variational parameters, the total number of elements to compute scales as $M^2 + 2M$, compared to $M^2 + M$ for purely real- or imaginary-time evolution.

Example: Computing $\mathrm{Im}[C_\mu]$ for the coherent state ansatz. Here, we relate $\mathrm{Im}[C_\mu]$ to the energy gradients $\partial_\mu \langle H \rangle$ for the coherent state ansatz with explicit normalization and phase factors, $|\psi\rangle = e^{\kappa + i\theta} e^{-(x^2+y^2)/2} e^{(x+iy)a^\dagger} \, |0\rangle$, with $\boldsymbol{z} = (\kappa, \theta, x, y) \in \mathbb{R}$. The tangent vectors corresponding to $\mu \in \{1, 2, 3, 4\}$ are,

$$|v_1\rangle = |\psi\rangle \, , \tag{7.7a}$$
$$|v_2\rangle = i \, |\psi\rangle \, , \tag{7.7b}$$
$$|v_3\rangle = (a^\dagger - x) \, |\psi\rangle \, , \tag{7.7c}$$
$$|v_4\rangle = (ia^\dagger - y) \, |\psi\rangle \, . \tag{7.7d}$$

We begin by relating $\mathrm{Im}[C_1] = \mathrm{Im}[\langle \psi | \, \hat{H} \, | v_1 \rangle]$ to $\partial_{z_2} E$,

$$\mathrm{Im}[C_1] = -[i \, \langle \psi | \, \hat{H} \, | v_1 \rangle - i \, \langle v_1 | \, \hat{H} \, | \psi \rangle]/2 = -\partial_{z_2} E/2. \tag{7.8}$$

Similarly for $\mathrm{Im}[C_2] = \mathrm{Im}[\langle \psi | \, \hat{H} \, | v_2 \rangle]$, we have $\mathrm{Im}[C_2] = \partial_{z_1} E/2$. To relate $\mathrm{Im}[C_3] = \mathrm{Im}[\langle \psi | \, H \, | v_3 \rangle]$ to gradients of E we notice that we can write $i \, |v_3\rangle$ as a *real* span of the tangent vectors, $i \, |v_3\rangle = |v_4\rangle + y \, |v_1\rangle - x \, |v_2\rangle$. Using this we obtain,

$$\mathrm{Im}[C_3] = - \left(\partial_{z_4} E + y \partial_{z_1} E - x \partial_{z_2} E \right) /2. \tag{7.9}$$

Finally, we obtain $\mathrm{Im}[\langle v_4 | \, H \, | \psi \rangle] = \left(\partial_{z_3} E + x \partial_{z_1} E + y \partial_{z_2} E \right) /2$, where we used $i \, |v_4\rangle = - \, |v_3\rangle - x \, |v_1\rangle - y \, |v_2\rangle$. Therefore, we have related the computation of $\mathrm{Im}[C_\mu]$ to the energy gradients of $E = \langle \hat{H} \rangle$. In this example, we explicitly noticed that $i \, |v_\mu\rangle$ can be written as a real span of tangent vectors $\{|v_\mu\rangle\}$. In the Supplemental Material of Sec. 7.5, we provide the constructions of $g_{\mu\nu}$, $\omega_{\mu\nu}$ and $J^\mu{}_\nu$ for this single-mode coherent state ansatz, showing that $|v_\nu\rangle = J^\mu{}_\nu \, |\mu\rangle$, as derived in Eq. (7.6). We also prove that $J^2 = -1$.

Finally, we consider a simple example of non-Hermitian dynamics using the SCS ansatz and the eoms of Eq. (7.4) for $N_b = 1$ bosonic mode with $\hat{H}_{\text{eff}} =$

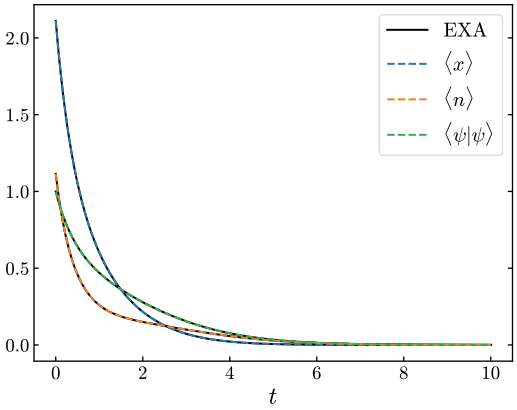


Figure 7.2: Dynamics of $\hat{H}_{\text{eff}} = \xi(\hat{a} + \hat{a}^\dagger) - (i/2)\kappa\hat{a}^\dagger\hat{a}$ with $\xi = 0.5$, $\kappa = 1.0$ using the SCS ansatz with $N_p = 2$. The non-Hermitian term corresponds to cavity loss jump operators. The initial state is a random superposition of two coherent states. SCS (dashed colors) agrees perfectly with exact numerics (solid black), including decay of the norm $\langle\psi|\psi\rangle$ due to the non-hermitian term.

7

$\xi(\hat{a}+\hat{a}^\dagger)-(i/2)\kappa\hat{a}^\dagger\hat{a}$. Because the Hamiltonian is a Gaussian operator, if the initial state can be accurately described by the SCS ansatz with N_p coherent states, SCS is exact in that it exactly captures the dynamics at all times also with N_p coherent states. Results for an $N_p = 2$ initial state and a comparison against exact numerics are shown in Fig. 7.2, depicting perfect agreement as expected.

7.1.2 Quantum jumps

We now incorporate the action of a quantum jump $\hat{c}_m$ in the SCS formalism. After each quantum jump the wavefunction may (i) remain in the variational manifold, or (ii) leave it. We discuss these two possibilities using the examples of single particle loss and gain, respectively. We have chosen these two processes as they are often the dominant sources of single particle decoherence in a variety of systems.

(i) Jumps inside the manifold

For a jump operator that produces a state that remains within the variational manifold, we consider single particle loss at rate $\kappa^{(1)}$. The jump operator is $\hat{c} = \sqrt{\kappa^{(1)}}\hat{a}$. The action of $\hat{c}$ on the single-mode SCS ansatz of Eq. (5.16) is,

$$\sqrt{\kappa^{(1)}}\hat{a}\,|\psi\rangle = \sqrt{\kappa^{(1)}}a\sum_p e^{\kappa_p+i\theta_p}\hat{D}(\alpha_p)\,|0\rangle = \sum_p e^{\kappa'_p+i\theta'_p}\hat{D}(\alpha_p)\,|0\rangle\,, \tag{7.10}$$

where we used $\hat{a}\,|\alpha\rangle = \alpha\,|\alpha\rangle$ and defined the updated norm and phase factors as,

$$\kappa'_p = \log\Big(\sqrt{\kappa^{(1)}}e^{\kappa_p}|\alpha_p|\Big), \tag{7.11a}$$

$$\theta'_p = \arg(\Big|\kappa^{(1)}\Big|e^{i\theta_p+\kappa_p}\alpha_p). \tag{7.11b}$$

We can easily extend the above analysis to the two-photon loss case with the jump operator $\hat{c} = \sqrt{\kappa^{(2)}}\hat{a}^2$, where the updated norm and phase factors are now,

$$\kappa'_p = \log\Big(\sqrt{\kappa^{(2)}}e^{\kappa_p}|\alpha_p|^2\Big), \tag{7.12a}$$

$$\theta'_p = \arg(\sqrt{\kappa^{(2)}}e^{i\theta_p+\kappa_p}\alpha_p^2). \tag{7.12b}$$

Importantly, our results rely on the coherent state being the eigenstate of the jump operator considered above. Thus, for any other state, e.g. the squeezed coherent state $|\alpha,\zeta\rangle$, the single-particle loss jump operator will take the state out of the variational manifold. This will be a more generic scenario for most jump operators. In the next section we describe how to deal with such situations.

(ii) Jumps outside the manifold

If the state after the jump is not within the variational manifold, we project it back to the manifold by maximizing its fidelity with the variational ansatz. To do so we use gradient descent (GD) as an efficient numerical procedure. We note that while simulated annealing (SA) finds a global extremum of a function in the asymptotic limit of infinitely slow cooling rate, we find that in all cases studied in this Chapter, the performance of GD is comparable to that of SA (the infidelity difference between the post-jump variational state found by each of the two methods is $\lesssim 10^{-3}$), with the advantage that GD is typically significantly faster.

Again, consider a single mode SCS ansatz, which for convenience we write as,

$$|\psi\rangle = \sum_{i=1}^{N_p} c_i\,|\alpha_i\rangle\,, \tag{7.13}$$

with complex coefficients c_i and complex amplitudes α_i. For single photon gain with jump operator $\hat{c} = \hat{a}^\dagger$, the state after applying the jump operator $\hat{a}^\dagger\,|\psi\rangle$ is projected back onto a generic variational state $|\tilde{\psi}\rangle$ by optimising its variational parameters $\tilde{c}_i, \tilde{\alpha}_i$ to maximize the normalized fidelity given by,

$$\mathcal{F} = \frac{|\langle\tilde{\psi}|\hat{a}^\dagger|\psi\rangle|^2}{|\langle\tilde{\psi}|\tilde{\psi}\rangle||\langle\psi|\hat{a}\hat{a}^\dagger|\psi\rangle|}, \tag{7.14}$$

where the un-normalized overlap is,

$$\langle\tilde{\psi}|\hat{a}^\dagger|\psi\rangle = \sum_{i,j}^{N_p} \tilde{c}_i^* c_j \tilde{\alpha}_i^* e^{-\frac{1}{2}(|\alpha|^2+|\tilde{\alpha}|^2)+\tilde{\alpha}_i^*\alpha_j}\,, \tag{7.15}$$

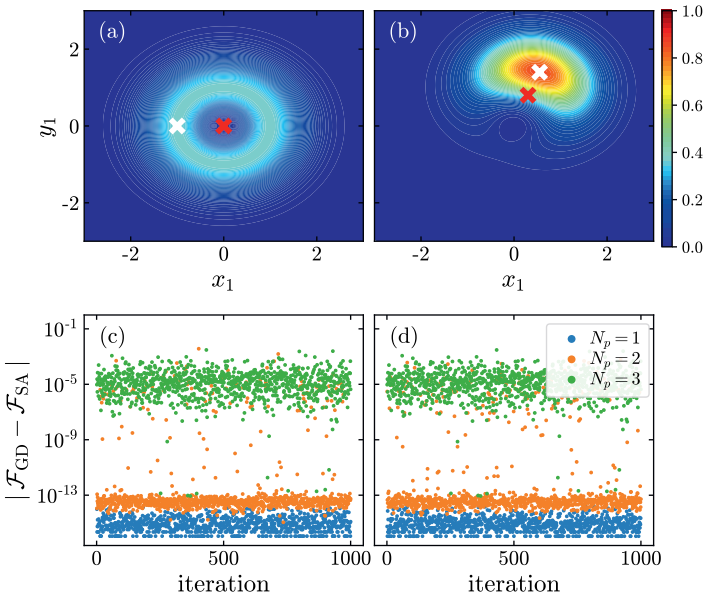


Figure 7.3: Panels **(a)** and **(b)** plot the fidelity of $\hat{a}^\dagger |\alpha\rangle$ projected back to the variational manifold formed by the set of all coherent states, $|\tilde{\alpha} = \tilde{x} + i\tilde{y}\rangle$, with initial states $|\alpha = 0\rangle$ (with a ring of global maxima due to the symmetry of $\hat{a}\,|0\rangle$) and $|\alpha = 0.3 + i0.8\rangle$, respectively. The red cross denotes the initial state, the white cross denotes the maximum of Eq. (7.15) found via GD. Panels **(c)** and **(d)** show the difference in optimized fidelities between GD versus bounded SA for jump operators $\hat{a}^\dagger$ and $\hat{x} = \hat{a} + \hat{a}^\dagger$, respectively.

and the normalization factors are,

$$\langle\psi|\psi\rangle = \sum_{i,j}^{N_p} c_i^* c_j e^{-\frac{1}{2}(|\alpha_i|^2 + |\alpha_j|^2 + \alpha_i^* \alpha_j)}, \tag{7.16a}$$

$$\langle\psi|\,\hat{a}\hat{a}^\dagger\,|\psi\rangle = \sum_{i,j}^{N_p} c_i^* c_j (1 + \alpha_i^* \alpha_j) e^{-\frac{1}{2}(|\alpha_i|^2 + |\alpha_j|^2) + \alpha_i^* \alpha_j}. \tag{7.16b}$$

In the case of $N_p = 1$, with $\alpha = |\alpha| e^{i\varphi_\alpha}$, $\tilde{\alpha} = |\tilde{\alpha}| e^{i\varphi_{\tilde{\alpha}}}$, Eq. (7.15) is maximized for $\varphi_{\tilde{\alpha}} = \varphi_\alpha$ and for amplitude of $\tilde{\alpha}$ which is the solution to $|\tilde{\alpha}|^2 - |\alpha|\,|\tilde{\alpha}| - 1 = 0$. For instance if $\alpha = 0$, $|\tilde{\alpha}| = 1$, $\forall \varphi_{\tilde{\alpha}}$, cf. Fig. 7.3(a), and similarly for $\alpha \neq 0$, cf. Fig. 7.3(b). The starting point of the GD search is denoted by the red cross and the maximum of the numerically found maximum of the overlap, Eq. (7.15), by the white cross. We remark that the achievable fidelity after projecting back to the manifold is strongly dependent on the jump operator and the number of coherent states. For instance, for the case shown in Fig. 7.3(a), the state after the jump is

a Fock state $|1\rangle$. As such, after projecting it back to a single coherent state, its fidelity is given by $\mathrm{e}^{-|\tilde{\alpha}|^2/2}|\alpha|^n/\sqrt{n!} \to \mathrm{e}^{-1/2} \approx 0.61$ with $n = 1$ and $|\tilde{\alpha}| = 1$.

In the case of the SCS ansatz with $N_p > 1$, the optimization landscape becomes more complex. In Fig. 7.3(c)-(d), for $N_p = 1$ (blue), $N_p = 2$ (orange) and $N_p = 3$ (green) we use Eq. (7.14) and plot the difference in optimized fidelities $|\mathcal{F}_{\mathrm{GD}} - \mathcal{F}_{\mathrm{SA}}|$, with the optimization performed by GD with backtracking ($\mathcal{F}_{\mathrm{GD}}$) and bounded SA ($\mathcal{F}_{\mathrm{SA}}$). We consider two quantum jumps, (c) single-particle gain $\hat{c} = \hat{a}^\dagger$ and (d) momentum kicks $\hat{c} = \hat{x} = \hat{a} + \hat{a}^\dagger$. Our choice of single-particle gain is motivated by its relevance to many spin-boson systems (see Sec. 7.3 and Sec. 7.4), whilst the momentum kick jump plays a crucial role in laser cooling large ion crystals [374]. We generate 10^3 initial (pre-jump) random states $|\psi\rangle$. As the generic variational starting state $|\tilde{\psi}\rangle$ to be optimized, for GD we use the pre-jump state $|\psi\rangle$, whilst for the SA we seed a random starting state $|\tilde{\psi}\rangle$ whose coefficients (see Eq. (7.13)) are drawn from a uniform unit distribution $\{c_i, \alpha_i, \tilde{c}_i, \tilde{\alpha}_i\} \in [0, 1]$. We set a sufficiently slow SA cooling rate such that the algorithm converges to the same local maxima irrespective of the randomly chosen starting point. For all the studied cases, the fidelities of the states obtained by the two numerical optimizers agree within $\lesssim 10^{-3}$.

7.1.3 Time evolution

We are now equipped to implement the quantum trajectories program for the SCS ansatz. In principle, one could evolve the wavefunction $|\psi\rangle$ between the jumps according to the equations of motion in Eq. (7.4) while tracking the decay of the norm to identify the time t_j of a jump. In practice we find it convenient to Trotterize the time evolution between jumps governed by $\hat{H}_{\mathrm{eff}}$ in the usual way as,

$$e^{-i(\hat{H}-i\hat{K})\delta t} \approx e^{-i\hat{H}\delta t} e^{-\hat{K}\delta t} \tag{7.17}$$

for sufficiently small δt. The norm during the unitary dynamics under $\mathrm{e}^{-i\hat{H}\delta t}$ is preserved due to the use of the norm factors κ as variational parameters (we note that the opposite case, namely the absence of a global norm factor as a variational parameter, can result in unphysical couplings, see Ref. [109]). During the imaginary-time evolution $\mathrm{e}^{-\hat{K}\delta t}$ we track the decay of the norm to determine the time of the jump t_j, at which point we apply the corresponding jump operator c_m.

7.2 Truncated Wigner Approximation for spins and bosons

The phase space picture of quantum mechanics provides alternative means to simulate and analyze the quantum many-body dynamics in systems with mixed spin and bosonic degrees of freedom, in particular in a semi-classical framework known as the truncated Wigner approximation (TWA) [373]. The Wigner-Weyl transform maps Hilbert space operators O of a quantum system to functions of classical phase space variables, known as Weyl symbols O_W. The Weyl symbol corresponding to

the density matrix is known as the Wigner function and provides a full ensemble description of arbitrary quantum states in terms of a (potentially negative) quasi-probability distribution.

A general Wigner-Weyl transform can be defined using the framework of phase point operators [375]. For example, considering particles in 1D with positions $\mathbf{x}$ and momenta $\mathbf{p}$, operators $\hat{\mathcal{A}}(\mathbf{x},\mathbf{p})$ for each point in phase space define the Wigner-Weyl transformation via $O_W(\mathbf{x},\mathbf{p}) = \mathrm{tr}[\hat{\mathcal{A}}(\mathbf{x},\mathbf{p})\hat{O}]/\sqrt{2\pi}$ and vice-versa, $\hat{O} = \int d\mathbf{x}d\mathbf{p}\, O_W(\mathbf{x},\mathbf{p})\hat{\mathcal{A}}(\mathbf{x},\mathbf{p})$. Given a proper orthonormal definition of phase point operators [375], for any state ρ and any observable $\hat{Q}$, expectation values can be evaluated from the Wigner function $W(\mathbf{x},\mathbf{p}) = \mathrm{tr}[\hat{\mathcal{A}}(\mathbf{x},\mathbf{p})\rho]/\sqrt{2\pi}$ via $\langle\hat{Q}\rangle = \int d\mathbf{x}d\mathbf{p}\, Q_W(\mathbf{x},\mathbf{p})W(\mathbf{x},\mathbf{p})$. Equivalent constructions can be made for spin phase spaces, either using spin-boson mappings (suitable for large spin scenarios) [373], using spherical coordinate representations of spins $A(\theta,\phi)$ [365], or for phase spaces using only a discrete set of points [375].

Closed system eoms can be obtained by Wigner-Weyl transforming the Heisenberg eoms, which leads to the exact quantum dynamics for Weyl symbols being governed by $\dot{Q}_W(\mathbf{x},\mathbf{p}) = \{Q_W(\mathbf{x},\mathbf{p}), H_W(\mathbf{x},\mathbf{p})\}_{\mathrm{MB}}$, using the Weyl symbol of the Hamiltonian H_W, and the Moyal bracket $\{Q_W, H_W\} = 2Q_W \sin(\mathbf{\Lambda}/\mathbf{2})H_W$, with $\mathbf{\Lambda}$ the symplectic operator (with $\hbar \equiv 1$), $\mathbf{\Lambda} = \sum_i \frac{\overleftarrow{\partial}}{\partial x_i}\frac{\overrightarrow{\partial}}{\partial p_i} - \frac{\overleftarrow{\partial}}{\partial p_i}\frac{\overrightarrow{\partial}}{\partial x_i}$. Expanding the sine function in the Moyal bracket at the lowest order is know as TWA and leads to a classical evolution of Weyl symbols, $\dot{Q}_W(\mathbf{x},\mathbf{p}) \approx \{Q_W(\mathbf{x},\mathbf{p}), H_W(\mathbf{x},\mathbf{p})\}_{\mathrm{P}}$, where $\{\cdot,\cdot\}_{\mathrm{P}}$ now denotes the classical Poisson bracket. The Poisson bracket ensures that the Weyl symbols for any complex observable will always factorize into phase-space variables, and therefore in TWA it suffices to only compute the classical evolution of the phase-space variables [361]. This makes TWA a very practical and efficient numerical method for the case of a positive initial Wigner function: Random positions and momenta can be sampled from the Wigner function and evolved in parallel using classical equations of motion giving $\mathbf{x}_\eta(t)$ and $\mathbf{p}_\eta(t)$ for trajectory η. Expectation values in TWA are then statistically approximated by $\langle\hat{Q}\rangle \approx \frac{1}{n_{\mathrm{traj}}}\sum_\eta^{n_{\mathrm{traj}}} Q_W(\mathbf{x}_\eta(t),\mathbf{p}_\eta(t))$, using n_{traj} trajectories.

Importantly, for small-spin systems, and in particular for spin-1/2 models as considered here, TWA can be drastically improved when using a sampling of the initial Wigner function using only a discrete set of initial phase points [102]. Considering a system consisting of a single spin-1/2 described by the Pauli operators $\hat{\boldsymbol{\sigma}} = (\hat{\sigma}_x, \hat{\sigma}_y, \hat{\sigma}_z)$, we define the corresponding phase-space variables as $\mathcal{S} = (S_x, S_y, S_z)$. One can then define discrete Wigner functions which are only defined for the 8 different discrete points, $\mathcal{S}_0 = (\pm 1, \pm 1, \pm 1)$. For example, taking a state of N_s spin-1/2 particles of the form $|\psi\rangle = \bigotimes_{i=1}^{N_s} |{\downarrow}\rangle_i$, any possible observable can be exactly described by sampling each spin from a discrete Wigner function with the only non-zero values of $W_i^{\downarrow}(S_x = \pm 1, S_y = \pm 1, S_z = -1) = 1/4$. Correspondingly, the state $|{\uparrow}\rangle_i$ is exactly described by the discrete distribution with non-zero elements $W_i^{\uparrow}(S_x = \pm 1, S_y = \pm 1, S_z = +1) = 1/4$.

Furthermore, it can be shown in general that equivalent discrete sampling strategies can lead to exact quantum state descriptions for general discrete D-level sys-

tems and for eigenstates of general spin-S operators, in the sense that the measurement statistics for any observable can be exactly reproduced from sampling the Wigner function [361]. Discrete sampling in combination with classical evolution is known as (generalized) discrete truncated Wigner approximation, (G)DTWA [102, 361]. Classical eoms for the spin-variables can be derived by Wigner-Weyl transforming the Heisenberg eoms while factorizing the Weyl symbols into the phase-space variables. (G)DTWA has been shown to capture quantum features in spin-model dynamics in several theory settings [369, 371, 376–378], and in comparison with experiments [368, 370, 379, 380].

Below, we consider a system consisting of spin and bosonic $\hat{a}(\hat{a}^\dagger)$ degrees of freedom. For the bosonic part we consider the complex numbers $\hat{a} \to A$ and $\hat{a}^\dagger \to A^*$ as the classical phase space. For additional bosonic degrees of freedom with operators $\hat{b}(\hat{b}^\dagger)$ one can introduce a corresponding classical phase space with $\hat{b}(\hat{b}^\dagger) \to B(B^*)$ (see for example Sec. 7.3). For a system with N_s spin-1/2 particles coupled to $N_{a/b}$ bosonic modes a/b, computing expectation values of an observable $\hat{Q}(\hat{\boldsymbol{\sigma}}_i, \hat{a}_j, \hat{b}_k)$ with TWA at time t corresponds to numerically evaluating,

$$\langle \hat{O}\left(t; \{\hat{\boldsymbol{\sigma}}_i, \hat{a}_j, \hat{b}_k\}\right)\rangle \approx \int \prod_{i=1}^{N_s}\prod_{j=1}^{N_a}\prod_{k=1}^{N_b} d\mathcal{S}_0^i d^2A_0^j d^2B_0^k \tag{7.18}$$
$$W_i(\mathcal{S}_0^i)W_j(A_0^j)W_k(B_0^k) O_W\left(\{\mathcal{S}_{\rm cl}^i(t), A_{\rm cl}^j(t), B_{\rm cl}^k(t)\}\right),$$

where $d\mathcal{S}_0 = dS_0^x dS_0^y dS_0^z$, $d^2A_0 = d\mathrm{Re}A_0 d\mathrm{Im}A_0/\pi$, and the subscript 0 indicates the initial values at $t = 0$. The classical variables for spin i and bosons j and k are sampled from the initial Wigner functions $W_i(\mathcal{S}_0^i)$, $W_j(A_0^j)$, and $W_k(B_0^k)$, respectively. Note that we always assume an initial product state between all degrees of freedoms such that the Wigner functions factorize. For the spins we will use the discrete distributions $W_i^{\uparrow/\downarrow}$ defined above, while for the bosonic modes we use standard continuous Wigner functions, in particular,

$$W_j(A_0^j) = \frac{1}{2\pi w_j^2}\exp\Big\{-|A_j - \bar{\alpha}_j|^2/(2w_j^2)\Big\}, \tag{7.19}$$

where $w_j^2 = (\bar{n}_j + 1/2)/2$ and α center of the Wigner function. For the vacuum state $\bar{n}_j = \bar{\alpha}_j = 0$, while for a coherent state $|\alpha\rangle$, $\bar{n}_j = 0$ and $\bar{\alpha}_j = \alpha$ (see Refs. [107, 373] for more details). $O_W\left(\{\mathcal{S}_{\rm cl}^i(t), A_{\rm cl}^j(t), B_{\rm cl}^k(t)\}\right)$ is the Weyl symbol corresponding to the observable of interest. We use the subscript cl on the time-dependent variables $\mathbf{S}_{\rm cl}^i(t)$, $A_{\rm cl}^j(t)$, and $B_{\rm cl}^k(t)$ to indicate that they obey the classical equations of motion for spin i, boson j, and boson k, respectively. In Sec. 7.3 below we will provide the full classical equations of motion for our problem of interest for examples of both closed and open system dynamics. (G)DTWA methods have been recently developed further to also include open-system dynamics under Lindblad master equations [280, 363–366]. For our simulations we follow the procedure in Ref. [365] and use a spherical coordinate parametrization of the phase space for spin i with

phase point operators defined as,

$$\mathcal{A}_i(\theta_i, \phi_i) = \frac{1}{2}[\mathbb{1}_i + \mathbf{s}(\theta_i, \phi_i) \cdot \boldsymbol{\sigma}_i], \tag{7.20}$$

where $\mathbf{s}_i = \sqrt{3}(\sin\theta_i \cos\phi_i, -\sin\theta_i \sin\phi_i, -\cos\theta_i)^\intercal$ is the vector on the surface of a sphere with radius $\sqrt{3}$.

In Ref. [365] it was shown that for open spin-1/2 models, it is convenient to work with flattened Wigner functions of the form $\chi_i(\theta_i, \phi_i) \equiv W_i(\theta_i, \phi_i)\frac{\sin\theta_i}{2\pi}$. The equations of motion for an open system can then be found by deriving correspondence rules (reminiscent of Bopp representations for for bosonic systems [373]), i.e. rules for mapping terms such as $X_i\rho_i$, $\rho_i X_i$, or $X_i\rho_i X_i^\dagger$ with Pauli operators $X = \sigma_i^{x,y,z}$ to the phase space, which leads to terms incorporating the four linearly independent differential operations $\mathbb{1}, \frac{d}{d\theta_i}, \frac{d}{d\phi_i}, \frac{d^2}{d\phi_i^2}$ acting on $\chi(\theta_i, \phi_i)$. It can be shown that the resulting EOMs lead to standard Fokker-Planck equations. This is only valid, without further approximations, for systems of non-interacting spins or if the initial state is a large coherent spin state. In these scenarios, the dynamics are given by the solution to the Fokker-Planck equations. Rather than solving these equations directly, we solve the corresponding Itô stochastic differential equations and average the relevant expectation values over many trajectories [269].

In our discrete sampling we select the initial angles θ_i, ϕ_i according to the parametrization given in Eq. (7.19). However, rather than sampling from the discrete $W_i^{\uparrow/\downarrow}$ Wigner distribution, we sample from a slightly modified flattened Wigner function,

$$\chi^{\uparrow/\downarrow}(\theta, \phi) = \frac{1}{2\pi}\delta(\theta \pm \arccos\frac{1}{\sqrt{3}}), \tag{7.21}$$

which is generated by rotating the discrete Wigner function $W_i^{\uparrow/\downarrow}$ around the z-axis. This initial Wigner function is uniform in ϕ and thus guarantees that $\frac{\partial^2}{\partial\phi_m\partial(\theta_n-\theta_{n+1})}$ cross diffusion terms, which are dropped in TWA, vanish at $t = 0$ [365]. For more details, we refer the reader to Ref. [365] and Sec. 7.3 where the detailed equations for our problem of interest are introduced.

7.3 Results

To evaluate the performance of our two numerical methods, we consider the disordered Holstein-Tavis-Cummings model describing a system of N_s spins coupled to a single bosonic mode (a), representing a coupling to a cavity mode, and N_s local vibrational modes (b_i) associated with each spin. The system is described by the Hamiltonian [104],

$$\hat{H} = \hat{H}_{\mathrm{TC}} + \hat{H}_{\mathrm{vib}} + \hat{H}_{\mathrm{H}} + \hat{H}_{\mathrm{dis}}, \tag{7.22}$$

where,

$$\hat{H}_{\mathrm{TC}} = \frac{\Delta}{2}\sum_{j=1}^{N_s}(\hat{\sigma}_j^z + \mathbb{1}) + \frac{g}{\sqrt{N_s}}\sum_{j=1}^{N_s}\hat{a}\hat{\sigma}_j^+ + \hat{a}^\dagger\hat{\sigma}_j^-, \tag{7.23a}$$

$$\hat{H}_{\mathrm{vib}} = \nu\sum_{j=1}^{N_s}\hat{b}_j^\dagger\hat{b}_j, \tag{7.23b}$$

$$\hat{H}_{\mathrm{H}} = -\frac{\lambda\nu}{2}\sum_{j=1}^{N_s}(\hat{b}_j + \hat{b}_j^\dagger)(\hat{\sigma}_j^z + \mathbb{1}), \tag{7.23c}$$

$$\hat{H}_{\mathrm{dis}} = -\frac{1}{2}\sum_{j=1}^{N_s}\epsilon_j(\hat{\sigma}_j^z + \mathbb{1}). \tag{7.23d}$$

Here Δ describes the detuning of the spin transition frequency relative to the cavity mode, $g/\sqrt{N_s}$ the single-spin coupling to the cavity, ν the frequency of the vibrational modes, λ the relative strength of the Holstein coupling, and ϵ_j the disorder in the transition frequency for spin j.

The dynamics of the Holstein-Tavis-Cummings model, in particular in the presence of disorder, has importance e.g. in the field of polaritonic chemistry [261]. It has been previously studied using a matrix product state method [104], and also using a similar non-Gaussian state framework to the one discussed here [118]. By tuning the relative strength of the various terms, this Hamiltonian can be reduced to spin-boson Hamiltonians applicable e.g. to trapped ion quantum simulators, impurity models, and quantum chemistry. The relative strength of g, λ, and ν allows us to go from the weak coupling regime between the spin and bosonic degrees of freedom, to a model governed by a Tavis-Cummings type interaction, to a Holstein coupling, or a combination thereof. We schematically illustrate the performance of the two numerical methods in each of these regimes in Fig. 7.4(a).

Furthermore, we investigate how both methods perform in the presence of sources of decoherence. In this case, we are interested in the evolution of the density matrix ρ as described by the Lindblad master equation given in Eq. (5.27). We study open dynamics with the following types of Lindblad jump operators,

- Cavity decay (rate κ): $\hat{c}_m = \sqrt{\kappa}\hat{a}$,
- Single spin decay (rate γ): $\hat{c}_m = \sqrt{\gamma}\hat{\sigma}_i^-$, and
- Collective spin decay (rate Γ): $\hat{c}_m = \sqrt{\Gamma}\sum_i \hat{\sigma}_i^-$.

We summarize the performance of the two methods in the presence of these decoherence sources schematically in Fig. 7.4(b).

7.3.1 Details of SCS and TWA simulations

In principle the SCS ansatz can be used directly to treat the spin degrees of freedom. However, to avoid the explicit exponential scaling with N_s, we use a Holstein-

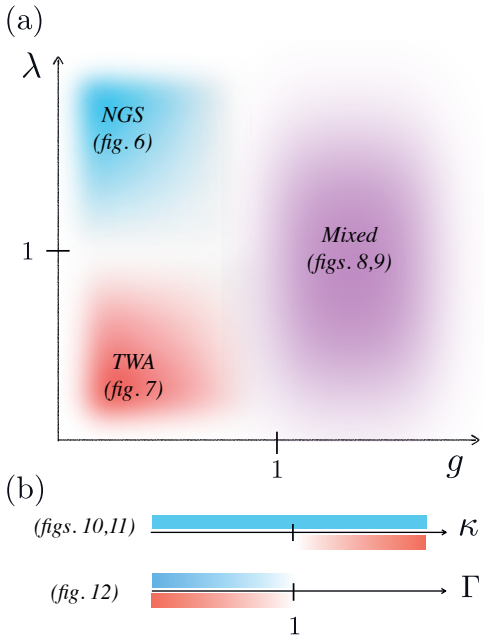


Figure 7.4: Schematic of the performance of SCS and TWA for **(a)** closed and **(b)** open dynamics. In this Chapter the NGS ansatz is an SCS ansatz (i.e. squeezing), limited to at most $N_p = 16$ multi-mode coherent states. **(a)** The performance in $g - \lambda$ parameter space for closed dynamics. When $g, \lambda \lesssim 1$, TWA performs well, whilst when $g \lesssim 1, \lambda \gtrsim 1$, SCS is the better choice. When $g \gtrsim 1$, TWA captures short-time dynamics, but can produce incorrect mid- to late-time results. In comparison, SCS typically does not capture quantitative details beyond the first spin relaxation, but does provide qualitative insights into the dynamics by correctly capturing the magnitude of the persistent spin-cavity dynamics. **(b)** Open dynamics. We operate in the $g \lesssim 1$, $\lambda \gtrsim 1$ region, so SCS outperforms TWA at small κ. At large κ, TWA performs well again, with both SCS and TWA agreeing. When evolving under only $\hat{H}_{\mathrm{TC}}$ with the spins decaying collectively at rate Γ, SCS and TWA agree when using the large N_s Holstein-Primakoff (HP) transformation at small Γ. At large Γ the collective spin quickly decays to the ground state, which is inaccessible as the first order expansion of the root in HP is no longer sufficient near the ground state since it was expanded around the excited state (small $a_s^\dagger a_s$), so neither method is able to capture intermediate- to late-time dynamics.

Primakoff (HP) transformation to map each spin-1/2 to a bosonic mode. We use the following form of the HP transformation [381],

$$\hat{S}_+ = (1 - \hat{a}_s^\dagger \hat{a}_s)\hat{a}_s, \tag{7.24a}$$

$$\hat{S}_z = 1/2 - \hat{a}_s^\dagger \hat{a}_s, \tag{7.24b}$$

which is exact for spin-1/2, and where we use the s subscript to denote a bosonic operator acting on the spin degree of freedom. As such, the dynamics are restricted to the $|0\rangle \equiv |e\rangle$ and $|1\rangle \equiv |g\rangle$ subspace, with $|g\rangle\langle g| = \hat{a}_s^\dagger \hat{a}_s$ and $|e\rangle\langle e| = 1 - \hat{a}_s^\dagger \hat{a}_s$. The vacuum is a Gaussian state and can therefore be described using only $N_p = 1$. The Fock state $|1\rangle$ can be described using $N_p = 2$, by $|1\rangle = 1/\mathcal{N} \lim_{\alpha\to 0}(|\alpha\rangle - |-\alpha\rangle)$, where $\mathcal{N}$ is a normalization factor [382], with $\alpha \sim 0.001$ sufficient to describe the state with high fidelity. As such, each spin can be captured using $N_p = 3$.

For the SCS simulations, we employ the SCS ansatz with $N_b = 2N_s + 1$ modes. We include cavity decay at strength γ using the parameter-update procedure of Sec. 7.3. Note that as a consequence of the HP mapping, the ansatz is not well-suited to some scenarios. For example, there is no spin-spin coupling when evolving under only $\hat{H}_{\text{dis}}$, so an unentangled initial state will evolve as a tensor product of single spins, each requiring $N_p = 3$. The required N_p therefore scales exponentially in the number of spins, 3^{N_s}. This limitation could potentially be mitigated by modifying the ansatz to be a superposition of squeezed displaced Fock states [258].

The initial state used for all SCS simulations includes a small amount of randomness for each variational parameter to break the degeneracy of the Gaussian states. We draw random values from a uniform distribution between $(0, 10^{-4})$. We find that this is sufficient to ensure each Gaussian state in the superposition evolves independently, whilst preserving extremely small infidelity with the true initial state, $1 - \mathcal{F}(t = 0) < \mathcal{O}(10^{-6})$, as seen in Fig. 7.12 in Sec. 7.5.

For the TWA simulations, to more accurately capture the dynamics of the cavity and vibrational modes, we extend the set of TWA equations by including the classical equations of motion for the mode excitation numbers $\hat{a}^\dagger \hat{a} \to N_A, \hat{b}_k^\dagger \hat{b}_k \to N_{B_k}$. Including all three sources of decoherence described above, the stochastic equations of motion for the spin degrees of freedom are,

$$\begin{aligned}\dot{\theta}_{i,\text{cl}} = {} & (\Gamma + \gamma)(\cot\theta_{i,\text{cl}} - \frac{\csc\theta_{i,\text{cl}}}{\sqrt{3}}) + \frac{2g}{\sqrt{N_s}} \text{Im}[e^{-i\phi_{i,\text{cl}}} A_{\text{cl}}] \\ & - \frac{\Gamma\sqrt{3}}{2} \sum_j \cos(\phi_{i,\text{cl}} - \phi_{j,\text{cl}}) \sin\theta_{j,\text{cl}},\end{aligned} \tag{7.25a}$$

$$\begin{aligned}d\phi_{i,\text{cl}} = {} & \big(-\Delta + \epsilon_n + 2\lambda\nu \,\text{Re}[B_{i,\text{cl}}] - \frac{2g}{\sqrt{N_s}} \cot\theta_{i,\text{cl}} \,\text{Re}[A_{\text{cl}} e^{-i\phi_{i,\text{cl}}}] \\ & - \frac{\Gamma\sqrt{3}}{2} \sum_j \cot\theta_{i,\text{cl}} \sin\theta_{j,\text{cl}} \sin(\phi_{i,\text{cl}} - \phi_{j,\text{cl}}) \big) dt \\ & + \sqrt{(\Gamma + \gamma) f(\theta_{i,\text{cl}})} dW_{\phi_i},\end{aligned} \tag{7.25b}$$

where we introduced the function $f(\theta_{i,\text{cl}}) = 1 + 2\cot\theta_{i,\text{cl}}{}^2 - 2\cot\theta_{i,\text{cl}} \csc\theta_{i,\text{cl}}/\sqrt{3}$. The stochastic behaviour of the equations of motion is generated by the Wiener increments dW_{ϕ_i} acting on ϕ_i. For each timestep dt, the Wiener increment dW_{ϕ_i} for each angle is independently drawn from a normal distribution with zero mean and a variance of dt.

The equations of motion for the bosonic degrees of freedom are given by,

$$\dot{A_{\rm cl}} = -\frac{\kappa}{2}A_{\rm cl} - i\frac{\sqrt{3}g}{2\sqrt{N_s}}\sum_i e^{i\phi_{i,\rm cl}}\sin\theta_{i,\rm cl}, \tag{7.26a}$$

$$\dot{N}_{A,\rm cl} = -\kappa N_{A,\rm cl} - \frac{\sqrt{3}g}{\sqrt{N_s}}\sum_i \sin\theta_{i,\rm cl}\,\mathrm{Im}[A_{\rm cl}e^{-i\phi_{i,\rm cl}}], \tag{7.26b}$$

$$\dot{B}_{k,\rm cl} = -i\nu B_{k,\rm cl} + i\frac{\lambda\nu}{2}\left(1-\sqrt{3}\cos\theta_{k,\rm cl}\right), \tag{7.26c}$$

$$\dot{N}_{B_{k,\rm cl}} = \lambda\nu\left(1-\sqrt{3}\cos\theta_{k,\rm cl}\right)\mathrm{Im}[B_{k,\rm cl}]. \tag{7.26d}$$

7.3.2 Closed system dynamics

Here, we compare the performance of the two numerical methods. We consider a system with $N_s = 3$ spins, the corresponding three phonon modes, and one cavity mode. For this system size and suitable initial states and Hamiltonian parameters, choosing a moderate Fock state truncation ~ 10 allows us to compare our results to exact numerics. Our initial state is spins polarized up, the vibrational modes in the vacuum, and the cavity in a coherent state, $|\psi(0)\rangle = |\uparrow\rangle^{\otimes N_s}|\alpha = 1\rangle_a|0\rangle_b^{\otimes N_s}$. Note in contrast to Ref. [118] our initial state is a superposition of several excitation manifolds precluding further simplifications to the ansatz.

For all closed dynamics simulations, we set $\Delta = 0$. For evolution under the Holstein-Tavis-Cummings model of Eq. (7.22), we find that while both methods are generally able to capture the short time dynamics, at later times they outperform one another in different parameter regimes. Our findings are summarized in Fig. 7.4(a), where we qualitatively depict the performance for different parameter regimes in the absence of decoherence. More detailed dynamics for each regime are plotted in Figs. 7.5-7.8, with the first and second rows of each figure showing dynamics without and with disorder ϵ, respectively.

We begin in the weak coupling regime $g = \lambda = 0.1$, shown in Fig. 7.5. Here the dynamics is slow on the considered time-scale. In both the disorder-free (first row) and disordered (second row) settings, SCS and TWA accurately capture the small fluctuations of the vibrational modes. Both methods also capture the initial spin relaxation, however SCS misses the revival time. TWA's ability to capture the first oscillation appears universally in all of the parameter regimes considered in this Chapter. This behaviour can be understood as follows: due to our choice of a factorizable initial state with a corresponding positive semi-definite Wigner function, the TWA sampling is able to reproduce the initial state, and the mean-field and low order correlations that are generated during the short-time dynamics. A generic feature of TWA is that when extending into the medium- to long-time dynamics, the potential buildup of higher order correlations is not captured by the method. While this not visible in Fig. 7.5, it can be seen clearly in the figures corresponding to the regimes discussed below.

The second regime we consider is the strong spin-vibrational coupling $\lambda \gg g$,

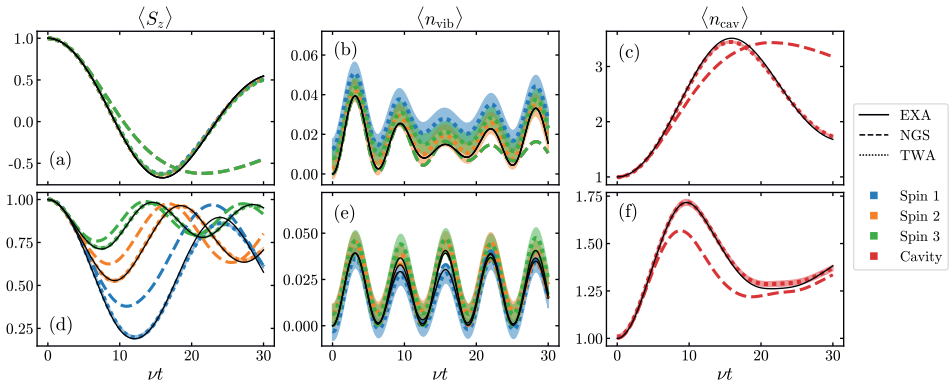


Figure 7.5: **Closed dynamics**: $g = \lambda = 0.1$, $\Delta = 0$. **Top row**: without disorder. Both SCS and TWA capture the initial spin relaxation, but SCS incorrectly predicts a slower revival. **Bottom row**: disordered, $\boldsymbol{\epsilon} = [2g, 3g, 4g]$. Here, TWA captures the dynamics more accurately compared to SCS. SCS is with $N_p = 4$, TWA is with $n_{\text{traj}} = 10^4$ with standard error shaded.

shown in Fig. 7.6. Here we expect SCS to perform well, as SCS is exact with any coherent state number N_p for $\hat{H}_{\text{H}}$. In the disorder-free regime (top row), although SCS with $N_p = 12$ does not fully capture the dynamics at late times, it does outperform TWA, which majorly underestimates the spin decay. In this case, the lack of disorder is challenging for our SCS ansatz: each spin evolves identically, requiring the superposition of coherent states to be factored into a product. This symmetry is broken when introducing disorder (second row), and we see that SCS captures accurately the dynamics for all considered times, including the initial decay and then revival of $\langle \hat{S}_z \rangle$. For TWA, although the numerics match better for the vibrational dynamics in the presence of disorder, this is primarily a consequence of the fact that the disorder causes the Holstein interactions to dominate, and the spin and cavity dynamics continue to disagree with the exact solution.

Thirdly, we move to the strong spin-cavity coupling regime, $g \gg \lambda$, shown in Fig. 7.7. After accurately capturing the first oscillation, the TWA spin dynamics equilibrate about $\langle \hat{S}_z \rangle \sim 0$ unlike the exact dynamics which, although they do oscillate about $\langle \hat{S}_z \rangle \sim 0$, exhibit persistent oscillations with magnitude $\langle \hat{S}_z \rangle \sim 1/2$. Similarly, NGS with $N_p = 4$ coherent states fails to capture any of the spin, vibration, or cavity dynamics. This is unsurprising because, in this regime where the Tavis-Cummings term dominates, we expect the number of coherent states required to scale as $\sim 3^{N_s}$, as each spin must be described using $N_p = 3$ coherent states. Although increasing N_p would eventually improve the accuracy, we found that increasing it up to $N_p \lesssim 16$ did not provide a substantial increase in accuracy, whilst increasing the computational cost. In principle, TWA does not suffer from the same problem. However, if one needs to access higher order correlations with TWA, the introduction of higher order cumulants and the BBGKY hierarchy may

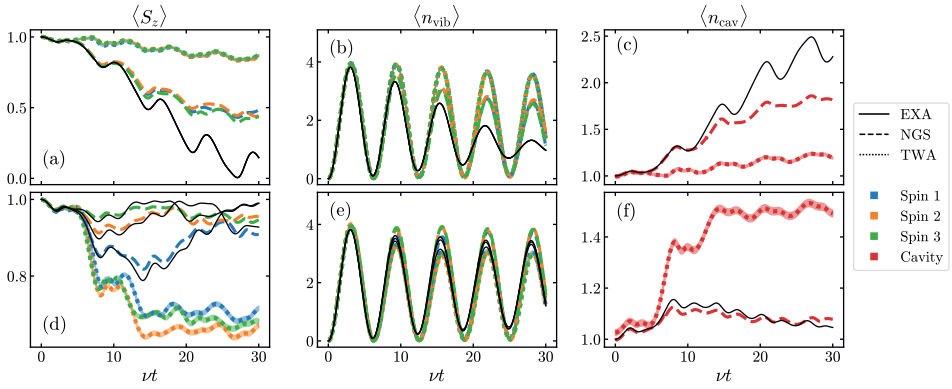


Figure 7.6: **Closed dynamics**: $g = 0.1, \lambda = 1, \Delta = 0$. **Top row**: without disorder. Neither TWA nor SCS completely capture the spin-cavity observables, but SCS more closely tracks the dynamics **Bottom row**: disordered, $\boldsymbol{\epsilon} = [2g, 3g, 4g]$. NGS performs well, capturing all dynamics with small error. Interestingly, here TWA over estimates the magnitude of changes in the spin-cavity observables. Here SCS uses $N_p = 12$, TWA is with $n_{\text{traj}} = 10^4$ with standard error shaded.

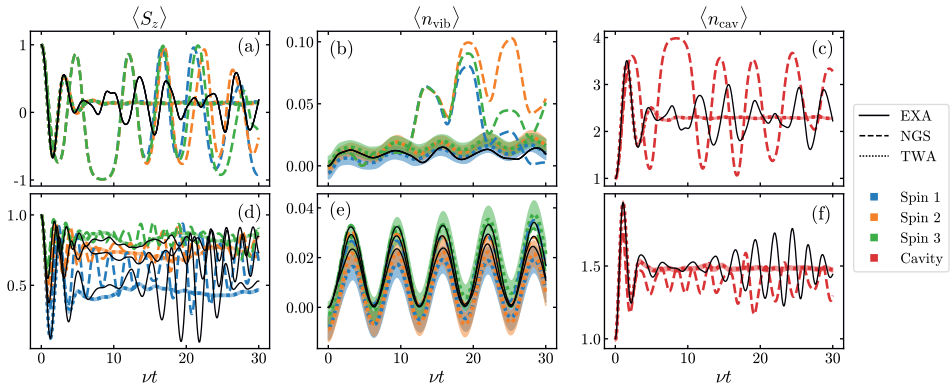


Figure 7.7: **Closed dynamics**: $g = 1$, $\lambda = 0.1$, $\Delta = 0$. **Top row**: without disorder. Beyond initial spin relaxation, both TWA and SCS perform relatively poorly. TWA incorrectly predicts equilibration of the spin-cavity dynamics. SCS does continue to produce spin-cavity dynamics, but overestimates the magnitude of the oscillations. **Bottom row**: disordered, $\boldsymbol{\epsilon} = [2.6g, 3.2g, 4.2g]$. TWA incorrectly predicts equilibration of both spin and cavity observables after the first oscillation, whilst SCS produces qualitatively correct dynamics, even with only $N_p = 4$ coherent states. Here SCS uses $N_p = 2$ for the first row and $N_p = 4$ for the second row, and TWA is with $n_{\text{traj}} = 10^4$ with standard error shaded.

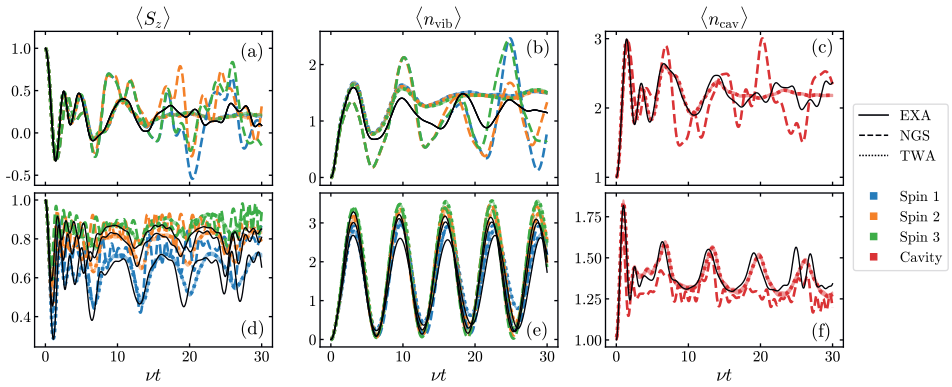


Figure 7.8: **Closed dynamics**: $g = 1$, $\lambda = 1$, $\Delta = 0$. **Top row**: without disorder. TWA accurately captures the dynamics at early times as compared to the SCS. **Bottom row**: disordered, $\boldsymbol{\epsilon} = [2.6g, 3.2g, 4.2g]$. TWA correctly captures key oscillations, even at late times. SCS also captures some of these features, but less accurately. Both methods perform similarly for the vibrational dynamics. Here SCS uses $N_p = 4$, TWA is with $n_{\text{traj}} = 10^4$ with standard error shaded.

become necessary. This poses an analogous problem to the number of Gaussian states in the ansatz: an exponentially increasing number of equations and potential numerical instabilities [1].

Fourthly, we consider the strong spin-cavity and spin-vibration regime $\lambda = g = 1$, shown in Fig. 7.8. Without disorder, both methods struggle to capture the dynamics at late times, although TWA in particular is able to capture qualitative features with reasonable accuracy. Introducing disorder breaks the collective nature of the spins, enabling both methods to more accurately track the dynamics. TWA is able to qualitatively reproduce the periodic peaks in the spin and cavity dynamics at even later times than SCS. Both methods correctly obtain the vibrational dynamics.

Finally, we note that an advantage of SCS is the accessibility of the wavefunction. This means that any desired quantity, including entanglement entropy, can be computed. Furthermore, for small systems, strict performance measures such as the fidelity can be easily computed. These are shown in the Supplemental Material of Sec. 7.5 for the four different coupling regimes (g, λ) considered in Figs. 7.5-7.8. The analogous plots for TWA cannot be generated.

[1] In the numerical implementation of SCS we observe that for certain initial states the equations of motion become numerically unstable, which we attribute to the singularity of the metric g and the associated need to perform a pseudo-inverse instead of the inverse in the evaluation of $G = g^{-1}$. Dealing with this issue is a matter of current and future work

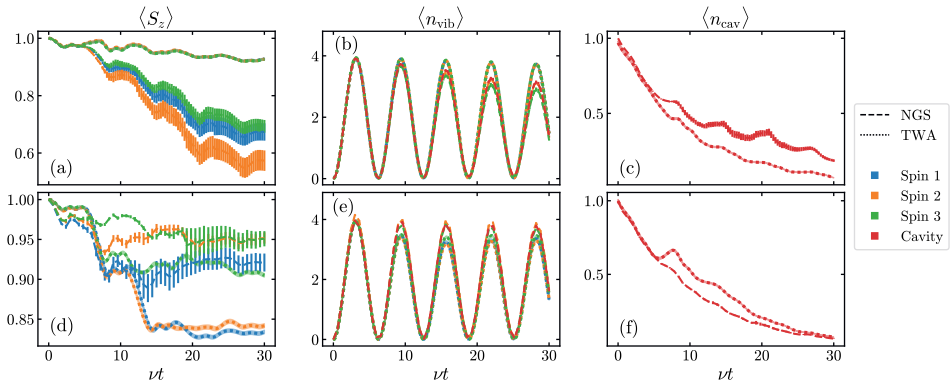


Figure 7.9: **Open dynamics**. $g = 0.1$, $\lambda = 1$, $\Delta = 0$ and cavity decay $\kappa = g$. **Top row:** without disorder. **Bottom row:** with disorder $\boldsymbol{\epsilon} = [2g, 3g, 4g]$. SCS and TWA capture the same short-time dynamics, but disagree beyond $\nu t \sim 5$. Based on the corresponding closed dynamics results Fig. 7.6, we expect SCS to be more reliable in this regime. Exact numerics is challenging for open dynamics of systems of this size, see Fig. 7.13 for benchmarking of smaller systems. Here SCS uses $N_p = 8$ and $n_{\text{traj}} = 40$ with standard error indicated by the error bars, TWA is with $n_{\text{traj}} = 10^4$ with standard error shaded.

7

7.3.3 Open system dynamics

Holstein Tavis-Cummings

Next, we introduce decoherence to our simulations. Fig. 7.9 and Fig. 7.10 show the spin and bosonic dynamics for $N_s = 3$ in the presence of cavity loss a at strength $\kappa = g$ (Fig. 7.9) and $\kappa = 10g$ (Fig. 7.10), and in the regime $\lambda \gg g$, where SCS provides more accurate predictions in the closed setting (cf. Fig. 7.6). In the top row we set the disorder $\epsilon = 0$, while the bottom row shows the dynamics in the presence of disorder, $\boldsymbol{\epsilon} = [2g, 3g, 4g]$. Although exact dynamics were accessible for a closed system of this size, obtaining exact numerics in the open dynamics setting is challenging. In the Supplemental Material of Sec. 7.5 we compare the two methods against exact numerics for a smaller system of $N_s = 1$.

For these parameters, we find that, perhaps unsurprisingly, SCS continues to perform well in both $\kappa = g$ and $\kappa = 10g$ decoherence regimes. In the weaker decay limit shown in Fig. 7.9, SCS and TWA agree only at short times. The under- and over-estimation of spin-cavity dynamics by TWA in the non-disordered and disordered systems respectively is consistent with the behaviour of TWA in the closed system, see Fig. 7.6. In the large decay limit shown in Fig. 7.10, SCS and TWA are in reasonable agreement with one another for the spin dynamics and in near total agreement for the vibrational and cavity dynamics. Both show fast decay of the cavity to the vacuum, and remarkably both capture small oscillatory dynamics at late times with excellent agreement. Physically, both methods demonstrate

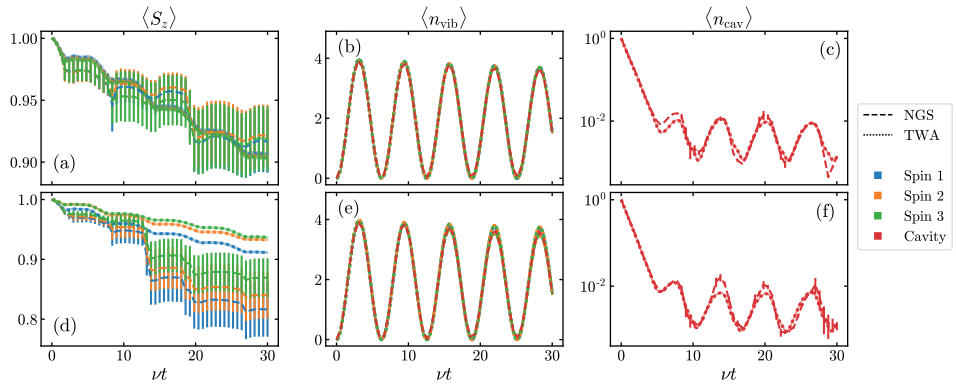


Figure 7.10: **Open dynamics**. $g = 0.1$, $\lambda = 1$, $\Delta = 0$ and cavity decay $\kappa = 10g$. **Top row:** without disorder. **Bottom row:** with disorder $\boldsymbol{\epsilon} = [2g, 3g, 4g]$. We observe compatible results for the spins and a remarkable agreement between SCS and TWA for the vibrational and cavity dynamics, including the small amplitude oscillations in $\langle n_{\mathrm{cav}} \rangle$ at late times. Here SCS uses $N_p = 8$ and $n_{\mathrm{traj}} = 40$ with standard error indicated by the error bars, TWA is with $n_{\mathrm{traj}} = 10^4$ with standard error shaded.

7

that strong cavity decay stabilizes the spin dynamics, which we attribute to the reduction of the effective Tavis-Cummings coupling strength and the prevention of the build up of correlations in the system between the spins, as well as spin-boson correlations, due to the loss of cavity excitations.

Tavis-Cummings

Next, we consider spin decay. We set $\epsilon, \lambda = 0$ such that evolution is only under $\hat{H}_{\mathrm{TC}}$, and include collective spin decay at rate Γ. We set $\Delta = 1$ and $g = 0.1$. Within the TWA formalism we treat the dynamics using two methods. First, we continue to treat the system as a collection of individual spins, as described in Sec. 7.2. In Fig. 7.11 we plot the resulting dynamics where TWA (CD) refers to implementing this sampling in the presence of collective spin decay at $\Gamma = 0.1g/\sqrt{N_s}$ and $g/\sqrt{N_s}$. TWA (SSD) uses the same sampling but the decay mechanism is single spin at the corresponding rate. The agreement between the two, and the disagreement with exact numerics (EXA) indicates that treating the spins individually with either of these two methods is inadequate to simulate collective spin decay.

This motivates our second strategy. Because the Hamiltonian is $\hat{H}_{\mathrm{TC}}$ which conserves the total excitation number $N_{\mathrm{ex}} = a^\dagger a + \sum_i \sigma_i^z$, the dynamics occurs in the collective Tavis-Cummings manifold. As such, we perform a Holstein-Primakoff

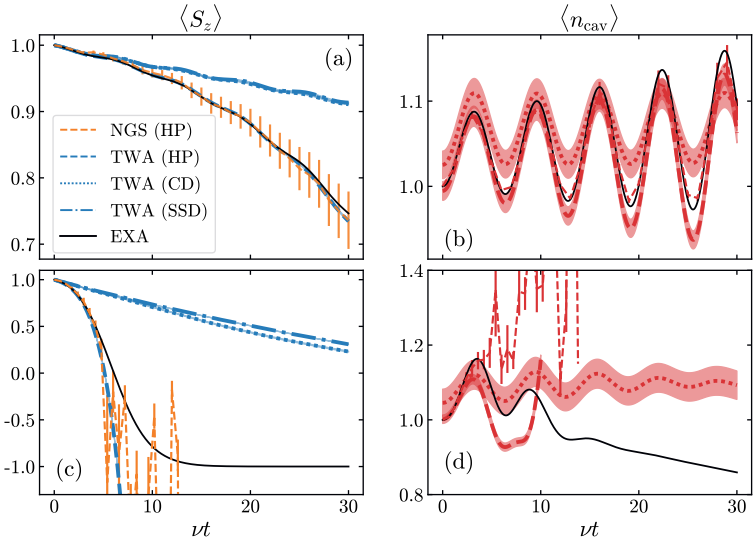


Figure 7.11: Collective spin dynamics. $\nu = \epsilon = \lambda = 0$, $\Delta = 1$, $g = 0.1$. **Top row:** $\Gamma = 0.1g/\sqrt{N_s}$. SCS (HP) and TWA (HP) use the Holstein-Primakoff representation of the collective spin and agree excellently with exact numerics (EXA). On the other hand, when TWA treats the spins individually, the collective decay dynamics TWA (CD) agrees with the single spin decay dynamics TWA (SSD), but both deviate from the exact evolution due to TWA's failure to capture the correlations. **Bottom row:** $\Gamma = g/\sqrt{N_s}$. SCS (HP) and TWA (HP) agree with exact numerics (EXA) until $t\nu \sim 5$, when the first order Taylor series expansion of the HP mapping breaks down. Here SCS uses $N_p = 8$ and $n_{\mathrm{traj}} = 40$ with standard error indicated by the error bars, TWA is with $n_{\mathrm{traj}} = 10^4$ with standard error shaded.

(HP) transformation to map the collective spin S to a single bosonic mode,

$$\hat{S}_+ = \sqrt{2s - \hat{a}_s^\dagger \hat{a}_s}\, \hat{a}_s, \tag{7.27a}$$

$$\hat{S}_z = s - \hat{a}_s^\dagger \hat{a}_s, \tag{7.27b}$$

where $s \equiv N_s/2$. We use a Taylor series to expand the square root in powers of $1/s$ to first order. The SCS simulation then proceeds using the SCS ansatz with $N_b = 2$ bosonic modes. We can include collective spin decay $\sum_i \sigma_i^-$ at strength Γ using the manifold projection technique described in Sec. (7.1.2).

For the TWA simulations, the eoms for the cavity mode A and the large spin HP mode B are,

$$\dot{A}_{\mathrm{cl}} = -\frac{\kappa}{2} A_{\mathrm{cl}} - i \frac{g}{2\sqrt{2s}} B_{\mathrm{cl}}^* \left(4s - N_{B,\mathrm{cl}}\right), \tag{7.28a}$$

$$\dot{N}_{A,\mathrm{cl}} = -\kappa N_{A,\mathrm{cl}} - \frac{g}{\sqrt{2s}} \mathrm{Im}[A_{\mathrm{cl}} B_{\mathrm{cl}}] \left(4s - N_{B,\mathrm{cl}}\right), \tag{7.28b}$$

$$\dot{B}_{\rm cl} = \Gamma B_{\rm cl}\left[s - \frac{1}{8s} + N_{B,\rm cl}\left(\frac{|B_{\rm cl}|^2}{16s} - \frac{1}{2}\right)\right] + \frac{ig}{2\sqrt{2s}}\left[A_{\rm cl}B_{\rm cl}^2 - 2A_{\rm cl}^*\left(2s - N_{B,\rm cl}\right)\right] + i\Delta B_{\rm cl}, \tag{7.28c}$$

$$\dot{N}_{B,\rm cl} = \Gamma\left[2S + N_{B,\rm cl}\left(\frac{1}{4s} + 2\left(s-1\right) + \mathcal{F}(B_{\rm cl})\right)\right] - \frac{g}{\sqrt{2s}}\,\mathrm{Im}[A_{\rm cl}B_{\rm cl}](4s - N_{B,\rm cl}), \tag{7.28d}$$

where we introduced $\mathcal{F}(B_{\rm cl}) = \frac{1}{8s}|B_{\rm cl}|^2\left(4 - 8s + \left|B_{\rm cl}^2\right|\right)$. We sample the cavity (mode A) assuming a coherent state $|\alpha = 1\rangle$ and sample the large spin (mode B) assuming the spins are polarized pointing up, which corresponds to sampling the vacuum for mode B.

Our results using this approach, including collective spin decay, are shown in Fig. 7.11 in the lines labeled as TWA (HP) and SCS (HP). In the weak spin decay limit $\Gamma = 0.1g/\sqrt{N_s}$, both SCS (HP) and TWA (HP) are in excellent agreement with the exact numerics (EXA). SCS in particular captures the cavity dynamics with little error, whilst the error bars on the spin dynamics are still somewhat large due to our use of relatively few trajectories, $n_{\rm traj} = 40$. In the large decay limit $\Gamma = g/\sqrt{N_s}$, both SCS and TWA correctly capture the rapid spin decay until $\nu t \sim 5$. Beyond this point, the first order Taylor series expansion of the HP mapping breaks down, as highly excited Fock states are populated. One can potentially circumvent this issue by simulating collective spin decay as was performed in Ref. [372] with DTWA. There, the spins were collectively coupled to a single cavity whose cavity loss was much stronger than the collective spin-cavity coupling, resulting in effective collective spin decay and without the utilization of the HP mapping. Comparing the performance of these approaches in different parameter regimes and for different models, e.g., for more complex forms of collective spin decay, represents an interesting future direction.

7.4 Conclusions and outlook

Summary and conclusions

In this chapter we presented a non-Gaussian variational ansatz approach to studying the dynamics of open quantum systems composed of spin and bosonic degrees of freedom. While several other works in recent years have utilized NGS-type ansatz to study the time evolution of open quantum systems, previous efforts have focused on developing an equivalent ansatz for the density matrix and simulating the Lindblad equations. Here, we utilized the quantum trajectories method, allowing us to take advantage of the previously developed machinery and analytic expressions obtained for real- and imaginary-time dynamics.

In addition to providing a comprehensive overview of this method, we performed extensive numerical simulations over a broad range of parameters of a spin-boson

Hamiltonian [Eq. (7.22)] with Tavis-Cummings (TC) and Holstein couplings, which is applicable to a broad range of quantum simulation platforms as well as problems of interest in quantum chemistry, atomic physics and condensed matter theory. We compared the performance of SCS with a method using the truncated Wigner approximation for systems with mixed bosonic and spin degrees of freedom, extended to open quantum systems following the approach in Ref. [365].

In the absence of decoherence our findings are as follows: for strong TC coupling, TWA is the more accurate method, while for strong Holstein couplings SCS is the better choice. When neither term dominates, for both weak and strong coupling regimes, TWA captures the short-time dynamics, while NGS generally displays the correct qualitative behaviour, even at late times. After introducing spin disorder the performance of SCS typically improves, whilst for TWA the vibrational dynamics match the exact dynamics better, which is attributable to the fact that disorder causes the Holstein interaction to dominate.

For open quantum dynamics we focused on the regime where the Holstein term dominates and considered the effect of cavity loss. At weak decay rates the SCS continues to perform well. TWA improves as the cavity decay rate increases due to the loss of quantum correlations, with both SCS and TWA showing excellent agreement. In the presence of collective spin decay we considered the TC model only, finding that in the limit of small collective decay, both methods perform well when using a Holstein-Primakoff transformation for the large spin. In the limit of large collective decay, SCS and TWA both only capture the short time dynamics as the Holstein-Primakoff transformation is no longer accurate at later times. Using TWA we were able to also treat each spin individually. However, TWA does not capture the collective nature of the decay, with the results closely matching the effect of single spin decay.

Further considerations should also be made when deciding between the two methods. Although the SCS can be made less computationally demanding by reducing the number N_p of coherent states, in general TWA methods are easier to implement and require fewer computational resources. The resource requirement and the complexity of SCS is offset by the advantages that it is a controlled approximation and gives access to the wavefunction, allowing one to access any observable, including higher-order correlations. The TWA framework needs to be amended to capture these correlations accurately. A potential strategy to remedy this can be to use a cluster TWA approach [383]. There, several sub-system parts are grouped into a single (discrete or continuous) large sub-system that, provided a proper sampling strategy, follows the fully exact quantum evolution, while correlations between clusters are approximated in TWA. Such approaches allow to use the cluster size as controllable parameter to enhance the simulation towards the exact one.

Outlook

The extension of SCS to open quantum systems using the quantum trajectories formulation that we presented in this chapter is perhaps the most natural pathway. For Hermitian jump operators, an alternative approach and a simple extension

would be to instead solve the stochastic partial differential equations that result from the unraveling of the master equation. Furthermore, one could explore the impact of the chosen unraveling on the performance of the SCS method at a fixed N_p, as it has been shown that this choice can have a large effect on the entanglement buildup in the trajectory [278, 384].

Another limitation of the present formulation is that the spin states in Eq. (5.16) are exact and span the full spin Hilbert space of dimension 2^{N_s}, thus limiting the use of the ansatz to a handful of spins unless approximations such as the large N_s expansion in the Holstein-Primakoff mapping used in Sec. 7.3.3 are invoked. On the one hand, studies using a fermionic Gaussian state representation of spins have been performed [325], and these might be combined in principle in a straightforward way with the SCS ansatz for bosons [108]. On the other hand, it would be highly interesting to combine the SCS ansatz with other variational techniques highly suitable for the spins such as tensor network based approaches [353–355]. Furthermore, similar to the present comparison between SCS and TWA, it would be beneficial to apply the here-presented non-Gaussian ansatz to the study of other systems which might be challenging to simulate otherwise. These include for instance purely bosonic models, such as the Bose-Hubbard model, with disorder and on non-regular lattices [385]. Such extensive studies will allow for a comparison between our approach and the corresponding master equation approach based on extending the ansatz of Eq. (5.16) to density matrices [258, 362].

Finally, we note that a particular promising application field of the methodologies introduced here could be in the emerging field of polaritonic chemistry [386–389]. There, recent experiments have demonstrated that large *collective* strong cavity couplings (e.g. $g_c = g\sqrt{N}$) can be functionalized to modify chemical reactivity. A theoretical understanding for such modifications are currently centered around the question how delocalized polaritonic state can play a role for changing chemistry on the single-molecule level, as local amplitudes of collective polaritons vanish in the thermodynamic limit. In spin-boson approximations to the problems, in particular for the disordered Holstein-Tavis-Cummings [261] model that we studied here, it was recently discovered that the interplay of disorder and collective cavity couplings can give rise to robust local quantum effects in the large-N limit in the form of non-Gaussian distributions of the nuclear coordinate [104]. Using matrix product state methods, it was possible to push simulations to systems with 160 effective molecules, but in particular the TWA approach discussed here would allow access to much larger systems. Typical parameter regimes discussed here are well covered by the TWA approach (e.g. the typical parameters from [104] corresponds to $\lambda \sim 0.1\nu$ and $g \ll \nu$) and thus hint to a general applicability of the method in the relevant regime. Further, the TWA approach can be straightforwardly adapted to simulate nuclear dynamics not only on harmonic but also arbitrary potential energy surfaces, whilst the SCS ansatz using the machinery presented here can also model anharmonic Hamiltonian terms. In the future this may allow for the analysis of quantum effects in realistic chemical reaction models, even in a macroscopic limit.

7.5 Supplemental Material

Here we show that the tangent space of the variational manifold for the NGS ansatz is a Kähler manifold, and benchmark SCS and TWA against exact numerics for a single spin $N_s = 1$.

7.5.1 On the complex structure of the NGS ansatz

In this section we specify the geometric structures for special cases of the general NGS ansatz. We begin with the example of a coherent state ansatz, i.e. $N_p = 1$, with explicit normalization and phase factors, $|\psi(\boldsymbol{z})\rangle = e^{\kappa+i\theta}\hat{D}(x+iy)\,|0\rangle$, with $\boldsymbol{z} = \{\kappa, \theta, x, y\}$. The tangent vectors for this ansatz were given in Eq. (7.7a), from which we can compute the metric and symplectic forms,

$$g_{\mu\nu} = \begin{pmatrix} 1 & 0 & 0 & 0 \\ 0 & 1 & -z_4 & z_3 \\ 0 & -z_4 & 1+z_4^2 & -z_3 z_4 \\ 0 & z_3 & -z_3 z_4 & 1+z_3^2 \end{pmatrix}, \quad \omega_{\mu\nu} = \begin{pmatrix} 0 & 1 & -z_4 & z_3 \\ -1 & 0 & 0 & 0 \\ z_4 & 0 & 0 & 0 \\ -z_3 & 0 & -1 & 0 \end{pmatrix} \tag{7.29}$$

as well as their respective inverses,

$$G = \begin{pmatrix} 1 & 0 & 0 & 0 \\ 0 & 1+z_3^2+z_4^2 & z_4 & -z_3 \\ 0 & z_4 & 1 & 0 \\ 0 & -z_3 & 0 & 1 \end{pmatrix}, \quad \Omega = \begin{pmatrix} 0 & -1 & 0 & 0 \\ 1 & 0 & -z_3 & -z_4 \\ 0 & z_3 & 0 & -1 \\ 0 & z_4 & 1 & 0 \end{pmatrix}. \tag{7.30}$$

Note that here the use of the pseudo-inverse would give the same as the inverse, as $\omega_{\mu\nu}$ and $g_{\mu\nu}$ are not singular for any values of the variational parameters $\boldsymbol{z}$. We can also compute the complex structure, $J^{\mu}{}_{\nu} = -G^{\mu\sigma}\omega_{\sigma\nu}$,

$$J^{\mu}{}_{\nu} = \begin{pmatrix} 0 & -1 & z_4 & -z_3 \\ 1 & 0 & -z_3 & z_4 \\ 0 & 0 & 0 & -1 \\ 0 & 0 & 1 & 0 \end{pmatrix}, \tag{7.31}$$

and verify that $J^2 = -\mathbb{1}$. Using the relation $i\,|v_\nu\rangle = J^{\mu}{}_{\nu}\,|v_\mu\rangle$ which holds if the tangent space of the variational manifold is a Kähler manifold as is the case here, we directly obtain the relations,

$$i\,|v_1\rangle = |v_2\rangle\,, \tag{7.32}$$
$$i\,|v_2\rangle = -i\,|v_1\rangle\,, \tag{7.33}$$
$$i\,|v_3\rangle = z_4\,|v_1\rangle - z_3\,|v_2\rangle + |v_4\rangle\,, \tag{7.34}$$
$$i\,|v_4\rangle = -z_3\,|v_1\rangle + z_4\,|v_2\rangle - |v_3\rangle\,, \tag{7.35}$$

which we derived explicitly and used in the main text to compute $\mathrm{Im}[C_\mu]$, see Sec. 7.1.1.

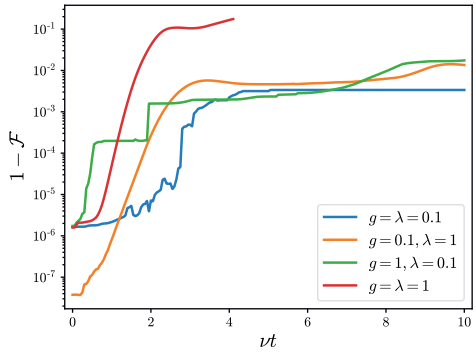


Figure 7.12: Infidelity $1-\mathcal{F}(t) = 1-|\langle\psi(t)|\Psi(t)\rangle|^2$ of real-time dynamics for $N_s = 1$ between SCS using $N_p = 8$ and numerically exact $|\Psi\rangle$ for the same four parameter regimes studied in the main text. The initial infidelity is due to the small randomness in the SCS initial state, which is used to lift the degeneracy between the different multi-mode coherent states to avoid over-parametrization of the equations of motion, cf. [4]. In all regions except $g = \lambda = 1$ where the rapid decrease in infidelity leads to unstable SCS eoms, SCS captures the dynamics even at late times with excellent infidelity, $1-\mathcal{F} \lesssim 10^{-2}$.

A similar calculation for the single-mode squeezed coherent state reveals that $J^2 = -1$, and therefore the tangent space of the single-mode Gaussian state ansatz is a Kähler manifold. For details of the calculation, see the Supplemental Material of Ref. [5]. We also note that,

$$\det(g) = \det(\omega) \propto \sinh(2r)^2, \tag{7.36}$$

which vanishes in the limit of vanishing squeezing $r \to 0$ and consequently $G = g^{-1}$ is ill-defined. When such a situation occurs, one can use instead the Moore-Penrose pseudo-inverse, as suggested in [109], to evaluate g^{-1}. In this case we recover $J^2 = -1$ and thus the Kähler space.

The above procedure for calculating the complex structure of a single-mode Gaussian ansatz generalizes to the construction of the complex structure for each Gaussian $p \in \{1, \ldots, N_p\}$ and each mode $k \in \{1, \ldots, N_b\}$ such that the tangent space remains Kähler manifold also in the generic NGS ansatz of a superposition of many-mode squeezed displaced states. In this case the complex structure J takes a block-diagonal form, where each block is labeled by the Gaussian and mode number (p, k) with the property $J^2 = -1$, which we could also verify numerically.

7.5.2 Benchmarking dynamics with single spin

A key advantage of NGS is the access to the wavefunction, allowing any desired quantity to be computed. A simple example of this benefit is the computation of the infidelity $1-\mathcal{F}(t) = 1-|\langle\psi(t)|\Psi(t)\rangle|^2$ between the SCS wavefunction $|\psi\rangle$ with

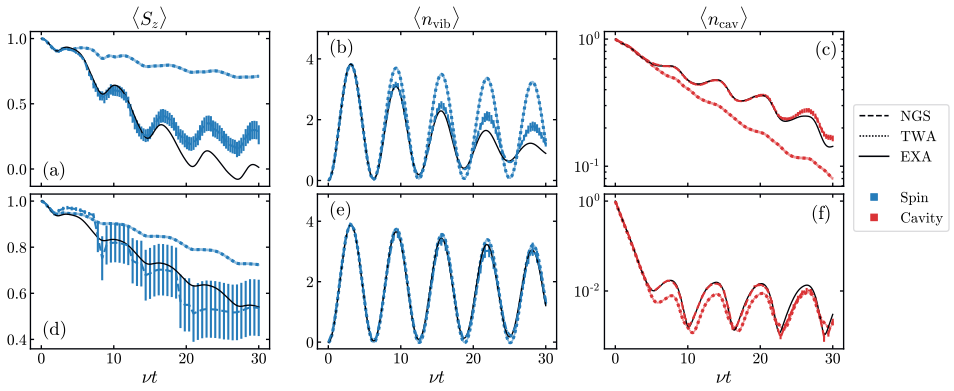


Figure 7.13: Benchmarking SCS and TWA against exact numerics. We use $N_s = 1$ spin in the $g = 0.1$, $\lambda = 1$ regime with cavity loss $\hat{c} = \sqrt{\kappa}\hat{a}$, i.e. the same parameters considered in the main text (there with $N_s = 3$). **Top row:** weaker cavity decay $\kappa = g$. SCS accurately captures the cavity dynamics, and captures the spin and vibrational mode decay until $\nu t \sim 15$. TWA significantly under-estimates the spin and vibrational decay, while over-estimating the cavity decay. **Bottom row:** strong cavity decay $\kappa = 10g$. Both methods capture the decay of cavity population and subsequent small oscillations, as well as the vibrational loss. SCS now agrees with exact numerics for the spin decay (albeit with large error bars due to the limited $n_{\rm traj}$). TWA still underestimates this observable, although the agreement is closer. We attribute this to the loss of quantum correlations due to the decoherence which makes it easier for the TWA to capture the true quantum state. Here SCS uses $N_p = 8$ and $n_{\rm traj} = 40$ with standard error indicated by the error bars, TWA is with $n_{\rm traj} = 10^4$ with standard error shaded.

$N_p = 8$ and the exact wavefunction $|\Psi\rangle$ for closed real-time dynamics. This is shown in Fig. 7.12 for $N_s = 1$ for the four parameter regimes studied in Figs. 7.5-7.8 (there with $N_s = 3$). Note that such a comparison for more spins becomes challenging as we cannot access exact numerics. We find that in all regimes except $g = \lambda = 1$, the infidelity of SCS is low, with $1 - \mathcal{F} < \mathcal{O}(10^{-2})$. We also note that the infidelity is not accessible in TWA.

Next, we benchmark TWA and SCS against exact numerics for open dynamics of $N_s = 1$ spin. In Fig. 7.13 we consider the same parameter regime as the main text, $g = 0.1$ and $\lambda = 1$ with cavity loss at rate $\kappa = g$ (top row) and $\kappa = 10g$ (bottom row). For weaker cavity loss $\kappa = g$ we find that SCS with $N_p = 8$ coherent states more closely tracks the exact numerics than TWA, particularly for the cavity dynamics which shows excellent agreement. At strong cavity decay rates $\kappa = 10g$ both methods accurately capture the cavity dynamics, with SCS also capturing the spin decay, albeit with large error bars as only $n_{\rm traj} = 40$ trajectories were used.

Chapter 8

Conclusions and Outlook

And if you were to ask me,
After all that we've been through.
Still believe in Magic?
Oh yes, I do.

Chris Martin, Guy Berryman,
Jonny Buckland & Will Champion,
Magic (2014)

Major scientific conclusions

In this Thesis, we studied how spin-boson systems can be harnessed for quantum simulations, sensing and state preparation. We also considered classical numerical methods for simulating the closed and open quantum dynamics of spin-boson systems, for applications in fast quantum state preparation and the study of phenomena such as bath dynamics, impurity physics and polaritonic chemistry. In reply to the research questions posed in the Introduction, we draw the following major scientific conclusions:

- After reviewing the theory of ion trapping in Ch. 1, in Ch. 2 we showed that although the programmability of 2D trapped-ion quantum simulators can be increased using optical tweezers, if micromotion is present it should be included in the numerical optimization of the tweezer pinning frequencies. Furthermore, along weaker confinement directions where micromotion is strongest, first-order Doppler shifts are expected to be a major source of error. Stress and strain forces due to tweezer misalignment have a negligible effect on the simulation if the tweezer is perturbative compared to the Paul trap and Coulomb interactions, while intensity noise should be controlled to the sub-percent level. In sum, optical tweezers are an experimentally-realizable method for increasing the programmability of trapped-ion quantum simulators.

- In Ch. 3 we investigated how to perform displacement sensing with many-body quantum systems. We proved that in terms of the bosonic mode occupation, spin-dependent squeezed states are optimal reference states. We proposed measurement protocols that follow Heisenberg scaling which can be implemented on current hybrid spin-boson quantum hardware platforms such as trapped-ion systems. To prepare spin-dependent squeezed states in trapped-ion systems we provided a fast and scalable protocol that uses dynamically modulated first-order sideband interactions. The potential applications of our sensing protocols range from measuring single-photon scattering to searches for dark matter. Our state preparation protocol also has immediate applications to quantum computing.

- In Ch. 4 we showed that arbitrary symmetric spin states can be prepared using a global variational quantum circuit with at most $2N/3$ layers of global rotations and one-axis twisting gates. Specific symmetric states such as the W-state and the $N/2$-excitation Dicke state can be prepared in $N = 300$ qubits with infidelities $1 - \mathcal{F} \leq 10^{-3}$ using only $P = 3$ and $P = 4$ layers, respectively. The $N = 9$ Ruskai and $N = 13$ Gross quantum error correcting codewords can be prepared with infidelities $1-\mathcal{F} \leq 10^{-4}$ in $P = 4$ and $P = 7$ layers, respectively.

- After reviewing the theory of Gaussian states and open quantum systems in Ch. 5, in Ch. 6 we employed a superposition of coherent state (SCS) as a variational ansatz to simulate the real- and imaginary-time dynamics of spin-boson systems using the time-dependent variational principle (TDVP). We demonstrated efficient numerical simulation of ground state properties and real-time dynamics in the spin-boson model, even beyond the Ohmic-coupling paradigm. By combining the framework with optimal control, we prepared near-critical ground states in a ten mode spin-boson model with up to five times lower infidelity compared to adiabatic ramp protocols.

- In Ch. 7 we used the SCS variational ansatz with TDVP to simulate open dynamics using the quantum trajectories method. After obtaining TDVP equations of motion for non-hermitian evolution and describing the action of the quantum jump operators, we studied a Holstein-Tavis-Cummings model. We benchmarked the SCS ansatz against the truncated Wigner approximation (TWA) method, and showed that there are regions where SCS outperforms TWA. The potential applications of our framework range from studies of impurity physics or polaritonic chemistry to robust quantum state preparation in hybrid spin-boson systems.

Future work

The end of each chapter contains an outlook with a discussion of possible future research directions. Here, we expand on a select number of those future directions.

Ch. 3: Many-body displacement sensing:

- One could investigate the performance of alternative spin-boson entangling unitaries for preparing the reference state. For example, dispersive spin-boson entangling unitaries have been studied for single-parameter displacement estimation [160, 161], but their performance for phase-insensitive or joint-parameter displacement estimation is unknown. Another possibility is spin-dependent displacements, which have been used for single-parameter displacement estimation [57]. Although we do not expect spin-dependent displaced states to be useful for joint-parameter estimation because their Wigner function is only $\mathbb{Z}_2$ symmetric, after phase-twirling [65] they may be suitable for phase-insensitive displacement amplitude estimation. Finding other suitable spin-boson entangling unitaries may permit quantum-enhanced sensing on a more diverse range of quantum hardware platforms.

- As discussed in Sec. 3.4.1, there is a plethora of reference states available for quantum-enhanced displacement sensing. The best choice often depends on the type of interactions and measurement observables that are natively available in a specific quantum hardware platform. A comparison between the metrological performance of these reference states, including their performance in the presence of noise, may help to guide experiments in choosing a protocol that is best-suited for their target hardware. Furthermore, establishing a "Zoo", similar to the Error Correction Zoo [329] for example, that summarizes the metrological capabilities of known reference states, including for sensing tasks beyond displacement sensing, would be a valuable resource for the community.

Ch. 4: Arbitrary symmetric spin state preparation

- The exact classical numerics used in this chapter to optimize the variational quantum circuit are efficient because the Hilbert space dimension of the symmetric states is $N+1$. However, we observed that the presence of local minima typically makes the numerical optimization challenging for more than about one hundred qubits. This problem could be avoided by deriving exact expressions for the optimal parameters of the circuit, which would also rigorously prove that the circuit provides universal control over the symmetric subspace.

Ch. 6 and Ch. 7: Classical simulation of spin-boson dynamics

- In Ch. 6 we used imaginary time-evolution to determine the ground state. However, determining excited states is also an important task. For example, to compute spectra in quantum chemistry [390] or to determine whether a quantum phase transition is characterized by a finite excitation gap [391]. Excited states can be found with the SCS ansatz by making a simple modification

to our existing framework. One approach is the *folded spectrum* method [392]. This involves imaginary time-evolving under an effective Hamiltonian $\hat{H}' = (\hat{H} - E)^2$, where $\hat{H}$ is the original Hamiltonian and E is a target energy. In the infinite-time limit, exact imaginary-time evolution converges to the eigenstate whose energy is closest to E. Another approach is *deflation* [393]. This involves imaginary time-evolving with $\hat{H}' = \hat{H} + \lambda \sum_{i=0}^{N_\epsilon} |\epsilon_i\rangle\langle\epsilon_i|$. Here λ is a controllable parameter and $|\epsilon_i\rangle$ is the ith eigenstate. Starting from $N_\epsilon = 0$, the ground state of $\hat{H}$ is found using imaginary-time evolution as usual. Next, setting $N_\epsilon = 1$ the previously-found ground state is included in the Hamiltonian, so that the energy of the ground state is increased, leaving the first eigenstate of $\hat{H}$ as the ground state of the new Hamiltonian $\hat{H}'$. That is, the energy of the next eigenstate has been "deflated". This process is repeated, iteratively increasing N_ϵ. In principle both folding and deflation can be efficiently performed using our existing SCS and TDVP framework.

- Finally, a key outstanding challenge for our SCS ansatz is the description of the spin degrees of freedom. Currently, the ansatz describes the spin state exactly, and therefore the number of variational parameters scales exponentially with the number of spins. We investigated one possible resolution to this in Ch. 7, namely a Holstein-Primakoff mapping. However, we observed that typically the required number of coherent states in the SCS ansatz, even after the mapping, can still scale exponentially for e.g. simple spin product states. To avoid this problem one could use the SCS ansatz to describe the bosonic degree of freedom while combining it with a more efficient method of describing the spins, such as tensor networks or fermionic Gaussian states.

Appendices

A: Floquet modes and quantized ion motion with micromotion

In this appendix, we use Floquet theory to decouple the ion motion when micromotion is included. We then quantize the solution into bosonic creation and annihilation operators.

Consider the differential equations $\dot{\boldsymbol{\phi}}(t) = \Pi(t)\boldsymbol{\phi}(t)$ where $\Pi(t)$ is T-periodic and $\boldsymbol{\phi}(t)$ vector of length $6N$. A key result of Floquet theory is that at any time $t' \in [0, T]$, for any integer $n \in \mathbb{Z}$ a solution $\boldsymbol{\phi}(nT + t')$ can always be determined from the initial conditions $\phi(0)$ according to [394],

$$\phi(nT + t') = \boldsymbol{U}(t')\boldsymbol{M}^n\phi(0). \tag{8.1}$$

Here, $\boldsymbol{U}(t)$ is the *fundamental solution* which is obtained by solving the T-period matrix differential equation $\dot{\boldsymbol{U}}(t) = \boldsymbol{\Pi}(t)\boldsymbol{U}(t)$ from $\boldsymbol{U}(0) = \mathbb{1}$. The matrix $\boldsymbol{M}$ is known as the *monodromy matrix*. It is simply the fundamental solution at one period, $\boldsymbol{M} = \boldsymbol{U}(T)$. Writing the solution in the form of Eq. (8.1) shows that we only have to solve the differential equations until time $t = T$, with the solution at an arbitrarily late time constructed by matrix multiplication.

The monodromy matrix can be diagonalized as $\boldsymbol{M} = \boldsymbol{B}\boldsymbol{\mu}\boldsymbol{B}^{-1}$. The eigenvalues $\boldsymbol{\mu}$ are the *characteristic multipliers*, while the columns of $\boldsymbol{B}$ are the $6N$ *Floquet modes* defined by the eigenequation,

$$\boldsymbol{M}\boldsymbol{b}_m = e^{i\omega_m T}\boldsymbol{b}_m, \tag{8.2}$$

where ω_m are the *quasienergies*, and are related to the characteristic multipliers as $\boldsymbol{\mu} = e^{i\boldsymbol{\omega}T}$. Substituting the diagonalization into Eq. (8.1) and left-multiplying by $\boldsymbol{B}^{-1}$, after setting $t' = 0$ we obtain the T-period evolution equation,

$$\boldsymbol{B}^{-1}\phi(nT) = \boldsymbol{\mu}\boldsymbol{B}^{-1}\phi(0). \tag{8.3}$$

In this thesis, we always set $t' = 0$ to focus on the T-period evolution, as justified in Sec. 1.2.2 of Ch.1.

It is convenient to write $\boldsymbol{B}$ in block-matrix form. For stable solutions one possible choice is,

$$\boldsymbol{B} = \begin{pmatrix} \boldsymbol{U} & \boldsymbol{U}^* \\ \boldsymbol{V} & \boldsymbol{V}* \end{pmatrix}, \tag{8.4}$$

A

so that the inverse is,

$$\boldsymbol{B}^{-1} = \begin{pmatrix} i\boldsymbol{V}^\dagger & -i\boldsymbol{U}^\dagger \\ -i\boldsymbol{V}^T & i\boldsymbol{U}^T \end{pmatrix}. \tag{8.5}$$

For this choice of $\boldsymbol{B}$, the characteristic multipliers take the form,

$$\boldsymbol{\mu} = \exp\left\{ i \begin{pmatrix} \omega_+ & 0 \\ 0 & -\omega_+ \end{pmatrix} T \right\}, \tag{8.6}$$

where we used the fact that for stable solutions the quasienergies come in complex conjugate pairs, and where we denoted the first $3N$ quasienergies by ω_+. We can then rewrite the T-period evolution equation of Eq. (8.3) as,

$$\begin{pmatrix} \boldsymbol{V}^\dagger \boldsymbol{q}(nT) - \boldsymbol{U}^\dagger \dot{\boldsymbol{q}}(nT) \\ -[\boldsymbol{V}^T \boldsymbol{q}(nT) - \boldsymbol{U}^T \dot{\boldsymbol{q}}(nT)] \end{pmatrix} = \begin{pmatrix} e^{i\boldsymbol{\omega}_+ nT}[\boldsymbol{V}^\dagger \boldsymbol{q}(0) - \boldsymbol{U}^\dagger \dot{\boldsymbol{q}}(0)] \\ -e^{-i\boldsymbol{\omega}_+ nT}[\boldsymbol{V}^T \boldsymbol{q}(0) - \boldsymbol{U}^T \dot{\boldsymbol{q}}(0)] \end{pmatrix}, \tag{8.7}$$

where we recalled that $\boldsymbol{\phi}(t) = (\boldsymbol{q}, \dot{\boldsymbol{q}})$. This equation describes coupled motion between the canonical position and momentum coordinates, which can be uncoupled by introducing new canonical coordinates. The new coordinates must satisfy the Poisson bracket, which for any functions $f(q_i, \dot{q}_i, t)$ and $g(q_i, \dot{q}_i, t)$, is defined as,

$$\{f_k, g_l\} = \sum_i \frac{\partial f_k}{\partial q_i}\frac{\partial g_l}{\partial \dot{q}_i} - \frac{\partial f_k}{\partial \dot{q}_i}\frac{\partial g_l}{\partial q_i}. \tag{8.8}$$

We define the new coordinates $\boldsymbol{Q}$ and $\boldsymbol{Q'}$ as,

$$\begin{pmatrix} \boldsymbol{Q}(nT) \\ \boldsymbol{Q'}(nT) \end{pmatrix} = \begin{pmatrix} -i & 0 \\ 0 & 1 \end{pmatrix} \boldsymbol{B}^{-1} \boldsymbol{\phi}(nT) = \begin{pmatrix} \boldsymbol{V}^\dagger \boldsymbol{q}(nT) - \boldsymbol{U}^\dagger \dot{\boldsymbol{q}}(nT) \\ -i[\boldsymbol{V}^T \boldsymbol{q}(nT) - \boldsymbol{U}^T \dot{\boldsymbol{q}}(nT)] \end{pmatrix}. \tag{8.9}$$

A

Then, at any time t and t', we have that,

$$\{Q_k(t), Q'_l(t')\} = i \sum_m V^\dagger_{km} U_{ml} - U^\dagger_{km} V_{ml}, \tag{8.10}$$

or equivalently in matrix notation,

$$\{\boldsymbol{Q}(t), \boldsymbol{Q'}(t')\} = i(\boldsymbol{V}^\dagger \boldsymbol{U} - \boldsymbol{U}^\dagger \boldsymbol{V}). \tag{8.11}$$

For the new coordinates to be canonical, at all times t and t' they must satisfy $\{\boldsymbol{Q}(t), \boldsymbol{Q}(t')\} = \{\boldsymbol{Q'}(t), \boldsymbol{Q'}(t')\} = 0$ and $\{\boldsymbol{Q}(t), \boldsymbol{Q'}(t')\} = \mathbb{1}$. This imposes the following condition on $\boldsymbol{U}$ and $\boldsymbol{V}$,

$$\boldsymbol{V}^\dagger \boldsymbol{U} - \boldsymbol{U}^\dagger \boldsymbol{V} = -i\mathbb{1}. \tag{8.12}$$

The T-period evolution of Eq. (8.3), using the new coordinates, is therefore,

$$\begin{pmatrix} \boldsymbol{Q}(nT) \\ \boldsymbol{Q'}(nT) \end{pmatrix} = \begin{pmatrix} e^{i\boldsymbol{\omega}_+ nT} \boldsymbol{Q}(0) \\ e^{-i\boldsymbol{\omega}_+ nT} \boldsymbol{Q'}(0) \end{pmatrix}, \tag{8.13}$$

which is decoupled as desired.

Next, we promote the canonical position and momentum coordinates to operators by making the replacement $q_i \to \hat{x}_i$ and $\dot{q}_i \to \hat{p}_i$. Canonical quantization requires replacing the Poisson bracket by commutators,

$$\{q_i, \dot{q}_j\} \to \frac{1}{i}[\hat{x}_i, \hat{p}_j], \tag{8.14}$$

where we set $\hbar = 1$. The $(\boldsymbol{Q}, \boldsymbol{Q'})$ coordinates will, in turn, also become operators, $Q_i \to \hat{Q}_i$ and $Q_i \to \hat{Q}'_i$. Their commutator can be evaluated by writing them in terms of the original $\hat{x}_i$ and $\hat{p}_i$ basis operators, which for convenience we do in index notation,

$$\hat{Q}_k = \sum_m V^\dagger_{km}\hat{x}_m - U^\dagger_{km}\hat{p}_m, \tag{8.15}$$

$$\hat{Q}'_l = -i\sum_m V^T_{lm}\hat{x}_m - U^T_{lm}\hat{p}_m. \tag{8.16}$$

Note that here, we dropped the explicit time-dependent of all of the operators for notational simplicity. The product of operators are,

$$\hat{Q}_k\hat{Q}'_l = -i\sum_{m,n} V^*_{mk}V_{nl}\hat{x}_m\hat{x}_n - V^*_{mk}U_{nl}\hat{x}_m\hat{p}_n - U^*_{mk}V_{nl}\hat{p}_m\hat{x}_n + U^*_{mk}U_{nl}\hat{p}_m\hat{p}_n, \tag{8.17}$$

and,

$$\hat{Q}'_l\hat{Q}_k = -i\sum_{m,n} V_{nl}V^*_{mk}\hat{x}_n\hat{x}_m - V_{nl}U^*_{mk}\hat{x}_n\hat{p}_m - U_{nl}V^*_{mk}\hat{p}_n\hat{x}_m + U_{nl}U^*_{mk}\hat{p}_n\hat{p}_m. \tag{8.18}$$

Using the fact that $[\hat{x}_i(t), \hat{p}_j(t')] = i\delta_{ij}$, the commutator is therefore,

$$\begin{aligned}[\hat{Q}_k(t), \hat{Q}'_l(t')] &= i\sum_{m,n}(iV^*_{mk}U_{nl} - iU^*_{mk}V_{nl})\delta_{mn} \\ &= -(\boldsymbol{V}^\dagger\boldsymbol{U} - \boldsymbol{U}^\dagger\boldsymbol{V}) \\ &= i\delta_{kl},\end{aligned} \tag{8.19}$$

where we reintroduced the time-dependence notation to emphasize the fact that this commutator holds at all times, and where the last equality follows from the condition of Eq. (8.12). This commutator equals the imaginary unit times the creation and annihilation operator commutator. In terms of the canonical creation and annihilation operators, we can therefore choose the identification,

$$\hat{Q}_k \to -i\hat{a}^\dagger_k, \qquad \hat{Q}'_k \to \hat{a}_k \tag{8.20}$$

Physically, these operators should be understood as creating or destroying an excitation of the motion in the uncoupled basis.

Finally, we ask how to write the physical position and momentum operators, $\hat{x}_i$ and $\hat{p}_i$ in terms of the uncoupled basis creation and annihilation operators $\hat{a}_k^\dagger$ and $\hat{a}_k$. Inverting the quantized equivalent of Eq. (8.9) results in,

$$\begin{pmatrix} \hat{\boldsymbol{x}} \\ \hat{\boldsymbol{p}} \end{pmatrix} = \boldsymbol{B} \begin{pmatrix} i & 0 \\ 0 & 1 \end{pmatrix} \begin{pmatrix} -i\hat{\boldsymbol{a}}(t) \\ \hat{\boldsymbol{a}}^\dagger(t) \end{pmatrix} = \begin{pmatrix} \boldsymbol{U}\hat{\boldsymbol{a}}(t) + \boldsymbol{U}^*\hat{\boldsymbol{a}}^\dagger(t) \\ \boldsymbol{V}\hat{\boldsymbol{a}}^\dagger(t) + \boldsymbol{V}^*\hat{\boldsymbol{a}}(t) \end{pmatrix}. \tag{8.21}$$

To simplify this equation, we use the fact that at times $t = nT$, $U(r) \in \mathbb{R}$ and $V(r) \in i\mathbb{R}$ [126]. Then,

$$\begin{pmatrix} \hat{\boldsymbol{x}} \\ \hat{\boldsymbol{p}} \end{pmatrix} = \begin{pmatrix} \boldsymbol{U}(\hat{\boldsymbol{a}} + \hat{\boldsymbol{a}}^\dagger) \\ i\boldsymbol{V}(\hat{\boldsymbol{a}}^\dagger - \hat{\boldsymbol{a}}) \end{pmatrix}. \tag{8.22}$$

Because we are interested in laser-ion interactions, we focus on the position operator and write it in terms of the $3N$ upper elements of the Floquet modes and quasienergies,

$$\hat{x}_{i,\alpha}(nT) = \sum_{m=1}^{3N} \boldsymbol{b}_{m,i,\alpha}[\hat{a}_m^\dagger(0)e^{i\omega_m nT} + \hat{a}_m(0)e^{-i\omega_m nT}]. \tag{8.23}$$

This describes the T-period evolution of the position operator in the Heisenberg picture. This is similar to the case that we studied in the pseudopotential approximation, except that the normal modes are replaced with the Floquet modes, and the normal mode frequencies are replaced with the quasienergies. This expression is reported in Eq. (1.27) of Ch. 1.

B: Off-resonant ion-light interactions

Here, we derive the effective Ising Hamiltonian that describes a system of N trapped ions interacting with a two-tone laser. The interaction Hamiltonian for a single-tone laser field in the Lamb-Dicke regime is described in Eq. (1.32) of Ch. 1. If we drive with two tones, the first at detuning $-\delta$ with phase ϕ_r and the second at detuning δ with phase ϕ_b, then the Hamiltonian is a sum of two $\hat{H}_{\rm int}(t)$ Hamiltonians,

$$\hat{H}_{\rm 2tone}(t) = -\frac{1}{2}\sum_j \left[\Phi(t)\Omega_j\hat{\sigma}_j^- \left(1 - i\sum_m \eta_{m,j}\hat{x}_m(t)\right) + \text{h.c.}\right], \tag{8.24}$$

where the bichromatic driving is described by the function,

$$\Phi(t) = e^{-i\delta t + i\phi_r} + e^{i\delta t + i\phi_b}. \tag{8.25}$$

For convenience, we decompose $\hat{H}_{\rm 2tone}(t)$ into a carrier and a sideband term,

$$\hat{H}_{\rm c}(t) = -\frac{1}{2}\sum_j \Omega_j \left[\Phi(t)\hat{\sigma}_j^- + \text{h.c.}\right], \tag{8.26a}$$

$$\hat{H}_{\rm sbs}(t) = \frac{1}{2}\sum_{j,m} \Omega_j\eta_{m,j} \left[i\Phi(t)\hat{\sigma}_j^-\hat{x}_m(t) + \text{h.c.}\right]. \tag{8.26b}$$

The dynamics of a time-dependent Hamiltonian $\hat{H}(t)$ are solved using the Magnus expansion of Eq. (1.40) of Ch. 1, which truncates at second order because for $\hat{H}_{\rm 2tone}(t)$, the higher-order terms vanish identically.

The first-order Magnus term for the Carrier term is,

$$-i\int \hat{H}_{\rm c}(t_1) = \frac{\sin(t\delta+\phi_d)+\sin(\phi_d)}{\delta}\sum_j \Omega_j \left[e^{i\phi_s}\hat{\sigma}_j^- - \text{h.c.}\right], \tag{8.27}$$

where we introduced the sum and difference of the phases, respectively, as,

$$\phi_s = \frac{\phi_b+\phi_r}{2} + \frac{\pi}{2}, \qquad \phi_d = \frac{\phi_b-\phi_r}{2}. \tag{8.28}$$

This term describes spin flips with phase determined by ϕ_s. Setting $\phi_s = 0$ results in $\hat{\sigma}_j^y$ driving, while $\phi_s = \pi/2$ results in $-\hat{\sigma}_j^x$ driving. Because the laser field is not resonant with the carrier transition, the population transfer between $|{\downarrow}\rangle_j$ and $|{\uparrow}\rangle_j$ is not perfect. In the limit of vanishing detuning we recover $\lim_{\delta\to 0}[\sin(\delta t+\phi_d) - \sin(\phi_d)]/\delta = t\cos(\phi_d)$, which describes perfect spin flips as expected.

The first-order term for the sideband term is,

$$-i\int \hat{H}_{\rm sbs}(t_1) = \sum_{m,j} i\frac{\eta_{m,j}\Omega_j}{\delta^2-\omega_m^2}\left[e^{i\phi_s}\hat{\sigma}_j^- + \text{h.c.}\right]\hat{x}_m(t), \tag{8.29}$$

B

where here the position operator $\hat{x}_m(t) = \hat{a}_m^\dagger(t) + \hat{a}_m(t)$ evolves as,

$$\hat{a}(t) = \hat{a}(\delta \sin(\phi_d) - i\omega_m \cos(\phi_d) + e^{-i\omega_m t}[\delta \sin(\delta t + \phi_d) - i\omega_m \cos(\delta t + \phi_d)]). \tag{8.30}$$

This term describes a time-dependent spin-dependent displacement which generates spin-boson entanglement. In the regime where $|\delta - \omega_m| \gg \eta_{m,j}\Omega_j$ the oscillations are fast and therefore average out.

At second order of the Magnus expansion, we must compute three two-time commutators: carrier-carrier, carrier-sideband and sideband-sideband. The two-time carrier-carrier commutator vanishes identically,

$$\iint [\hat{H}_c(t_1), \hat{H}_c(t_2)] = 0, \tag{8.31}$$

because $\Phi(t_1)\Phi^*(t_2) = \Phi^*(t_1)\Phi(t_2)$, while $[\hat{\sigma}_j^+, \hat{\sigma}_k^-] = -[\hat{\sigma}_j^-, \hat{\sigma}_k^+] = \delta_{jk}\hat{\sigma}_j^z$. For the same reason, the carrier-sideband commutators also vanish,

$$\iint [\hat{H}_c(t_1), \hat{H}_{sbs}(t_2)] + [\hat{H}_{sbs}(t_1), \hat{H}_c(t_2)] = 0, \tag{8.32}$$

To evaluate the sideband-sideband two-time commutator we note that there are four two-time commutators. The two diagonal terms are [1],

$$[i\hat{\sigma}_j^- \hat{x}_m(t_1), i\hat{\sigma}_k^- \hat{x}_n(t_2)] = -|\delta_{jk} - 1|\delta_{mn}\hat{\sigma}_j^-\hat{\sigma}_k^-[\hat{x}_m(t_1), \hat{x}_m(t_2)], \tag{8.33a}$$

$$[-i\hat{\sigma}_j^+ \hat{x}_m(t_1), -i\hat{\sigma}_k^+ \hat{x}_n(t_2)] = -|\delta_{jk} - 1|\delta_{mn}\hat{\sigma}_j^+\hat{\sigma}_k^+[\hat{x}_m(t_1), \hat{x}_m(t_2)], \tag{8.33b}$$

and the two cross terms are,

$$[i\hat{\sigma}_j^- \hat{x}_m(t_1), -i\hat{\sigma}_k^+ \hat{x}_n(t_2)] = \delta_{mn}\hat{\sigma}_j^-\hat{\sigma}_k^+[\hat{x}_m(t_1), \hat{x}_n(t_2)] - \delta_{jk}\hat{\sigma}_j^z\hat{x}_n(t_2)\hat{x}_m(t_1), \tag{8.34a}$$

$$[-i\hat{\sigma}_j^+ \hat{x}_m(t_1), i\hat{\sigma}_k^- \hat{x}_n(t_2)] = \delta_{mn}\hat{\sigma}_j^+\hat{\sigma}_k^-[\hat{x}_m(t_1), \hat{x}_n(t_2)] + \delta_{jk}\hat{\sigma}_j^z\hat{x}_n(t_2)\hat{x}_m(t_1). \tag{8.34b}$$

All of these terms involve the motional commutator, which evaluates to,

$$[\hat{x}_m(t_1), \hat{x}_m(t_2)] = e^{-i\omega_m(t_2-t_1)} - e^{i\omega_m(t_2-t_1)}. \tag{8.35}$$

We now compute, term by term, the integrals of each two-time commutator. Integrating the first diagonal two-time commutator yields,

$$\begin{aligned} &\sum_{m,n,j,k} \iint \Phi(t)^2 [i\hat{\sigma}_j^- \hat{x}_m(t_1), i\hat{\sigma}_k^- \hat{x}_n(t_2)] \\ &= -\sum_{j\neq k,m} \frac{2ie^{2i\phi_s}}{\delta^2 - \omega_m^2} \left[2t\omega_m + \mathcal{O}\left(\frac{\omega_m}{\delta}, \frac{\delta_m^s}{\delta_m^d}, \frac{\delta_m^d}{\delta_m^s}\right)\right] \hat{\sigma}_j^-\hat{\sigma}_k^-. \end{aligned} \tag{8.36}$$

[1] Note the commutator identity $[AB, CD] = A[B, C]D + AC[B, D] + [A, C]DB + C[A, D]B$.

Here, we introduced the difference and sum of the detuning and the mth mode, respectively, as,

$$\delta_m^s = \delta + \omega_m, \qquad \delta_m^d = \delta - \omega_m. \tag{8.37}$$

Also, we used big O notation for terms that do not grow in time. Specifically for this commutator of Eq. (8.36), the terms hidden in the big O notation are,

$$\frac{\delta_m^d}{\delta_m^s}\sin(t\delta_m^s) - \frac{\delta_m^s}{\delta_m^d}\sin(t\delta_m^d) + \cos(t\delta + 2\phi_d)\left[\frac{2\omega_m \sin(t\delta)}{\delta} - 2\sin(t\omega_m)\right]. \tag{8.38}$$

A similar calculation for the second diagonal term yields,

$$\begin{aligned}&\sum_{m,n,j,k} \iint \Phi^*(t)^2[-i\hat{\sigma}_j^+\hat{x}_m(t_1), -i\hat{\sigma}_k^+\hat{x}_n(t_2)] \\ &= -\sum_{j\neq k,m} \frac{2ie^{-2i\phi_s}}{\delta^2-\omega_m^2}\left[2t\omega_m + \mathcal{O}\left(\frac{\omega_m}{\delta}, \frac{\delta_m^s}{\delta_m^d}, \frac{\delta_m^d}{\delta_m^s}\right)\right]\hat{\sigma}_j^+\hat{\sigma}_k^+,\end{aligned} \tag{8.39}$$

with the big O term the same as Eq. (8.38). For the cross terms, after using the fact that the second terms in Eq. (8.34a) and Eq. (8.34b) cancel to preemptively simplify the next two expressions, the first cross term is,

$$\begin{aligned}&\sum_{m,n,j,k} \iint \Phi(t_1)\Phi^*(t_2)[i\hat{\sigma}_j^-\hat{x}_m(t_1), -i\hat{\sigma}_k^+\hat{x}_n(t_2)] \\ &= -\sum_{j,k,m} \frac{2i}{\delta^2-\omega_m^2}\left[2t\omega_m + \mathcal{O}\left(\frac{\omega_m}{\delta}, \frac{\delta_m^s}{\delta_m^d}, \frac{\delta_m^d}{\delta_m^s}\right)\right]\hat{\sigma}_j^-\hat{\sigma}_k^+,\end{aligned} \tag{8.40}$$

and the second cross term is,

$$\begin{aligned}&\sum_{m,n,j,k} \iint \Phi^*(t_1)\Phi(t_2)[-i\hat{\sigma}_j^+\hat{x}_m(t_1), i\hat{\sigma}_k^-\hat{x}_n(t_2)] \\ &= -\sum_{j,k,m} \frac{2i}{\delta^2-\omega_m^2}\left[2t\omega_m + \mathcal{O}\left(\frac{\omega_m}{\delta}, \frac{\delta_m^s}{\delta_m^d}, \frac{\delta_m^d}{\delta_m^s}\right)\right]\hat{\sigma}_j^+\hat{\sigma}_k^-,\end{aligned} \tag{8.41}$$

where the terms collected in the big O notation are identical to those in Eq. (8.38).

At this point, we observe that all terms at second order are either linear or bounded (sinusoidal) in t. The linear term will dominate when $t \gg 1/\delta$ and $|\delta - \omega_m| \gg \eta_{m,j}\Omega_j$. In this regime where we can ignore the first-order Magnus term and the bounded terms at second order. After reintroducing the $-1/2$ factor from the definition of the second-order Magnus term and the $\Omega_j\eta_{m,j}/2$ prefactors from $\hat{H}_{\text{sbs}}(t)$, the Magnus unitary is,

$$\hat{U}(t) = \exp\left(-it\sum_{j,k,m}\frac{\omega_m\Omega_j\Omega_k\eta_{m,j}\eta_{m,k}}{\delta^2-\omega_m^2}\hat{\sigma}_j^{\phi_s}\hat{\sigma}_k^{\phi_s}\right) \tag{8.42}$$

B

where we used the definition $\hat{\sigma}_j^{\phi} = \cos(\phi)\hat{\sigma}_j^x + \sin(\phi)\hat{\sigma}_j^y$ that was introduced in Eq. (1.36) to write,

$$e^{2i\phi_s}\hat{\sigma}_j^-\hat{\sigma}_k^- + \hat{\sigma}_j^-\hat{\sigma}_k^+ + \hat{\sigma}_k^-\hat{\sigma}_j^+ + e^{-2i\phi_s}\hat{\sigma}_j^+\hat{\sigma}_k^+ = \hat{\sigma}_j^{\phi_s}\hat{\sigma}_k^{\phi_s} \tag{8.43}$$

The evolution is therefore described by an effective spin-spin Ising Hamiltonian,

$$\hat{H}_{\text{Ising}} = \sum_{j,k} J_{j,k}\hat{\sigma}_j^{\phi_s}\hat{\sigma}_k^{\phi_s}, \tag{8.44}$$

where the coupling strength between the jth and kth ion is determined by,

$$J_{j,k} = \Omega_j\Omega_k \sum_m \frac{\omega_m \eta_{m,j}\eta_{m,k}}{\delta^2 - \omega_m^2}. \tag{8.45}$$

Setting $\phi_b = 0$ and $\phi_r = \pi$ results in $\phi_s = \pi$, and therefore $\hat{\sigma}_j^x\hat{\sigma}_j^x$ interactions. Meanwhile, setting $\phi_b = \phi_r = 0$ results in $\phi_s = \pi/2$, and therefore $\hat{\sigma}_j^y\hat{\sigma}_j^y$ interactions. This derivation forms the basis of Sec. 1.4.3 of Ch. 1 on off-resonant (dispersive) driving, and shows how trapped ions can be used as an analogue quantum simulator of Ising Hamiltonians.

Summary

The aim of this Thesis is to understand and harness hybrid spin-boson systems. Motivated by the prospect of realizing a quantum advantage, in Part One we consider quantum simulations, sensing and state preparation in spin-boson systems. Exactly describing spin-boson systems is often extremely challenging, so in Part Two we develop efficient classical numerical methods for simulating their closed and open quantum dynamics.

We begin **Part One** in Ch. 1 with a review of trapped-ion systems, a well-established spin-boson hardware platform. The theory of ion trapping is introduced, including a detailed treatment of micromotion using Floquet theory. We discuss how a qubit is encoded in each ion's internal electronic energy levels, and how laser light realizes effective spin-spin interactions that are well-described by an Ising model, enabling quantum simulations of spin-spin models. Finally we review optical tweezers and how they can increase the programmability of the trapped-ion quantum simulator.

In Ch. 2 we numerically study the effect of expected sources of experimental error in quantum simulations with trapped ions in optical tweezers. We show that micromotion should be included when numerically optimizing the tweezer pinning frequencies, while first-order Doppler shifts may be a major source of error along the weaker confinement direction where micromotion is largest. Additional stress and strain forces do not increase the simulator's programmability, while tweezer intensity noise should be stabilized to the sub-percent level to realize high-fidelity quantum simulations.

In Ch. 3 we continue with the theme of harnessing spin-boson systems, asking how many-body spin-boson systems can be used for displacement sensing. We prove that in terms of the bosonic mode's occupation, spin-dependent squeezed states are optimal reference states. Specifically, they saturate the Heisenberg limit for estimating a displacement's amplitude, and for jointly estimating a displacement's real and imaginary components. With trapped-ion systems in mind, we provide experimentally-realizable measurement schemes that follow Heisenberg scaling. We also introduce a fast and scalable protocol for preparing spin-dependent squeezed states that uses dynamically modulated first-order sideband interactions, achieving a preparation time that scales as $1/\sqrt{N}$ in systems with N ions. We numerically demonstrate the preparation of 8.7 dB of spin-dependent squeezing 15 times faster than the standard trapped-ion approach using second-order sidebands. The potential applications of our metrology protocols include quantum-logic enabled photon-recoil spectroscopy of molecular and highly charged ions, and searches for physics beyond the Standard Model by sensing a displacement induced by theorized

interactions between Standard Model fields and certain forms of dark matter such as axions.

In Ch. 4 we conclude Part One by asking if arbitrary symmetric spin states can be efficiently prepared using only global control. Symmetric spin states are defined as any quantum state that is invariant when two particles are exchanged, while the development of protocols that do not require individual qubit addressing is crucial for platforms where single-qubit addressing is not available, and for reducing experimental demands more broadly. Using a variational quantum circuit built from global rotations and global spin squeezing, we provide numerical evidence and an analytical argument that at most $2N/3$ circuit layers are required to prepare arbitrary symmetric states. We highlight the capabilities of our approach by preparing symmetric states that are useful for quantum metrology and quantum error correction. We expect the variational circuit to be immediately realizable on current quantum hardware platforms, and in particular discuss how our protocol can be realized in trapped-ion platforms.

In **Part Two** we aim to understand hybrid spin-boson systems by developing classical numerical methods for simulating their quantum dynamics. In Ch. 5 we introduce the framework, namely a variational ansatz for the quantum state and the time-dependent variational principle (TDVP) to simulate dynamics. For the ansatz we choose a non-Gaussian state (NGS), specifically a superposition of bosonic Gaussian states (SCS). We also review the study of open quantum systems, including the quantum trajectories method.

In Ch. 6 we study ground-state properties using imaginary-time evolution and non-equilibrium dynamics using real-time evolution. Focusing on the spin-boson model, a paradigmatic model that describes a single spin coupled to a set of bosonic modes, we demonstrate that the ansatz is efficient and controllable even beyond the regime of Ohmic-type couplings. We also use our framework to study bath dynamics, and combine it with optimal control for the fast preparation of near-critical ground states.

In Ch. 7 we extend the NGS and TDVP framework to study open dynamics using quantum trajectories. We study a Holstein-Tavis-Cummings Hamiltonian, a paradigmatic model which in the context of polaritonic chemistry describes low-energy electronic excitations coupled to local molecular vibrations and a collective cavity mode, and features enhanced chemical reaction rates. We benchmark our framework against the truncated Wigner approximation (TWA), showing that there are parameter regimes where the NGS outperforms our TWA implementation. While the NGS framework can be applied to a range of problems, some bottlenecks remain such as a limited number of spins. Possible future applications range from studies of polaritonic chemistry and impurity physics to robust quantum state preparation in hybrid spin-boson systems.

Samenvatting

Het doel van dit proefschrift is het begrijpen en benutten van hybride spin-boson systemen. In Deel Een bestuderen wij quantumsimulaties, sensing en toestandspreparatie in spin-boson systemen. Dit is gemotiveerd door de mogelijkheid een quantumvoordeel te realiseren. Een exacte beschrijving van spin-boson systemen is vaak zeer complex. Daarom ontwikkelen wij in Deel Twee efficiënte klassieke numerieke methoden voor het simuleren van hun gesloten en open quantumdynamica.

Wij beginnen Deel Een in Hoofdstuk 1 met een overzicht van gevangen-ionen systemen, een uitgebreid onderzocht hardwareplatform voor spin-boson systemen. De theorie van ionenvangst wordt geïntroduceerd, inclusief een gedetailleerde behandeling van micromotie met behulp van Floquet-theorie. Er wordt besproken hoe een qubit gecodeerd wordt in de interne elektronische energieniveaus van elk ion en hoe laserlicht effectieve spin-spin interacties realiseert. Deze interacties worden goed beschreven door een Ising-model. Dit maakt quantumsimulaties van spin-spin modellen mogelijk. Tot slot wordt ingegaan op optische pincetten en hoe deze de programmeerbaarheid van de gevangen-ionenquantumsimulator kunnen vergroten.

In Hoofdstuk 2 bestuderen wij het effect van verwachte experimentele foutenbronnen in quantumsimulaties met gevangen ionen in optische pincetten met numerieke methoden. Uit de resultaten blijkt dat micromotie moet worden meegenomen bij het numeriek optimaliseren van de pincet-pinfrequenties. Eerste-orde Dopplerverschuivingen kunnen een belangrijke foutenbron vormen langs de richting van zwakkere opsluiting, waar de micromotie het grootst is. Extra spanning- en rekkrachten vergroten de programmeerbaarheid van de simulator niet. Ruis in de intensiteit van de pincetten moet worden gestabiliseerd tot op sub-procentniveau om quantumsimulaties met hoge nauwkeurigheid te realiseren.

In Hoofdstuk 3 gaan wij verder in op het benutten van spin-boson systemen. Wij onderzoeken hoe spin-boson systemen met veel deeltjes gebruikt kunnen worden voor *displacement sensing*. Wij bewijzen dat spin-afhankelijke *squeezed states* optimale referentietoestanden zijn in termen van de bezetting van de bosonische modus. Deze toestanden bereiken het Heisenberg-limiet voor het schatten van de amplitude van een verplaatsing en voor het gezamenlijk schatten van de reële en imaginaire componenten van een verplaatsing. Wij presenteren realiseerbare meetmethoden gericht op gevangen-ionen systemen, die voldoen aan de Heisenbergschaling. Daarnaast wordt een snel en schaalbaar protocol geïntroduceerd voor het prepareren van spin-afhankelijke *squeezed states*. Dit protocol maakt gebruik van het dynamisch moduleren van eerste-orde *sideband* interaction en bereikt een preparatietijd die schaalt als $1/\sqrt{N}$ in systemen van N ionen. De preparatie van 8.7 dB spin-afhankelijke squeezing wordt numeriek gedemonstreerd. Dit is 15 keer

sneller dan de standaard gevangen-ionen benadering met tweede-orde *sidebands*. Toepassingen van deze meetkundige protocollen zijn onder andere quantum-logic ondersteunde foton-recoilspectroscopie en ondersteuning in de zoektocht naar de natuurkunde buiten het Standaardmodel door het detecteren van verplaatsingen.

In Hoofdstuk 4 onderzoeken wij of willekeurige symmetrische spin-toestanden efficiënt geprepareerd kunnen worden met globale controle. Symmetrische spin-toestanden zijn gedefineerd als invariant bij uitwisseling van twee deeltjes. De ontwikkeling van protocollen die geen individuele qubit-adressering vereisen, is cruciaal voor platforms waar *single-qubit* adressering niet beschikbaar is. Met behulp van een variationeel quantumcircuit, opgebouwd uit globale rotaties en globale spin-squeezing, wordt numeriek bewijs geleverd en een analytisch argument gegeven dat ten hoogste $2N/3$ circuitlagen nodig zijn om willekeurige symmetrische toestanden te prepareren. De mogelijkheden van deze aanpak worden benadrukt door het prepareren van symmetrische toestanden die nuttig zijn voor quantummetrologie en quantumfoutcorrectie. Het variationele circuit wordt direct realiseerbaar geacht op huidige quantumhardwareplatforms. Er wordt specifiek ingegaan op hoe het protocol gerealiseerd kan worden in gevangen-ionen systemen.

In **Deel Twee** gebruiken wij klassieke numerieke methoden voor het simuleren van de quantumdynamica van hybride spin-boson systemen. In Hoofdstuk 5 introduceren wij het raamwerk, bestaande uit een variationele ansatz voor de quantumtoestand en het tijdsafhankelijke variationele principe (TDVP) om dynamica te simuleren. Voor de ansatz wordt gekozen voor een niet-Gaussische toestand (NGS), specifiek een superpositie van bosonische Gaussische toestanden (SCS). Daarnaast worden open-quantumsystemen besproken, inclusief de methode van quantumtrajecten.

In Hoofdstuk 6 worden eigenschappen van grondtoestanden bestudeerd met behulp van imaginaire-tijdsevolutie en die van *non-equilibrium* dynamica met behulp van reële-tijdsevolutie. Wij tonen aan dat de ansatz efficiënt en controleerbaar is in de context van het spin-boson model, een paradigmatisch model dat een enkele spin gekoppeld aan een set bosonische modi beschrijft. Deze techniek wordt ook gebruikt om bad-dynamica te bestuderen en gecombineerd met optimale controle voor de snelle preparatie van bijna-kritische grondtoestanden.

In Hoofdstuk 7 wordt het NGS- en TDVP-raamwerk uitgebreid om open dynamica te bestuderen met behulp van quantumtrajecten. Er wordt een Holstein-Tavis-Cummings-Hamiltoniaan bestudeerd, een paradigmatisch model dat in de context van polaritonische chemie lage-energie elektronische excitaties beschrijft. Deze excitaties zijn gekoppeld aan lokale moleculaire vibraties en een collectieve caviteitsmodus en vertonen verhoogde chemische reactiesnelheden. Het raamwerk wordt vergeleken met de *truncated Wigner approximation* (TWA). Hieruit blijkt dat er parameterregimes zijn waarin de NGS beter presteert dan de TWA-implementatie. Hoewel het NGS-raamwerk toegepast kan worden op een reeks problemen, blijven er enkele knelpunten bestaan, zoals een beperkt aantal spins. Mogelijke toekomstige toepassingen variëren van studies van polaritonische chemie en onzuiverheidsfysica tot robuuste quantumtoestandspreparatie in hybride spin-boson systemen.

Bibliography

1. **L. Bond**, L. Lenstra, R. Gerritsma & A. Safavi-Naini. *Effect of micromotion and local stress in quantum simulations with trapped ions in optical tweezers*. Phys. Rev. A **106**, 042612 (2022).
2. **L. J. Bond**, C. H. Valahu, A. Shankar, T. R. Tan & A. Safavi-Naini. *Optimal Displacement Sensing with Spin-Dependent Squeezed States*. arXiv: 2510.25870 (2025).
3. **L. J. Bond**, M. J. Davis, J. Minář, R. Gerritsma, G. K. Brennen & A. Safavi-Naini. *Global variational quantum circuits for arbitrary symmetric state preparation*. Phys. Rev. Res. **7**, L022072 (2025).
4. **L. J. Bond**, A. Safavi-Naini & J. Minář. *Fast Quantum State Preparation and Bath Dynamics Using Non-Gaussian Variational Ansatz and Quantum Optimal Control*. Phys. Rev. Lett. **132**, 170401 (2024).
5. **L. J. Bond**, B. Gerritsen, J. Minář, J. T. Young, J. Schachenmayer & A. Safavi-Naini. *Open Quantum Dynamics with Variational Non-Gaussian States and the Truncated Wigner Approximation*. J. Chem. Phys. **161**, 184113 (2024).
6. D. Bluvstein *et al. Logical Quantum Processor Based on Reconfigurable Atom Arrays*. Nature **626**, 58 (2024).
7. R. Haghshenas *et al. Digital Quantum Magnetism at the Frontier of Classical Simulations*. arXiv: 2503.20870 (2025).
8. F. Arute *et al. Quantum Supremacy Using a Programmable Superconducting Processor*. Nature **574**, 505 (2019).
9. I. M. Georgescu, S. Ashhab & F. Nori. *Quantum Simulation*. Rev. Mod. Phys. **86**, 153 (2014).
10. A. J. Daley, I. Bloch, C. Kokail, S. Flannigan, N. Pearson, M. Troyer & P. Zoller. *Practical Quantum Advantage in Quantum Simulation*. Nature **607**, 667 (2022).
11. M. A. Nielsen & I. L. Chuang. *Quantum Computation and Quantum Information: 10th Anniversary Edition* (Cambridge University Press, Cambridge, 2010).
12. R. P. Feynman. *Simulating Physics with Computers*. Int J Theor Phys **21**, 467 (1982).
13. S. Lloyd. *Universal Quantum Simulators*. Science **273**, 1073 (1996).
14. B. P. Lanyon *et al. Universal Digital Quantum Simulation with Trapped Ions*. Science **334**, 57 (2011).
15. R. Barends *et al. Digital Quantum Simulation of Fermionic Models with a Superconducting Circuit*. Nat Commun **6**, 7654 (2015).
16. Y. Salathé *et al. Digital Quantum Simulation of Spin Models with Circuit Quantum Electrodynamics*. Phys. Rev. X **5**, 021027 (2015).

17. S. J. Evered *et al. Probing the Kitaev Honeycomb Model on a Neutral-Atom Quantum Computer*. Nature **645**, 341 (2025).

18. M. Greiner, O. Mandel, T. Esslinger, T. W. Hänsch & I. Bloch. *Quantum Phase Transition from a Superfluid to a Mott Insulator in a Gas of Ultracold Atoms*. Nature **415**, 39 (2002).

19. A. Friedenauer, H. Schmitz, J. T. Glueckert, D. Porras & T. Schaetz. *Simulating a Quantum Magnet with Trapped Ions*. Nat. Phys. **4**, 757 (2008).

20. K. Kim, M.-S. Chang, S. Korenblit, R. Islam, E. E. Edwards, J. K. Freericks, G.-D. Lin, L.-M. Duan & C. Monroe. *Quantum Simulation of Frustrated Ising Spins with Trapped Ions*. Nature **465**, 590 (2010).

21. J. W. Britton, B. C. Sawyer, A. C. Keith, C.-C. J. Wang, J. K. Freericks, H. Uys, M. J. Biercuk & J. J. Bollinger. *Engineered two-dimensional Ising interactions in a trapped-ion quantum simulator with hundreds of spins*. Nature **484**, 489 (2012).

22. R. Gerritsma, G. Kirchmair, F. Zähringer, E. Solano, R. Blatt & C. F. Roos. *Quantum Simulation of the Dirac Equation*. Nature **463**, 68 (2010).

23. J. Zhang, G. Pagano, P. W. Hess, A. Kyprianidis, P. Becker, H. Kaplan, A. V. Gorshkov, Z.-X. Gong & C. Monroe. *Observation of a Many-Body Dynamical Phase Transition with a 53-Qubit Quantum Simulator*. Nature **551**, 601 (2017).

24. B. Yan, S. A. Moses, B. Gadway, J. P. Covey, K. R. A. Hazzard, A. M. Rey, D. S. Jin & J. Ye. *Observation of Dipolar Spin-Exchange Interactions with Lattice-Confined Polar Molecules*. Nature **501**, 521 (2013).

25. H. Bernien *et al. Probing Many-Body Dynamics on a 51-Atom Quantum Simulator*. Nature **551**, 579 (2017).

26. T. Hensgens, T. Fujita, L. Janssen, X. Li, C. J. Van Diepen, C. Reichl, W. Wegscheider, S. Das Sarma & L. M. K. Vandersypen. *Quantum Simulation of a Fermi–Hubbard Model Using a Semiconductor Quantum Dot Array*. Nature **548**, 70 (2017).

27. R. Blatt & C. F. Roos. *Quantum Simulations with Trapped Ions*. Nat. Phys. **8**, 277 (2012).

28. C. D. Bruzewicz, J. Chiaverini, R. McConnell & J. M. Sage. *Trapped-ion quantum computing: Progress and challenges*. Appl. Phys. Rev. **6**, 021314 (2019).

29. P. Wang, C.-Y. Luan, M. Qiao, M. Um, J. Zhang, Y. Wang, X. Yuan, M. Gu, J. Zhang & K. Kim. *Single Ion Qubit with Estimated Coherence Time Exceeding One Hour*. Nat Commun **12**, 233 (2021).

30. A. C. Hughes, R. Srinivas, C. M. Löschnauer, H. M. Knaack, R. Matt, C. J. Ballance, M. Malinowski, T. P. Harty & R. T. Sutherland. *Trapped-Ion Two-Qubit Gates with >99.99% Fidelity without Ground-State Cooling*. arXiv: 2510.17286 (2025).

31. C. M. Löschnauer *et al. Scalable, High-Fidelity All-Electronic Control of Trapped-Ion Qubits*. arXiv: 2407.07694 (2024).

32. J. I. Cirac & P. Zoller. *Quantum Computations with Cold Trapped Ions*. Phys. Rev. Lett. **74**, 4091 (1995).

33. A. Sørensen & K. Mølmer. *Quantum Computation with Ions in Thermal Motion*. Phys. Rev. Lett. **82**, 1971 (1999).

34. D. Porras & J. I. Cirac. *Effective Quantum Spin Systems with Trapped Ions*. Phys. Rev. Lett. **92**, 207901 (2004).

35. R. Nath, M. Dalmonte, A. W. Glaetzle, P. Zoller, F. Schmidt-Kaler & R. Gerritsma. *Hexagonal plaquette spin–spin interactions and quantum magnetism in a two-dimensional ion crystal*. New J. Phys. **17**, 065018 (2015).

36. T. Lauprêtre, R. B. Linnet, I. D. Leroux, H. Landa, A. Dantan & M. Drewsen. *Controlling the Potential Landscape and Normal Modes of Ion Coulomb Crystals by a Standing-Wave Optical Potential*. Phys. Rev. A **99**, 031401 (2019).

37. Y. H. Teoh, M. Sajjan, Z. Sun, F. Rajabi & R. Islam. *Manipulating phonons of a trapped-ion system using optical tweezers*. Phys. Rev. A **104**, 022420 (2021).

38. T. Olsacher, L. Postler, P. Schindler, T. Monz, P. Zoller & L. M. Sieberer. *Scalable and Parallel Tweezer Gates for Quantum Computing with Long Ion Strings*. PRX Quantum **1**, 020316 (2020).

39. J. D. Arias Espinoza, M. Mazzanti, K. Fouka, R. X. Schüssler, Z. Wu, P. Corboz, R. Gerritsma & A. Safavi-Naini. *Engineering spin-spin interactions with optical tweezers in trapped ions*. Phys. Rev. A **104**, 013302 (2021).

40. C. L. Degen, F. Reinhard & P. Cappellaro. *Quantum sensing*. Rev. Mod. Phys. **89**, 035002 (2017).

41. D. Griffiths. *Introduction to Quantum Mechanics* (Cambridge University Press, 2017).

42. C. M. Caves. *Quantum-Mechanical Noise in an Interferometer*. Phys. Rev. D **23**, 1693 (1981).

43. J. Aasi *et al. Enhanced Sensitivity of the LIGO Gravitational Wave Detector by Using Squeezed States of Light*. Nature Photon **7**, 613 (2013).

44. M. Tse, H. Yu, N. Kijbunchoo, *et al. Quantum-Enhanced Advanced LIGO Detectors in the Era of Gravitational-Wave Astronomy*. Phys. Rev. Lett. **123**, 231107 (2019).

45. D. J. Wineland, J. J. Bollinger, W. M. Itano, F. L. Moore & D. J. Heinzen. *Spin Squeezing and Reduced Quantum Noise in Spectroscopy*. Phys. Rev. A **46**, R6797 (1992).

46. M. Kitagawa & M. Ueda. *Squeezed spin states*. Phys. Rev. A **47**, 5138 (1993).

47. D. Leibfried, M. D. Barrett, T. Schaetz, J. Britton, J. Chiaverini, W. M. Itano, J. D. Jost, C. Langer & D. J. Wineland. *Toward Heisenberg-Limited Spectroscopy with Multiparticle Entangled States*. Science **304**, 1476 (2004).

48. O. Hosten, N. J. Engelsen, R. Krishnakumar & M. A. Kasevich. *Measurement Noise 100 Times Lower than the Quantum-Projection Limit Using Entangled Atoms*. Nature **529**, 505 (2016).

49. A. D. Ludlow, M. M. Boyd, J. Ye, E. Peik & P. O. Schmidt. *Optical Atomic Clocks*. Rev. Mod. Phys. **87**, 637 (2015).

50. M. S. Turner. *Windows on the Axion*. Physics Reports **197**, 67 (1990).

51. D. Budker, P. W. Graham, H. Ramani, F. Schmidt-Kaler, C. Smorra & S. Ulmer. *Millicharged Dark Matter Detection with Ion Traps*. PRX Quantum **3**, 010330 (2022).

52. N. Du *et al. Search for Invisible Axion Dark Matter with the Axion Dark Matter Experiment*. Phys. Rev. Lett. **120**, 151301 (2018).

53. P. Zheng *et al. Quantum-Enhanced Dark Matter Detection Using Schrödinger Cat States*. arXiv: 2507.23538 (2025).

54. C. Braggio *et al. Quantum-Enhanced Sensing of Axion Dark Matter with a Transmon-Based Single Microwave Photon Counter*. Phys. Rev. X **15**, 021031 (2025).

55. A. V. Dixit, S. Chakram, K. He, A. Agrawal, R. K. Naik, D. I. Schuster & A. Chou. *Searching for Dark Matter with a Superconducting Qubit*. Phys. Rev. Lett. **126**, 141302 (2021).

56. K. M. Backes *et al. A Quantum Enhanced Search for Dark Matter Axions*. Nature **590**, 238 (2021).

57. K. A. Gilmore, M. Affolter, R. J. Lewis-Swan, D. Barberena, E. Jordan, A. M. Rey & J. J. Bollinger. *Quantum-Enhanced Sensing of Displacements and Electric Fields with Two-Dimensional Trapped-Ion Crystals*. Science **373**, 673 (2021).

58. S. Kolkowitz, A. C. Bleszynski Jayich, Q. P. Unterreithmeier, S. D. Bennett, P. Rabl, J. G. E. Harris & M. D. Lukin. *Coherent Sensing of a Mechanical Resonator with a Single-Spin Qubit*. Science **335**, 1603 (2012).

59. S. Schreppler, N. Spethmann, N. Brahms, T. Botter, M. Barrios & D. M. Stamper-Kurn. *Optically Measuring Force near the Standard Quantum Limit*. Science **344**, 1486 (2014).

60. K. A. Gilmore, J. G. Bohnet, B. C. Sawyer, J. W. Britton & J. J. Bollinger. *Amplitude Sensing below the Zero-Point Fluctuations with a Two-Dimensional Trapped-Ion Mechanical Oscillator*. Phys. Rev. Lett. **118**, 263602 (2017).

61. R. D. Delaney, A. P. Reed, R. W. Andrews & K. W. Lehnert. *Measurement of Motion beyond the Quantum Limit by Transient Amplification*. Phys. Rev. Lett. **123**, 183603 (2019).

62. F. Wolf, C. Shi, J. C. Heip, M. Gessner, L. Pezzè, A. Smerzi, M. Schulte, K. Hammerer & P. O. Schmidt. *Motional Fock States for Quantum-Enhanced Amplitude and Phase Measurements with Trapped Ions*. Nat Commun **10**, 2929 (2019).

63. X. Deng *et al. Quantum-Enhanced Metrology with Large Fock States*. Nat. Phys. **20**, 1874 (2024).

64. P. T. Grochowski & R. Filip. *Optimal Phase-Insensitive Force Sensing with Non-Gaussian States*. arXiv: 2505.20832 (2025).

65. W. Górecki, A. Riccardi & L. Maccone. *Quantum Metrology of Noisy Spreading Channels*. Phys. Rev. Lett. **129**, 240503 (2022).

66. W. J. Munro, K. Nemoto, G. J. Milburn & S. L. Braunstein. *Weak-Force Detection with Superposed Coherent States*. Phys. Rev. A **66**, 023819 (2002).

67. C. H. Valahu, M. P. Stafford, Z. Huang, V. G. Matsos, M. J. Millican, T. Chalermpusitarak, N. C. Menicucci, J. Combes, B. Q. Baragiola & T. R. Tan. *Quantum-enhanced multiparameter sensing in a single mode*. Sci. Adv. **11**, eadw9757 (2025).

68. K. Duivenvoorden, B. M. Terhal & D. Weigand. *Single-mode displacement sensor*. Phys. Rev. A **95**, 012305 (2017).

69. L. Labarca, S. Turcotte, A. Blais & B. Royer. *Quantum Sensing of Displacements with Stabilized GKP States*. arXiv: 2506.20627 (2025).

70. F. R. Cardoso, D. Z. Rossatto, G. P. L. M. Fernandes, G. Higgins & C. J. Villas-Boas. *Superposition of Two-Mode Squeezed States for Quantum Information Processing and Quantum Sensing*. Phys. Rev. A **103**, 062405 (2021).

71. M. G. Genoni, M. G. A. Paris, G. Adesso, H. Nha, P. L. Knight & M. S. Kim. *Optimal Estimation of Joint Parameters in Phase Space*. Phys. Rev. A **87**, 012107 (2013).

72. Y. Li *et al. Multi-Parameter Quantum Metrology with Stabilized Multi-Mode Squeezed State*. arXiv: 2312.10379 (2023).

73. X. Zhang *et al. Digital Quantum Simulation of Floquet Symmetry-Protected Topological Phases*. Nature **607**, 468 (2022).

74. T. Kadowaki & H. Nishimori. *Quantum Annealing in the Transverse Ising Model*. Phys. Rev. E **58**, 5355 (1998).

75. S. Lee *et al. Evaluating the Evidence for Exponential Quantum Advantage in Ground-State Quantum Chemistry*. Nat Commun **14**, 1952 (2023).

76. C. Marconi, G. Müller-Rigat, J. Romero-Pallejà, J. Tura & A. Sanpera. *Symmetric Quantum States: A Review of Recent Progress*. arXiv: 2506.10185 (2025).

77. R. H. Dicke. *Coherence in Spontaneous Radiation Processes*. Phys. Rev. **93**, 99 (1954).

78. H. Lipkin, N. Meshkov & A. Glick. *Validity of Many-Body Approximation Methods for a Solvable Model*. Nuclear Physics **62**, 188 (1965).

79. Y. Ouyang. *Permutation-invariant quantum codes*. Phys. Rev. A **90**, 062317 (2014).

80. M. B. Ruskai. *Pauli Exchange Errors in Quantum Computation*. Phys. Rev. Lett. **85**, 194 (2000).

81. J. A. Gross. *Designing Codes around Interactions: The Case of a Spin*. Phys. Rev. Lett. **127**, 010504 (2021).

82. M. Plesch & V. Bu žek. *Efficient compression of quantum information*. Phys. Rev. A **81**, 032317 (2010).

83. D. Bacon, I. L. Chuang & A. W. Harrow. *Efficient Quantum Circuits for Schur and Clebsch-Gordan Transforms*. Phys. Rev. Lett. **97**, 170502 (2006).

84. R. Prevedel, G. Cronenberg, M. S. Tame, M. Paternostro, P. Walther, M. S. Kim & A. Zeilinger. *Experimental Realization of Dicke States of up to Six Qubits for Multiparty Quantum Networking*. Phys. Rev. Lett. **103**, 020503 (2009).

85. G. Tóth. *Multipartite entanglement and high-precision metrology*. Phys. Rev. A **85**, 022322 (2012).

86. S. Aktar, A. Bärtschi, A.-H. A. Badawy & S. Eidenbenz. *A Divide-and-Conquer Approach to Dicke State Preparation*. IEEE Transactions on Quantum Engineering **3**, 1 (2022).

87. A. Bärtschi & S. Eidenbenz. *Short-Depth Circuits for Dicke State Preparation*. in *2022 IEEE International Conference on Quantum Computing and Engineering (QCE)* (2022), 87.

88. H. Buhrman, M. Folkertsma, B. Loff & N. M. P. Neumann. *State Preparation by Shallow Circuits Using Feed Forward*. Quantum **8**, 1552 (2024).

89. M. T. Johnsson, N. R. Mukty, D. Burgarth, T. Volz & G. K. Brennen. *Geometric Pathway to Scalable Quantum Sensing*. Phys. Rev. Lett. **125**, 190403 (2020).

90. S. S. Ivanov, N. V. Vitanov & N. V. Korolkova. *Creation of arbitrary Dicke and NOON states of trapped-ion qubits by global addressing with composite pulses*. New J. Phys. **15**, 023039 (2013).

91. V. M. Stojanovic & J. K. Nauth. *Dicke-State Preparation through Global Transverse Control of Ising-coupled Qubits*. Phys. Rev. A **108**, 012608 (2023).

92. D. B. Hume, C. W. Chou, T. Rosenband & D. J. Wineland. *Preparation of Dicke states in an ion chain*. Phys. Rev. A **80**, 052302 (2009).

93. C. Wu, C. Guo, Y. Wang, G. Wang, X.-L. Feng & J.-L. Chen. *Generation of Dicke states in the ultrastrong-coupling regime of circuit QED systems*. Phys. Rev. A **95**, 013845 (2017).

94. K. D. B. Higgins, S. C. Benjamin, T. M. Stace, G. J. Milburn, B. W. Lovett & E. M. Gauger. *Superabsorption of Light via Quantum Engineering*. Nat Commun **5**, 4705 (2014).

95. Y. Zhao, R. Zhang, W. Chen, X.-B. Wang & J. Hu. *Creation of Greenberger-Horne-Zeilinger States with Thousands of Atoms by Entanglement Amplification*. npj Quantum Inf **7**, 24 (2021).

96. A. Bärtschi & S. Eidenbenz. in *Fundamentals of Computation Theory* edited by L. A. Gasieniec, J. Jansson & C. Levcopoulos, 126 (Springer International Publishing, Cham, 2019).

97. X. Zou, K. Pahlke & W. Mathis. *Generation of arbitrary superpositions of the Dicke states of excitons in optically driven quantum dots*. Phys. Rev. A **68**, 034306 (2003).

98. J. Preskill. *Quantum Computing in the NISQ era and beyond*. Quantum **2**, 79 (2018).

99. V. G. Matsos, C. H. Valahu, T. Navickas, A. D. Rao, M. J. Millican, X. C. Kolesnikow, M. J. Biercuk & T. R. Tan. *Robust and Deterministic Preparation of Bosonic Logical States in a Trapped Ion*. Phys. Rev. Lett. **133**, 050602 (2024).

100. M. J. Millican, V. G. Matsos, C. H. Valahu, T. Navickas, **L. J. Bond** & T. R. Tan. *Engineering Continuous-Variable Entanglement in Mechanical Oscillators with Optimal Control*. arXiv: 2505.20844 (2025).

101. R. Orús. *Tensor Networks for Complex Quantum Systems*. Nat Rev Phys **1**, 538 (2019).

102. J. Schachenmayer, A. Pikovski & A. M. Rey. *Many-Body Quantum Spin Dynamics with Monte Carlo Trajectories on a Discrete Phase Space*. Phys. Rev. X **5**, 011022 (2015).

103. H. Weimer, A. Kshetrimayum & R. Orús. *Simulation methods for open quantum many-body systems*. Rev. Mod. Phys. **93**, 015008 (2021).

104. D. Wellnitz, G. Pupillo & J. Schachenmayer. *Disorder Enhanced Vibrational Entanglement and Dynamics in Polaritonic Chemistry*. Commun Phys **5**, 120 (2022).

105. M. L. Wall, A. Safavi-Naini & A. M. Rey. *Simulating generic spin-boson models with matrix product states*. Phys. Rev. A **94**, 053637 (2016).

106. C. Guo, A. Weichselbaum, J. von Delft & M. Vojta. *Critical and Strong-Coupling Phases in One- and Two-Bath Spin-Boson Models*. Phys. Rev. Lett. **108**, 160401 (2012).

107. A. Piñeiro Orioli, A. Safavi-Naini, M. L. Wall & A. M. Rey. *Nonequilibrium dynamics of spin-boson models from phase-space methods*. Phys. Rev. A **96**, 033607 (2017).

108. T. Shi, E. Demler & J. Ignacio Cirac. *Variational Study of Fermionic and Bosonic Systems with Non-Gaussian States: Theory and Applications*. Annals of Physics **390**, 245 (2018).

109. L. Hackl, T. Guaita, T. Shi, J. Haegeman, E. Demler & I. Cirac. *Geometry of Variational Methods: Dynamics of Closed Quantum Systems*. SciPost Phys. **9**, 048 (2020).

110. Y. Ashida, T. Shi, R. Schmidt, H. R. Sadeghpour, J. I. Cirac & E. Demler. *Quantum Rydberg Central Spin Model*. Phys. Rev. Lett. **123**, 183001 (2019).

111. J. Knörzer, T. Shi, E. Demler & J. I. Cirac. *Spin-Holstein Models in Trapped-Ion Systems*. Phys. Rev. Lett. **128**, 120404 (2022).

112. A. Christianen, J. I. Cirac & R. Schmidt. *Chemistry of a Light Impurity in a Bose-Einstein Condensate*. Phys. Rev. Lett. **128**, 183401 (2022).

113. P. E. Dolgirev, Y.-F. Qu, M. B. Zvonarev, T. Shi & E. Demler. *Emergence of a Sharp Quantum Collective Mode in a One-Dimensional Fermi Polaron*. Phys. Rev. X **11**, 041015 (2021).

114. L. Chen, Y. Yan, M. F. Gelin & Z. Lü. *Dynamics of the spin-boson model: The effect of bath initial conditions*. J. Chem. Phys. **158**, 104109 (2023).

115. Y. Zhao. *The hierarchy of Davydov's Ansätze: From guesswork to numerically "exact" many-body wave functions*. J. Chem. Phys. **158**, 080901 (2023).

116. H.-D. Meyer, U. Manthe & L. Cederbaum. *The Multi-Configurational Time-Dependent Hartree Approach*. Chem. Phys. Letters **165**, 73 (1990).

117. A. J. Leggett, S. Chakravarty, A. T. Dorsey, M. P. A. Fisher, A. Garg & W. Zwerger. *Dynamics of the Dissipative Two-State System*. Rev. Mod. Phys. **59**, 1 (1987).

118. K. Sun, C. Dou, M. F. Gelin & Y. Zhao. *Dynamics of disordered Tavis–Cummings and Holstein–Tavis–Cummings models*. J. Chem. Phys. **156**, 024102 (2022).

119. D. Leibfried, R. Blatt, C. Monroe & D. Wineland. *Quantum dynamics of single trapped ions*. Rev. Mod. Phys. **75**, 281 (2003).

120. R. Alheit, S. Kleineidam, F. Vedel, M. Vedel & G. Werth. *Higher order non-linear resonances in a Paul trap*. International Journal of Mass Spectrometry and Ion Processes **154**, 155 (1996).

121. D. J. Berkeland, J. D. Miller, J. C. Bergquist, W. M. Itano & D. J. Wineland. *Minimization of ion micromotion in a Paul trap*. J. Appl. Phys. **83**, 5025 (1998).

122. H. Landa, M. Drewsen, B. Reznik & A. Retzker. *Modes of oscillation in radiofrequency Paul traps*. New J. Phys. **14**, 093023 (2012).

123. H. Kaufmann, S. Ulm, G. Jacob, U. Poschinger, H. Landa, A. Retzker, M. B. Plenio & F. Schmidt-Kaler. *Precise Experimental Investigation of Eigenmodes in a Planar Ion Crystal*. Phys. Rev. Lett. **109**, 263003 (2012).

124. P. Richerme. *Two-dimensional ion crystals in radio-frequency traps for quantum simulation*. Phys. Rev. A **94**, 032320 (2016).

125. S.-T. Wang, C. Shen & L.-M. Duan. *Quantum computation under Micromotion in a planar Ion Crystal*. Sci Rep **5** (2015).

126. H. Landa, M. Drewsen, B. Reznik & A. Retzker. *Classical and Quantum Modes of Coupled Mathieu Equations*. J. Phys. A: Math. Theor. **45**, 455305 (2012).

127. C. Flühmann, T. L. Nguyen, M. Marinelli, V. Negnevitsky, K. Mehta & J. P. Home. *Encoding a Qubit in a Trapped-Ion Mechanical Oscillator*. Nature **566**, 513 (2019).

128. V. G. Matsos, C. H. Valahu, M. J. Millican, T. Navickas, X. C. Kolesnikow, M. J. Biercuk & T. R. Tan. *Universal Quantum Gate Set for Gottesman–Kitaev–Preskill Logical Qubits*. Nat. Phys. **21**, 1664 (2025).

129. B. de Neeve, T.-L. Nguyen, T. Behrle & J. P. Home. *Error Correction of a Logical Grid State Qubit by Dissipative Pumping*. Nat. Phys. **18**, 296 (2022).

130. D. Gottesman, A. Kitaev & J. Preskill. *Encoding a qubit in an oscillator*. Phys. Rev. A **64**, 012310 (2001).

131. D. Wineland, C. Monroe, W. Itano, D. Leibfried, B. King & D. Meekhof. *Experimental issues in coherent quantum-state manipulation of trapped atomic ions*. J. Res. Natl. Inst. Stand. Technol. **103**, 259 (1998).

132. P. C. Haljan, K.-A. Brickman, L. Deslauriers, P. J. Lee & C. Monroe. *Spin-Dependent Forces on Trapped Ions for Phase-Stable Quantum Gates and Entangled States of Spin and Motion*. Phys. Rev. Lett. **94**, 153602 (2005).

133. R. Islam. *Quantum Simulation of Interacting Spin Models with Trapped Ions*. PhD thesis (University of Maryland, 2012). HDL: `1903/13218`.

134. D. F. Walls & G. J. Milburn. *Quantum Optics* (Springer Nature Switzerland, Cham, 2025).

135. S. Kirchhoff, F. K. Wilhelm & F. Motzoi. *Correction Formulas for the Mølmer-Sørensen Gate Under Strong Driving*. PRX Quantum **6**, 010328 (2025).

136. E. Jaynes & F. Cummings. *Comparison of Quantum and Semiclassical Radiation Theories with Application to the Beam Maser*. Proceedings of the IEEE **51**, 89 (1963).

137. C. Monroe, D. M. Meekhof, B. E. King & D. J. Wineland. *A "Schrödinger Cat" Superposition State of an Atom*. Science **272**, 1131 (1996).

138. J. Hastrup, K. Park, J. B. Brask, R. Filip & U. L. Andersen. *Measurement-Free Preparation of Grid States*. npj Quantum Inf **7**, 17 (2021).

139. A. Sørensen & K. Mølmer. *Entanglement and quantum computation with ions in thermal motion*. Phys. Rev. A **62**, 022311 (2000).

140. G. Milburn, S. Schneider & D. James. *Ion Trap Quantum Computing with Warm Ions*. Fortschritte der Physik **48**, 801 (2000).

141. W. Magnus. *On the Exponential Solution of Differential Equations for a Linear Operator*. Comm. Pure Appl. Math. **7**, 649 (1954).

142. S. Blanes, F. Casas, J. Oteo & J. Ros. *The Magnus Expansion and Some of Its Applications*. Physics Reports **470**, 151 (2009).

143. J. Ma, X. Wang, C. P. Sun & F. Nori. *Quantum Spin Squeezing*. Physics Reports **509**, 89 (2011).

144. K. Mølmer & A. Sørensen. *Multiparticle entanglement of hot trapped ions*. Phys. Rev. Lett. **82**, 1835 (1999).

145. C. Monroe *et al. Programmable Quantum Simulations of Spin Systems with Trapped Ions*. Rev. Mod. Phys. **93**, 025001 (2021).

146. R. Grimm, M. Weidemüller & Y. B. Ovchinnikov. *Optical Dipole Traps for Neutral Atoms*, in *Advances In Atomic, Molecular, and Optical Physics* edited by B. Bederson & H. Walther (Academic Press, 2000), pp. 95–170.

147. M. Mazzanti. *Trapped Ions in Optical Tweezers and their Applications to Quantum Computing*. PhD thesis (University of Amsterdam, 2023).

148. P. K. Mogensen & A. N. Riseth. *Optim: A mathematical optimization package for Julia*. Journal of Open Source Software **3**, 615 (2018).

149. J. Bezanson, A. Edelman, S. Karpinski & V. B. Shah. *Julia: A fresh approach to numerical computing*. SIAM review **59**, 65 (2017).

150. A. Khan, B. Yoshimura & J. K. Freericks. *Theoretical basis for quantum simulation with a planar ionic crystal in a Penning trap using a triangular rotating wall*. Phys. Rev. A **92**, 043405 (2015).

151. D. H. E. Dubin. *Theory of structural phase transitions in a trapped Coulomb crystal*. Phys. Rev. Lett. **71**, 2753 (1993).

152. D. G. Enzer *et al. Observation of Power-Law Scaling for Phase Transitions in Linear Trapped Ion Crystals*. Phys. Rev. Lett. **85**, 2466 (2000).

153. M. Enderlein, T. Huber, C. Schneider & T. Schaetz. *Single Ions Trapped in a One-Dimensional Optical Lattice*. Phys. Rev. Lett. **109**, 233004 (2012).

154. B. P. Abbott, R. Abbott, T. D. Abbott, *et al. Observation of Gravitational Waves from a Binary Black Hole Merger*. Phys. Rev. Lett. **116**, 061102 (2016).

155. A. Aeppli, K. Kim, W. Warfield, M. S. Safronova & J. Ye. *Clock with* 8×10^{-19} *Systematic Uncertainty*. Phys. Rev. Lett. **133**, 023401 (2024).

156. A. L. Shaw, P. Scholl, R. Finkelstein, R. B.-S. Tsai, J. Choi & M. Endres. *Erasure Cooling, Control, and Hyperentanglement of Motion in Optical Tweezers*. Science **388**, 845 (2025).

157. P. Campagne-Ibarcq *et al. Quantum Error Correction of a Qubit Encoded in Grid States of an Oscillator*. Nature **584**, 368 (2020).

158. S. Saner, O. Băzăvan, D. J. Webb, G. Araneda, D. M. Lucas, C. J. Ballance & R. Srinivas. *Generating Arbitrary Superpositions of Nonclassical Quantum Harmonic Oscillator States*. arXiv: 2409.03482 (2024).

159. M. Penasa, S. Gerlich, T. Rybarczyk, V. Métillon, M. Brune, J. M. Raimond, S. Haroche, L. Davidovich & I. Dotsenko. *Measurement of a Microwave Field Amplitude beyond the Standard Quantum Limit*. Phys. Rev. A **94**, 022313 (2016).

160. R. J. Lewis-Swan, D. Barberena, J. A. Muniz, J. R. K. Cline, D. Young, J. K. Thompson & A. M. Rey. *Protocol for Precise Field Sensing in the Optical Domain with Cold Atoms in a Cavity*. Phys. Rev. Lett. **124**, 193602 (2020).

161. D. Barberena, R. J. Lewis-Swan, J. K. Thompson & A. M. Rey. *Atom-light entanglement for precise field sensing in the optical domain*. Phys. Rev. A **102**, 052615 (2020).

162. O. Katz, M. Cetina & C. Monroe. *N -Body Interactions between Trapped Ion Qubits via Spin-Dependent Squeezing*. Phys. Rev. Lett. **129**, 063603 (2022).

163. O. Katz, L. Feng, A. Risinger, C. Monroe & M. Cetina. *Demonstration of Three- and Four-Body Interactions between Trapped-Ion Spins*. Nat. Phys. **19**, 1452 (2023).

164. Y. Shapira, S. Cohen, N. Akerman, A. Stern & R. Ozeri. *Robust Two-Qubit Gates for Trapped Ions Using Spin-Dependent Squeezing*. Phys. Rev. Lett. **130**, 030602 (2023).

165. M. Ayyash, X. Xu, S. Ashhab & M. Mariantoni. *Driven Multiphoton Qubit-Resonator Interactions*. Phys. Rev. A **110**, 053711 (2024).

166. M. K. Hope, J. Lidal & F. Massel. *Preparation of Conditionally-Squeezed States in Qubit-Oscillator Systems*. arXiv: 2504.01664 (2025).

167. S. C. Burd *et al. Experimental Speedup of Quantum Dynamics through Squeezing*. PRX Quantum **5**, 020314 (2024).

168. L. Pezzè & A. Smerzi. *Advances in Multiparameter Quantum Sensing and Metrology*. arXiv: 2502.17396 (2025).

169. J. Liu, H. Yuan, X.-M. Lu & X. Wang. *Quantum Fisher information matrix and multiparameter estimation*. J. Phys. A: Math. Theor. **53**, 023001 (2019).

170. R. T. Sutherland & R. Srinivas. *Universal hybrid quantum computing in trapped ions*. Phys. Rev. A **104**, 032609 (2021).

171. M. Ayyash & S. Ashhab. *Dispersive Regime of Multiphoton Qubit-Oscillator Interactions*. Phys. Rev. A **112**, 023713 (2025).

172. Y. Liu *et al. Hybrid Oscillator-Qubit Quantum Processors: Instruction Set Architectures, Abstract Machine Models, and Applications*. arXiv: 2407.10381 (2025).

173. M. Drechsler, M. Belén Farías, N. Freitas, C. T. Schmiegelow & J. P. Paz. *State-dependent motional squeezing of a trapped ion: Proposed method and applications*. Phys. Rev. A **101**, 052331 (2020).

174. N. F. Del Grosso, R. G. Cortiñas, P. I. Villar, F. C. Lombardo & J. P. Paz. *Controlled-Squeeze Gate in Superconducting Quantum Circuits*. Phys. Rev. A **111**, 042606 (2025).

175. D. M. Greenberger, M. A. Horne & A. Zeilinger. *Going Beyond Bell's Theorem*, in *Bell's Theorem, Quantum Theory and Conceptions of the Universe* edited by M. Kafatos (Springer Netherlands, Dordrecht, 1989), pp. 69–72.

176. B. C. Sanders. *Superposition of Two Squeezed Vacuum States and Interference Effects*. Phys. Rev. A **39**, 4284 (1989).

177. Arman & P. K. Panigrahi. *Generating Overlap between Compass States and Squeezed, Displaced, or Fock States*. Phys. Rev. A **109**, 033724 (2024).

178. F. Toscano, D. A. R. Dalvit, L. Davidovich & W. H. Zurek. *Sub-Planck Phase-Space Structures and Heisenberg-limited Measurements*. Phys. Rev. A **73**, 023803 (2006).

179. A. Carollo, B. Spagnolo, A. A. Dubkov & D. Valenti. *On Quantumness in Multi-Parameter Quantum Estimation*. J. Stat. Mech. **2019**, 094010 (2019).

180. O. Băzăvan, S. Saner, D. J. Webb, E. M. Ainley, P. Drmota, D. P. Nadlinger, G. Araneda, D. M. Lucas, C. J. Ballance & R. Srinivas. *Squeezing, Trisqueezing, and Quadsqueezing in a Spin-Oscillator System*. arXiv: 2403.05471 (2024).

181. P. H. Leung, K. A. Landsman, C. Figgatt, N. M. Linke, C. Monroe & K. R. Brown. *Robust 2-Qubit Gates in a Linear Ion Crystal Using a Frequency-Modulated Driving Force*. Phys. Rev. Lett. **120**, 020501 (2018).

182. A. R. Milne, C. L. Edmunds, C. Hempel, F. Roy, S. Mavadia & M. J. Biercuk. *Phase-Modulated Entangling Gates Robust to Static and Time-Varying Errors*. Phys. Rev. Appl. **13**, 024022 (2020).

183. L. J. Bond, C. H. Valahu, T. R. Tan & A. Safavi-Naini. *Universal control of collective-spin boson systems. In preparation.*

184. N. Kotibhaskar, C.-Y. Shih, S. Motlakunta, A. Vogliano, L. Hahn, Y.-T. Chen & R. Islam. *Programmable XY-type Couplings through Parallel Spin-Dependent Forces on the Same Trapped Ion Motional Modes*. Phys. Rev. Res. **6**, 033038 (2024).

185. S. Krämer, D. Plankensteiner, L. Ostermann & H. Ritsch. *QuantumOptics.jl: A Julia framework for simulating open quantum systems*. Computer Physics Communications **227**, 109 (2018).

186. S. C. Burd, R. Srinivas, J. J. Bollinger, A. C. Wilson, D. J. Wineland, D. Leibfried, D. H. Slichter & D. T. C. Allcock. *Quantum amplification of mechanical oscillator motion*. Science **364**, 1163 (2019).

187. D. Kienzler, H.-Y. Lo, B. Keitch, L. de Clercq, F. Leupold, F. Lindenfelser, M. Marinelli, V. Negnevitsky & J. P. Home. *Quantum harmonic oscillator state synthesis by reservoir engineering*. Science **347**, 53 (2015).

188. I. Arrazola, M. Plenio, E. Solano & J. Casanova. *Hybrid Microwave-Radiation Patterns for High-Fidelity Quantum Gates with Trapped Ions*. Phys. Rev. Appl. **13**, 024068 (2020).

189. F. Wolf, Y. Wan, J. C. Heip, F. Gebert, C. Shi & P. O. Schmidt. *Non-destructive state detection for quantum logic spectroscopy of molecular ions*. Nature **530**, 457 (2016).

190. C.-w. Chou, C. Kurz, D. B. Hume, P. N. Plessow, D. R. Leibrandt & D. Leibfried. *Preparation and coherent manipulation of pure quantum states of a single molecular ion*. Nature **545**, 203 (2017).

191. M. G. Kozlov, M. S. Safronova, J. R. Crespo López-Urrutia & P. O. Schmidt. *Highly charged ions: Optical clocks and applications in fundamental physics*. Rev. Mod. Phys. **90**, 045005 (2018).

192. P. Micke, T. Leopold, S. A. King, E. Benkler, L. J. Spieß, L. Schmöger, M. Schwarz, J. R. Crespo López-Urrutia & P. O. Schmidt. *Coherent laser spectroscopy of highly charged ions using quantum logic*. Nature **578**, 60 (2020).

193. S. A. King *et al. An optical atomic clock based on a highly charged ion*. Nature **611**, 43 (2022).

194. M. S. Safronova, D. Budker, D. DeMille, D. F. J. Kimball, A. Derevianko & C. W. Clark. *Search for new physics with atoms and molecules*. Rev. Mod. Phys. **90**, 025008 (2018).

195. G. Bressanini, M. G. Genoni, M. S. Kim & M. G. A. Paris. *Multi-parameter quantum estimation of single- and two-mode pure Gaussian states*. J. Phys. A: Math. Theor. **57**, 315305 (2024).

196. R. Demkowicz-Dobrzański, W. Górecki & M. Guţă. *Multi-parameter estimation beyond quantum Fisher information*. J. Phys. A: Math. Theor. **53**, 363001 (2020).

197. M. Fadel, N. Roux & M. Gessner. *Quantum metrology with a continuous-variable system*. Reports on Progress in Physics **88**, 106001 (2025).

198. S. Krinner *et al. Realizing Repeated Quantum Error Correction in a Distance-Three Surface Code*. Nature **605**, 669 (2022).

199. V. V. Sivak *et al. Real-Time Quantum Error Correction beyond Break-Even*. Nature **616**, 50 (2023).

200. B. M. Terhal. *Quantum error correction for quantum memories*. Rev. Mod. Phys. **87**, 307 (2015).

201. Y. Ouyang & G. K. Brennen. *Finite-Round Quantum Error Correction on Symmetric Quantum Sensors*. arXiv: 2212.06285 (2025).

202. H. J. Briegel & R. Raussendorf. *Persistent Entanglement in Arrays of Interacting Particles*. Phys. Rev. Lett. **86**, 910 (2001).

203. X. Wang & K. Mølmer. *Pairwise Entanglement in Symmetric Multi-Qubit Systems*. Eur. Phys. J. D **18**, 385 (2002).

204. J. K. Stockton, J. M. Geremia, A. C. Doherty & H. Mabuchi. *Characterizing the Entanglement of Symmetric Many-Particle Spin- 1 2 Systems*. Phys. Rev. A **67**, 022112 (2003).

205. A. Neven, J. Martin & T. Bastin. *Entanglement Robustness against Particle Loss in Multiqubit Systems*. Phys. Rev. A **98**, 062335 (2018).

206. L. Pezzè, A. Smerzi, M. K. Oberthaler, R. Schmied & P. Treutlein. *Quantum metrology with nonclassical states of atomic ensembles*. Rev. Mod. Phys. **90**, 035005 (2018).

207. D. J. Wineland, J. J. Bollinger, W. M. Itano & D. J. Heinzen. *Squeezed Atomic States and Projection Noise in Spectroscopy*. Phys. Rev. A **50**, 67 (1994).

208. M. Koashi, V. Bužek & N. Imoto. *Entangled Webs: Tight Bound for Symmetric Sharing of Entanglement*. Phys. Rev. A **62**, 050302 (2000).

209. W. Dür, G. Vidal & J. I. Cirac. *Three qubits can be entangled in two inequivalent ways*. Phys. Rev. A **62**, 062314 (2000).

210. J. J. . Bollinger, W. M. Itano, D. J. Wineland & D. J. Heinzen. *Optimal frequency measurements with maximally correlated states*. Phys. Rev. A **54**, R4649 (1996).

211. T. Monz, P. Schindler, J. T. Barreiro, M. Chwalla, D. Nigg, W. A. Coish, M. Harlander, W. Hänsel, M. Hennrich & R. Blatt. *14-Qubit Entanglement: Creation and Coherence*. Phys. Rev. Lett. **106**, 130506 (2011).

212. A. Omran *et al. Generation and manipulation of Schrödinger cat states in Rydberg atom arrays*. Science **365**, 570 (2019).

213. C. Song *et al. Generation of multicomponent atomic Schrödinger cat states of up to 20 qubits*. Science **365**, 574 (2019).

214. E. Knill, R. Laflamme & L. Viola. *Theory of Quantum Error Correction for General Noise*. Phys. Rev. Lett. **84**, 2525 (2000).

215. S. C. Carrasco, M. H. Goerz, Z. Li, S. Colombo, V. Vuletić & V. S. Malinovsky. *Extreme Spin Squeezing via Optimized One-Axis Twisting and Rotations*. Phys. Rev. Appl. **17**, 064050 (2022).

216. R. Kaubruegger, D. V. Vasilyev, M. Schulte, K. Hammerer & P. Zoller. *Quantum Variational Optimization of Ramsey Interferometry and Atomic Clocks*. Phys. Rev. X **11**, 041045 (2021).

217. R. Kaubruegger, P. Silvi, C. Kokail, R. Van Bijnen, A. M. Rey, J. Ye, A. M. Kaufman & P. Zoller. *Variational Spin-Squeezing Algorithms on Programmable Quantum Sensors*. Phys. Rev. Lett. **123**, 260505 (2019).

218. N. Gutman, A. Gorlach, O. Tziperman, R. Ruimy & I. Kaminer. *Universal Control of Symmetric States Using Spin Squeezing*. Phys. Rev. Lett. **132**, 153601 (2024).

219. C. D. Marciniak, T. Feldker, I. Pogorelov, R. Kaubruegger, D. V. Vasilyev, R. Van Bijnen, P. Schindler, P. Zoller, R. Blatt & T. Monz. *Optimal Metrology with Programmable Quantum Sensors*. Nature **603**, 604 (2022).

220. F. Albertini & D. D'Alessandro. *Controllability of Symmetric Spin Networks*. J. Math. Phys. **59**, 052102 (2018).

221. H. A. Rabitz, M. M. Hsieh & C. M. Rosenthal. *Quantum Optimally Controlled Transition Landscapes*. Science **303**, 1998 (2004).

222. J. Nocedal & S. J. Wright. *Numerical Optimization* (Springer New York, 2006).

223. T. Keating, C. H. Baldwin, Y.-Y. Jau, J. Lee, G. W. Biedermann & I. H. Deutsch. *Arbitrary Dicke-State Control of Symmetric Rydberg Ensembles*. Phys. Rev. Lett. **117**, 213601 (2016).

224. D. C. Liu & J. Nocedal. *On the Limited Memory BFGS Method for Large Scale Optimization*. Mathematical Programming **45**, 503 (1989).

225. I. Apellaniz, B. Lücke, J. Peise, C. Klempt & G. Tóth. *Detecting metrologically useful entanglement in the vicinity of Dicke states*. New J. Phys. **17**, 083027 (2015).

226. Y. Ouyang, N. Shettell & D. Markham. *Robust Quantum Metrology With Explicit Symmetric States*. IEEE Transactions on Information Theory **68**, 1809 (2022).

227. P. W. Shor. *Scheme for reducing decoherence in quantum computer memory*. Phys. Rev. A **52**, R2493 (1995).

228. K. Kim, M.-S. Chang, R. Islam, S. Korenblit, L.-M. Duan & C. Monroe. *Entanglement and Tunable Spin-Spin Couplings between Trapped Ions Using Multiple Transverse Modes*. Phys. Rev. Lett. **103**, 120502 (2009).

229. G. Kirchmair, J. Benhelm, F. Zähringer, R. Gerritsma, C. F. Roos & R. Blatt. *Deterministic entanglement of ions in thermal states of motion*. New J. Phys. **11**, 023002 (2009).

230. W. Ge, B. C. Sawyer, J. W. Britton, K. Jacobs, J. J. Bollinger & M. Foss-Feig. *Trapped Ion Quantum Information Processing with Squeezed Phonons*. Phys. Rev. Lett. **122**, 030501 (2019).

231. Y. Shapira, R. Shaniv, T. Manovitz, N. Akerman, L. Peleg, L. Gazit, R. Ozeri & A. Stern. *Theory of robust multiqubit nonadiabatic gates for trapped ions*. Phys. Rev. A **101**, 032330 (2020).

232. J. D. Arias Espinoza, K. Groenland, M. Mazzanti, K. Schoutens & R. Gerritsma. *High-fidelity method for a single-step N-bit Toffoli gate in trapped ions*. Phys. Rev. A **103**, 052437 (2021).

233. J. R. McClean, J. Romero, R. Babbush & A. Aspuru-Guzik. *The Theory of Variational Hybrid Quantum-Classical Algorithms*. New J. Phys. **18**, 023023 (2016).

234. A. Peruzzo, J. McClean, P. Shadbolt, M.-H. Yung, X.-Q. Zhou, P. J. Love, A. Aspuru-Guzik & J. L. O'Brien. *A Variational Eigenvalue Solver on a Photonic Quantum Processor*. Nat Commun **5**, 4213 (2014).

235. G. Tóth, W. Wieczorek, D. Gross, R. Krischek, C. Schwemmer & H. Weinfurter. *Permutationally Invariant Quantum Tomography*. Phys. Rev. Lett. **105**, 250403 (2010).

236. G. Tóth, W. Wieczorek, R. Krischek, N. Kiesel, P. Michelberger & H. Weinfurter. *Practical Methods for Witnessing Genuine Multi-Qubit Entanglement in the Vicinity of Symmetric States*. New J. Phys. **11**, 083002 (2009).

237. U. Schollwöck. *The Density-Matrix Renormalization Group*. Rev. Mod. Phys. **77**, 259 (2005).

238. J. I. Cirac, D. Pérez-García, N. Schuch & F. Verstraete. *Matrix Product States and Projected Entangled Pair States: Concepts, Symmetries, Theorems*. Rev. Mod. Phys. **93**, 045003 (2021).

239. X. Yuan, S. Endo, Q. Zhao, Y. Li & S. C. Benjamin. *Theory of variational quantum simulation*. Quantum **3**, 191 (2019).

240. J. Haegeman, J. I. Cirac, T. J. Osborne, I. Pižorn, H. Verschelde & F. Verstraete. *Time-Dependent Variational Principle for Quantum Lattices*. Phys. Rev. Lett. **107**, 070601 (2011).

241. M. Cerezo *et al. Variational Quantum Algorithms*. Nat Rev Phys **3**, 625 (2021).

242. E. Farhi, J. Goldstone & S. Gutmann. *A Quantum Approximate Optimization Algorithm*. arXiv: 1411.4028 (2014).

243. S. McArdle, T. Jones, S. Endo, Y. Li, S. C. Benjamin & X. Yuan. *Variational Ansatz-Based Quantum Simulation of Imaginary Time Evolution*. npj Quantum Inf **5**, 75 (2019).

244. G. Adesso, S. Ragy & A. R. Lee. *Continuous Variable Quantum Information: Gaussian States and Beyond*. Open Systems & Information Dynamics **21**, 1440001 (2014).

245. A. Kenfack & K. Zyczkowski. *Negativity of the Wigner Function as an Indicator of Nonclassicality*. Opt. B: Quantum Semiclass. Opt. **6**, 396 (2004).

246. W. P. Schleich. *Wigner Function*, in *Quantum Optics in Phase Space* (John Wiley & Sons, Ltd, 2001), pp. 67–98.

247. J. M. Radcliffe. *Some Properties of Coherent Spin States*. J. Phys. A: Gen. Phys. **4**, 313 (1971).

248. A. Serafini, M. Lostaglio, S. Longden, U. Shackerley-Bennett, C.-Y. Hsieh & G. Adesso. *Gaussian Thermal Operations and The Limits of Algorithmic Cooling*. Phys. Rev. Lett. **124**, 010602 (2020).

249. G. Giedke & J. Ignacio Cirac. *Characterization of Gaussian Operations and Distillation of Gaussian States*. Phys. Rev. A **66**, 032316 (2002).

250. C. Weedbrook, S. Pirandola, R. García-Patrón, N. J. Cerf, T. C. Ralph, J. H. Shapiro & S. Lloyd. *Gaussian Quantum Information*. Rev. Mod. Phys. **84**, 621 (2012).

251. J. Fu, J. Knolle & N. B. Perkins. *Three types of representation of spin in terms of Majorana fermions and an alternative solution of the Kitaev honeycomb model*. Phys. Rev. B **97**, 115142 (2018).

252. Y. Ashida, T. Shi, R. Schmidt, H. R. Sadeghpour, J. I. Cirac & E. Demler. *Efficient variational approach to dynamics of a spatially extended bosonic Kondo model*. Phys. Rev. A **100**, 043618 (2019).

253. A. Christianen, J. I. Cirac & R. Schmidt. *Bose polaron and the Efimov effect: A Gaussian-state approach*. Phys. Rev. A **105**, 053302 (2022).

254. N. Zhou, L. Chen, D. Xu, V. Chernyak & Y. Zhao. *Symmetry and the critical phase of the two-bath spin-boson model: Ground-state properties*. Phys. Rev. B **91**, 195129 (2015).

255. N. Zhou, L. Chen, Y. Zhao, D. Mozyrsky, V. Chernyak & Y. Zhao. *Ground-state properties of sub-Ohmic spin-boson model with simultaneous diagonal and off-diagonal coupling*. Phys. Rev. B **90**, 155135 (2014).

256. N. Wu, L. Duan, X. Li & Y. Zhao. *Dynamics of the sub-Ohmic spin-boson model: A time-dependent variational study*. J. Chem. Phys. **138**, 084111 (2013).

257. S. Bera, A. Nazir, A. W. Chin, H. U. Baranger & S. Florens. *Generalized Multipolaron Expansion for the Spin-Boson Model: Environmental Entanglement and the Biased Two-State System*. Phys. Rev. B **90**, 075110 (2014).

258. D. S. Schlegel, F. Minganti & V. Savona. *Coherent-State Ladder Time-Dependent Variational Principle for Open Quantum Systems*. arXiv: 2306.13708 (2023).

259. P.-L. Dallaire-Demers, J. Romero, L. Veis, S. Sim & A. Aspuru-Guzik. *Low-Depth Circuit Ansatz for Preparing Correlated Fermionic States on a Quantum Computer*. Quantum Sci. Technol. **4**, 045005 (2019).

260. I. I. Rabi. *Space Quantization in a Gyrating Magnetic Field*. Phys. Rev. **51**, 652 (1937).

261. F. Herrera & F. C. Spano. *Cavity-Controlled Chemistry in Molecular Ensembles*. Phys. Rev. Lett. **116**, 238301 (2016).

262. K. B. Møller, T. G. Jørgensen & J. P. Dahl. *Displaced squeezed number states: Position space representation, inner product, and some applications*. Phys. Rev. A **54**, 5378 (1996).

263. G. J. Milburn. *Quantum and classical Liouville dynamics of the anharmonic oscillator*. Phys. Rev. A **33**, 674 (1986).

264. F. R. Halpern. *Quantum mechanics of the anharmonic oscillator*. J. Math. Phys. **14**, 219 (1973).

265. C. M. Bender & T. T. Wu. *Anharmonic Oscillator. II. A Study of Perturbation Theory in Large Order*. Phys. Rev. D **7**, 1620 (1973).

266. C. M. Bender & T. T. Wu. *Anharmonic Oscillator*. Phys. Rev. **184**, 1231 (1969).

267. H.-P. Breuer & F. Petruccione. *The Theory of Open Quantum Systems* (Oxford University Press, 2007).

268. U. Weiss. *Quantum Dissipative Systems* (World Scientific, 2012).

269. C. W. Gardiner & P. Zoller. *Quantum Noise: A Handbook of Markovian and Non-Markovian Quantum Stochastic Methods with Applications to Quantum Optics* 3rd ed (Springer, Berlin ; New York, 2004).

270. J. Dalibard, Y. Castin & K. Mølmer. *Wave-function approach to dissipative processes in quantum optics*. Phys. Rev. Lett. **68**, 580 (1992).

271. K. Mølmer, Y. Castin & J. Dalibard. *Monte Carlo wave-function method in quantum optics*. J. Opt. Soc. Am. B **10**, 524 (1993).

272. M. B. Plenio & P. L. Knight. *The quantum-jump approach to dissipative dynamics in quantum optics*. Rev. Mod. Phys. **70**, 101 (1998).

273. A. J. Daley. *Quantum trajectories and open many-body quantum systems*. Advances in Physics **63**, 77 (2014).

274. H. Carmichael. *An Open Systems Approach to Quantum Optics*. Edited by H. Araki *et al.* (Springer, Berlin, Heidelberg, 1993).

275. G. Preisser, D. Wellnitz, T. Botzung & J. Schachenmayer. *Comparing bipartite entropy growth in open-system matrix-product simulation methods*. Phys. Rev. A **108**, 012616 (2023).

276. D. Jaksch, C. Bruder, J. I. Cirac, C. W. Gardiner & P. Zoller. *Cold Bosonic Atoms in Optical Lattices*. Phys. Rev. Lett. **81**, 3108 (1998).

277. H. Pichler, J. Schachenmayer, A. J. Daley & P. Zoller. *Heating Dynamics of Bosonic Atoms in a Noisy Optical Lattice*. Phys. Rev. A **87**, 033606 (2013).

278. T. Vovk & H. Pichler. *Entanglement-Optimal Trajectories of Many-Body Quantum Markov Processes*. Phys. Rev. Lett. **128**, 243601 (2022).

279. D. Jaschke, S. Montangero & L. D. Carr. *One-Dimensional Many-Body Entangled Open Quantum Systems with Tensor Network Methods*. Quantum Sci. Technol. **4**, 013001 (2018).

280. V. P. Singh & H. Weimer. *Driven-Dissipative Criticality within the Discrete Truncated Wigner Approximation*. Phys. Rev. Lett. **128**, 200602 (2022).

281. S. Lloyd & S. Montangero. *Information Theoretical Analysis of Quantum Optimal Control*. Phys. Rev. Lett. **113**, 010502 (2014).

282. P. Doria, T. Calarco & S. Montangero. *Optimal Control Technique for Many-Body Quantum Dynamics*. Phys. Rev. Lett. **106**, 190501 (2011).

283. S. van Frank *et al.* *Optimal Control of Complex Atomic Quantum Systems*. Sci Rep **6**, 34187 (2016).

284. I. Brouzos, A. I. Streltsov, A. Negretti, R. S. Said, T. Caneva, S. Montangero & T. Calarco. *Quantum speed limit and optimal control of many-boson dynamics*. Phys. Rev. A **92**, 062110 (2015).

285. L. Wang, L. Chen, N. Zhou & Y. Zhao. *Variational dynamics of the sub-Ohmic spin-boson model on the basis of multiple Davydov D1 states*. J. Chem. Phys. **144**, 024101 (2016).

286. K. L. Hur. *Entanglement entropy, decoherence, and quantum phase transitions of a dissipative two-level system*. Annals of Physics **323**, 2208 (2008).

287. R. Bulla, N.-H. Tong & M. Vojta. *Numerical Renormalization Group for Bosonic Systems and Application to the Sub-Ohmic Spin-Boson Model*. Phys. Rev. Lett. **91**, 170601 (2003).

288. P. P. Orth, D. Roosen, W. Hofstetter & K. Le Hur. *Dynamics, synchronization, and quantum phase transitions of two dissipative spins*. Phys. Rev. B **82**, 144423 (2010).

289. P. Nalbach & M. Thorwart. *Ultraslow quantum dynamics in a sub-Ohmic heat bath*. Phys. Rev. B **81**, 054308 (2010).

290. D. Kast & J. Ankerhold. *Persistence of Coherent Quantum Dynamics at Strong Dissipation*. Phys. Rev. Lett. **110**, 010402 (2013).

291. P. Nalbach & M. Thorwart. *Crossover from coherent to incoherent quantum dynamics due to sub-Ohmic dephasing*. Phys. Rev. B **87**, 014116 (2013).

292. S. Bera, S. Florens, H. U. Baranger, N. Roch, A. Nazir & A. W. Chin. *Stabilizing Spin Coherence through Environmental Entanglement in Strongly Dissipative Quantum Systems*. Phys. Rev. B **89**, 121108 (2014).

293. F. Otterpohl, P. Nalbach & M. Thorwart. *Hidden Phase of the Spin-Boson Model*. Phys. Rev. Lett. **129**, 120406 (2022).

294. B. Peropadre, D. Zueco, D. Porras & J. J. García-Ripoll. *Nonequilibrium and Nonperturbative Dynamics of Ultrastrong Coupling in Open Lines*. Phys. Rev. Lett. **111**, 243602 (2013).

295. F. Yoshihara, T. Fuse, S. Ashhab, K. Kakuyanagi, S. Saito & K. Semba. *Superconducting Qubit–Oscillator Circuit beyond the Ultrastrong-Coupling Regime*. Nat. Phys. **13**, 44 (2017).

296. P. Forn-Díaz, J. J. García-Ripoll, B. Peropadre, J.-L. Orgiazzi, M. A. Yurtalan, R. Belyansky, C. M. Wilson & A. Lupascu. *Ultrastrong Coupling of a Single Artificial Atom to an Electromagnetic Continuum in the Nonperturbative Regime*. Nat. Phys. **13**, 39 (2017).

297. L. Magazzù, P. Forn-Díaz, R. Belyansky, J.-L. Orgiazzi, M. A. Yurtalan, M. R. Otto, A. Lupascu, C. M. Wilson & M. Grifoni. *Probing the Strongly Driven Spin-Boson Model in a Superconducting Quantum Circuit*. Nat Commun **9**, 1403 (2018).

298. M. Marcuzzi, J. ř. Miná ř, D. Barredo, S. de Léséleuc, H. Labuhn, T. Lahaye, A. Browaeys, E. Levi & I. Lesanovsky. *Facilitation Dynamics and Localization Phenomena in Rydberg Lattice Gases with Position Disorder*. Phys. Rev. Lett. **118**, 063606 (2017).

299. F. M. Gambetta, W. Li, F. Schmidt-Kaler & I. Lesanovsky. *Engineering NonBinary Rydberg Interactions via Phonons in an Optical Lattice*. Phys. Rev. Lett. **124**, 043402 (2020).

300. H. Tamura, T. Yamakoshi & K. Nakagawa. *Analysis of coherent dynamics of a Rydberg-atom quantum simulator*. Phys. Rev. A **101**, 043421 (2020).

301. P. Méhaignerie, C. Sayrin, J.-M. Raimond, M. Brune & G. Roux. *Spin-motion coupling in a circular-Rydberg-state quantum simulator: Case of two atoms*. Phys. Rev. A **107**, 063106 (2023).

302. D. James. *Quantum Dynamics of Cold Trapped Ions with Application to Quantum Computation*. Appl. Phys. B **66**, 181 (1998).

303. D. Porras & J. I. Cirac. *Bose-Einstein Condensation and Strong-Correlation Behavior of Phonons in Ion Traps*. Phys. Rev. Lett. **93**, 263602 (2004).

304. C. Schneider, D. Porras & T. Schaetz. *Experimental quantum simulations of many-body physics with trapped ions*. Rep. Prog. Phys. **75**, 024401 (2012).

305. H.-Y. Lo, D. Kienzler, L. de Clercq, M. Marinelli, V. Negnevitsky, B. C. Keitch & J. P. Home. *Spin–Motion Entanglement and State Diagnosis with Squeezed Oscillator Wavepackets*. Nature **521**, 336 (2015).

306. D. Kienzler, H.-Y. Lo, V. Negnevitsky, C. Flühmann, M. Marinelli & J. P. Home. *Quantum Harmonic Oscillator State Control in a Squeezed Fock Basis*. Phys. Rev. Lett. **119**, 033602 (2017).

307. Q.-X. Mei, B.-W. Li, Y.-K. Wu, M.-L. Cai, Y. Wang, L. Yao, Z.-C. Zhou & L.-M. Duan. *Experimental Realization of the Rabi-Hubbard Model with Trapped Ions*. Phys. Rev. Lett. **128**, 160504 (2022).

308. D. Lv, S. An, Z. Liu, J.-N. Zhang, J. S. Pedernales, L. Lamata, E. Solano & K. Kim. *Quantum Simulation of the Quantum Rabi Model in a Trapped Ion*. Phys. Rev. X **8**, 021027 (2018).

309. M.-L. Cai, Z.-D. Liu, W.-D. Zhao, Y.-K. Wu, Q.-X. Mei, Y. Jiang, L. He, X. Zhang, Z.-C. Zhou & L.-M. Duan. *Observation of a Quantum Phase Transition in the Quantum Rabi Model with a Single Trapped Ion*. Nat Commun **12**, 1126 (2021).

310. A. A. Michailidis, C. J. Turner, Z. Papić, D. A. Abanin & M. Serbyn. *Slow Quantum Thermalization and Many-Body Revivals from Mixed Phase Space*. Phys. Rev. X **10**, 011055 (2020).

311. M.-J. Hwang, R. Puebla & M. B. Plenio. *Quantum Phase Transition and Universal Dynamics in the Rabi Model*. Phys. Rev. Lett. **115**, 180404 (2015).

312. Z.-J. Ying, M. Liu, H.-G. Luo, H.-Q. Lin & J. Q. You. *Ground-state phase diagram of the quantum Rabi model*. Phys. Rev. A **92**, 053823 (2015).

313. M. Gärttner, J. G. Bohnet, A. Safavi-Naini, M. L. Wall, J. J. Bollinger & A. M. Rey. *Measuring Out-of-Time-Order Correlations and Multiple Quantum Spectra in a Trapped-Ion Quantum Magnet*. Nat. Phys. **13**, 781 (2017).

314. M. Gärttner, P. Hauke & A. M. Rey. *Relating Out-of-Time-Order Correlations to Entanglement via Multiple-Quantum Coherences*. Phys. Rev. Lett. **120**, 040402 (2018).

315. R. J. Lewis-Swan, A. Safavi-Naini, J. J. Bollinger & A. M. Rey. *Unifying Scrambling, Thermalization and Entanglement through Measurement of Fidelity out-of-Time-Order Correlators in the Dicke Model*. Nat Commun **10**, 1581 (2019).

316. A. V. Kirkova, D. Porras & P. A. Ivanov. *Out-of-time-order correlator in the quantum Rabi model*. Phys. Rev. A **105**, 032444 (2022).

317. K. Agarwal, R. N. Bhatt & S. L. Sondhi. *Fast Preparation of Critical Ground States Using Superluminal Fronts*. Phys. Rev. Lett. **120**, 210604 (2018).

318. J. S. Pedernales, I. Lizuain, S. Felicetti, G. Romero, L. Lamata & E. Solano. *Quantum Rabi Model with Trapped Ions*. Sci Rep **5**, 15472 (2015).

319. T. Caneva, T. Calarco & S. Montangero. *Chopped random-basis quantum optimization*. Phys. Rev. A **84**, 022326 (2011).

320. J. Roland & N. J. Cerf. *Quantum Search by Local Adiabatic Evolution*. Phys. Rev. A **65**, 042308 (2002).

321. P. Richerme, C. Senko, J. Smith, A. Lee, S. Korenblit & C. Monroe. *Experimental Performance of a Quantum Simulator: Optimizing Adiabatic Evolution and Identifying Many-Body Ground States*. Phys. Rev. A **88**, 012334 (2013).

322. A. Lucas. *Quantum Many-Body Dynamics on the Star Graph*. arXiv: 1903.01468 (2019).

323. T. Guaita, L. Hackl, T. Shi, C. Hubig, E. Demler & J. I. Cirac. *Gaussian time-dependent variational principle for the Bose-Hubbard model*. Phys. Rev. B **100**, 094529 (2019).

324. R. Menu & T. Roscilde. *Gaussian-state Ansatz for the non-equilibrium dynamics of quantum spin lattices*. SciPost Phys. **14**, 151 (2023).

325. M. P. Kaicher, D. Vodola & S. B. Jäger. *Mean-field treatment of the long-range transverse field Ising model with fermionic Gaussian states*. Phys. Rev. B **107**, 165144 (2023).

326. C. H. Valahu *et al. Direct Observation of Geometric-Phase Interference in Dynamics around a Conical Intersection*. Nat. Chem. **15**, 1503 (2023).

327. H. R. Grimsley, S. E. Economou, E. Barnes & N. J. Mayhall. *An Adaptive Variational Algorithm for Exact Molecular Simulations on a Quantum Computer*. Nat Commun **10**, 3007 (2019).

328. O. R. Meitei, B. T. Gard, G. S. Barron, D. P. Pappas, S. E. Economou, E. Barnes & N. J. Mayhall. *Gate-Free State Preparation for Fast Variational Quantum Eigensolver Simulations*. npj Quantum Inf **7**, 155 (2021).

329. *The Error Correction Zoo*. Edited by V. V. Albert & P. Faist (2025).

330. R. Puebla, A. Smirne, S. F. Huelga & M. B. Plenio. *Universal Anti-Kibble-Zurek Scaling in Fully Connected Systems*. Phys. Rev. Lett. **124**, 230602 (2020).

331. N. A. Kamar & M. Maghrebi. *Hybrid Quantum-Classical Stochastic Approach to Dissipative Spin-Boson Models*. Phys. Rev. X **15**, 021073 (2025).

332. N. A. Kamar, D. A. Paz & M. F. Maghrebi. *Spin-boson model under dephasing: Markovian versus non-Markovian dynamics*. Phys. Rev. B **110**, 075126 (2024).

333. M. L. Wall, A. Safavi-Naini & A. M. Rey. *Boson-Mediated Quantum Spin Simulators in Transverse Fields: X Y Model and Spin-Boson Entanglement*. Phys. Rev. A **95**, 013602 (2017).

334. R. Puebla, M.-J. Hwang, J. Casanova & M. B. Plenio. *Probing the Dynamics of a Superradiant Quantum Phase Transition with a Single Trapped Ion*. Phys. Rev. Lett. **118**, 073001 (2017).

335. A. E. Webb, S. C. Webster, S. Collingbourne, D. Bretaud, A. M. Lawrence, S. Weidt, F. Mintert & W. K. Hensinger. *Resilient Entangling Gates for Trapped Ions*. Phys. Rev. Lett. **121**, 180501 (2018).

336. Y. Shapira, J. Markov, N. Akerman, A. Stern & R. Ozeri. *Programmable Quantum Simulations on a Trapped-Ion Quantum Computer with a Global Drive*. Phys. Rev. Lett. **134**, 010602 (2025).

337. C. Rackauckas & Q. Nie. *DifferentialEquations.jl – A Performant and Feature-Rich Ecosystem for Solving Differential Equations in Julia*. Journal of Open Research Software (2017).

338. J. Pérez-Ríos. *Cold chemistry: a few-body perspective on impurity physics of a single ion in an ultracold bath*. Molecular Physics **119**, 1881637 (2021).

339. R. S. Lous & R. Gerritsma. *Ultracold ion-atom experiments: cooling, chemistry, and quantum effects*, in *Advances in Atomic, Molecular, and Optical Physics* edited by L. F. DiMauro, H. Perrin & S. F. Yelin (Academic Press, 2022), pp. 65–133.

340. F. J. Garcia-Vidal, C. Ciuti & T. W. Ebbesen. *Manipulating matter by strong coupling to vacuum fields*. Science **373**, eabd0336 (2021).

341. D. Lee, N. Salwen & D. Lee. *The diagonalization of quantum field Hamiltonians*. Physics Letters B **503**, 223 (2001).

342. T. Rakovszky, M. Mestyán, M. Collura, M. Kormos & G. Takács. *Hamiltonian truncation approach to quenches in the Ising field theory*. Nuclear Physics B **911**, 805 (2016).

343. D. Szász-Schagrin & G. Takács. *False vacuum decay in the $(1+1)$-dimensional φ^4 theory*. Phys. Rev. D **106**, 025008 (2022).

344. T. Rakovszky, M. Mestyán, M. Collura, M. Kormos & G. Takács. *Hamiltonian truncation approach to quenches in the Ising field theory.* Nuclear Physics B **911**, 805 (2016).

345. N. Anand, A. L. Fitzpatrick, E. Katz, Z. U. Khandker, M. T. Walters & Y. Xin. *Introduction to Lightcone Conformal Truncation: QFT Dynamics from CFT Data*. arXiv: 2005.13544 (2020).

346. H. Chen, A. L. Fitzpatrick & D. Karateev. *Bootstrapping 2d $\phi 4$ Theory with Hamiltonian Truncation Data*. J. High Energ. Phys. **2022**, 146 (2022).

347. L. V. Delacrétaz, A. L. Fitzpatrick, E. Katz & M. T. Walters. *Thermalization and Chaos in a 1+1d QFT*. J. High Energ. Phys. **2023**, 45 (2023).

348. J. del Pino, F. A. Y. N. Schröder, A. W. Chin, J. Feist & F. J. Garcia-Vidal. *Tensor Network Simulation of Non-Markovian Dynamics in Organic Polaritons*. Phys. Rev. Lett. **121**, 227401 (2018).

349. N. Makri & D. E. Makarov. *Tensor propagator for iterative quantum time evolution of reduced density matrices. II. Numerical methodology*. J. Chem. Phys. **102**, 4611 (1995).

350. M. Thorwart, P. Reimann, P. Jung & R. Fox. *Quantum hysteresis and resonant tunneling in bistable systems*. Chem. Phys. **235**, 61 (1998).

351. M. Thorwart, P. Reimann & P. Hänggi. *Iterative algorithm versus analytic solutions of the parametrically driven dissipative quantum harmonic oscillator*. Phys. Rev. E **62**, 5808 (2000).

352. T. L. Schmidt, P. Werner, L. Mühlbacher & A. Komnik. *Transient dynamics of the Anderson impurity model out of equilibrium*. Phys. Rev. B **78**, 235110 (2008).

353. U. Schollwöck. *The Density-Matrix Renormalization Group in the Age of Matrix Product States*. Annals of Physics **326**, 96 (2011).

354. R. Orús. *A Practical Introduction to Tensor Networks: Matrix Product States and Projected Entangled Pair States*. Annals of Physics **349**, 117 (2014).

355. S. Montangero. *Introduction to Tensor Network Methods* (Springer, 2018).

356. S. R. White & A. E. Feiguin. *Real-Time Evolution Using the Density Matrix Renormalization Group*. Phys. Rev. Lett. **93**, 076401 (2004).

357. P. Schmitteckert. *Nonequilibrium electron transport using the density matrix renormalization group method*. Phys. Rev. B **70**, 121302 (2004).

358. M. Nuss, M. Ganahl, E. Arrigoni, W. von der Linden & H. G. Evertz. *Nonequilibrium spatiotemporal formation of the Kondo screening cloud on a lattice*. Phys. Rev. B **91**, 085127 (2015).

359. B. Dóra, M. A. Werner & C. P. Moca. *Information scrambling at an impurity quantum critical point*. Phys. Rev. B **96**, 155116 (2017).

360. M. Zwolak & G. Vidal. *Mixed-State Dynamics in One-Dimensional Quantum Lattice Systems: A Time-Dependent Superoperator Renormalization Algorithm*. Phys. Rev. Lett. **93**, 207205 (2004).

361. B. Zhu, A. M. Rey & J. Schachenmayer. *A generalized phase space approach for solving quantum spin dynamics*. New J. Phys. **21**, 082001 (2019).

362. L. Joubert-Doriol & A. F. Izmaylov. *Problem-free time-dependent variational principle for open quantum systems*. J. Chem. Phys. **142**, 134107 (2015).

363. J. Huber, P. Kirton & P. Rabl. *Phase-space methods for simulating the dissipative many-body dynamics of collective spin systems*. SciPost Phys. **10**, 045 (2021).

364. J. Huber, A. M. Rey & P. Rabl. *Realistic simulations of spin squeezing and cooperative coupling effects in large ensembles of interacting two-level systems*. Phys. Rev. A **105**, 013716 (2022).

365. C. D. Mink, D. Petrosyan & M. Fleischhauer. *Hybrid discrete-continuous truncated Wigner approximation for driven, dissipative spin systems*. Phys. Rev. Res. **4**, 043136 (2022).

366. C. D. Mink & M. Fleischhauer. *Collective radiative interactions in the discrete truncated Wigner approximation*. SciPost Phys. **15**, 233 (2023).

367. K. Nagao, I. Danshita & S. Yunoki. *Discrete-phase-space method for driven-dissipative dynamics of strongly interacting bosons in optical lattices*. Phys. Rev. A **110**, 063310 (2024).

368. S. Lepoutre, J. Schachenmayer, L. Gabardos, B. Zhu, B. Naylor, E. Maréchal, O. Gorceix, A. M. Rey, L. Vernac & B. Laburthe-Tolra. *Out-of-Equilibrium Quantum Magnetism and Thermalization in a Spin-3 Many-Body Dipolar Lattice System*. Nat Commun **10**, 1714 (2019).

369. M. A. Perlin, C. Qu & A. M. Rey. *Spin Squeezing with Short-Range Spin-Exchange Interactions*. Phys. Rev. Lett. **125**, 223401 (2020).

370. J. Franke, S. R. Muleady, R. Kaubruegger, F. Kranzl, R. Blatt, A. M. Rey, M. K. Joshi & C. F. Roos. *Quantum-Enhanced Sensing on Optical Transitions through Finite-Range Interactions*. Nature **621**, 740 (2023).

371. S. R. Muleady, M. Yang, S. R. White & A. M. Rey. *Validating Phase-Space Methods with Tensor Networks in Two-Dimensional Spin Models with Power-Law Interactions*. Phys. Rev. Lett. **131**, 150401 (2023).

372. J. T. Young, E. Chaparro, A. Piñeiro Orioli, J. K. Thompson & A. M. Rey. *Engineering One Axis Twisting via a Dissipative Berry Phase Using Strong Symmetries*. Phys. Rev. Lett. **134**, 040801 (2025).

373. A. Polkovnikov. *Phase space representation of quantum dynamics*. Annals of Physics **325**, 1790 (2010).

374. B. Gerritsen, **L. J. Bond**, J. Minář, R. Spreeuw, R. Gerritsma & A. Safavi-Naini. *Sub-Doppler cooling of trapped ions using optical tweezers. In preparation.*

375. W. K. Wootters. *A Wigner-function formulation of finite-state quantum mechanics*. Annals of Physics **176**, 1 (1987).

376. J. Schachenmayer, A. Pikovski & A. M. Rey. *Dynamics of correlations in two-dimensional quantum spin models with long-range interactions: a phase-space Monte-Carlo study*. New J. Phys. **17**, 065009 (2015).

377. O. L. Acevedo, A. Safavi-Naini, J. Schachenmayer, M. L. Wall, R. Nandkishore & A. M. Rey. *Exploring many-body localization and thermalization using semiclassical methods*. Phys. Rev. A **96**, 033604 (2017).

378. M. Kunimi, K. Nagao, S. Goto & I. Danshita. *Performance evaluation of the discrete truncated Wigner approximation for quench dynamics of quantum spin systems with long-range interactions*. Phys. Rev. Res. **3**, 013060 (2021).

379. A. P. Orioli, A. Signoles, H. Wildhagen, G. Günter, J. Berges, S. Whitlock & M. Weidemüller. *Relaxation of an Isolated Dipolar-Interacting Rydberg Quantum Spin System*. Phys. Rev. Lett. **120**, 063601 (2018).

380. Y. Aziz Alaoui, S. R. Muleady, E. Chaparro, Y. Trifa, A. M. Rey, T. Roscilde, B. Laburthe-Tolra & L. Vernac. *Measuring Bipartite Spin Correlations of Lattice-Trapped Dipolar Atoms*. Phys. Rev. Lett. **133**, 203401 (2024).

381. M. Vogl, P. Laurell, H. Zhang, S. Okamoto & G. A. Fiete. *Resummation of the Holstein-Primakoff expansion and differential equation approach to operator square roots*. Phys. Rev. Res. **2**, 043243 (2020).

382. J. Marshall & N. Anand. *Simulation of quantum optics by coherent state decomposition*. Optica Quantum **1**, 78 (2023).

383. J. Wurtz, A. Polkovnikov & D. Sels. *Cluster truncated Wigner approximation in strongly interacting systems*. Annals of Physics **395**, 341 (2018).

384. T. Vovk & H. Pichler. *Quantum trajectory entanglement in various unravelings of Markovian dynamics*. Phys. Rev. A **110**, 012207 (2024).

385. E. Gottlob & U. Schneider. *Hubbard models for quasicrystalline potentials*. Phys. Rev. B **107**, 144202 (2023).

386. J. A. Hutchison, T. Schwartz, C. Genet, E. Devaux & T. W. Ebbesen. *Modifying Chemical Landscapes by Coupling to Vacuum Fields*. Angew. Chem. Int. Ed. **51**, 1592 (2012).

387. B. S. Simpkins, A. D. Dunkelberger & J. C. Owrutsky. *Mode-Specific Chemistry through Vibrational Strong Coupling (or A Wish Come True)*. J. Phys. Chem. C **125**, 19081 (2021).

388. D. S. Wang & S. F. Yelin. *A Roadmap Toward the Theory of Vibrational Polariton Chemistry*. ACS Photonics **8**, 2818 (2021).

389. J. A. Campos-Gonzalez-Angulo, Y. R. Poh, M. Du & J. Yuen-Zhou. *Swinging between shine and shadow: Theoretical advances on thermally activated vibropolaritonic chemistry*. J. Chem. Phys. **158** (2023).

390. S. Grimme. *Calculation of the Electronic Spectra of Large Molecules*, in *Reviews in Computational Chemistry* (John Wiley & Sons, Ltd, 2004), pp. 153–218.

391. S. Sachdev. *A first course*, in *Quantum Phase Transitions* (Cambridge University Press, 2011), pp. 27–28.

392. L.-W. Wang & A. Zunger. *Solving Schrödinger's equation around a desired energy: Application to silicon quantum dots*. J. Chem. Phys. **100**, 2394 (1994).

393. O. Higgott, D. Wang & S. Brierley. *Variational Quantum Computation of Excited States*. Quantum **3**, 156 (2019).

394. M. Holthaus. *Floquet engineering with quasienergy bands of periodically driven optical lattices*. J. Phys. B: At. Mol. Opt. Phys. **49**, 013001 (2015).

Acknowledgments

> "While it is always best to believe in oneself, a little help from others can be a great blessing."
>
> Uncle Iroh, Avatar: The Last Airbender (S2E15)

Firstly, thank you to my advisor, Arghavan. Thank you for giving me the opportunity to do a PhD, for being a role model and an inspiration, and for believing in me at every step, even when I doubted myself. You are an extraordinary scientist who brought creative ideas, insights and solutions to our meetings. Thank you for being kind and caring, and for always making my day with photos of Pashmak.

Jiri, thank you for your unwavering support, infectious work ethic, and patient reminders to make sharp statements. I learnt much during our many discussions, where I always felt that I could ask questions without judgement. I look forward to future discussions, and hold out hope that one day you will give up rope climbing for bouldering.

Rene, thank you for letting a starry-eyed theoretical PhD student invade your experimental group, and for our successful collaborations. Working with you was always fun, and I learned a lot from your fast intuition and inventive thinking.

When I first arrived at the UvA, I was welcomed with open arms by the experimentalists in the Hyqs group. Rianne and Henrik, thank you for being kind and encouraging during my first months. Rima, thank you for establishing the milk co-op with me, for our ADE and wine tasting outings, and for reminding me to value work-life balance. I hope I can visit you and Julian soon. Elly, thank you for being a bright, positive influence. Our Taskmaster evenings and many concerts together (including one sunrise set) were true highlights. I'm excited to hear your new Australian accent.

Although I don't remember exactly how we first met, in 2022 Matteo and I decided, rather ambitiously in retrospect, to plan a ski trip. This was the first of many, many adventures together. Matteo, thank you for all of these adventures, for your patient support, and for teaching me so much about physics. I promise that one day we will go to Yellowstone.

Since I began at the UvA, many new people have joined the group. Ilango,

thank you for the cricket banter and our nice collaboration (minus our descent into the depths of Floquet theory). Bas, thank you for allowing me to sit on your wheel during bike rides and for coming to see Sungazer with me. Lorenzo, thank you for always joining me on coffee breaks, no matter how late I arrived at Science Park. I greatly enjoyed our conversations, dinners, and (ongoing) collaboration. Zeger, Louis, Clara, Katya, Egor, Jeremy, Lisa and everyone "across the hall" in the quantum gases and quantum information group, thank you for interesting discussions and many laughs over coffee, and for teaching me many things.

Nella, thank you for your emotional support during these final months, for always being someone I could complain with, and for translating my Summary into Dutch. I loved our Taskmaster evenings, and especially our Zurich trip. I promise that on the next trip we will eat dinner before 10pm.

Despite my attempts to masquerade as an experimentalist, I am still a theorist at heart. To the theorists "down the corridor", Bart, Alberto, Yining, Stijn, Emilio and Anahita, thank you for many engaging discussions and CMT journal clubs. Rebekka, thank you for your support and a fantastic trip to Albarracin, I hope you can join next year. Lieuwe, thank you for your wrong opinions on su(2) algebra and for sharing your thesis template.

Thank you to Joost, Anne-Marieke and Jessie for managing the IoP department so smoothly and professionally. Thank you also to the wizards who have worked, often behind the scenes, in the IoP Secretariat during my time: Astrid, Jirina, Gianny, Rose, Daniela and Marjanne. Dropping by to pick up a coffee pod and practice my Dutch always brightened my day.

Beyond UvA, I have learned a lot from many outstanding scientists. My thanks to Tyler Neely, Guillaume Gauthier and Matt Davis for being my first physics supervisors and for inspiring me to pursue research. Thank you to Athreya Shankar and Gavin Brennen for patiently teaching me about metrology and symmetric states, respectively, and to Tim Harris for inviting me to visit Munich. Thank you to Johannes Schachenmayer and the CQMT group in Strasbourg for so kindly welcoming me during my visit there. And thank you to Ting Rei Tan, Chris Valahu, Maverick Millican and the Sydney QCL group for our collaborations, which have been both a lot of fun and scientifically deeply rewarding.

Over the past four years, I have spent an inordinate amount of time at the bouldering gym and used almost all my holidays on bouldering trips. This is squarely the fault of a superb group of people. Erik, thank you for the fun sessions at Beta. Gergő, thank you for inviting me on my first climbing trip, for teaching me to be fearless, and for being a fellow Coldplay fan. George, thank you for showing me how to topout in Font, and for the gentle reminders that climbing should be fun. Ric, thank you for being kind and a calming influence, and for always taking the group photo. My thanks to Miguel for pushing me to improve and the "we got you" reassurances, to Juan for inspiring me to climb harder and for indulging my (admittedly egregiously wrong) opinions on Avalonia. Thank you also to Sasha for the reminders to "hold", to Dima for sharing my love of Prince Pockets, and to Coco for always making me wish that I traveled more.

When I moved to Amsterdam during COVID, I first lived at Hotel Jansen. To

all the incredible friends that I made there, thank you for the memorable evenings in the kitchen and the adventures. Special thanks to Maaike for introducing me to the group and for many fun evenings at your apartment, Fran for your positive energy and for always being willing to laugh with me, Sophia for hosting me in Brooklyn and Xiaoli for always making time to catch up when visiting Amsterdam. And Kate, thank you for being my bouldering and concert-going buddy, and for a wonderful stay in Birmingham.

Throughout my PhD, I was kept afloat by the members of "team cool". Maria, thank you for the creative chaos, and for spending so much time at our apartment that I often wondered when you would be moving in. I still use my "PhD tears" mug to this day. Sarah, thank you for being my fellow Australian in Amsterdam, for your endless energy and for always swimming with me at Westlandgracht. I have almost forgiven you for your Bilbao "facts". Pasq, thank you for our many movie evenings, fun trips to Intratuin and fascinating conversations. Your support and reassurances got me through tough times more than once. I can't wait for our interval training together in Sydney! And Kunal, you have been a constant throughout my time in Amsterdam. Thank you for listening to my rants and for your sage advice. Most of all, I appreciate the small moments we shared: trying a new bakery near our apartment, adding yet another sport to our watch roster, and making fun of each other for rushing up and down the stairs when running late.

Back home in Australia, I am incredibly fortunate to have a network of wonderful friends. Thank you to all of you for the catch ups, for coming to visit me, and for whisking me away on rejuvenating holidays.

Thank you to my extended family for your love, and for always making me laugh.

And finally, thank you to my family. Rachel, thank you for being the best sister, and for letting me visit you in Banff for what is still one of my favorite weeks ever. Truly, you inspire me more than you will ever know. Mum and Dad, thank you for the many, many hours of video calls, for visiting me often, and for your wisdom, reassurances and encouragement. You taught me by example to always try 100% at the things that I care about, and I hope that is reflected in this thesis. Your support and love means the world to me. From the bottom of my heart, thank you.

